Volume 66 • Number 3 • June 2018

Acta Geophysica

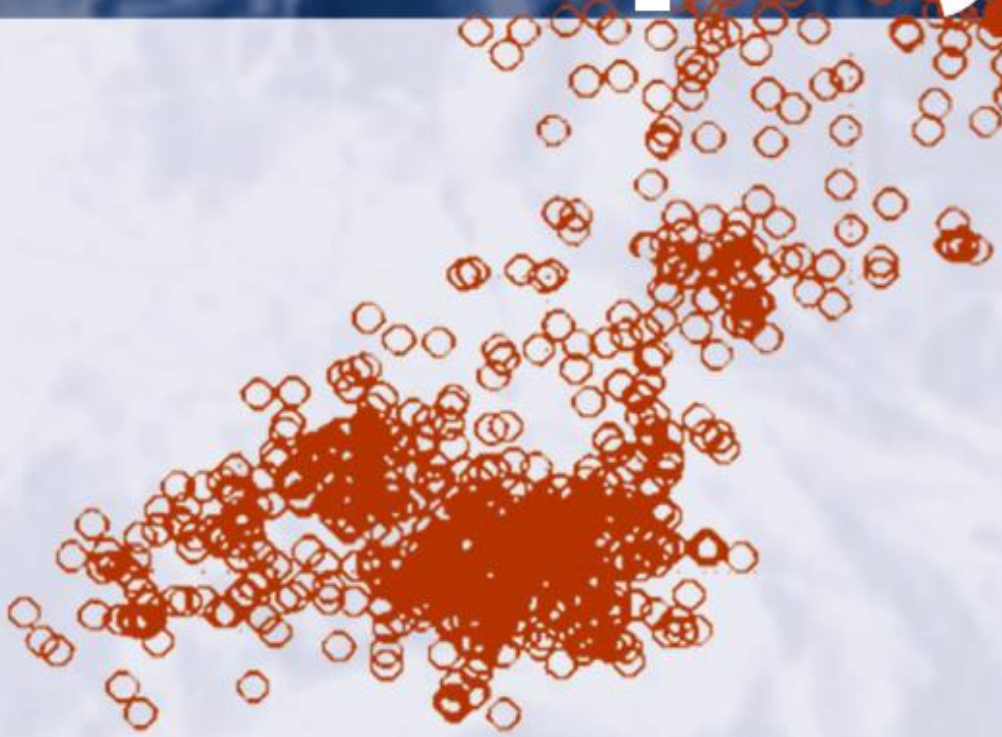

PAN
POLISH ACADEMY OF SCIENCES

Institute of Geophysics
Polish Academy of Sciences

Springer

Acta Geophysica (2018) 66:243–266
https://doi.org/10.1007/s11600-018-0132-3

RESEARCH ARTICLE - SOLID EARTH SCIENCES

Stochastic porous media modeling and high-resolution schemes for numerical simulation of subsurface immiscible fluid flow transport

Eric Thompson Brantson[1] · Binshan Ju[1,2] · Dan Wu[3] · Patricia Semwaah Gyan[4]

Received: 10 July 2017 / Accepted: 24 March 2018 / Published online: 7 April 2018

Abstract

This paper proposes stochastic petroleum porous media modeling for immiscible fluid flow simulation using Dykstra–Parson coefficient (V_{DP}) and autocorrelation lengths to generate 2D stochastic permeability values which were also used to generate porosity fields through a linear interpolation technique based on Carman–Kozeny equation. The proposed method of permeability field generation in this study was compared to turning bands method (TBM) and uniform sampling randomization method (USRM). On the other hand, many studies have also reported that, upstream mobility weighting schemes, commonly used in conventional numerical reservoir simulators do not accurately capture immiscible displacement shocks and discontinuities through stochastically generated porous media. This can be attributed to high level of numerical smearing in first-order schemes, oftentimes misinterpreted as subsurface geological features. Therefore, this work employs high-resolution schemes of SUPERBEE flux limiter, weighted essentially non-oscillatory scheme (WENO), and monotone upstream-centered schemes for conservation laws (MUSCL) to accurately capture immiscible fluid flow transport in stochastic porous media. The high-order schemes results match well with Buckley Leverett (BL) analytical solution without any non-oscillatory solutions. The governing fluid flow equations were solved numerically using simultaneous solution (SS) technique, sequential solution (SEQ) technique and iterative implicit pressure and explicit saturation (IMPES) technique which produce acceptable numerical stability and convergence rate. A comparative and numerical examples study of flow transport through the proposed method, TBM and USRM permeability fields revealed detailed subsurface instabilities with their corresponding ultimate recovery factors. Also, the impact of autocorrelation lengths on immiscible fluid flow transport were analyzed and quantified. A finite number of lines used in the TBM resulted into visual artifact banding phenomenon unlike the proposed method and USRM. In all, the proposed permeability and porosity fields generation coupled with the numerical simulator developed will aid in developing efficient mobility control schemes to improve on poor volumetric sweep efficiency in porous media.

Keywords Permeability and porosity fields · Turning bands method · Carman–Kozeny equation · SUPERBEE flux limiter · Monotone upstream-centered schemes for conservation laws · Weighted essentially non-oscillatory schemes

✉ Eric Thompson Brantson
ericthompson785@yahoo.com

✉ Binshan Ju
jubs2936@163.com

Dan Wu
wudan52087@126.com

Patricia Semwaah Gyan
triciagyan@gmail.com

[1] School of Energy Resources, China University of Geosciences (Beijing), Beijing 100083, China

[2] Key Laboratory of Marine Reservoir Evolution and Hydrocarbon Accumulation Mechanism, Ministry of education, China University of Geosciences (Beijing), Beijing, China

[3] Patent Examination Cooperation Centre, SIPO, Beijing 100081, China

[4] Faculty of Earth Resources, China University of Geosciences, Wuhan 430074, China

Introduction

In reality, it is impossible to physically sample at every infinitesimal point in space in a geological porous media for reservoir fluid flow analyses. Hence, Monte Carlo simulations in geostatistics and numerical reservoir simulation are commonly used to create numerous numbers of realizations over a grid mesh to predict future reservoir fluid flow performance and uncertainty quantification. However, Dubrule (1988) and Haldorsen and Damsleth (1990) carried out a number of stochastic modeling on discrete (Markov fields, two-point histograms, truncated random functions, and Boolean schemes), continuous (fractals, universal and indicator kriging, random Gaussian fields) and hybrid approach of both techniques. Moreover, the continuous type of stochastic models are generally suitable for modeling the spatial distribution of petrophysical properties with an assumption of more or less stationarity (Haldorsen and Damsleth 1990). But, Gaussian (Deutsch and Journel 1992) and continuous spectral methods (Shinozuka and Jan 1972) are the most widely used approximate algorithms for generating numerical geological model architectures. However, TBM (Matheron 1973) as one of the oldest methods is also used for simulating spatially correlated multidimensional random field which is still rarely used in geostatistical and numerical simulation applications (Emery and Lantuéjoul 2006). The TBM and USRM (Sabelfeld 1991) was considered in this study for immiscible fluid flow transport. Furthermore, the characterization of heterogeneous petroleum reservoirs using geostatistical tools and stochastic simulation methods are often preferred to traditional interpolation techniques in which hydrocarbon fluids are transported. With regards to this assertion, Lake and Malik (1993) compared deterministic and conditional simulation results and came to the conclusion that, conditional simulation must be tailored to specific geological environment to be in a reliable agreement with deterministic simulation. All these techniques permit accurate capture of internal heterogeneous fine-scale details and quantification of uncertainties for reliable reserve estimation (De Lucia et al. 2011).

Correlation length defines the spatial correlation that exists between pore spaces in porous media which provide details of correlated reservoir heterogeneity for quantitative analyses (Bijeljic et al. 2013; Babaei and Joekar-Niasar 2016). In addition, the importance of correlation length for multiphase fluid flow simulation was demonstrated by Kalia and Balakotaiah (2009) in their study. Also, correlation length was incorporated into pore network models to describe correlated reservoir heterogeneity impact on two-phase flows (Knackstedt et al. 2001; Leng 2013; Babaei and Joekar-Niasar 2016). Araktingi and Orr (1993) also reported that, permeability field distribution and correlation length have a significant effect on the fingering pattern in porous media. Johnson (1956) also pointed out that reservoir heterogeneity has a strong negative impact on oil recovery. It is also important to note that, most petroleum porous media used for reservoir modeling lack heterogeneity, thereby preventing capturing of real subsurface instabilities (Islam et al. 2010). Craig (1971) noticed that the existence of fingering as a subsurface instability on different length scales in petroleum reservoirs appears to be one of the unresolved challenges in the petroleum industry. One enhanced oil recovery (EOR) method of great potential in overcoming water mobility is through polymer flooding (Daripa et al. 1988; Delamaide 2014) which increases injected fluid viscosity by preventing viscous fingering. Despite the reliability of polymer flooding in improving sweep efficiency, its performance still requires optimization for flow stability, but not treated in this work.

Nevertheless, the generation of these stochastic porous media realizations require high-resolution schemes, not to misinterpret numerical dispersion as subsurface geological features inherent in porous media. According to Zhang and Al Kobaisi (2017), despite many years of intensive investigation into simultaneous flow of water and oil in petroleum reservoirs, yet, it still poses serious challenges for reliable and accurate numerical reservoir simulation. Meanwhile, thorough investigation of the weakness of commonly used upstream mobility weighting schemes in conventional black oil simulators oftentimes result into substantial amount of spurious oscillations and unphysical solutions (Taggart and Pinczewski 1985). Even, properly constrained two-point upstream weighting scheme proposed as an alternative method is not monotonicity-preserving (Rubin and Blunt 1991) and such a limitation has also motivated the present work. Furthermore, higher order differencing schemes (central differencing scheme (CD), quadratic upstream interpolation for convective kinematics (QUICK), etc.) have been developed and implemented for discretizing convective terms in multiphase fluid flow simulation. But then, the implementation of boundary conditions, over and undershoot in numerical solutions are a source of concern for high-order schemes which led to the development of second-order TVD schemes to obtain oscillation-free solutions of higher order schemes (Versteeg and Malalasekera 2007).The insight gathered from these studies is that, the implementation of high-resolution second-order schemes into fully implicit method (FIM) conventional simulators to capture and characterize subsurface fluid flow dynamics and transport is a challenge in reservoir modeling (Rubin and Blunt 1991; Marcu 2004).

In view of the above developments, the first objective of this paper involves finite volume (FV) stochastic simulation

using Dykstra–Parson coefficient and autocorrelation lengths to generate 2D plausible stochastic permeability field values which were also used to generate porosity fields through a linear interpolation technique based on Carman–Kozeny equation. The proposed method was compared to other well-known methods of generating permeability fields, such as TBM and USRM which are scarcely used for fluid flow simulation. The second objective of this work is to apply some robust and powerful high-resolution schemes to attenuate large wiggles in low order schemes to capture accurately immiscible fluid flow subsurface details. In this study, SUPERBEE flux limiter (Roe 1985), MUSCL scheme (Van Leer 1979) and WENO scheme (Liu et al. 1994) were tested on a one-dimensional waterflood. Also, a validation test with classical BL analytical solution (Buckley and Leverett 1942) to detect overshoot and undershoot in numerical solutions was conducted.

Third, a comparative analysis was carried out between two-phase flow linearization schemes (simultaneous solution, SEQ and iterative IMPES) to find the most efficient and stable scheme with regards to ill-conditioning of the Jacobian matrix that may arise. However, Newton–Raphson method is the most commonly used algorithm for solving coupled nonlinear system of equations (Monteagudo and Firoozabadi 2007a, b). But, computational cost and memory requirement become expensive when the immiscible displacement problem is very large with restrictions. Byer (2000) stated in his study that, precondition approaches can be employed to simulate petroleum reservoirs by increasing the convergence rate of the Newton-type techniques. Another technique to improve this convergence rate is to apply regularization step under additional constraints on the discretization parameters (Radu et al. 2006), and automatic differentiation also speed up the Newton method. The problem associated with the Newton–Raphson method (NRM) is that, it is quadratic with local convergence rate. This notwithstanding, NRM also strongly depends on the initial estimate (List and Radu 2016) as well as computation of derivatives have motivated this study to test other linearization schemes.

Therefore, the system of nonlinear time-dependent partial differential equations were solved numerically (temporal and spatial discretization) using FIM (unconditional stable, large timestep size), iterative IMPES (conditionally stable, less computational cost and memory requirement with smaller timestep size) which is more stable than classical IMPES (Chen 2007; Kou and Sun 2010), and sequential solution method (MacDonald 1970) (solving pressure and saturation implicitly but not simultaneously in two conservative steps) were applied to solve the basic fluid flow equations. It is important to mention that both iterative IMPES and SEQ methods are easier to implement computationally (Pacheco et al. 2016). The significance of correlation lengths on immiscible fluid flow transport in correlated stochastic porous media were also explored in this study. In summary, this study will serve as an indispensable tool in understanding spatial heterogeneity and the formulation of stabilized mobility control schemes to enhance better volumetric sweep efficiency in porous media.

This paper is structured into the following five sections. "Methodology" in section describes the physical model formulation, generation of permeability and porosity fields with illustrative examples using the proposed method, TBM and USRM techniques. The mathematical model and high-resolution schemes for oil and water fluid flow transport governing equations were formulated. "Computer model development" in section talks about the computer model development workflow and implementation strategy for reservoir description. Then, "Numerical results and discussion" in section dwells on numerical examples, results and discussion. Finally, "Conclusions" in section states key major conclusions drawn from the study.

Methodology

Physical model description

The 2D horizontal plane model consists of water injected at the left boundary with the right boundary producing water and oil (Fig. 1) similar to a direct line drive. In the reservoir physical model, the domain was initially saturated with oil without water saturation. The injector and producer horizontal wells were both perforated along the whole width of the structured computational model for linear flow pattern. The reservoir length is principal to flow direction and the reservoir width direction is perpendicular to flow direction. The side walls of the porous medium in Fig. 1 are impermeable to fluid flow. The rock and fluid properties used are summarized in Table 1 for the numerical experiments. The model consists of $100 \times 100 \times 1$ cell volumes with cell faces and cell centers discretized by finite volume method (FVM) which is mass conservative.

Stochastic modeling techniques for porous media architecture

The following procedures below were used to generate the 2D stochastic correlated permeability (dynamic property) field realizations, whereas these permeability field values were in turn used to generate 2D porosity field spatial variability (volumetric property) through a linear interpolation technique based on Carman–Kozeny equation. The proposed method of permeability field images generated were based on the idea of signal processing methodology to create random Gaussian field models. In addition, the

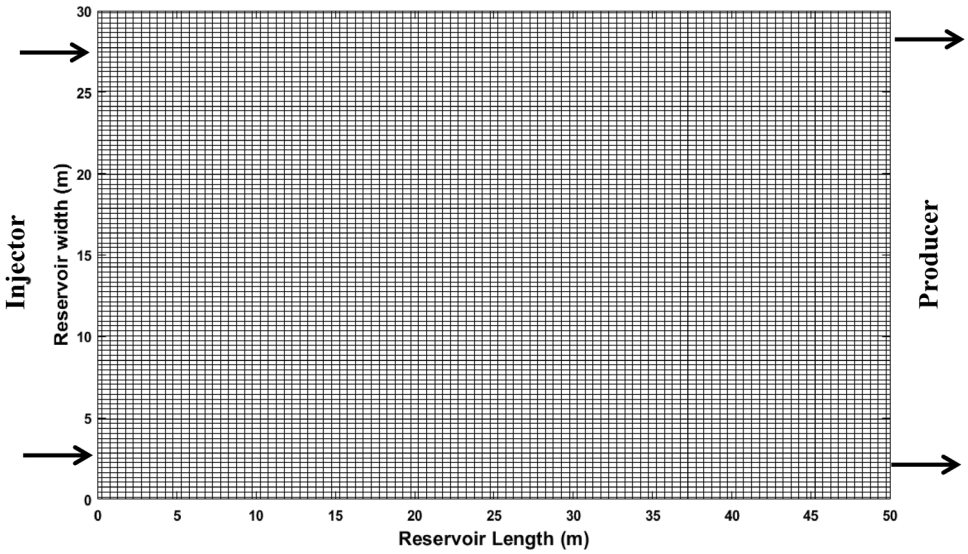

Fig. 1 2D Geometry of the discretized reservoir model (100 × 100 × 1 gridblocks)

Table 1 Numerical model validation data

Reservoir parameters	Data values	English units
Oil viscosity (μ_o)	10×10^{-3}	Pa.s
Water viscosity (μ_o)	1×10^{-3}	Pa.s
Number of cell volume (N_x)	100	
Number of cell volume (N_y)	100	
Reservoir length (L_x)	50	m
Reservoir width (L_y)	30	m
Reservoir initial pressure (P_i)	1×10^5	Pa
Well injection pressure (P_{inj})	2×10^5	Pa
Water saturation (S_w)	0	Fraction
Oil saturation (S_o)	1	Fraction
Average porosity (ϕ)	0.20	Fraction
Average permeability ($K_{average}$)	2×10^{-12}	m^2
Correlation length (λ_x)	0.0–0.05	m
Correlation length (λ_y)	0.0–0.05	m
End point oil relative permeability (K_{ro})	1	
End point water relative permeability (K_{rw})	1	
Corey water exponent (n_w)	2	
Corey water exponent (n_o)	2	
Pressure accuracy	0.0001	
Saturation accuracy	0.0001	
Dykstra–Parsons coefficient (V_{DP})	0.0–0.9	

proposed method spelt out here is compared to widely known TBM and USRM for analyzing permeability maps and fluid flow simulations through them.

Methodology of the proposed permeability field

1. Rectangular grid mesh tessellation of the petrophysical properties (permeability and porosity fields) were created as shown in Fig. 1.
2. Dykstra and Parsons (1950) coefficient (V_{DP}) is the most common static measure of permeability variation as expressed in Eq. (1) which was used for perturbation. When $V_{DP} = 0$, then the reservoir is homogeneous, while $V_{DP} = 1$, the reservoir is highly heterogeneous.

$$V_{\mathrm{DP}} = \frac{\log \bar{k} - \log k\sigma}{\log \bar{k}} = \frac{\text{standard deviation of Log}(k)}{\text{Average of Log}(k)}, \quad (1)$$

where $\bar{k}$ is the median permeability or permeability value with 50 percent probability and $k\sigma$ is the permeability at 84.1 percent of the cumulative sample and σ is the standard deviation.

3. However, from the definition of V_{DP} (variance of the log-normal permeability distribution) in Eq. (1), an estimator relationship between V_{DP} and sample standard deviation (σ) of Log (k) is rearranged as defined in Eq. (2) as:

$$\sigma = -\log(1 - V_{\mathrm{DP}}). \quad (2)$$

4. Then, sample mean (μ) for log-normal randomly distributed field was estimated as written in Eq. (3) as:

$$\mathrm{Log}\left(k_{\mathrm{average}}\right) = \mu + 1/2\sigma^2, \quad (3)$$

where k_{average} is the average permeability.

5. The uncorrelated Gaussian random permeability field distribution (which amounts to adding a white noise to the simulated random field) was generated by using Eq. (4), but this noise needed to be filtered out by convolution with Gaussian kernel:

$$R = \sigma.\ \mathrm{randn}\ \left(N_x, N_y\right), \quad (4)$$

where R is the uncorrelated Gaussian random function distribution, N_x and N_y are the number of cells in x and y direction, respectively, randn function for generating random numbers drawn from a normal distribution.

6. With the obtained standard deviation [Eq. (2)] and a known average permeability, the Gaussian log-normal uncorrelated permeability field distribution generated from step 5 with white noise was pass through a Gaussian filter (smooth dataset). In two dimensions (x, y), the mathematical expression for the product of two Gaussian functions for the Gaussian filter impulse response (Gaussian surface) is given by Eq. (5) (Haddad and Akansu 1991; Mark et al. 2008) as:

$$\mathrm{GF}(x, y) = \frac{1}{2\pi\sigma^2} \times \mathrm{e}^{-\left(\frac{x^2+y^2}{2\sigma^2}\right)}, \quad (5)$$

where GF is the gaussian filter in two dimensions, x and y define the distance from the origin in the horizontal and vertical axis.

7. A convolution (faltning) with Gaussian filtering algorithm was used to achieve a correlated hydraulic conductivity field from the uncorrelated hydraulic conductivity field generated in step 5. This convolution was efficiently performed using Matlab (2016) discrete 2D fast Fourier transform (FFT) [Eq. (6)], and 2D inverse fast Fourier transform (IFFT) [Eq. (7)] as well as normalization of prefactors:

$$Y_{k+1,j+1} = \sum_{p=0}^{a-1} \sum_{q=0}^{b-1} \omega_a^{pk} \omega_b^{qj} X_{p+1,q+1}, \quad (6)$$

ω_a and ω_b are complex roots of unity, $\omega_a = \mathrm{e}^{-2\pi i/a}$, $\omega_b = \mathrm{e}^{-2\pi i/b}$, where a-by-b is matrix, i is the imaginary unit, k and p are indices that run from 0 to $a - 1$, j and q are indexes that run from 0 to $b - 1$.

$$X_{k,j} = \frac{1}{a} \sum_{p=1}^{a} \frac{1}{b} \sum_{q=1}^{b} \omega_a^{pk} \omega_b^{qj} Y_{p,q}, \quad (7)$$

ω_a and ω_b are complex roots of unity, $\omega_a = \mathrm{e}^{2\pi i/a}$, $\omega_b = \mathrm{e}^{2\pi i/b}$, where k runs from 1 to a, and j runs from 1 to b.

8. The results of R in step 5 and the Gaussian filter (GF) in step 6 are transformed and evaluated by 2D FFT and the results are multiplied as indicated in Eq. (8). The FFT transformation is back transformed using 2D IFFT to obtain convoluted Gaussian correlated field. In furtherance, the correlated surface generated with convolution, 2D FFT, 2D IFFT and normalization of prefactors through another filter is expressed in Eq. (8) (Bergström 2012). However, according to Garcia and Stoll (1984), proper care must be taken in choosing appropriate prefactors during IFFT (FFT back transformation) to ensure satisfied relations of spatially correlated Gaussian random fields.

$$f = \frac{2}{\sqrt{\pi}} \times \left[\frac{\frac{L_x}{\sqrt{N_x \times N_y}}}{\sqrt{\frac{\lambda_x}{\lambda_y}}}\right] \times X_{k,j}\left[Y_{k+1,j+1}(R) \times Y_{k+1,j+1}(F)\right], \quad (8)$$

where L_x is the length of computational domain, λ_x and λ_y represents autocorrelation lengths in both x and y directions, respectively.

9. The correlation lengths (λ_x and λ_y) in Eq. (8) represent the maximum distance at which two points display a correlation used in generating the spatial variability of the geological media. If one autocorrelation length is used, then the medium is termed homogeneous. The final permeability field is generated by computing the

summation of sample mean [Eq. (3)] and the real part of Eq. (8) raised to an exponent ($K = e^{[\mu+\text{real}(f)]}$) (Eftekhari and Schüller 2015).

10. The porosity field through a linear interpolation scheme is generated based on the permeability field values created using Dykstra–Parsons coefficient and autocorrelation lengths by employing Carman–Kozeny relation expressed in Eq. (9) (Lie 2014) as:

$$K = \frac{1}{8\tau A_v^2}\frac{\phi^3}{(1-\phi)^2}, \tag{9}$$

where ϕ is the porosity which is a function of permeability, τ is tortuosity, A_v is the specific surface area.

Uniform sampling randomization method

USRM was used to generate homogeneous random permeability field compared to our proposed method and for fluid flow simulation. However, the uniform sampling variant of the randomization is made up of superposition of independent (Gaussian random variables of mean zero and unit variance) random sine modes (Radu et al. 2011). In this method (second-order homogeneous), isotropic correlation description is given by a function consisting of Euclidian norm and correlation length. This randomization method also exhibits good ergodic properties during simulation process of generating log-hydraulic conductivity field realizations. However, details about the mathematical implementation of this algorithm over a uniform grid can be found in Sabelfeld (1991) and Radu et al. (2011).

Turning bands simulation method

TBM is one of the earliest multidimensional random number generator simulation method used to generate spatially correlated permeability fields with its accuracy depending on the number of lines used. Whenever insufficient number of lines are used, it results into striping (artifact banding) in the simulated map (Emery and Lantuéjoul 2006). TBM performs simulation along unidimensional lines instead of synthesizing the multidimensional field directly with computational efficiency over a space domain and more efficient than LU decomposition algorithm (Gotway and Rutherford 1994). A non-conditional realization can be generated for visual inspections. The detailed and comprehensive mathematical algorithm of TBM for Gaussian random fields implemented in this study can be found in (Matheron 1973; Mantoglou and Wilson 1982; Emery and Lantuéjoul 2006).

Mathematical modeling

Mathematical model basic assumptions

1. Immiscible fluids and rock properties are incompressible.
2. The solid matrix is non-deformable
3. Molecular diffusion, surface tension and capillary pressure were ignored.
4. The fluids are Newtonian and gravitational force is ignored.
5. Chemical reactions are not included and no phases change.
6. Viscous forces dominate, and capillary effects were neglected.

Immiscible two-phase flow transport in porous media

Applying macroscopic Darcy law as a momentum transport equation for saturated flow of oil and water in porous media for each control volume (CV) is written in Eq. (10) as:

$$\vec{u}_\alpha = -\frac{kk_{r\alpha}}{\mu_\alpha}\nabla p_\alpha, \tag{10}$$

where $\vec{u}$ is the velocity vector, $k_{r\alpha}$ is the relative permeability of a phase, k is absolute permeability tensor, μ is the viscosity of fluid, p is the reservoir pressure, ∇ is the gradient operator, α is the oil and water phase. Total fluid mobility is the summation (λ_T) of water phase mobility (λ_w) and oil phase mobility (λ_o) as defined in Eq. (11) as:

$$\lambda_T = k(x)\left[\frac{k_{rw}(S_w(x,t))}{\mu_w} + \frac{k_{ro}(S_o(x,t))}{\mu_o}\right], \tag{11}$$

where $S_w(x, t)$ and $S_o(x, t)$ are saturation of water and oil phase, respectively, defined in space and time. A displacement stability criterion for unstable flow is when mobility ratio is greater than one (upstream mobility greater than downstream mobility), and vice versa. The total Darcy velocity (u_T) is the summation of water and oil velocities given in Eq. (12) as:

$$u_T = -\lambda_T \nabla p. \tag{12}$$

Therefore, for an incompressible fluid flow, the continuity equation is read by Eq. (13) as:

$$\nabla . u_T = 0. \tag{13}$$

Substituting Eqs. (11) and (12) into Eq. (13) leads to Eq. (14) as:

$$\nabla.\left[-k\left(\frac{k_{\mathrm{rw}}(S_{\mathrm{w}})}{\mu_{\mathrm{w}}}+\frac{k_{\mathrm{ro}}(S_{\mathrm{w}})}{\mu_{\mathrm{o}}}\right)\nabla p\right]=0. \tag{14}$$

Linearizing Eq. (14) using Taylor series expansion resulted into Eq. (15) as:

$$\begin{aligned}&\nabla.\left[-k\left(\frac{k_{\mathrm{rw}}(S_{\mathrm{wi}})}{\mu_{\mathrm{w}}}+\frac{k_{\mathrm{ro}}(S_{\mathrm{wi}})}{\mu_{\mathrm{o}}}\right)\nabla p\right]\\&\quad+\nabla.\left[k\left(\frac{\partial k_{\mathrm{rw}}(S_{\mathrm{wi}})}{\mu_{\mathrm{w}}\partial S_{\mathrm{w}}}+\frac{\partial k_{\mathrm{ro}}(S_{\mathrm{wi}})}{\mu_{\mathrm{o}}\partial S_{\mathrm{w}}}\right)\nabla p_i S_{\mathrm{w}}\right]\\&\quad=\nabla.\left[k\left(\frac{\partial k_{\mathrm{rw}}(S_{\mathrm{wi}})}{\mu_{\mathrm{w}}\partial S_{\mathrm{w}}}+\frac{\partial k_{\mathrm{ro}}(S_{\mathrm{wi}})}{\mu_{\mathrm{o}}\partial S_{\mathrm{w}}}\right)\nabla p_i S_{\mathrm{wi}}\right],\end{aligned} \tag{15}$$

where S_{wi} is the initial water saturation, S_{w} is the new values of water saturation, p_{i} is the initial reservoir pressure, k is the absolute permeability, k_{ro} and k_{rw} are relative permeability of oil and water, respectively.The relative permeability function in Eq. (15) for immiscible fluid flow transport was modeled using Corey (1954) correlation illustrated in Eqs. (16) and (17) for oil and water, respectively as:

$$k_{\mathrm{ro}}=\left[\frac{1-S_{\mathrm{o}}}{1-S_{\mathrm{wi}}}\right]^{\mathrm{no}}\left[1-\left(\frac{S_{\mathrm{o}}-S_{\mathrm{wi}}}{1-S_{\mathrm{wi}}}\right)\right]^{\mathrm{no}}, \tag{16}$$

$$k_{\mathrm{rw}}=\left[\left(\frac{S_{\mathrm{w}}-S_{\mathrm{wi}}}{1-S_{\mathrm{wi}}}\right)\right]^{\mathrm{nw}}, \tag{17}$$

where S_{wi} is the initial water saturation, n_{o} is the Corey constant parameter for oil, n_{w} is the Corey constant parameter for water.The nonlinear flow equation in Eq. (15) for pressure gradient field has the following discretization terms in Eq. (18) as:

$$\begin{aligned}&-\text{ Diffusion term }\left[k\left(\frac{k_{\mathrm{rw}}(S_{\mathrm{wi}})}{\mu_{\mathrm{w}}}+\frac{k_{\mathrm{ro}}(S_{\mathrm{wi}})}{\mu_{\mathrm{o}}}\right),p\right]\\&+\text{Convection term }\left[u\left(\frac{k_{\mathrm{rw}}(S_{\mathrm{wi}})}{\mu_{\mathrm{w}}}+\frac{k_{\mathrm{ro}}(S_{\mathrm{wi}})}{\mu_{\mathrm{o}}}\right),p\right]\\&=\text{Divergence term }\left[k\left(\frac{k_{\mathrm{rw}}(S_{\mathrm{wi}})}{\mu_{\mathrm{w}}}+\frac{k_{\mathrm{ro}}(S_{\mathrm{wi}})}{\mu_{\mathrm{o}}}\right),\nabla p_{\mathrm{i}}\right]\end{aligned} \tag{18}$$

Whenever the pressure gradient is known from Eq. (18), then water velocity from Eq. (12) can be estimated to be used in the water transport Eq. (19). For simultaneous oil and water flow transport in a stochastic porous medium, the conservation equation of the water transport is specified in Eq. (19) as hyperbolic saturation equation:

$$\phi\frac{\partial S_{\mathrm{w}}}{\partial t}+\nabla.\left(-\frac{kk_{\mathrm{rw}}(S_{\mathrm{w}})}{\mu_{\mathrm{w}}}\nabla p\right)=0. \tag{19}$$

Again, linearizing Eq. (19) using Taylor series expansion for a function of two independent variables yielded Eq. (20) as:

$$\begin{aligned}&\varphi\frac{\partial S_{\mathrm{w}}}{\partial t}+\nabla.\left(-\frac{kk_{\mathrm{rw}}(S_{\mathrm{wi}})}{\mu_{\mathrm{w}}}\nabla p\right)\\&\quad+\nabla.\left(-\frac{k}{\mu_{\mathrm{w}}}\frac{\partial k_{\mathrm{rw}}(S_{\mathrm{wi}})}{\partial S_{\mathrm{w}}}\nabla p_{\mathrm{i}}S_{\mathrm{w}}\right)\\&\quad=\nabla.\left(-\frac{k}{\mu_{\mathrm{w}}}\frac{\partial k_{\mathrm{rw}}(S_{\mathrm{wi}})}{\partial S_{\mathrm{w}}}\nabla p_{\mathrm{i}}S_{\mathrm{wi}}\right)\end{aligned} \tag{20}$$

But the total saturation of both oil and water flow in porous media is defined in Eq. (21) as:

$$S_{\mathrm{o}}+S_{\mathrm{w}}=1. \tag{21}$$

The nonlinear water transport flow equation in Eq. (20) has the following discretization terms in Eq. (22) as:

$$\begin{aligned}&\text{Transient term }(\Delta t,S_{\mathrm{w}})\\&-\text{ Diffusion term}\left[\left(-\frac{kk_{\mathrm{rw}}(S_{\mathrm{wi}})}{\mu_{\mathrm{w}}}\nabla p\right),S_{\mathrm{w}}\right]+\\&\text{Convection term}\left[u\left(-\frac{k}{\mu_{\mathrm{w}}}\frac{\partial k_{\mathrm{rw}}(S_{\mathrm{wi}})}{\partial S_{\mathrm{w}}}\nabla p_{\mathrm{i}}\right),S_{\mathrm{w}}\right]\\&=\text{Divergence term}\left[\left(-\frac{k}{\mu_{\mathrm{w}}}\frac{\partial k_{\mathrm{rw}}(S_{\mathrm{wi}})}{\partial S_{\mathrm{w}}}\nabla p_{\mathrm{i}}\right),S_{\mathrm{wi}}\right].\end{aligned} \tag{22}$$

With regards to discretization terms in Eqs. (20) and (22), these result into a system of coupled linear simultaneous equations expressed in Eq. (23). The primary unknowns in Eq. (23) are pressure and saturation for the simultaneous solution (SS) method (Douglas et al. 1959; Eftekhari and Schüller 2015):

$$\begin{bmatrix}J_{\mathrm{pm}}+M_{\mathrm{bcp}} & J_{\mathrm{Swm}}\\ J_{\mathrm{pn}} & J_{\mathrm{Swn}}+M_{\mathrm{bcSw}}\end{bmatrix}\begin{bmatrix}P\\S_{\mathrm{w}}\end{bmatrix}=\begin{bmatrix}\mathrm{RHS_m}+\mathrm{RHS_{bcp}}\\ \mathrm{RHS_n}+\mathrm{RHS_{bcSw}}\end{bmatrix}, \tag{23}$$

where J is the Jacobian matrix, m denotes the continuity equation for pressure while n indicates water saturation equation, M_{bc} terms denotes boundary conditions matrix terms for pressure and water saturation equations, P is pressure, S_{w} is water saturation, RHS indicates right-hand side of the coupled equations, $\mathrm{RHS_{bc}}$ term signifies right-hand side boundary conditions matrix terms for pressure and water saturation equations.

Solution technique to immiscible fluid flow in porous media transport

Newton–Raphson method (NRM) The method used to solve the system of linearized equations in Eq. (23) is Newton–Raphson powerful iterative method which is quadratic but only locally convergent with computation of derivatives (Bergamashi and Putti 1999). However, at every timestep, Eq. (23) needs to be solved in a loop until new values converge to initial values (Farnstrom and Ertekin 1987). This is because the convergence of the

Newton–Raphson algorithm is not guaranteed when the initial guess is not close enough to the solution, which implies a restriction on the timestep size (computational cost and memory requirement when problem size increases). The tractable iterative algorithm implemented in this study is solved concurrently and expressed in Eqs. (24) and (25), respectively as:

$$X_{k+1} = X_k - \frac{f(X_n)}{f'(X_n)}, \tag{24}$$

$$\begin{bmatrix} P^{n+1} \\ S_{\mathrm{w}}^{n+1} \end{bmatrix} = \begin{bmatrix} P_{\mathrm{o}} \\ S_{\mathrm{wo}} \end{bmatrix} - \begin{bmatrix} \frac{\partial(J_{\mathrm{pm}} + M_{\mathrm{bcp}})}{\partial P} & \frac{\partial(J_{\mathrm{Swm}})}{\partial S_{\mathrm{w}}} \\ \frac{\partial(J_{\mathrm{pn}})}{\partial P} & \frac{\partial(J_{\mathrm{Swn}} + M_{\mathrm{bcSw}})}{\partial(S_{\mathrm{w}})} \end{bmatrix}^{-1}_{(P_{\mathrm{o}}, S_{\mathrm{wo}})} \times \begin{bmatrix} (J_{\mathrm{pm}} + M_{\mathrm{bcp}})P_{\mathrm{o}} + (J_{\mathrm{Sw1}})S_{\mathrm{wo}} - (\mathrm{RHS_m} + \mathrm{RHS_{bcp}}) \\ (J_{\mathrm{pn}})P_{\mathrm{o}} + (J_{\mathrm{Swm}} + M_{\mathrm{bcSw}})S_{\mathrm{wo}} - (\mathrm{RHS_n} + \mathrm{RHS_{bcSw}}) \end{bmatrix}. \tag{25}$$

It is important to state here that the FIM Newton–Raphson iterative method for two-phase fluid flow in stochastic porous media was compared in terms of convergence rate and stability to iterative IMPES and SEQ linearization schemes. The details of these linearization schemes implemented in this study can be found in (Lacroix et al. 2003; Pacheco et al. 2016).

Methodology of high-resolution models for immiscible fluid flow transport

Here, it is the discretisation of the convective flux term that requires special attention to represent fluid flow patterns, since our goal is to find a scheme with a higher order of accuracy without wiggles for high-resolution (Harten 1983) shock-capture. Additionally, to estimate the average value of water saturation at cell faces over the mesh structure as shown in Fig. 1 based on velocity direction. Equation (19) describing incompressible fluid flow in porous media is rewritten in Eq. (26) as:

$$\phi \frac{\partial S_{\mathrm{w}}}{\partial t} + \nabla.(f_{\mathrm{w}} u_T) = 0, \tag{26}$$

where $f(s_{\mathrm{w}}) = \frac{\lambda_{\mathrm{w}}}{\lambda_{\mathrm{T}}}$ is the fractional flow of water.

The spatial domain (Fig. 1) is divided into finite volume cells (ith) and taking volume integral over the total volume of a cell (v_i) from Eq. (26) is expressed in Eq. (27) as:

$$\int_{v_i} \frac{\partial s}{\partial t} \mathrm{d}v + \int_{v_i} \nabla.f(s) \mathrm{d}v = 0. \tag{27}$$

Also, the volume integrals in the partial differential equation in Eq. (27) contain a divergence term which is converted into surface integrals by employing the divergence theorem given in Eq. (28) as:

$$\oint_v \nabla.f \mathrm{d}v = \oint_S f \mathrm{d}S. \tag{28}$$

Integrating the first term in Eq. (27) yields volume average and applying divergence theorem in Eq. (28) to Eq. (27) second term results into Eq. (29) as:

$$v_i \frac{d\bar{s}_i}{dt} + \oint_{S_i} f(s).\, n dS = 0, \tag{29}$$

where n is a unit vector normal to the surface and pointing outward, S_i denotes the total surface area of the cell.

The final general conservative result obtained in Eq. (30) is equivalent to Eq. (26) as:

$$\frac{\mathrm{d}\bar{s}_i}{\mathrm{d}t} + \frac{1}{v_i} \oint_{S_i} f(s).n \mathrm{d}S = 0 \tag{30}$$

The application of high-resolution scheme consists of adding a diffusive term to second-order Lax–Wendroff scheme (Wendroff 1960). Equation 31 describes incompressible flow of a linear convection equation in a one-dimensional porous media and assuming that the flow is from left to right which can be extended to two dimensions with the same flow properties. Therefore, the numerical approximations to scalar conservation hyperbolic equation by recalling Eq. (26) is given by:

$$\begin{aligned} &\frac{\partial s}{\partial t} + \frac{\partial f(s)}{\partial x} = 0, \\ &s(x,\ 0) = s_0(x), \end{aligned} \tag{31}$$

where the flux $f(s)$ is a known function of s as the saturation of water phase.

The upwind differencing (transportiveness, conservativeness, boundedness and accurate) or 'donor cell' differencing scheme takes into account flow direction when determining cell face value. Applying first order upwind scheme to Eq. (31) leads to a numerical scheme written in a conservative form as Eq. (32) as:

$$s_i^{n+1} = s_i^n - \eta\left(\Delta s_{i-1/2}^{n+1}\right), \tag{32}$$

where s_{i}^n is the nodal values.

Meanwhile, the conservative form of Lax–Wendroff scheme for a nonlinear equation yields Eq. (33) as:

$$s_i^{n+1} = s_i^n - \frac{\eta}{2}\left(\Delta s_{i-1/2}^{n+1} + \Delta s_{i+1/2}^{n+1}\right) + \frac{\eta^2}{2}\left(\Delta s_{i+1/2}^{n+1} - \Delta s_{i-1/2}^{n+1}\right), \tag{33}$$

where upstream face/edge, $\Delta s_{i+1/2} = s_i - s_{i-1}$; downstream face/edge $\Delta s_{i-1/2} = s_i - s_{i-1}$ of the ith cell, courant number (mesh ratio) $\eta = \frac{\Delta t}{\Delta x}$

Therefore, reorganizing equation Eq. (33) results into Eq. (34) as:

$$s_i^{n+1} = s_i^n - \eta \Delta s_{i-1/2}^{n+1} - \frac{1}{2}\eta\,(1-\eta)\left(\Delta s_{i+1/2}^{n+1} - \Delta s_{i-1/2}^{n+1}\right). \quad (34)$$

From Eq. (33) which represents Lax–Wendroff scheme amounts to adding an anti-diffusion flux to an upwind scheme. However, this anti-diffusion term makes Lax–Wendroff scheme second-order accurate, although it creates non-physical oscillations in the presence of shocks and discontinuity. TVD is a property that is used in the discretisation of equations governing multiphase fluid flow in porous media. Hence, high-order resolution schemes (SUPERBEE, WENO and MUSCL) were imposed to limit anti-diffusion flux to obtain second-order high-resolution scheme between fluxes of a high-order scheme and that of a low order scheme. Therefore, the flux limiter is a function of the ratio of two consecutive gradients applied to Eq. (34). This application resulted into Eq. (35) as TVD fluid flow equation:

$$s_i^{n+1} = s_i^n - \eta \Delta s_{i-1/2}^{n+1} - \frac{1}{2}\eta\,(1-\eta)\left[\psi\left(r_{i+1/2}^{n+1}\right)\Delta s_{i+1/2}^{n+1} - \psi\left(r_{i-1/2}^{n+1}\right)\Delta s_{i-1/2}^{n+1}\right], \quad (35)$$

where ψ is the flux limiter function taken to be non-negative so as to maintain the sign of the anti-diffusive flux.

The ratio of the second-order term is also expressed in Eq. (36), where $\psi\left(r_{i+1/2}^{n+1}\right)$ is chosen so that it is approximately $\psi(1) = 1$ in smooth regions of the profile, giving accurate results. In regions where an unrestrained second-order contribution would produce oscillations (where the value of the second derivative is large), this term is allowed to vary in a manner which precisely eliminates their formation and $\left(r_{i+1/2}^{n+1}\right)$ is chosen to be a ratio of the successive second-order terms and a function of consecutive gradients.

$$\psi_{i+1/2}^{n+1} = \psi\left(r_{i+1/2}^{n+1}\right), r_{i+1/2}^{n+1} = \frac{\Delta s_{i-1/2}^{n+1}}{\Delta s_{i+1/2}^{n+1}} \quad (36)$$

According to Roe (1985), accurate solutions are obtained without spurious oscillations using TVD flux limiters that satisfies Sweby (1984) constraints. The computational codes developed in this work implements Sweby (1984) monotonicity-preserving sufficient conditions necessary for a scheme to be TVD in terms of the $r - \psi$ relationship. This implies that, they are designed to pass through TVD regions to guarantee stability of the scheme. Thus, the requirement for second-order accuracy in terms of the relationship for linear upwind terms are as follows (Brantson et al. 2018):

1. If $0 < r < 1$ the upper limit is $\psi(r) = 2r$, for TVD schemes $\psi(r) \leq 2r$
2. If $r \geq 1$ the upper limit is $\psi(r) = 2r$, for TVD schemes $\psi(r) \leq 2r$
3. For the relationship in terms of $\psi = \psi(r)$, a second-order accurate scheme should pass through the point (1, 1) in the $r - \psi$ diagram.

The TVD flux limiter scheme applied to first order scheme sharp concavity profile changes is known by Roe (1985) as SUPERBEE applied to Eq. (35) expressed in Eq. (37) as:

$$\psi(r) = \max[0,\ \min(2r, 1),\ \min(r, 2)];\ \lim_{r\to\infty}\psi(r) = 2 \quad (37)$$

The weighted essentially non-oscillatory (WENO) schemes can numerically approximate solutions of hyperbolic conservation laws and other convection dominated problems with high-order accuracy in smooth regions and essentially non-oscillatory transition for solution discontinuities. WENO construction (Eq. (38)) is an improvement on essentially non-oscillatory (ENO) applied to Eq. (35). Equation 38 describes the implementation of the scheme used in this study by Liu et al. (1994) as:

$$\psi(r) = \max[0,\ \min(r + b)]\,, \quad (38)$$

The MUSCL scheme is also tested as a second-order TVD scheme to obtain spatial accuracy in the smooth parts of the numerical solution defined in Eq. (39) as applied to Eq. (35):

$$\psi(r) = \max[0, \min(2r,\ \min\ (0.5\ (1 + r),\ 2)]\,, \quad (39)$$

where $\psi(r)$ is the flux limiter function, b is the biasing parameter.

Monotonicity-preserving second-order schemes have the property that the total variation of the discrete solution should diminish with time. Hence, the term TVD. The total variation (TV) is stated in Eq. (40) for the hyperbolic advective term in Eq. (31) as:

$$\mathrm{TV} = \int \frac{\partial f(s)}{\partial x}\partial x = 0. \quad (40)$$

The TV in saturation is non-increasing and the TV for a discrete case solution is defined in Eq. (41) as:

$$\mathrm{TV}\left(s_i^{n+1}\right) = \sum_i \left|s_{i+1}^{n+1} - s_i^{n+1}\right|. \quad (41)$$

A numerical method at every timestep is said to be TVD, if Eq. (42) is satisfied as:

$$\mathrm{TV}\left(s_i^{n+1}\right) \leq \mathrm{TV}\left(s_i^n\right), \quad (42)$$

where n and $n + 1$ are previous and current timestep, respectively.

Initial and boundary conditions

To complete the formulation of the model, the initial and boundary conditions are required by imposing restrictive conditions. The following initial and boundary constraints were specified for the simultaneous two-phase flow in a stochastic porous media for the modeling process.

$S_o = 1; S_w = 0$, where S_o is saturation of oil and S_w is saturation of water.

For an advancement of pressure and saturation solution in time until final simulation is reached is given by:

$t = t_o + \Delta t$, where t is the new timestep, t_o is the initial timestep = 0, Δt is the timestep size.

The boundary conditions were specified for both inflow (left) and outflow (right) of the stochastic porous medium using ghost border cells approach. In this current study, Dirichlet pressure boundary was specified for the left (constant injection pressure) and right-hand side (constant pressure boundary) of the porous medium. While Dirichlet constant water saturation boundary condition was specified for the left-hand side (LHS) of the perforated porous medium. The lateral walls of the computational domain are impermeable with no flow boundary conditions.

Computer model development

The mathematical models obtained from the previous sections require high-speed digital computer for implementation due to the size of the Jacobian matrix. In this paper, the steps used to develop the computer model is shown in Fig. 15 (Appendix). In Fig. 15, the workflow consists of internal nonlinear solver loop and external time loop under different flow conditions.

Numerical results and discussion

This section presents results, discussion and implementation of stochastic porous media modeling approaches as well as the linearization schemes. All simulations were conducted on a standard laptop (Samsung NP8500GM notebook with an intel i5 processor and 16 GB RAM) in Matlab (2016) programming environment.

Numerical reservoir simulator validation

BL analytical displacement (ideal case) was used to validate the high-order resolution schemes (SUPERBEE, WENO and MUSCL schemes) by considering one-dimensional linear (1 m) petroleum reservoir (40 gridblocks) in a homogeneous medium. This is because, BL is free from numerical dispersion. A comparative analysis was made between saturation distributions provided by the various schemes to check significant numerical dispersion (smearing) effect (Fig. 2) and the stability of the schemes. There was a good agreement of identical solution between the analytical solution, SUPERBEE, WENO and MUSCL schemes with lower numerical smearing than upwind scheme without no flux limiting scheme (ahead of other schemes) in capturing the shock front. This can be attributed to the fact that, despite upwind scheme being most stable and unconditionally bounded scheme, it gives false diffusion when transport properties are not aligned with gridlines and its low first order accuracy (Brantson et al. 2018). It is also important to state that, there was no over or undershoot in the numerical solutions confirming the robustness of the high-order resolution schemes for capturing fluid flow transport in porous media with acceptable level of numerical dispersion. It can clearly be seen from Fig. 2 that, Newton–Raphson method used converges despite being quadratic with a local convergence for a unidirectional flow. It is noteworthy to mention that the augmentation of grid cells (mesh resolution) will further reduce the level of numerical dispersion (Marcu 2004).

Numerical convergence criteria for the linearization schemes

The same one-dimensional model used as classical BL solution benchmark was solved by FIM method compared to

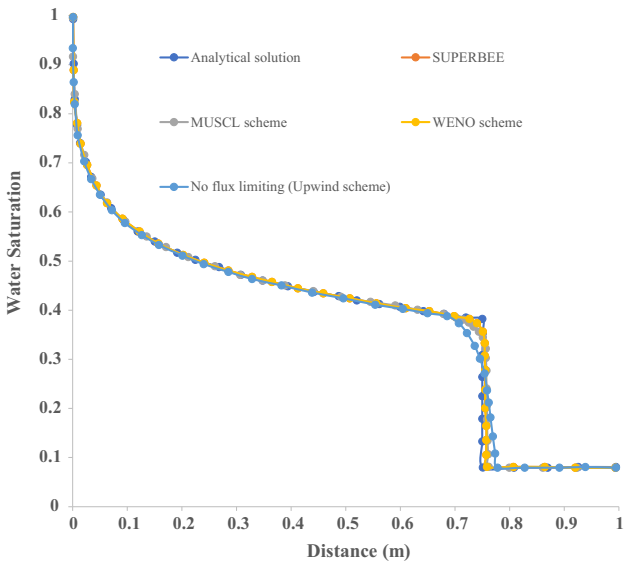

Fig. 2 Validation of the high resolution schemes with Buckley Leverett analytical solution (one dimensional water flood)

iterative IMPES and SEQ methods for numerical convergence rate analyses. These schemes were compared in terms of results accuracy, stability and computational time. The computation of residuals is the basic measure of a linearization scheme's solution convergence by quantifying the system of conserved equations errors in the solution field. The convergence rate of the solution is monitored by checking the water saturation residuals of the numerically solved governing equations as an indicator. Also, the minimum allowable saturation (difference between current iteration and last saturation iteration in any cell volume) and specified residual tolerance limit was set to 0.01 (Eftekhari and Schüller 2015) and 10^{-3} (Radu et al. 2015), respectively, before the start of the numerical simulation. Figure 3a shows a snapshot of the three linearization schemes tested in this study with their obtained water saturation residuals plot. It is also a known fact that any iterative numerical solution will never be exactly zero, but can be within an acceptable tolerance limit. Although the three linearization schemes were within the specified tolerance limit for capturing shock front. It can be observed from the residual monitors in Fig. 3a that, the three linearization schemes residuals reduce as simulation progresses. However, as the residuals decrease rapidly because of solution convergence, the water saturation residuals change less between iteration levels without any imbalance in the system. Furthermore, the lower the residual value is, the more numerically accurate the solution for conserved quantities. It can be inferred from Fig. 3a that the saturation error estimates decrease as the number of iterations and timesteps increases. The linearization schemes residual monitors exhibit monotonic conserved convergence after about 200 iterations with stable numerical solutions. In addition, the residuals of SS method achieve more stability with lower residuals as compared to iterative IMPES and SEQ techniques. Similarly, the residuals drop and level off and become stable for each scheme. The SEQ method combines the advantage of SS and IMPES methods to attained stability and efficiency (Watts and Shaw 2005) as seen in Fig. 3a. But, it also has the problem of handling complicated capillary pressure curves which was ignored in our study. Numerical comparison of iterative IMPES, SS method and SEQ techniques for field scale numerical simulation of oil reservoirs for both saturated and undersaturated states were also performed by Chen et al. (2006). In summary, despite NRM being quadratic with local convergence, the numerical solutions were within acceptable tolerance limit.

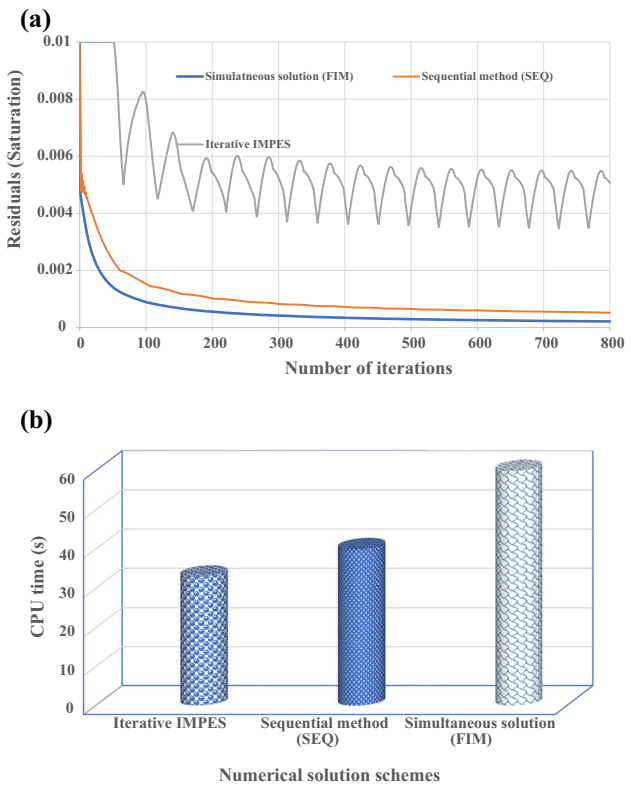

Fig. 3 **a** Residual monitors and rate of convergence plot **b** linearization schemes CPU time

Linearization schemes computational time

Another indicator test is the computational time taken by each linearization scheme for the 1D waterflood simulation. The three linearization schemes were tested on a unidirectional flow by recording the simulation CPU time. When the same number of grid nodes (100) were used for the same number of iterations (800), Fig. 3b indicates that the iterative IMPES scheme uses less CPU time (less costly method) in this study for simulating the fluid flow transport compared to SS and SEQ methods. This is then followed by SEQ method which also solves pressure and saturation equations implicitly, but in sequence, which reduces computational cost and memory (Chen et al. 2006) as seen in Fig. 3b. Lastly, SS method has larger system of equations with larger CPU time despite its stability and robustness (Fig. 3a). Therefore, it can be inferred that the SS required excessive computational cost and memory requirement. It can also be noticed from Fig. 3a, b that, CPU time will increase correspondingly as cell volumes increases for defined timestep.

Geostatistical simulation of permeability fields

This section compares the different stochastic methods for generating equiprobable permeability fields with different parametric setup in this study through geostatistical simulation. The plausible realizations have different petrophysical properties with different recovery factors when subjected to reservoir fluid flow simulation. Herein, the CPU simulation times for the geologic architectures were

also recorded for each realization generated on the rectangular grid mesh (Fig. 1). The colorbar in each figure give details about the ranges of permeability variations.

The proposed permeability map

In this part, plausible stochastic permeability field realizations were generated when correlation lengths were the same in both horizontal and vertical direction with different V_{DP} values. Figure 4a with V_{DP} of 0.2 indicates fairly homogeneous field, but when V_{DP} was increased to 0.5, the heterogeneity of the field increases as compared to Fig. 4a. In addition, Fig. 4c displayed a highly spatial heterogeneous field with V_{DP} of 0.8 unlike Fig. 4a, b for reservoir fluid flow simulation.

Uniform sampling randomization method permeability map

Three permeability map realizations were generated with uniform sampling randomization method (USRM) with statistically distributed samples of homogeneous fields. Figure 5a is highly permeable than Fig. 5b, c with Fig. 5c having slight heterogeneity in the random field. The uniform sampling variant of the uniform sampling randomization method is made up of superposition of random sine modes (Radu et al. 2011 and references therein). In the numerical simulation of the random field, exponential correlation exhibits good ergodic properties of the log-hydraulic conductivity field. All the realizations generated here are more homogeneous as compared to the realizations (Fig. 4) using our proposed method.

TBM permeability map

TBM is a highly efficient multidimensional simulation method that was used in this study to generate 2D equiprobable permeability field realizations through a series of one-dimensional simulation along lines with an exponential covariance model. Here, the model type that was implemented was exponential covariance model for stationary Gaussian random fields. From Fig. 6a, b, a visual impression and appreciation of artifact banding discontinuities occurred in the simulated maps when finite number of lines of 15 (Journel and Huijbregts 1978; Mantoglou and Wilson 1982) and 64 (Gneiting 1999) were used, respectively. This can be attributed to the fact that the lines were insufficient to generate the permeability maps. Hence, not ideal realizations for fluid flow simulation. But in Fig. 6c where the number of lines were increased to 1000 (Tompson et al. 1989; Freulon and de Fouquet 1991), no artifact banding/stripping occurred in the random field with improvement in the ergodic properties of the simulated map. Emery and Lantuéjoul (2006) also obtained artifact banding with 15 lines, but with 1000 lines, the realization texture obtained improved with no perceptible artifacts as seen in our study (Fig. 6c). Comparatively, no artifacts were also observed in our proposed method and USRM. To validate the quality of the simulated permeability field (Fig. 6c) to be used for fluid flow simulation due to the problem of artifact banding beyond visual check. The simulated variogram was compared to the theoretical variogram algorithm plotted against distance when 1000 lines were used. It can be noticed from Fig. 6d that the average simulated statistics match the theoretical model almost perfectly.

CPU run-time for the simulated permeability maps

The three permeability map methods analyzed in this study CPU times were comparatively compared for the realizations generated. This is because, memory storage requirement becomes important when large number of random fields are to be generated with speed and accuracy. Figure 7 shows that USRM has the least CPU run-time in seconds followed by our proposed method and lastly the TBM technique, when a single realization was produced with each method. TBM has the highest CPU run-time due to CPU time devoted to post-processing the realization to be generated (Emery and Lantuéjoul 2006), but its simulation along lines is usually fast. In all, the three approaches achieved fast efficient simulation time at good computational cost.

Homogeneous immiscible displacement

Under homogeneous stable base case model for immiscible displacement scheme in this research, all rock (porosity and permeability values equal to the mean values) and fluid properties were kept constant (isotropic) in the computational domain. This implies horizontal permeability is equal to vertical permeability. Figure 8a shows non-perturbed field with no subsurface instability (flat interface) with stable recovery rate about 27% in 60 days. The plumes of unstable structures (Fig. 8b, c) were generated when a random distribution of permeability was introduced only at the inlet face (restricted to the ghost border cells near the injection well) of the porous medium at (t = 0 s), while the non-perturbed parts of the porous medium remain homogeneous. The merits of this method (spatial restriction to perturbation) of perturbing the initial saturation field was also applied by Riaz and Tchelepi (2006), Islam et al. (2010), Henderson et al. (2015), and Bouquet et al. (2017) in their studies for oil displacement in reservoirs. It can also be seen in Fig. 8b, c that, the oil displacement was piston-like, where oil in front of the shock was pushed out

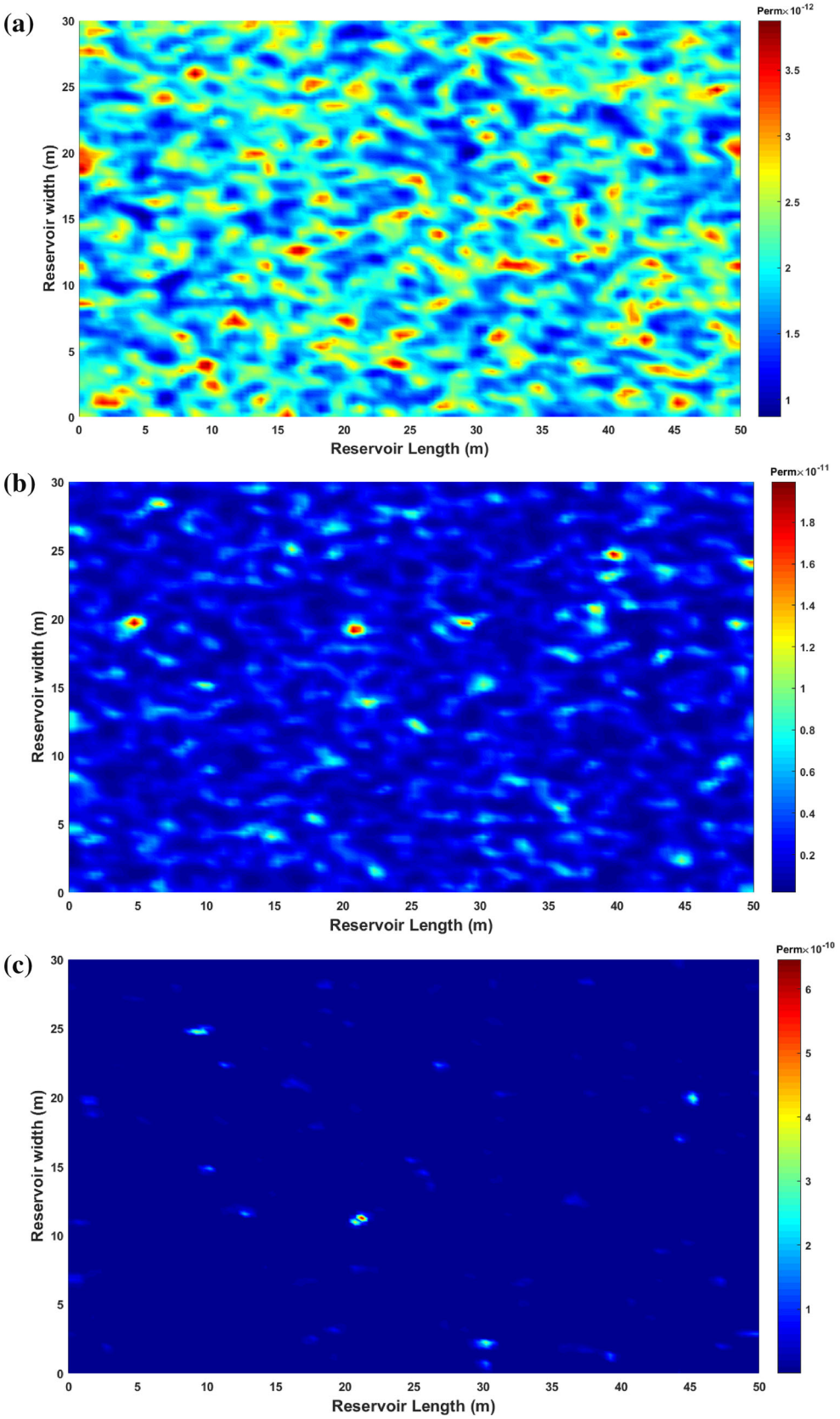

Fig. 4 Proposed permeability map **a** (V_{DP} = 0.2, λ_x = 0.04 m, λ_y = 0.04 m); **b** (V_{DP} = 0.5, λ_x = 0.04 m, λ_y = 0.04 m); **c** (V_{DP} = 0.8, λ_x = 0.04 m, λ_y = 0.04 m)

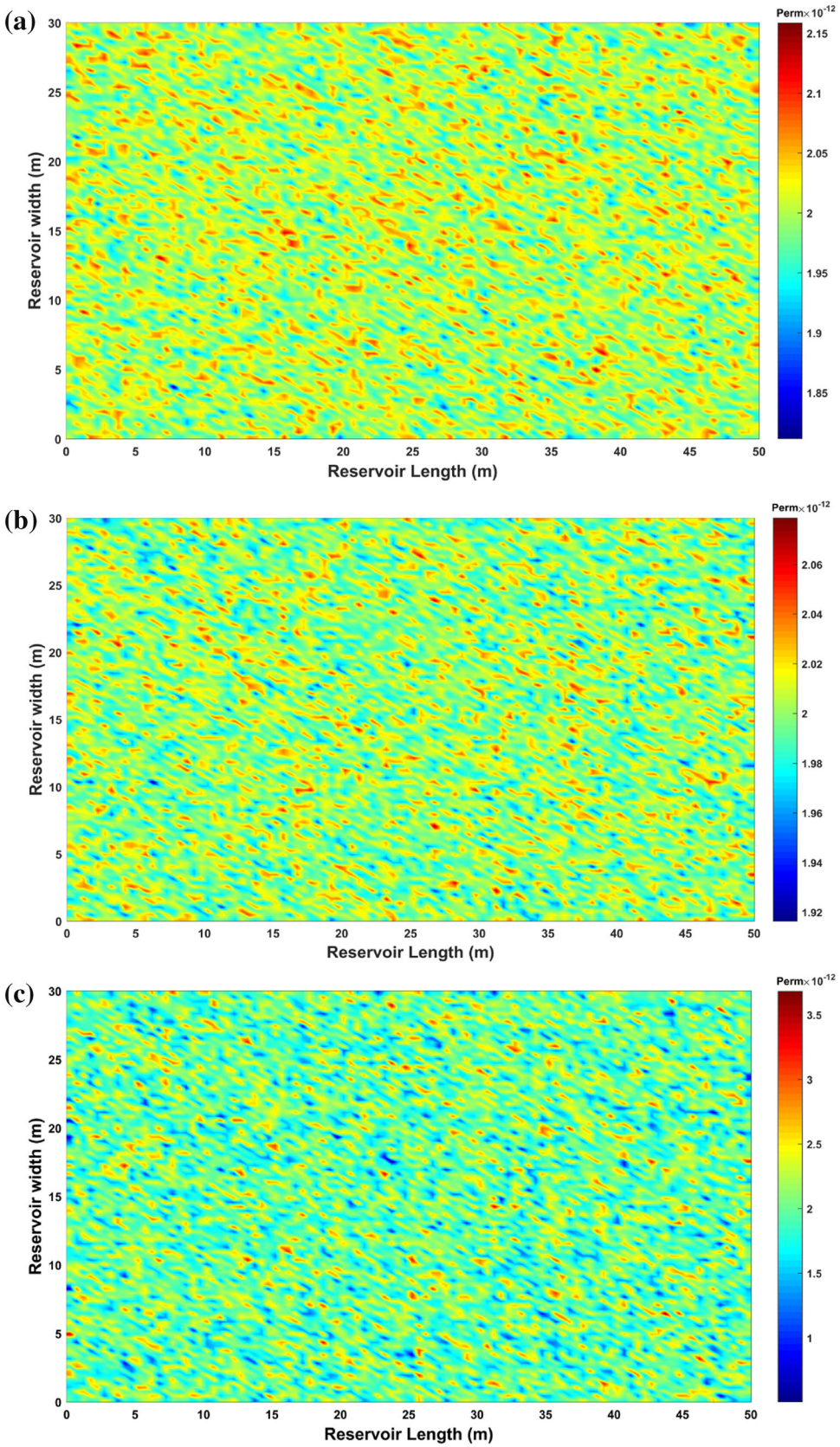

Fig. 5 Uniform sampling randomization simulation method permeability maps (**a**, **b** and **c**, $E(\mathrm{K}) = 2 \times 10^{-12}$ m^2, $\sigma^2 = 0.130$, $\lambda_x = 1$ m, $\lambda_y = 1$ m)

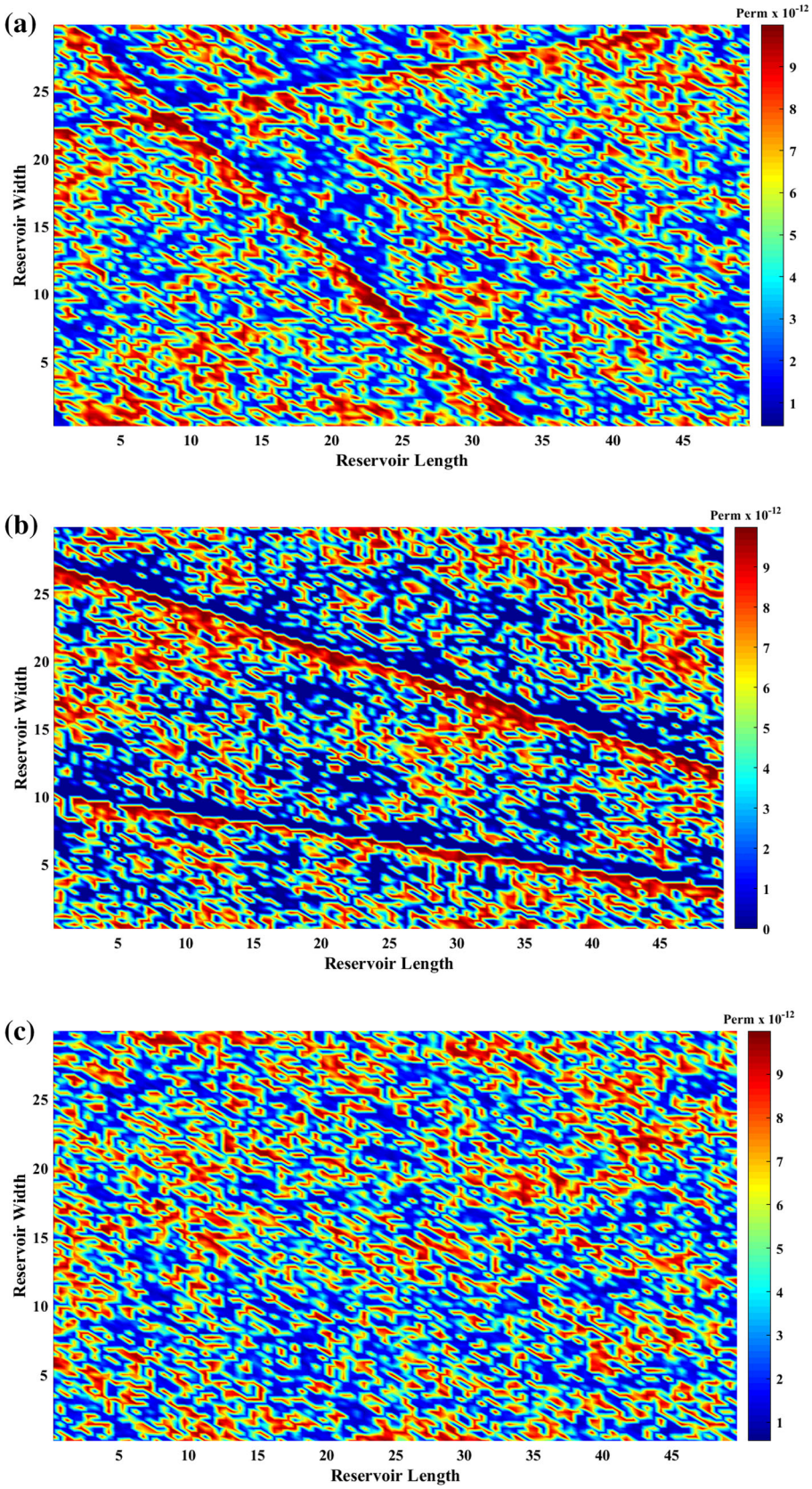

Fig. 6 TBM permeability map **a** 15 lines **b** 64 lines **c** 1000 lines

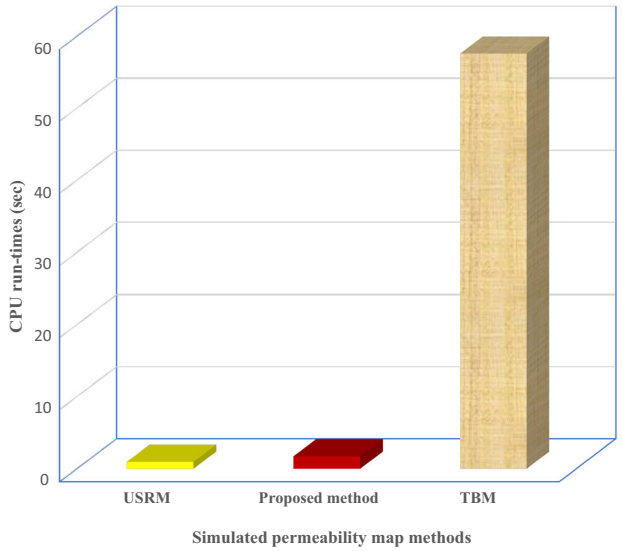

Fig. 7 CPU run-times for proposed method, TBM and USRM

of the domain having water behind shock with small subsurface instabilities. It can be detected from Fig. 8c that, instabilities initiated grow as oil was pushed out of the domain due to sufficient saturation fringe in the numerical simulation process (Bouquet et al. 2017). Eftekhari and Schüller (2015) also stated that V_{DP} of 0.01 which makes about 3% perturbation in a permeability field does not result into flow channeling, but can trigger viscous fingering initiations. The recovery factor for the piston-like quasi-homogeneous (Fig. 8c) displacement was approximately 24% in about 60 days as seen in Fig. 9, but less than Fig. 8a recovery factor due to fingering phenomenon.

Heterogeneous surface instabilities

Proposed method fluid flow simulation

This section dwells on heterogeneous permeability field fluid flow simulation through the three techniques used to generate the permeability fields. The porosity field is a function of permeability which was generated based on Carman–Kozeny relation as shown in Fig. 10. Figure 4a, c permeability realizations were used to simulate fluid flow through the stochastic field to observe subsurface instabilities. Figure 11a, b illustrate subsurface instabilities larger than the quasi-homogeneous base case (Fig. 8b, c). These instabilities were mainly characterized with tip splitting (bifurcation), spreading and coalescence of finger-like structures. However, these instabilities merge together as they are driven toward the wake of larger fingers because of the larger ones moving faster and preventing the growth of smaller ones. The specific spatial paths taken by the instabilities correspond to paths of local higher permeability zone. Hence, channeling phenomenon is susceptible in such high permeability zones (Doorwar and Mohanty 2016). Erandi et al. (2015) and Luo et al. (2017) also observed in their research that, fingering regime of a layer can be completely disrupted by modest levels of heterogeneity leading to channeling regime. Therefore, when Fig. 4a permeability field (V_{DP} = 0.2) was used for fluid flow simulation (Fig. 11a), the recovery factor was 23% in approximately 60 days. This recovery factor is almost close to Fig. 8c recovery factor of 24% denoting homogeneity for both cases, despite observation of fingering phenomenon. The displacement (Fig. 11a) is also piston-like with larger surface instabilities of viscous fingers due to weak perturbation with no significant impact of fingers' behavior.

On the other hand, the characterization of reservoir heterogeneity by permeability variation of most reservoirs falls within the range of 0.5–0.9 (Willhite 1986). Figure 11b shows a heterogeneous permeability map (Fig. 4c) with V_{DP} = 0.8. It can be inferred from Fig. 11b that, the subsurface instabilities were more severe as compared to when V_{DP} = 0.0 (Fig. 8a–c) and V_{DP} = 0.2 (Fig. 11a). Additionally, it can be noticed from Fig. 11b that, at the start of the simulation, the finger tips were more unstable and propagate further forward with the strong media heterogeneity causing the splitting phenomenon with continuous repetition till water breakthrough. This erratic behavior was observed as more mobile fingers ahead of their neighboring fingers outruns and shielded less mobile ones from further growth (Fig. 11b). Tip splitting and spreading pattern were also seen in (Fig. 11a, b) as pressure gradient is also larger near the tip of the finger causing the finger to split leading to different flow paths. The oil recovery factor due to subsurface instabilities can be seen in Fig. 9 when V_{DP} = 0.8 with 13% recovery rate in approximately 60 days. Therefore, the higher the permeability variation in porous media, the lesser the amount of oil recovered with increment in recovery time. Similarly, Fig. 11b depicts skeletal viscous fingers similar to Brownian trees of diffusion limited aggregation (DLA) formed possessing self-similarity nature of fractals (Zhang and Liu 1998).

Uniform sampling randomization method fluid flow simulation

In this part, the dynamic fluid flow simulation was simulated through Fig. 5c which was generated through USRM which has slight heterogeneity than Fig. 5a, b. The fingers behavior shown in Fig. 12 are similar to the homogeneous case demonstrated in Fig. 8c with unstable piston-like displacement characteristics. In Fig. 12, there is no bypass of oil unlike Fig. 11b due to permeability variation. The

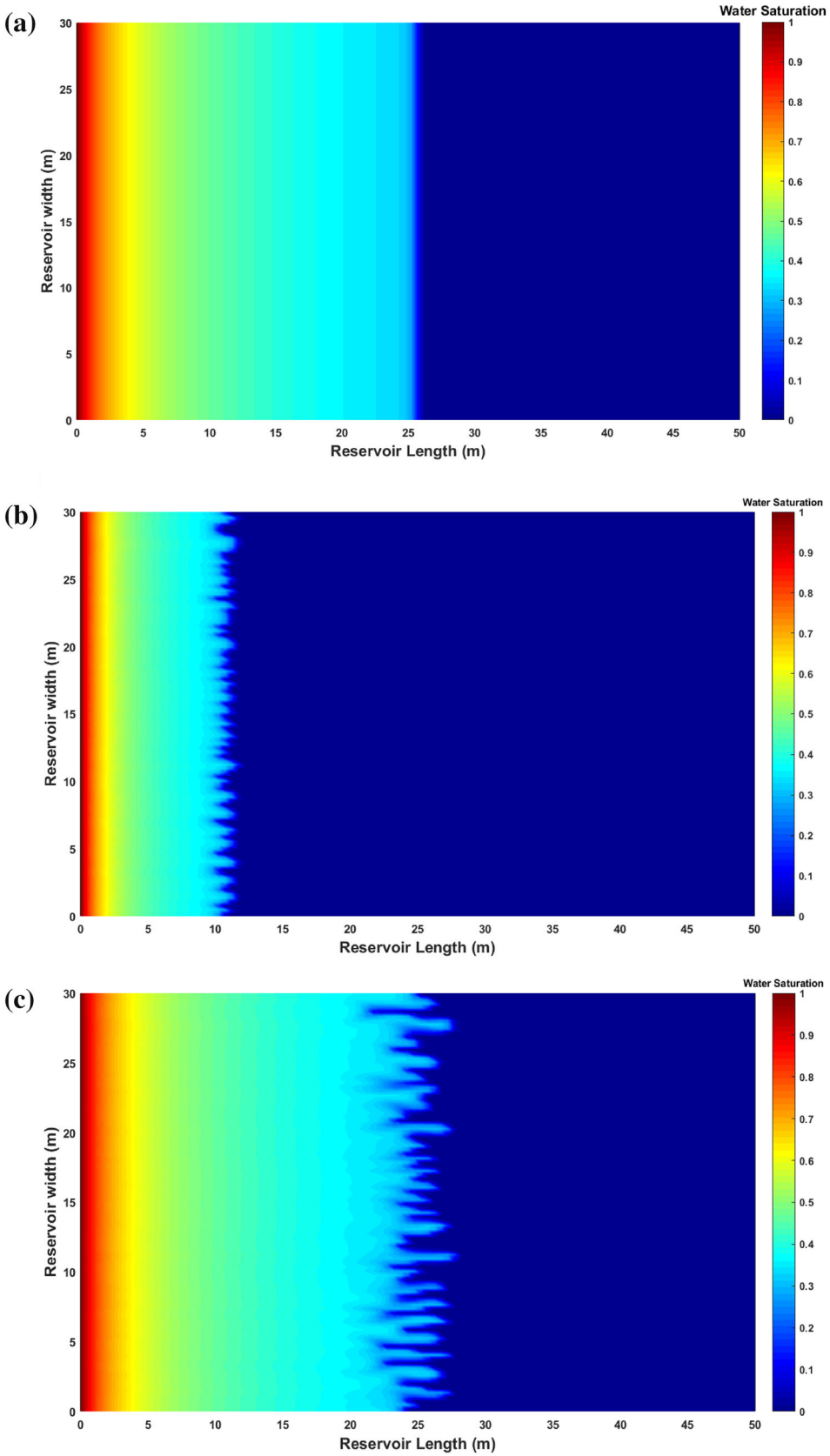

Fig. 8 Homogeneous water saturation maps (V_{DP} = 0.0, λ_x = 0.04 m (**a**) t = 5.2261 × 10^6 s (**b**) t = 2.5398 × 10^6 s, (**c**) t = 5.1877 × 10^6 s)

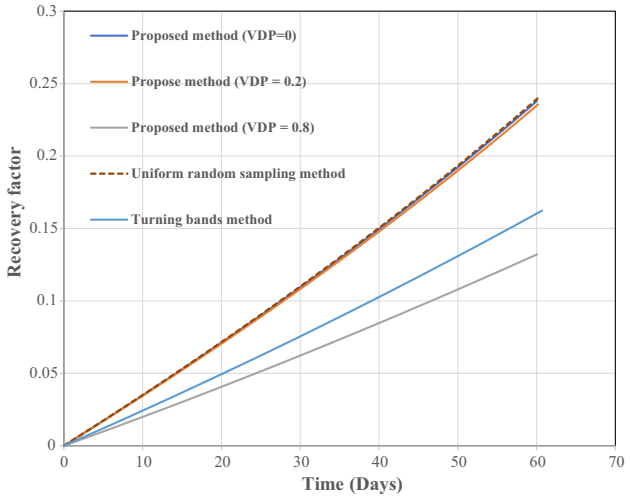

Fig. 9 Recovery factor for homogeneous and heterogeneous fields

obtained recovery rate for Fig. 12 is 24% in approximately 60 days in Fig. 9 similar to V_{DP} = 0.0 and V_{DP} = 0.2 which are indication of a more homogeneous system.

Turning bands method fluid flow simulation

Figure 6c TBM permeability field with good ergodic properties was employed for numerical simulation experiment to observe subsurface instabilities during water injection process. Furthermore, bypass of unswept regions were seen in Fig. 13 similar to Fig. 11b unlike Figs. 8a–c and 12 with no such phenomenon. Spreading and tip splitting were the dominant features seen on the water saturation map (Fig. 13). The recovery factor for Fig. 13 was 16% in 60 days as shown in Fig. 9 was higher than that of Fig. 11b due to higher permeability field values in Fig. 6c, but less than the recovery rate for Fig. 8c.

Water breakthrough time and the impact of correlation lengths on immiscible fluid flow distribution

Herein, correlated correlation lengths of 0.03 m (Fig. 14a) and 0.05 m (Fig. 14b) (below and above 0.04 m used in our analyses) same in both vertical and horizontal direction were employed with the proposed method to generate permeability realizations with V_{DP} of 0.5 to observe their impact on fluid flow simulation in subsurface. The various subsurface instabilities of spreading, shielding, merging, tip-splitting can clearly be visualized from both Fig. 14a, b with unswept regions coupled with unstable displacement. The sweep efficiency in Fig. 14a is better than in Fig. 14b with less residual oil saturation. One crucial observation noticed from both plots is that, there are islands of oil (bypass) surrounded by the invading fluid leading to breakthrough in both Fig. 14a, b. Inference drawn from Fig. 14b indicates that, increase in correlation lengths yielded more viscous fingers than in Fig. 14a. The oil recovered due to variation in correlation lengths for Fig. 14a and b are 32% and 27% when water breakthrough in 103 and 84 days, respectively, which had significant impact on fluid distribution in the stochastic media. The sensitivity of correlation lengths in reservoir fluid flow simulation should be considered when predicting future performance of petroleum reservoirs.

Fig. 10 Porosity field realization

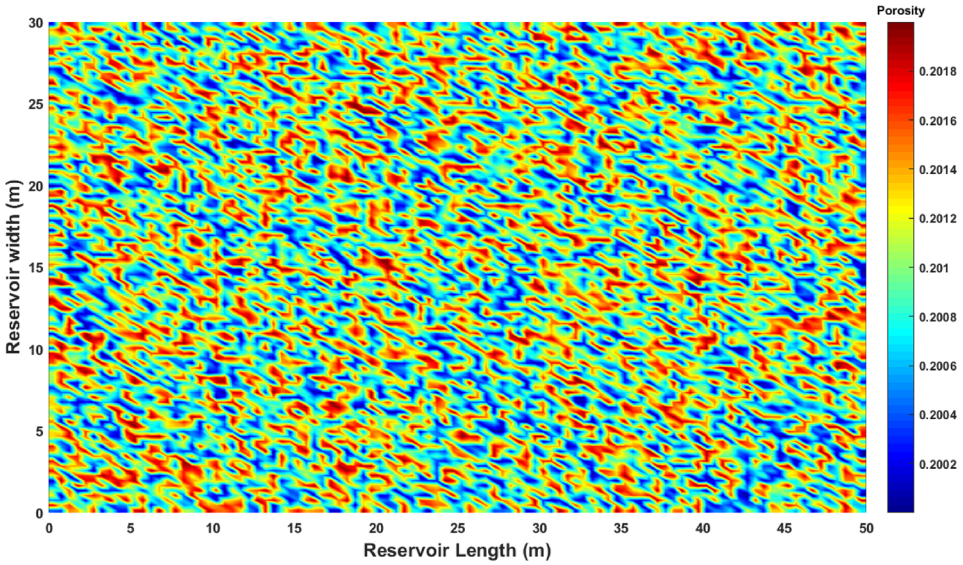

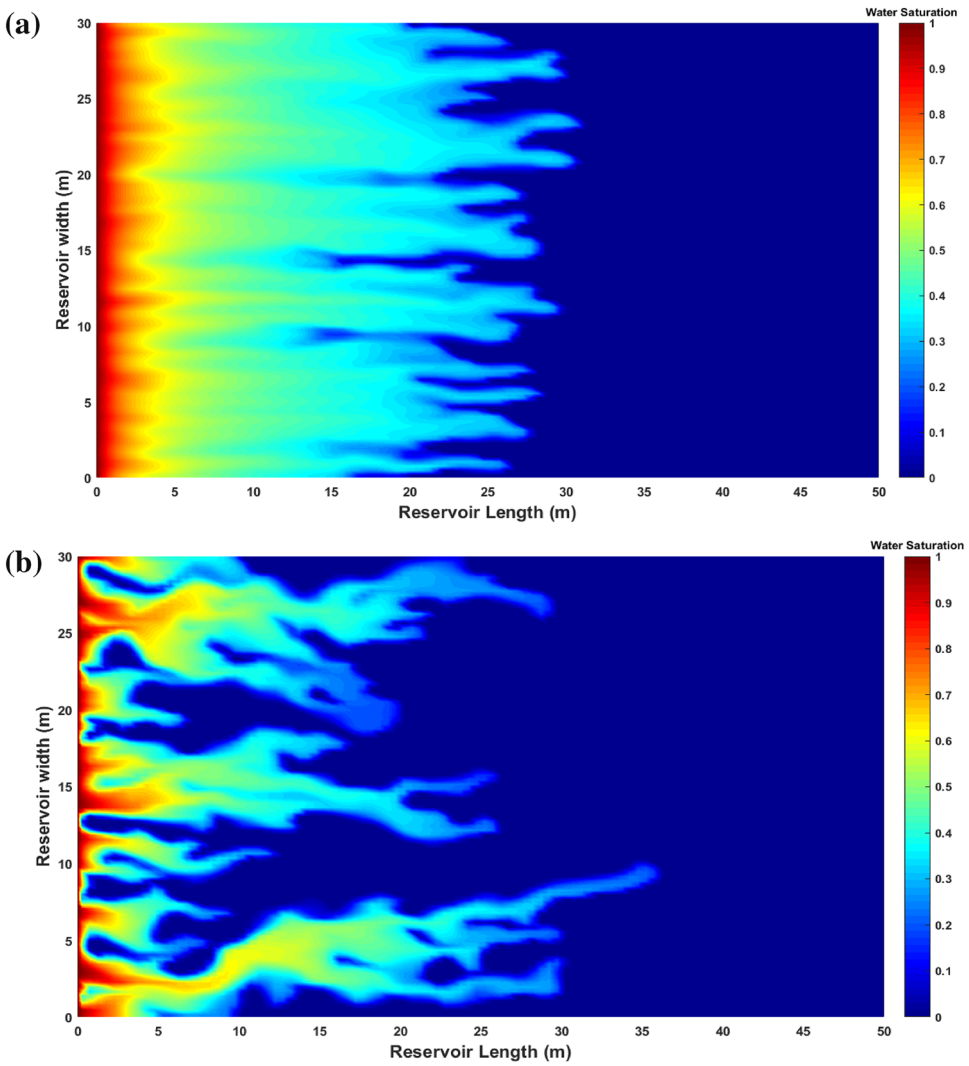

Fig. 11 Heterogeneous permeability field water saturation maps **a** (V_{DP} = 0.2, t = 5.1985 × 10^6 s), **b** (V_{DP} = 0.8, t = 5.1893 × 10^6 s)

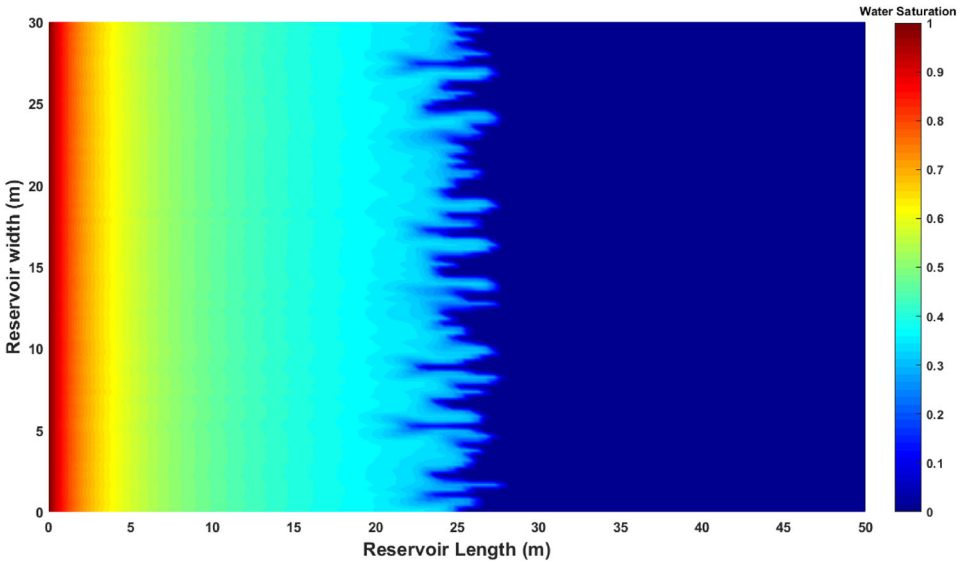

Fig. 12 Uniform sampling randomization method saturation field (t = 5.1972 × 10^6 s)

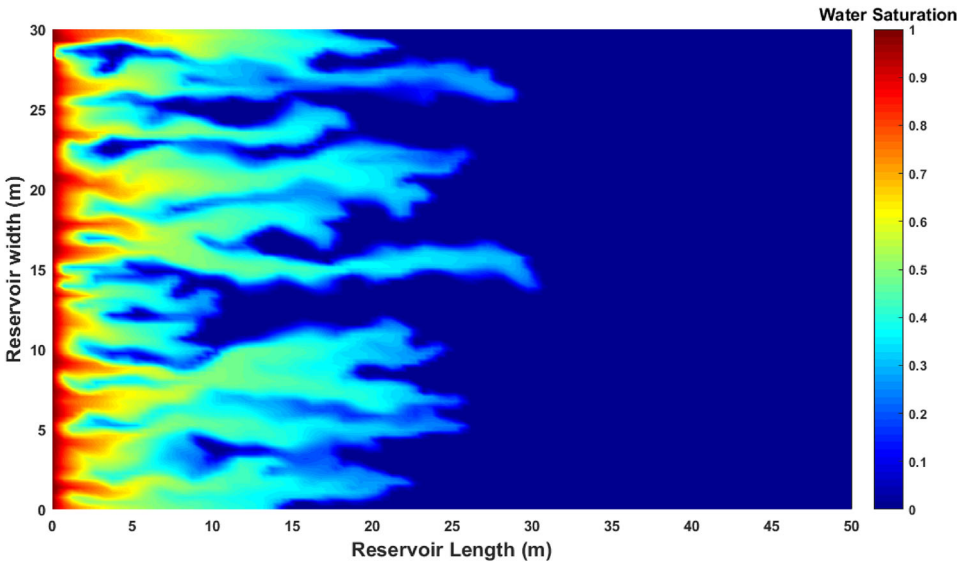

Fig. 13 Turning bands method water saturation map ($t = 5.1972 \times 10^6$ s)

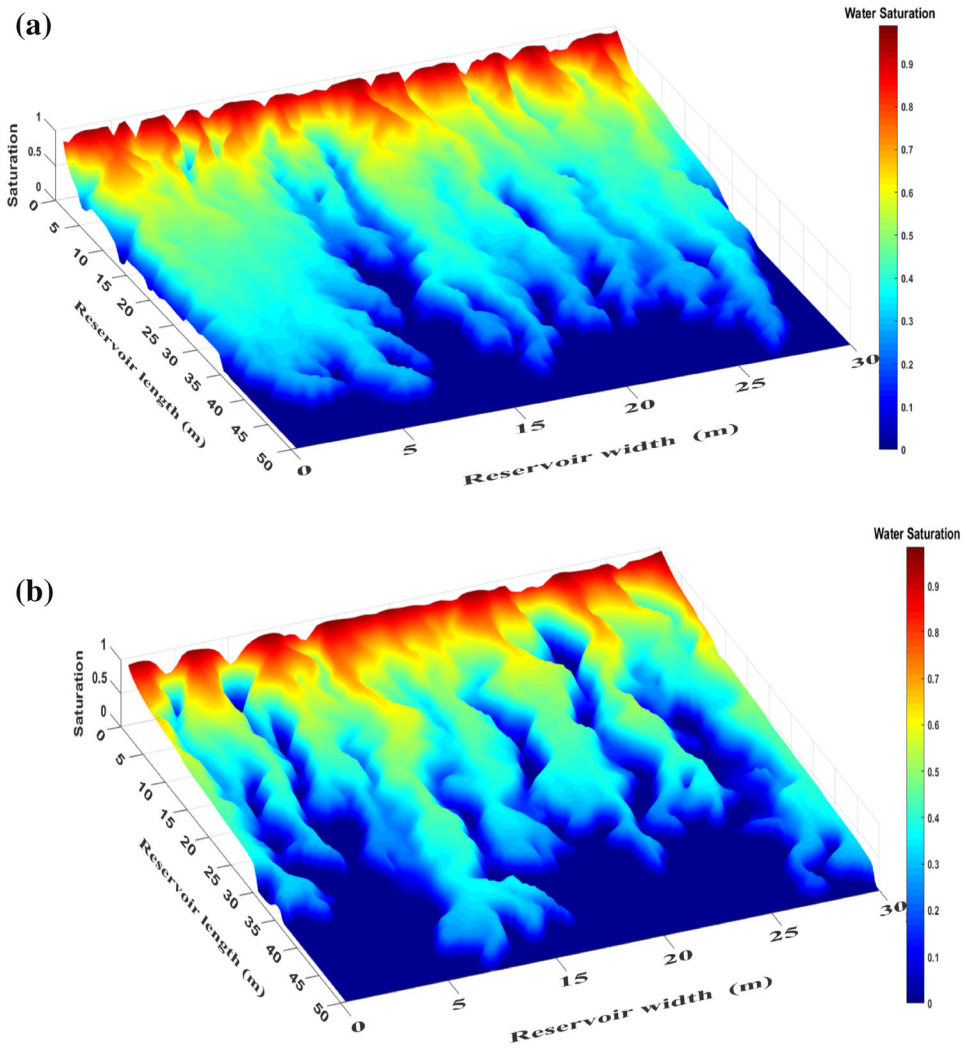

Fig. 14 Water saturation breakthrough time maps **a** ($V_{DP} = 0.5$, $\lambda_x = 0.03$ m, $\lambda_y = 0.03$ m, $t = 7.233953 \times 10^6$ s), **b** ($V_{DP} = 0.5$, $\lambda_x = 0.05$ m, $\lambda_y = 0.05$ m, $t = 8.823839 \times 10^6$ s)

Conclusions

In this present work, a two-dimensional numerical reservoir simulator developed was used to generate stochastic porous media for simulating subsurface instabilities during immiscible fluid flow displacement process. The following conclusions were made from the study:

- A proposed stochastic modeling approach for generating petroleum porous media (permeability and porosity fields) was incorporated into reservoir fluid flow simulation to improve production forecast in heterogeneous formations.
- The TBM and USRM techniques used for generating equiprobable spatial permeability fields were incorporated into reservoir fluid flow simulation. But banding artifacts were observed in the TBM permeability fields when finite number of lines were used.
- The linearization schemes of SS method, iterative IMPES and SEQ method were used for solving the two-phase problem without any non-physical solutions around shocks and discontinuities.
- High-resolution schemes of SUPERBEE flux limiter, WENO and MUSCL employed in the numerical simulator were monotonicity-preserving and fit well to the BL analytical solution with minimal smearing.
- A comparison was made between homogeneous and heterogeneous stochastic porous media in terms of recovery factor with less oil recovered in the heterogeneous formations due to interactions between heterogeneity and viscous fingering unlike the homogeneous formation media.
- Quantitative subsurface instabilities including shielding, coalescence, spreading, successive tip splitting, channeling and skeletal fingers were observed on the permeability fields of the proposed method, TBM and USRM techniques.
- Finger widths which are often much smaller than typical reservoir simulation grid blocks were captured through numerical simulation.
- The effect of correlation lengths on immiscible fluid flow transport was investigated with larger correlation lengths yielding more significant viscous fingering effects.

Unit conversion

$$1 \text{ Darcy} = 9.86923 \times 10^{-13} \text{ m}^2$$

Acknowledgements The work was supported by the Fundamental Research Funds for National Science and Technology Major Projects (2016ZX05011-002) and the Central Universities (2652015142). The kind effort from Dr. Y.Y Ziggah, Dr. A.A Eftekhari, Dr. K. Schüller, and Dr. X. Emery for their tireless assistance in carrying out this research. We also thank Mr. Bright Junior Addo for his kind assistance with fruitful and constructive criticism of this research paper. We would also like to thank the anonymous reviewers for their comments and suggestions that were helpful in improving the manuscript.

Compliance with ethical standards

Conflict of interest The authors declare that they have no conflicts of interest with respect to the research, authorship, and/or publication of this article.

Appendix

See Fig. 15.

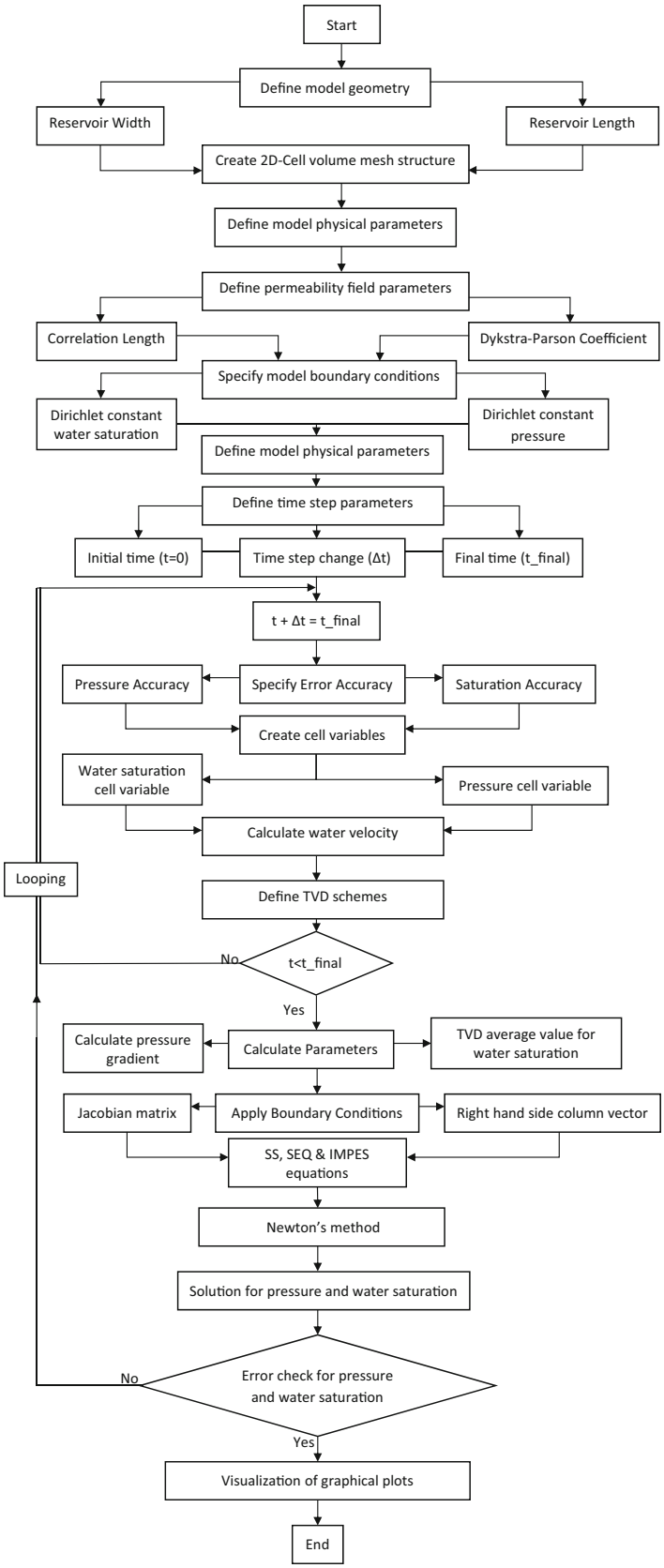

Fig. 15 Computer modeling development flowchart

References

Araktingi U, Orr F Jr (1993) Viscous fingering in heterogeneous porous media. SPE Adv Technol Ser 1(1):71

Babaei M, Joekar-Niasar V (2016) A transport phase diagram for pore-level correlated porous media. Adv Water Resour 92:23–29

Bergamashi N, Putti M (1999) Mixed finite elements and Newton-type linearization for the solution of Richards' equation. Int J Numer Methods Eng 45:1025–1046

Bergström D (2012) MySimLabs. http://www.mysimlabs.com/about.html

Bijeljic B, Raeini A, Mostaghimi P, Blunt MJ (2013) Predictions of non-Fickian solute transport in different classes of porous media using direct simulation on pore-scale images. Phys Rev E 87(1):013011

Bouquet S, Leray S, Douarche F, Roggero F (2017) Characterization of viscous unstable flow in porous media at pilot scale-application to heavy oil polymer flooding. In: IOR 2017-19th European symposium on improved oil recovery

Brantson ET, Ju B, Wu D (2018) Numerical simulation of viscous fingering and flow channeling phenomena in perturbed stochastic fields: finite volume approach with tracer injection tests. Arab J Sci Eng. https://doi.org/10.1007/s13369-018-3070-0

Buckley SE, Leverett M (1942) Mechanism of fluid displacement in sands. Trans AIME 146(01):107–116

Byer TJ (2000) Preconditioned newton methods for simulation of reservoirs with surface facilities. Department of Petroleum Engineering

Chen Z (2007) Reservoir simulation: mathematical techniques in oil recovery. Society for Industrial and Applied Mathematics, pp 103–128. https://doi.org/10.1137/1.9780898717075

Chen Z, Huan G, Ma Y (2006) Computational methods for multiphase flows in porous media. Soc Ind Appl Math

Corey AT (1954) The interrelation between gas and oil relative permeabilities. Prod Mon 19(1):38–41

Craig FG (1971) The reservoir engineering aspect of water of waterflooding. SPE Monograph series, Vol 3, Richardson, TX, pp 10–11

Daripa P, Glimm J, Lindquist B, McBryan O (1988) Polymer floods: a case study of nonlinear wave analysis and of instability control in tertiary oil recovery. SIAM J Appl Math 48(2):353–373

De Lucia M, Lagneau V, De Fouquet C, Bruno R (2011) The influence of spatial variability on 2D reactive transport simulations. CR Geosci 343(6):406–416

Delamaide E (2014) Polymer flooding of heavy oil-from screening to full-field extension. In: SPE heavy and extra heavy oil conference: Latin America. Society of Petroleum Engineers

Deutsch CV, Journel AG (1992) GSLB: geostatistical software library and user's guide. Oxford University Press, Oxford

Doorwar S, Mohanty KK (2016) Viscous-Fingering Function for Unstable Immiscible Flows, University of Texas at Austin

Douglas JJ, Peaceman DW, Rachford H.H (1959) A method for calculating multi-dimensional immiscible displacement. Trans AIME 216:297–306

Dubrule 0 (1988) A review of stochastic models for petroleum reservoirs. Paper presented at the 1988 British Soc. Reservoir geologists meeting on quantification of sediment body geometries and their internal heterogeneities, London

Dykstra H, Parsons RL (1950) The prediction of oil recovery by waterflood. Second Recover Oil USA 2:160–174

Eftekhari AA, Schüller K (2015) FVTool: a finite volume toolbox for Matlab (Version v0.11). Zenodo. http://doi.org/10.5281/zenodo.32745

Emery X, Lantuéjoul C (2006) Tbsim: a computer program for conditional simulation of three-dimensional gaussian random fields via the turning bands method. Comput Geosci 32(10):1615–1628

Erandi DI, Wijeratne N, Britt M, Halvorsen BM (2015) Computational study of fingering phenomenon in heavy oil reservoir with water drive. Fuel 158:306–314. https://doi.org/10.1016/j.fuel.2015.05.052

Farnstrom KL, Ertekin T (1987). A versatile, fully implicit, black oil simulator with variable bubble-point option. In: SPE California regional meeting. Society of Petroleum Engineers

Freulon X, de Fouquet C (1991) Remarques sur la pratique des bandes tournantes a 3D. Cahiers de Gostatistique, Fascicule 1:101–117

Garcia N, Stoll E (1984) Monte Carlo calculation for electromagnetic-wave scattering from random rough surfaces. Phys Rev Lett 52(20):1798

Gneiting T (1999) Correlation functions for atmospheric data analysis. Quart J R Meteorol Soc 125(559):2449–2464

Gotway CA, Rutherford BM (1994. Stochastic simulation for imaging spatial uncertainty: comparison and evaluation of available algorithms. In: Geostatistical simulations. Springer, Netherlands, pp 1–21

Haddad RA, Akansu AN (1991) A class of fast Gaussian binomial filters for speech and image processing. IEEE Trans Signal Process 39(3):723–772

Haldorsen HH, Damsleth E (1990) Stochastic Modeling (includes associated papers 21255 and 21299). J Petrol Technol 42(04):404–412

Harten A (1983) High resolution schemes for hyperbolic conservation laws. J Comput Phys 49:357–393. https://doi.org/10.1006/jcph.1997.5713 **(Bibcode:1997JCoPh. 135.260H)**

Henderson N, Brêttas JC, Sacco WF (2015) Applicability of the three-parameter Kozeny–Carman generalized equation to the description of viscous fingering in simulations of waterflood in heterogeneous porous media. Adv Eng Softw 85:73–80

Islam MR, Moussavizadegan SH, Mustafiz S, Abou-Kassem JH (2010) Advanced petroleum reservoir simulation. Wiley, Hoboken, p 277

Johnson CE (1956) Production of oil recovery by water flood—a simplified graphical treatment of the Dykstra-Parsons method. J Petr Tech Trans AIME 207:345–346

Journel AG, Huijbregts CJ (1978) Mining geostatistics. Academic Press, Cambridge

Kalia N, Balakotaiah V (2009) Effect of medium heterogeneities on reactive dissolution of carbonates. Chem Eng Sci 64:376–390

Knackstedt MA, Sheppard AP, Sahimi M (2001) Pore network modelling of two-phase flow in porous rock: the effect of correlated heterogeneity. Adv Water Resour 24(3):257–277

Kou J, Sun S (2010) On iterative IMPES formulation for two-phase flow with capillarity in heterogeneous porous media. Int J Numer Anal Model Ser B 1(1):20–40

Lacroix S, Vassilevski YV, Wheeler JA, Wheeler MF (2003) Iterative solution methods for modeling multiphase flow in porous media fully implicitly. SIAM J Sci Comput 25(3):905–926

Lake LW, Malik MA (1993) Modelling fluid flow through geologically realistic media. Geol Soc Lond Spec Publ 73(1):367–375

Leng CC (2013) The effect of spatial correlation on viscous fingering in a dynamic pore-network model with Delaunay tessellated structure (Master's thesis)

Lie KA (2014) An introduction to reservoir simulation using MATLAB user guide for the MATLAB reservoir simulation toolbox (MRST). SINTEF ICT, Department of Applied Mathematics

List F, Radu FA (2016) A study on iterative methods for solving Richards' equation. Comput Geosci 20(2):341–353

Liu XD, Osher S, Chan T (1994) Weighted essentially non-oscillatory schemes. J Comput Phys 115(1):200–212

Luo H, Delshad M, Pope GA, Mohanty KK (2017) Interactions between viscous fingering and channeling for unstable water/polymer floods in heavy oil reservoirs. In: SPE Reservoir simulation conference. Society of Petroleum Engineers

MacDonald RC (1970) Methods for numerical simulation of water and gas coning. Soc Petrol Eng J 10(04):425–436

Mantoglou A, Wilson JW (1982) The turning bands methods for simulation of random fields using line generation by a spectral method. Water Res 18(5):1379–1394

Marcu GI (2004) Application of TVD flux limiting schemes in simulation of multiphase flow through porous media. The 6th international conference on hydraulic machinery and hydrodynamics Timisoara, Romania. pp 643–648

Matheron G (1973) The intrinsic random functions and their applications. Adv Appl Probab 5(3):439–468

MATLAB and Statistics Toolbox Release R (2016) The MathWorks, Inc., Natick, Massachusetts, United States

Monteagudo JE, Firoozabadi A (2007a) Control-volume model for simulation of water injection in fractured media: incorporating matrix heterogeneity and reservoir wettability effects. SPE J 12(03):355–366

Monteagudo JEP, Firoozabadi A (2007b) Comparison of fully implicit and IMPES formulations for simulation of water injection in fractured and unfractured media. Int J Numer Meth Eng 69(4):698–728

Nixon MS, Aguado AS (2008) Feature extraction and image processing. Academic Press, Cambridge, p 88

Pacheco TB, da Silva AFC, Maliska CR (2016) Comparison of IMPES, sequential, and fully implicit formulations for two-phase flow in porous media with the element-based finite volume method

Radu FA, Pop IS, Knabner P (2006) On the convergence of the Newton method for the mixed finite element discretization of a class of degenerate parabolic equation. Numerical Mathematics and Advanced Applications, pp 1194–1200

Radu FA, Suciu N, Hoffmann J, Vogel A, Kolditz O, Park CH, Attinger S (2011) Accuracy of numerical simulations of contaminant transport in heterogeneous aquifers: a comparative study. Adv Water Resour 34(1):47–61

Radu FA, Nordbotten JM, Pop IS, Kumar K (2015) A robust linearization scheme for finite volume based discretizations for simulation of two-phase flow in porous media. J Comput Appl Math 289:134–141

Riaz A, Tchelepi HA (2006) Numerical simulation of immiscible two-phase flow in porous media. Phys Fluids 18(1):014104

Roe PL (1985) Some contributions to the modeling of discontinuous flows, Lectures in Applied Mechanics, Vol. 22, Springer, Berlin, pp 163–193

Rubin B, Blunt MJ (1991) Higher-order implicit flux limiting schemes for black oil simulation. Paper SPE 21222 presented at 11-th SPE symposium on reservoir simulation, Anaheim, pp. 219–228

Sabelfeld KK (1991) Monte Carlo methods in boundary value problems. Springer, Berlin

Shinozuka M, Jan CM (1972) Digital simulation of random processes and its applications. J Sound Vib 25(1):111–128

Sweby PK (1984) High resolution schemes using flux limiters for hyperbolic conservation laws. SIAM J Numer Ana006C 21:995–1011

Taggart IJ, Pinczewski WV (1985) The use of higher order differencing techniques in reservoir simulation. Paper resented at the sixth SPE symposium on reservoir simulation, Dallas, Texas

Tompson AF, Ababou R, Gelhar LW (1989) Implementation of the three-dimensional turning bands random field generator. Water Resour Res 25(10):2227–2243

Van Leer B (1979) Towards the ultimate conservative difference scheme. V. A second-order sequel to Godunov's method. J Comput Phys 32(1):101–136

Versteeg HK, Malalasekera W (2007) An introduction to computational fluid dynamics: the finite, vol method. Pearson Education, London

Watts JW, Shaw JS (2005) A new method for solving the implicit reservoir simulation matrix equation. In: SPE reservoir simulation symposium. Society of Petroleum Engineers

Wendroff BLP (1960) Systems of conservation laws. Commun Pure Appl Math 13:217–237

Willhite GP (1986) Waterflooding, SPE textbook series Vol. 3, Richardson, pp 1–2

Zhang W, Al Kobaisi M (2017) A two-step finite volume method for the simulation of multiphase fluid flow in heterogeneous and anisotropic reservoirs. J Petrol Sci Eng 156:282–298

Zhang JH, Liu ZH (1998) Study of the relationship between fractal dimension and viscosity ratio for viscous fingering with a modified DLA model. J Petrol Sci Eng 21(1):123–128

Acta Geophysica (2018) 66:267–282
https://doi.org/10.1007/s11600-018-0136-z

RESEARCH ARTICLE - SOLID EARTH SCIENCES

Three-dimensional discrete element method simulation of core disking

Shunchuan Wu[1,2,3] · Haoyan Wu[1,2] · John Kemeny[4]

Received: 16 October 2017 / Accepted: 29 March 2018 / Published online: 6 April 2018

Abstract
The phenomenon of core disking is commonly seen in deep drilling of highly stressed regions in the Earth's crust. Given its close relationship with the in situ stress state, the presence and features of core disking can be used to interpret the stresses when traditional in situ stress measuring techniques are not available. The core disking process was simulated in this paper using the three-dimensional discrete element method software PFC^{3D} (particle flow code). In particular, PFC3D is used to examine the evolution of fracture initiation, propagation and coalescence associated with core disking under various stress states. In this paper, four unresolved problems concerning core disking are investigated with a series of numerical simulations. These simulations also provide some verification of existing results by other researchers: (1) Core disking occurs when the maximum principal stress is about 6.5 times the tensile strength. (2) For most stress situations, core disking occurs from the outer surface, except for the thrust faulting stress regime, where the fractures were found to initiate from the inner part. (3) The anisotropy of the two horizontal principal stresses has an effect on the core disking morphology. (4) The thickness of core disk has a positive relationship with radial stress and a negative relationship with axial stresses.

Keywords Core disking · Discrete element method · Numerical simulation · Axial stress · Radial stress

Introduction

Rock core fractures with uniform spacing and shapes are common to see in deep drilling of highly stressed regions in the Earth's crust. Known as "core disking",the drilling-induced core fracture phenomenon was first found by Hast (1958) during diamond-drilling in 1958. Core disking is dependent on a series of factors such as in situ stress, rock properties, drilling bit geometry, fluid pressure and temperature. High in situ stresses are generally considered to be the most import influence. Important information about the in situ stress state such as magnitude and orientations is contained in the core disking details, making a study of core disking essential to understanding stresses in the deep crust. Due to the necessity and difficulty in measuring in situ stresses in deep regions of the crust, research on core disking has been going on since 1963 (Jaeger and Coox 1963).

Measuring in situ stresses in the Earth is a very complex problem. It is not only a matter of depth and gravity, but also depends on the history of tectonic events and terrestrial forces that have occurred at a location. Core disking is a regular phenomenon in vertical drill holes, but it also occurs in horizontal drill holes associated with underground excavations such as tunnels (Takehiro 2001). As a sign of high stress perpendicular to the drilling-hole axis, core disking occurs not only in hard rocks like granite or sandstone but also at soft rocks like tuff (Takehiro 2001). High horizontal stresses are particularly associated with reverse faulting stress states (Flottmann et al. 2004).

Hydraulic fracturing, wellbore breakouts and core drilling methods have been used to estimate in situ stress (Crawford et al. 1995). Most of these studies are focusing on solid core disking without inner holes, but some

✉ Haoyan Wu
wuhaoyan@live.cn

[1] University of Science and Technology Beijing, Beijing 100083, China

[2] Key Laboratory of Ministry for Efficient Mining and Safety of Metal Mines, University of Science and Technology Beijing, Beijing 100083, China

[3] Kunming University of Science and Technology, Kunming 650093, Yunnan, China

[4] University of Arizona, Tucson, AZ 85721, USA

researchers (Ishida and Saito 1989) also investigated the hollow core disking, referred to as ring disking, that occurs during the overcoring stress measurement technique. There is some agreement that ring-like disking occurs under a lower stress condition than the solid core disking.

Corthesy and Leite (2008) argued that the estimation of in situ stress from core disking was much too inaccurate and could only be used as a general indicator of high stresses. As pointed out by Chenghu (2014), due to the difficulties in the accurate determination of in situ stress orientation and obtaining the necessary rock properties, in situ stress information examined from the core disking characteristics is not as reliable as expected. Estimating in situ stresses from core disking is challenging and remains an imprecise science to this day. Based on the published research, there are four problems about core disking that still need to be solved.

The first problem is when the fractures initiate and develop during core drilling. It is well known that the core fractures appear due to the stress relief while drilling, due to the abrupt change and redistribution of the in situ stress causing local stress concentration. However, concerning the failure mechanism of rock core fractures, some researchers hold the opinion that it is a shear failure mechanism causing the core disking (Obert and Stephenson 1965; Hast 1979; Hou and Jia 1984), while others believe that it is the tensile failure mechanism causing the disking (Jaeger and Coox 1963; Stacey 1982; Bankwitz 1997; Li and Schmitt 1998; Kaga et al. 2003). And some researchers (Corthésy and Leite 2008; Tianhui et al. 2016) even hold the opinion that the core disking is a combination of tensile and shear failure depending on specific stress situation. Matsuki et al. (2003) believes that the core disking occurs due to tensile stress when the minimum principal stress is nearly the same direction as the core axis. Huang et al. (2016) state that the core disking would occur when the maximum principal stress was more than 5–6 times the tensile strength. Lim (2013) proposed the averaged maximum tensile stress (AMTS) criteria as the core disking criteria. He also pointed out that core disking occurred when the maximum stress was about 6.5 times tensile strength based on Canada's Underground Research Laboratory (URL) data. Several researchers have developed their own stress condition formulas for the core disking as shown in Table 1. Ishida and Saito (1995) compared the measured stress with two criterion of core disking, and found both agreements and disagreements. He also concluded that more accurate core disking criteria was needed in the future. Some core disking criterions are listed in Table 1.

The second controversial problem is the fracture initiating location of core disking and whether it initiates from the surface of the core or the axial center of the core. Obert and Stephenson (1965) thought that the fracture initiated from the surface of the core. Li (1997) pointed out in his thesis that fracture initiating on the core axis can be an indicator of thrust faulting stress. Stacey (1982) came to the conclusion that core disking fractures can start from the exterior surface or the interior axial center of core depending on the effective length of core stub and the geometry of the drill groove.

The third problem is the relationship between in situ stress orientation and the core disking fracture surface geometry. The fracture surfaces take a variety of shapes like flat disking, cup disking, saddle disking, ellipse, petal, and petal-centerline fractures. Kulander et al. (1990) collected a large amount of natural and induced fractures pictures. The orientation of the stress can be determined from different morphologies of core disking. Dyke (1989) indicated that for a vertical borehole with high horizontal stresses, the core disking can turn to saddle disking when the horizontal stress changes from uniform to unequal. The

Table 1 Published core disking criteria

Stress conditions required to occur core disking	Developer
$S_r = k_1 + k_2 S_a$;	By Obert and Stephenson (1965)
$k_1 = -3400 - 2.0S_0$	*Sr* applied radial stress, *Sa* applied axial stress, k_1 *Sr* axis intercept, *k2* slope of the least square line, S_0 shear strength
$1/2(P_x + P_y) \geq -4S_t + P_z$;	By Katsuhiko et al. (1978)
$2.5 \geq P_x/P_y \geq 0.4$; $\sigma_r/S_t = 4.0 + \sigma_z/S_t$	*Pz* axial stress, *Px*,*Py* radial biaxial stresses, *St* Brazilian tensile stress
$S_t = -A\sigma_m + B\sigma_x - C\sigma_x^2/\sigma_m - D(\sigma_x - \sigma_y)$	By Kaga et al. (2003)
	A, B, C, D coefficients that depend on core length, σ_m mean in situ stress
$S_t = 0.302\sigma_m - 0.340\sigma_z + 0.0910(\sigma_z - \sigma_3)$	By Matsuki et al. (1997a)
	σ_z is stress in z direction, σ_m is mean stress and σ_3 is the minimum principal stress
$S_t = \left(-\frac{A}{3} + B - D\right)\sigma_x + \left(-\frac{A}{3} + D\right)\sigma_y - \frac{A}{3}\sigma_z$	By Matsuki et al. (2004)
	σ_x, σ_y, σ_z are stresses in three directions, A, B, D are coefficients

minimum principal stress direction is usually given by the concave axis and the maximum principal stress direction is usually given by the convex axis in the saddle shape.

The last problem is the dependency of core disk thickness on in situ stress magnitude. The spacing of the fracture, called thickness of the core disk, is strongly related to in situ stress magnitude. Many field measurements, observations and theoretical analyses show that the magnitude of in situ stress is closely related to the core disking occurrence and the thickness of core disking. It is well known that the thickness decreases with increasing stress. Hongwei et al. (2014) studied the mechanism of rock core disking in a coal mine from the perspective of stress condition and energy theory and he found that the core disking thickness was nearly equal to the drilling interval depth of 20 mm. Shang and Sun (1991) collected and analyzed the core disking features from the TianHuangCheng power station in China and it was found that core thickness ranged from 0.5 to 3 cm, where 1 cm was most common. As Lim (2013) mentioned in his thesis, four categories were defined based on the disk thickness t and diameter D: thin ($t/D < 0.2$), medium ($0.2 < t/D < 0.4$), thick ($0.4 < t/D < 2.2$), and partial disking.

A number of numerical studies with FEM or BEM have been carried out to research the stress distribution and in particular the stress concentrations during the drilling process. Bahrani et al. (2015) used both continuum and discontinuum codes to investigate the stress path during drilling, and the core damage induced by drilling. He also pointed out that future work on the simulation of the drilling process utilizing the three-dimensional discrete element method PFC3D would enhance our understanding of core disking.

Most of the core disking papers are focused on the concentration and distribution of stresses during drilling. It is rare to find papers concerning fracture evolution and propagation as it relates to core disking, which is exactly the subject of this paper. This paper looks in detail at fracture propagation during drilling using the PFC3D software, and in doing so helps to address the four problems discussed above. The effects of pre-existing discontinuities (joints, faults, bedding planes) in the rock mass on the core disking process are not considered in the present paper.

Discrete element modeling

Besides field observation (Zhu et al. 1985), theoretical research (listed in Table 1), and more combination of these two methods, the rapid development of computing now allows numerical modeling to become an important method for core disking studies. Based on the current numerical research in this area, most of the simulations are done using the finite element method (Matsuki et al. 1997b; Li and Schmitt 1997a, b) or the boundary element method (Dyke 1989; Obara et al. 1998). Actually, the discrete element method, developed by Cundall and Strack (1979), has a significant advantage over these methods, particularly in the area of micro-fracture evolution.

The PFC includes PFC2D (two-dimensional particle flow code) and PFC3D (three-dimensional particle code). In PFC, the specimen rock can be simulated by rigid particles (circle disks in PFC2D and balls in PFC3D) and contacts. Particles move according to Newton's second law; the contacts can transmit both forces and moments to particles. The movements are updated according to the force–displacement law. When the stresses exceed the bonding strength between particles, the contact bond breaks and a fracture appears. More information about PFC can be referred to the guide (Itasca Consulting Group 2015). Although the computing speed in PFC3D is far slower than in PFC2D, the simulation is more real and the result is more believable. So PFC3D is adopted in this study and the results are compared with other methods for a better understanding of core disking. This provides a detailed insight into the coring process as given in this paper.

As validated by McGarr and Gay (1978), it is appropriate to assume that the vertical borehole is in one of the principal stress directions. This assumption was also taken in PFC simulations described here and the vertical stress was calculated by the overburden stress as one of the principal stresses.

The coring process is modeled by deleting particles between the inner cylinder and outer cylinder in the same manner as the actual drilling procedure. It should be noted that the weight of the drilling bit, the wellbore fluid pressure and the drill bit geometry are not taken into consideration in this work for simplification. The coring is simulated from a zero core stub length to 20 mm using an increment of 10 mm.

For simplification, the three principal stresses are assumed to lie along the x, y, and z axis, and the drilling is along the vertical z direction. The boundary condition of the numerical model is vertical stress S_v, maximum horizontal stress S_H and minimum horizontal stress S_h. Despite the simplifications of the numerical modeling, the core disking phenomenon does occur from the discrete element method modeling and some reasonable correlations can be obtained between the stress states and core disking.

A variety of stress situations are simulated by PFC3D in this paper for a detailed investigation of core disking fracture evolution, as described in the next several sections.

Initial stress of rock core disking

Indiana limestone mechanical properties adopted from Obert and Stephenson (1965) were used for the numerical parameters calibration in this research. The UCS (unconfined compression strength) was 60.67 MPa (8800psi) and TS (direct tensile strength) was 4.69 MPa (680psi). The calibrated uniaxial compressive strength and tensile strength of the numerical rock specimen are 62.17 MPa (UCS) and 4.76 MPa (TS).

The enhanced bonded particle model (EBPM) is used in this paper, which can better fit the high ratio of UCS/TS of brittle rocks. More information about EBPM can be found in Vallejos et al. (2016). Micro parameters are calibrated based on the given UCS and TS values of Indiana limestone using a trial and error method. Table 2 gives the micro parameters of the enhanced parallel bonds. More information about parameters can be referred to the guide (Itasca Consulting Group 2015).

To investigate the initiation stress of core disking, precluding the other influences, four hydrostatic pressure states including 10, 20, 30 and 40 MPa were considered for numerical simulations. For a high computing efficiency, a 60 × 60 × 60 mm cubic assembly containing 76,798 balls with diameters ranging from 1.4 to 1.7 mm is generated and the confining pressures are applied using the servo-controlling walls in PFC3D.

Referring to Holt et al. (2000, 2001), the drilling process is separated into 3 procedures. Firstly, a layer of balls with diameter of 34 mm and height of 3 mm was deleted to release the vertical stress of the drilling hole. Then, the core was drilled to a height of 10 mm with a diameter of 26 mm, following the drilling bit width of 4 mm. Finally, another layer of balls of 10 mm in height was deleted.

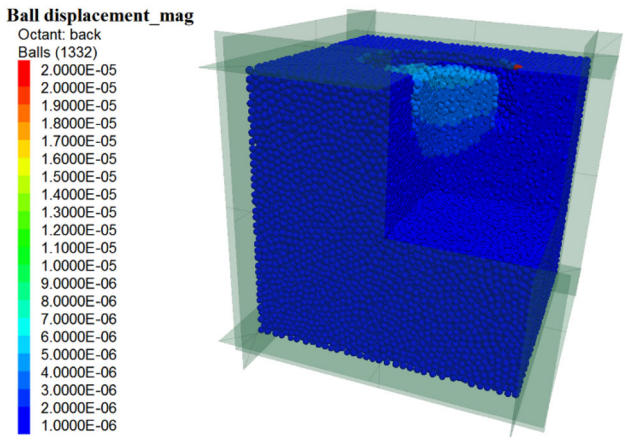

Fig. 1 Octant sectional view of model (The color bar on the left represents particle displacement magnitude, with units in meters. The warmer colors represent larger displacements.)

Table 2 Micro parameters of the enhanced parallel bond model for Indiana Limestone

Micro parameter	Definition	Value
pbm_mcf	Moment contribution factor	0
pbm_ten_m	Tensile strength of the bonds (MPa)	3.3
pbm_coh_m	Cohesion of the bonds (MPa)	25
pbm_bkrat	Ratio of parallel-bond normal to shear stiffness	1.5
pbm_emod	Young's modulus of parallel bonds (GPa)	30

A sectional view of the three-dimensional model is shown in Fig. 1. However, for a better view of the core disking fracture evolution process, cutaway views from the center with normal directions (1, 0, 0) (0, 1, 0) and (0, 0, 1) are shown in the following figures.

In Figs. 2, 3, 4, and 5, the three drilling stages (3, + 10, + 10 mm) are shown in cutaway views along *x* axis through the center for each of the four stress situations (10, 20, 30, 40 MPa), respectively. Induced fractures are shown by short black lines and are marked by red circles for additional clarity. In PFC3D, the fractures are formed by the breakage of contact between balls, and this breakage simulates the formation of micro-cracks from pores, pre-existing micro-cracks, grain boundaries, etc. Further cracks are then formed by the breakage of neighboring ball contacts.

From Figs. 2, 3, 4, and 5, it is clear that all the fractures initiate from the outer surface of the core. When the stress is 10 MPa, it is hard to find any obvious fractures during the three drilling stages. During the third drilling stage of the 20 MPa stress condition, fractures are occurring from the outer edge of the drilling core. Obvious fractures appear at the second drilling stage under the 30 MPa stress condition. And it is not until 40 MPa that the fractures run though the inner part of the core, which forms the core disking phenomenon. Based on these results, the initial hydrostatic stress for core disking can be defined as 40 MPa, which is about 6.7 times the tensile strength of the simulated Indiana limestone. The result corresponds well with current results as mentioned in the introduction section. Table 3 summarizes the results, showing fracture counts in the drilling process under the 10–40 MPa in situ stress cases. Table 3 shows that the larger the in situ stress, the more the fractures appear. What is more, the number of additional cracks is significantly larger as the in situ stress increases.

Initial position of rock core disking

A common theory about core disking is that it happens due to the stress release after drilling. Hence, fractures are conventionally thought to begin from the drilling kerf

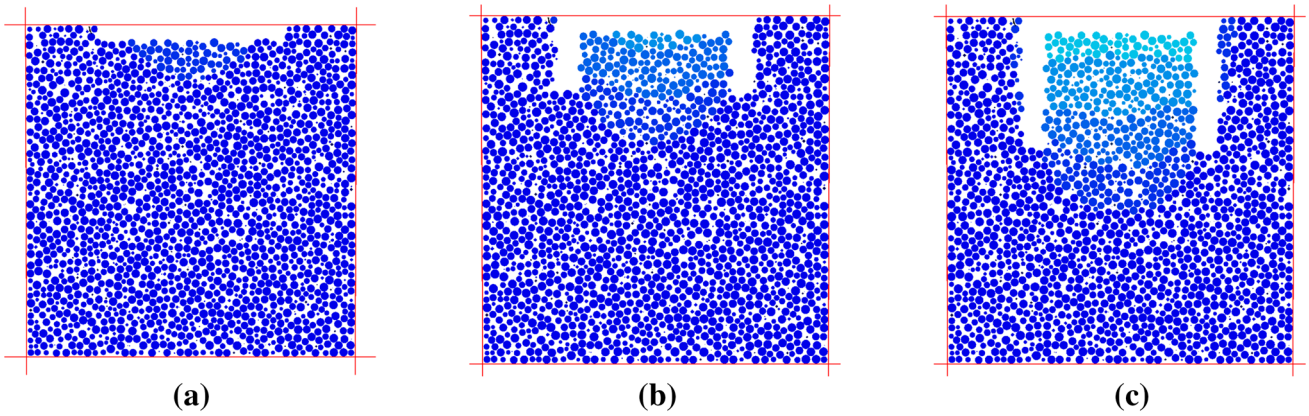

Fig. 2 Ball displacements and fracture evolutions of under hydrostatic stress of 10 MPa; **a** 1st drilling stage, **b** 2nd drilling stage, **c** 3rd drilling stage

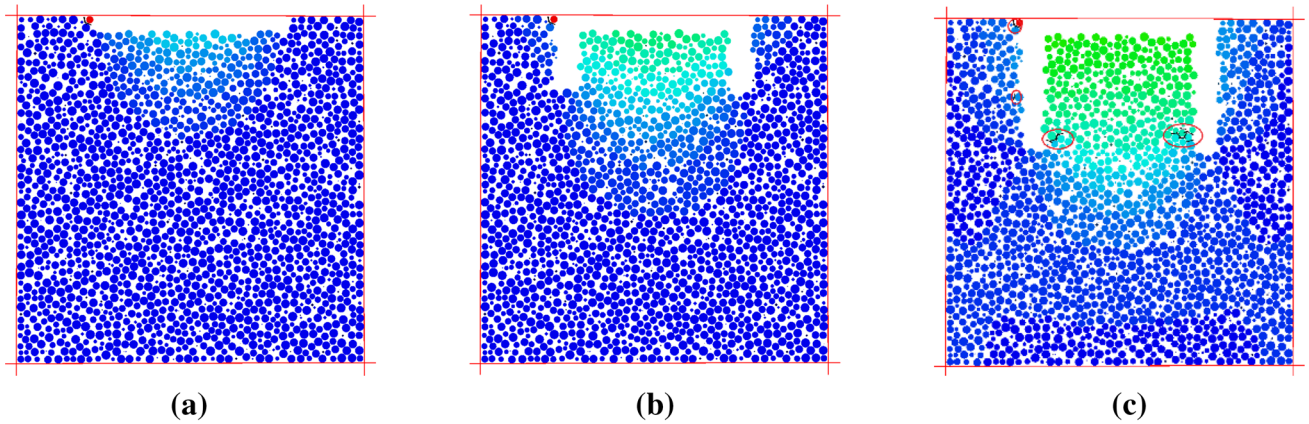

Fig. 3 Ball displacements and fracture evolutions of under hydrostatic stress of 20 MPa; **a** 1st drilling stage, **b** 2nd drilling stage, **c** 3rd drilling stage

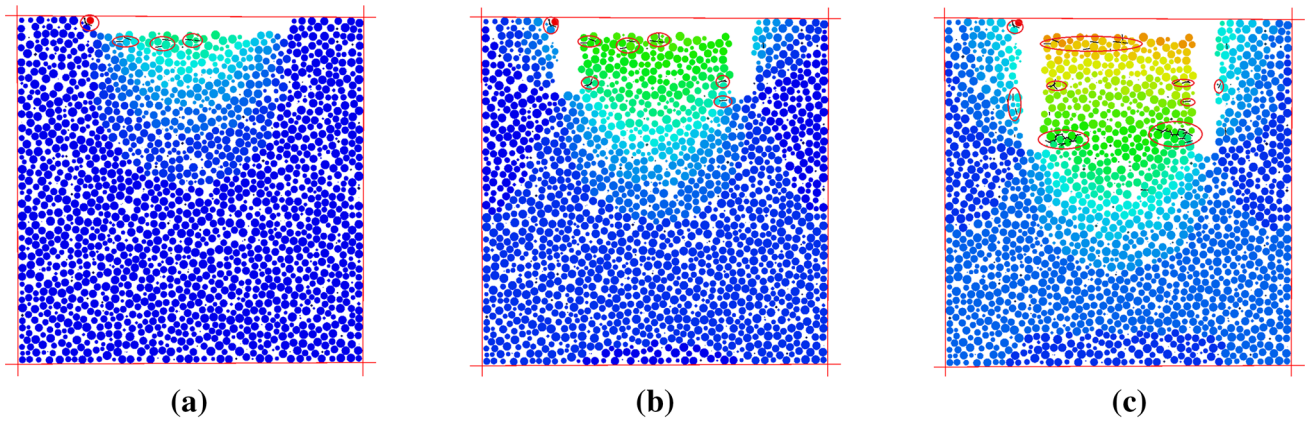

Fig. 4 Ball displacements and fracture evolutions of under hydrostatic stress of 30 MPa; **a** 1st drilling stage, **b** 2nd drilling stage, **c** 3rd drilling stage

vicinity where the stress concentrations are highest. The detailed observation of the initiation and propagation of fractures is the main technique for studying core disking in this paper. Here, we focus on the second stage of drilling (10 mm annular kerf) to better understand fracture initiation and propagation resulting in core disking. Cross-section views of this stage are shown in Fig. 6. Figure 6 considers three cases where the in situ stresses are not

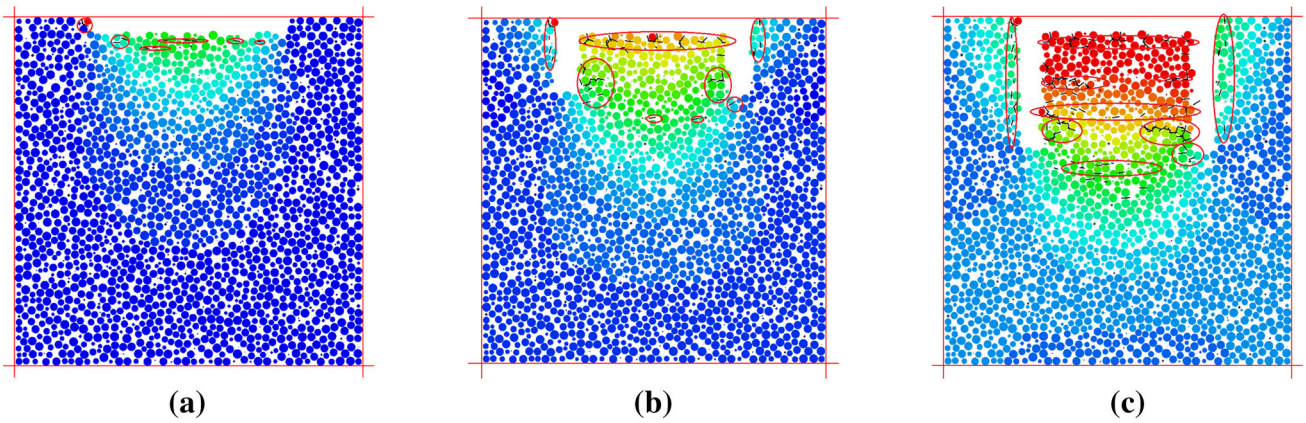

Fig. 5 Ball displacements and fracture evolutions of under hydrostatic stress of 40 MPa; **a** 1st drilling stage, **b** 2nd drilling stage, **c** 3rd drilling stage

Table 3 Fracture counts during drilling under the four stress cases shown in Figs. 2, 3, 4, and 5

Stress cases (MPa)	1st drilling stage	2nd drilling stage	3rd drilling stage
10	27	28	30
20	82	174	620
30	141	685	1783
40	248	1701	3937

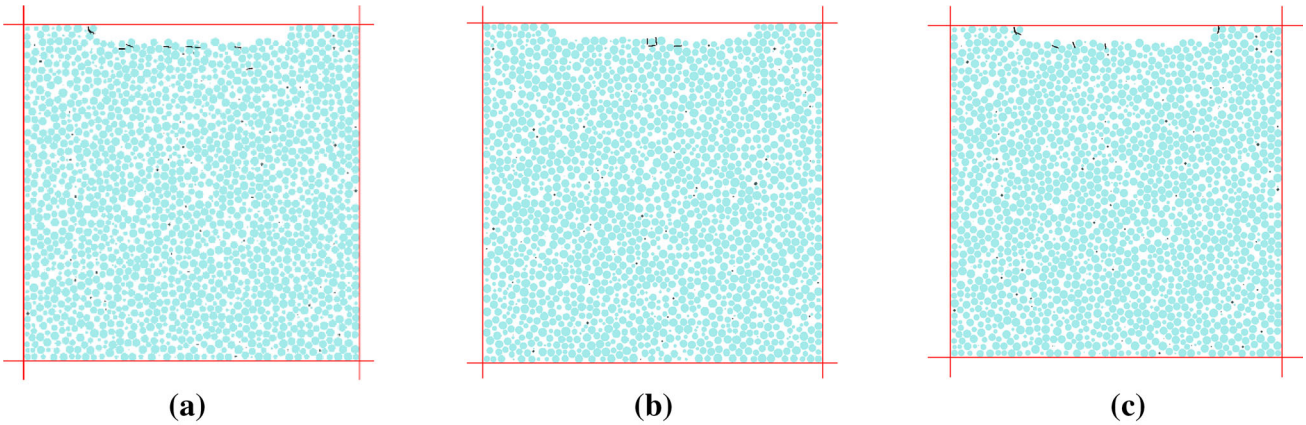

Fig. 6 Core disking fractures during stage 1 at 0 cycles. **a** $\sigma_x = 20$MPa, $\sigma_y = 40$MPa, $\sigma_z = 10$MPa, **b** $\sigma_x = 40$MPa, $\sigma_y = 10$MPa, $\sigma_z = 20$MPa, **c** $\sigma_x = 10$MPa, $\sigma_y = 20$MPa, $\sigma_z = 40$MPa

equal but have values of 10, 20, and 40 MPa. The first case is a thrust faulting condition (maximum principal stress horizontal, minimum principal stress vertical), the second case is a strike-slip faulting condition (both max and min principal stresses are horizontal), and the third case is a normal faulting condition (max is vertical, minimum is horizontal).

In the strike-slip and normal faulting stress condition cases, most fractures initiate from the drilling kerf and then propagate to the inner core. On the other hand, fractures begin from the inner core under the thrust fault condition ($\sigma H > \sigma h > \sigma v$). Although dozens of stress cases were simulated, Fig. 6 shows three of these cases and, in particular, cases where core disking fractures initiate from both the inner core and outer core surfaces. Each black short line in the figures represents a fracture which means a bond break in the PFC software.

For the three different stress conditions, eight representative running cycles are picked out to show the fracture initiation and propagation process. Aside from the first stress case ($\sigma_x = 20$ MPa, $\sigma_y = 40$ MPa, $\sigma_z = 10$ MPa), fractures do not coalesce to form core disks in the other two stress cases. Nevertheless, the focus in this chapter is on the fracture initiating location rather than other aspects.

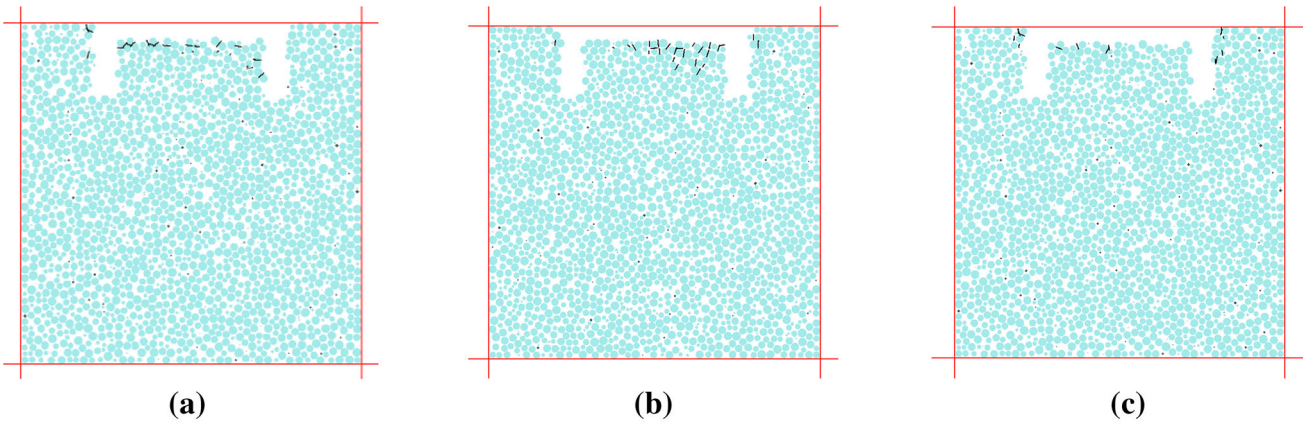

Fig. 7 Core disking fractures during stage 2 at 100 cycles. **a** $\sigma_x = 20$MPa, $\sigma_y = 40$MPa, $\sigma_z = 10$MPa, **b** $\sigma_x = 40$MPa, $\sigma_y = 10$MPa, $\sigma_z = 20$MPa, **c** $\sigma_x = 10$MPa, $\sigma_y = 20$MPa, $\sigma_z = 40$MPa

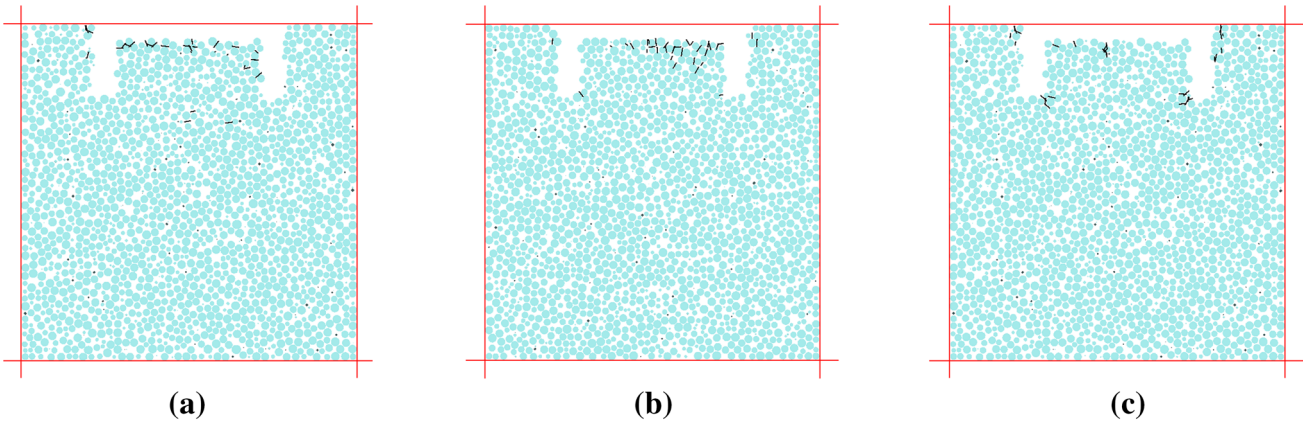

Fig. 8 Core disking fractures during stage 2 at 200 cycles. **a** $\sigma_x = 20$MPa, $\sigma_y = 40$MPa, $\sigma_z = 10$MPa, **b** $\sigma_x = 40$MPa, $\sigma_y = 10$MPa, $\sigma_z = 20$MPa, **c** $\sigma_x = 10$MPa, $\sigma_y = 20$MPa, $\sigma_z = 40$MPa

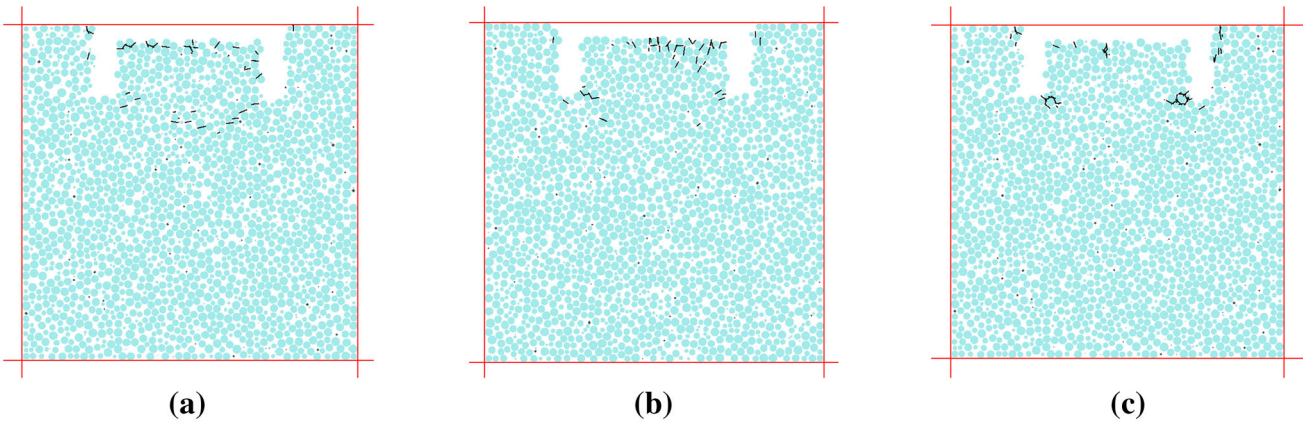

Fig. 9 Core disking fractures during stage 2 at 300 cycles. **a** $\sigma_x = 20$MPa, $\sigma_y = 40$MPa, $\sigma_z = 10$MPa, **b** $\sigma_x = 40$MPa, $\sigma_y = 10$MPa, $\sigma_z = 20$MPa, **c** $\sigma_x = 10$MPa, $\sigma_y = 20$MPa, $\sigma_z = 40$MPa

The results in Figs. 6, 7, 8, 9, 10, 11, 12, and 13 demonstrate rather conclusively that core disking initiates from the outer surface rather than inner core, except in the case of thrust faulting conditions. Figs. 6, 7, 8, 9, 10, 11, 12, and 13 are cross-section views along x axis through the center of the model. This result is immediately useful in

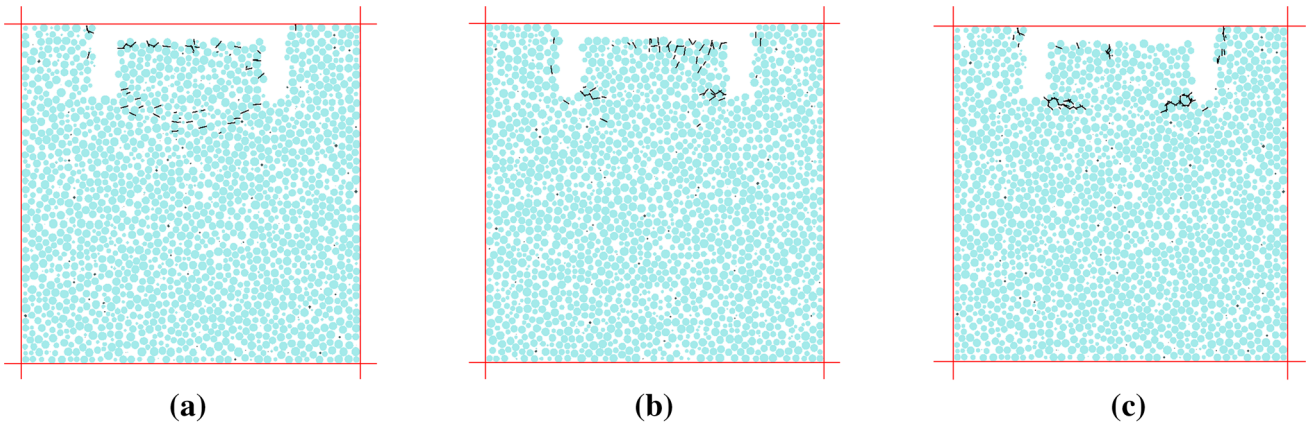

Fig. 10 Core disking fractures during stage 2 at 500 cycles. **a** $\sigma_x = 20$MPa, $\sigma_y = 40$MPa, $\sigma_z = 10$MPa, **b** $\sigma_x = 40$MPa, $\sigma_y = 10$MPa, $\sigma_z = 20$MPa, **c** $\sigma_x = 10$MPa, $\sigma_y = 20$MPa, $\sigma_z = 40$MPa

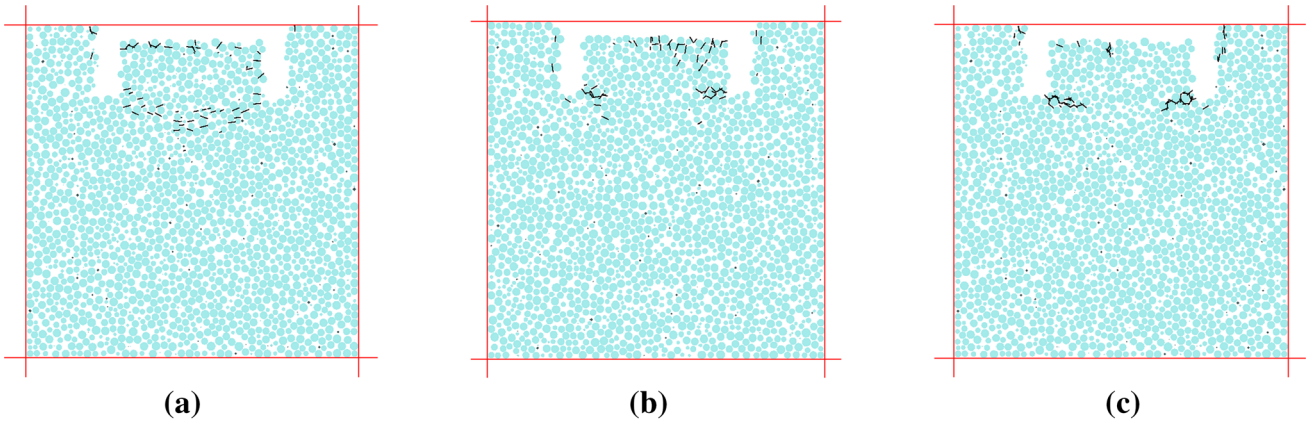

Fig. 11 Core disking fractures during stage 2 at 1000 cycles. **a** $\sigma_x = 20$MPa, $\sigma_y = 40$MPa, $\sigma_z = 10$MPa, **b** $\sigma_x = 40$MPa, $\sigma_y = 10$MPa, $\sigma_z = 20$MPa, **c** $\sigma_x = 10$MPa, $\sigma_y = 20$MPa, $\sigma_z = 40$MPa

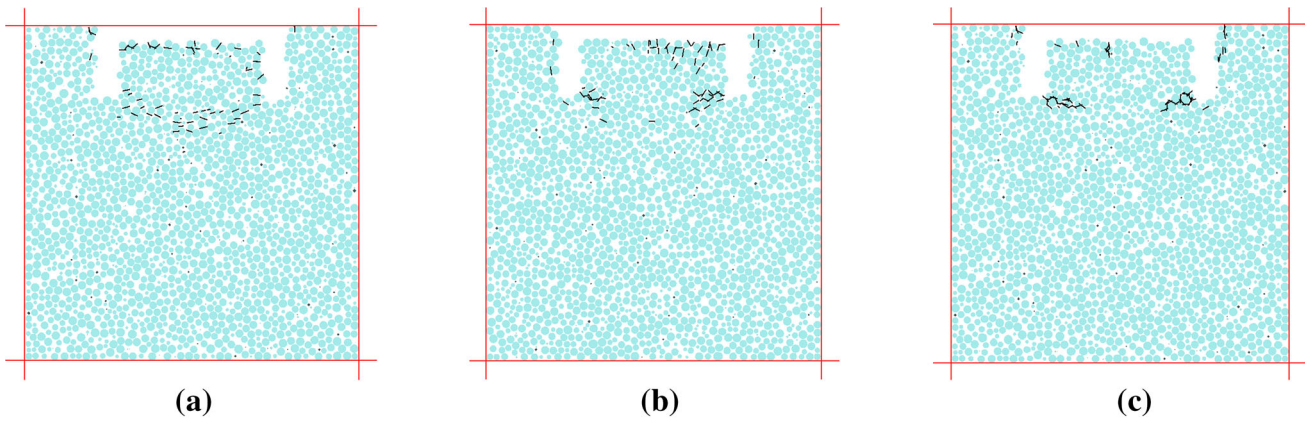

Fig. 12 Core disking fractures during stage 2 at 2000 cycles. **a** $\sigma_x = 20$MPa, $\sigma_y = 40$MPa, $\sigma_z = 10$MPa, **b** $\sigma_x = 40$MPa, $\sigma_y = 10$MPa, $\sigma_z = 20$MPa, **c** $\sigma_x = 10$MPa, $\sigma_y = 20$MPa, $\sigma_z = 40$MPa

judging the in situ stress state from core samples. In field observation, the fracture evolution process is invisible. However, the drilled cores can be examined by hand, and if partial disking is occurring (fractures have not gone through the inner core), we can directly deduce that the stress condition is not a thrust fault condition (with the

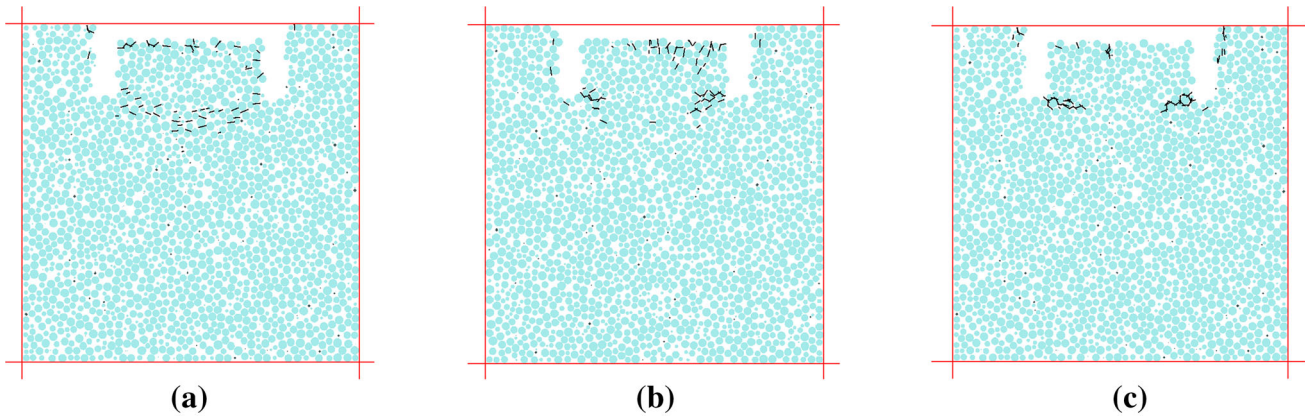

Fig. 13 Core disking fractures during stage 2 at 3000 cycles. **a** $\sigma_x = 20$MPa, $\sigma_y = 40$MPa, $\sigma_z = 10$MPa, **b** $\sigma_x = 40$MPa, $\sigma_y = 10$MPa, $\sigma_z = 20$MPa, **c** $\sigma_x = 10$MPa, $\sigma_y = 20$MPa, $\sigma_z = 40$MPa

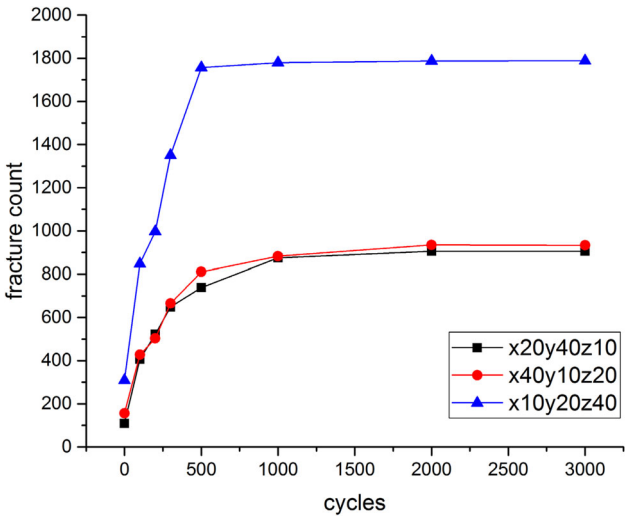

Fig. 14 Evolution of fracture counts under three different stress conditions

assumption that the vertical z direction is the drilling direction). We can also estimate the stress magnitude range for the three directions based on the numerical results in the following sections.

The numbers of fractures were also counted for the three cases shown in Fig. 6, 7, 8, 9, 10, 11, 12, and 13. These fracture counts are plotted in Fig. 14. As the real time is not the same as the steps in PFC modeling, the time in x axis is represented by cycles. Curves of fracture count versus cycles have similar shapes for the three cases, showing a rapid increase in early stages and a stable tendency thereafter. When the curve becomes stable, it means that no additional fractures are initiating. Even though only three stress cases are shown on the figure, what is very clear is that the normal faulting case (vertical stress 40 MPa, horizontal stresses 10 and 20 MPa) results in a significantly larger number of fracture counts. The number of fractures under the larger axial stress case (40 MPa) is almost two times of those under the smaller axial stress cases (10 and 20 MPa) as shown in Fig. 14.

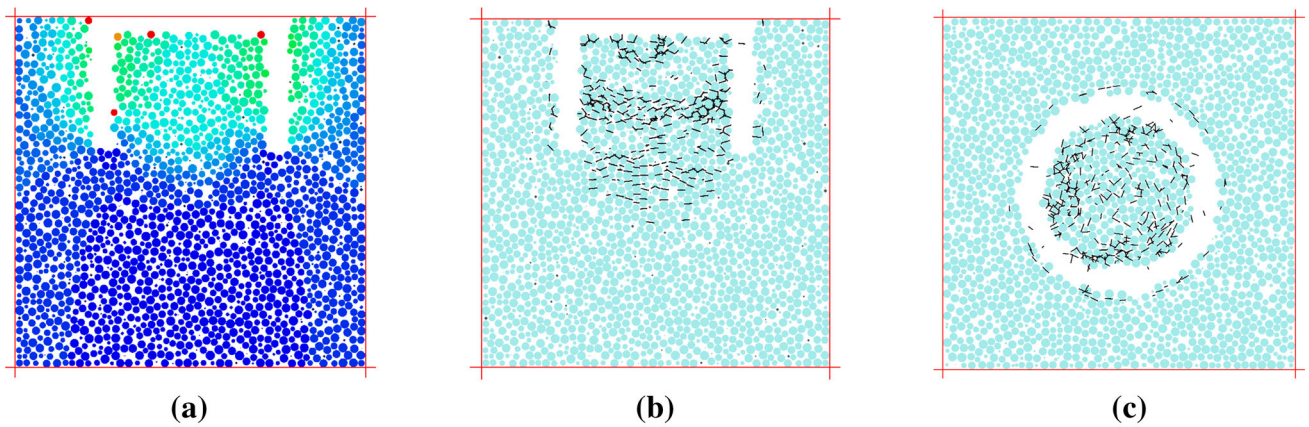

Fig. 15 Stress case ($\sigma_x = 40$MPa, $\sigma_y = 40$MPa, $\sigma_z = 10$MPa); **a** ball displacement, **b** fracture morphology in sectional view along y axis, **c** fracture morphology in sectional view along z axis

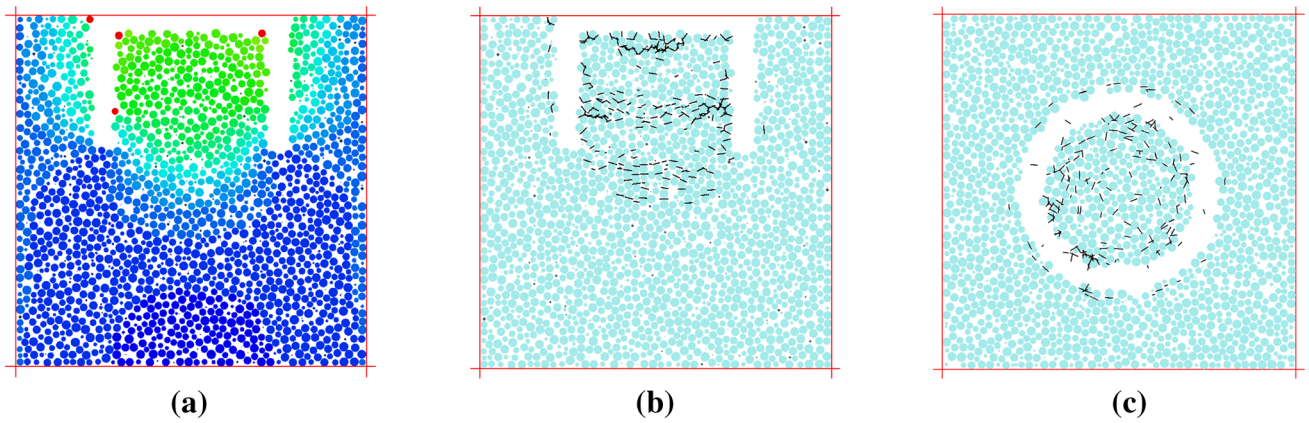

Fig. 16 Stress case ($\sigma_x = 40$MPa, $\sigma_y = 40$MPa, $\sigma_z = 20$MPa); **a** ball displacement, **b** fracture morphology in sectional view along y axis, **c** fracture morphology in sectional view along z axis

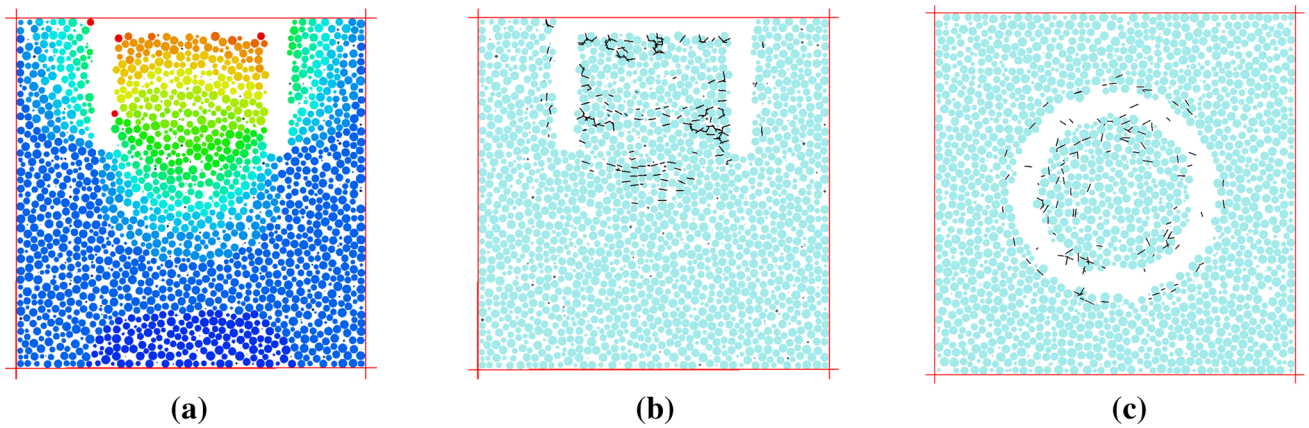

Fig. 17 Stress case ($\sigma_x = 40$MPa, $\sigma_y = 40$MPa, $\sigma_z = 30$MPa); **a** ball displacement, **b** fracture morphology in sectional view along y axis, **c** fracture morphology in sectional view along z axis

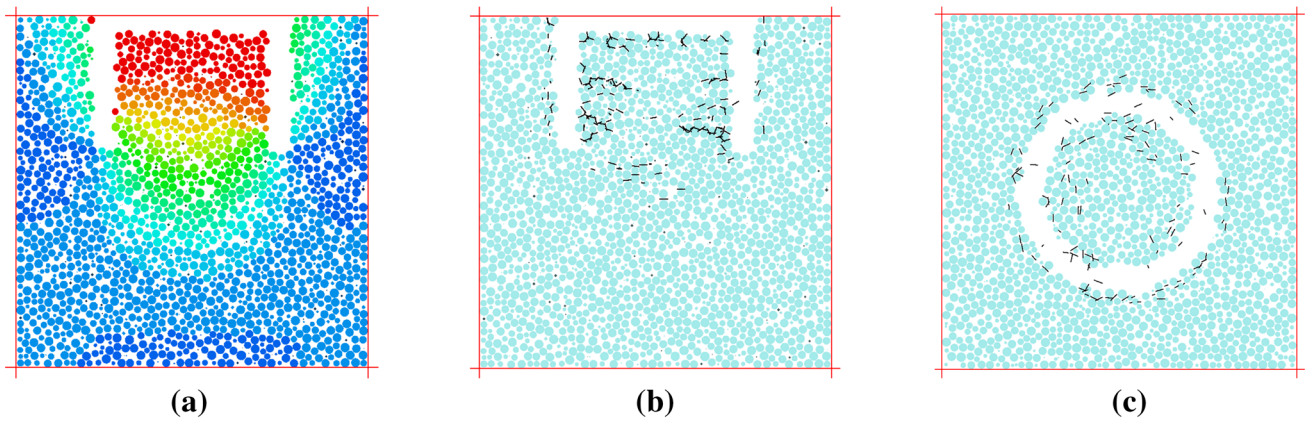

Fig. 18 Stress case ($\sigma_x = 40$MPa, $\sigma_y = 40$MPa, $\sigma_z = 40$MPa); **a** ball displacement, **b** fracture morphology in sectional view along y axis, **c** fracture morphology in sectional view along z axis

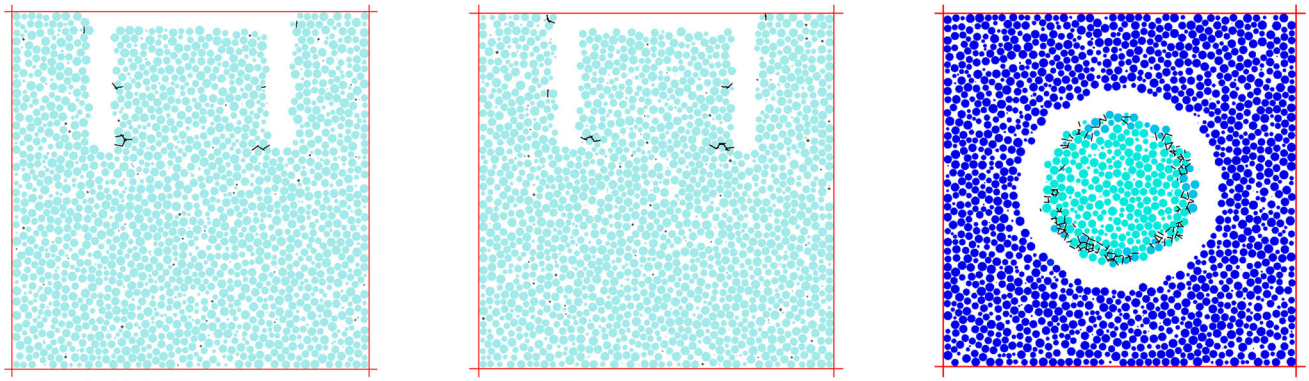

Fig. 19 Stress case (σ_x = 10MPa, σ_y = 10MPa, σ_z = 20MPa); **a** fracture morphology in sectional view along y axis, **b** fracture morphology in sectional view along x axis, **c** ball displacements and fracture morphology in sectional view along z axis

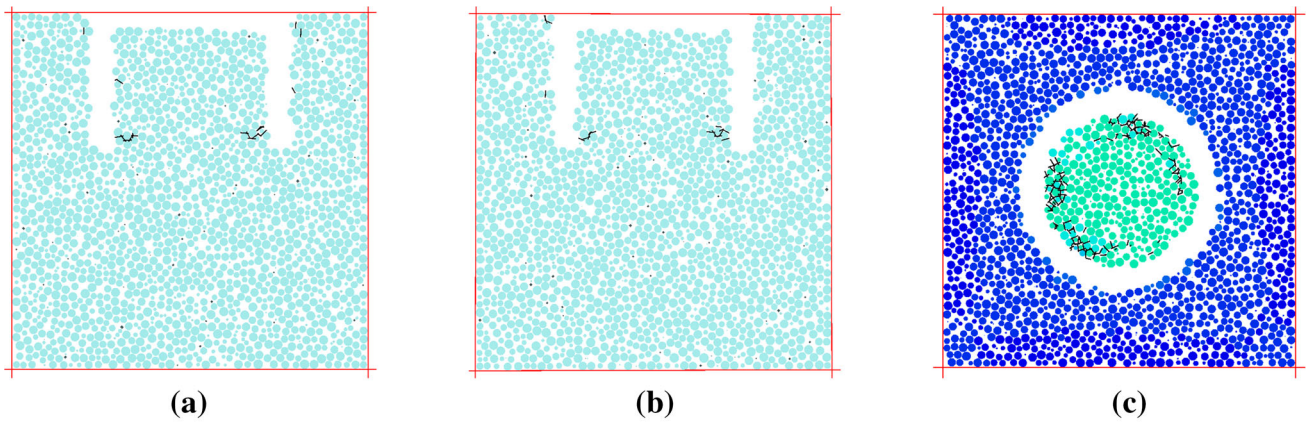

Fig. 20 Stress case (σ_x = 20MPa, σ_y = 20MPa, σ_z = 20MPa); **a** fracture morphology in sectional view along y axis, **b** fracture morphology in sectional view along x axis, **c** ball displacements and fracture morphology in sectional view along z axis

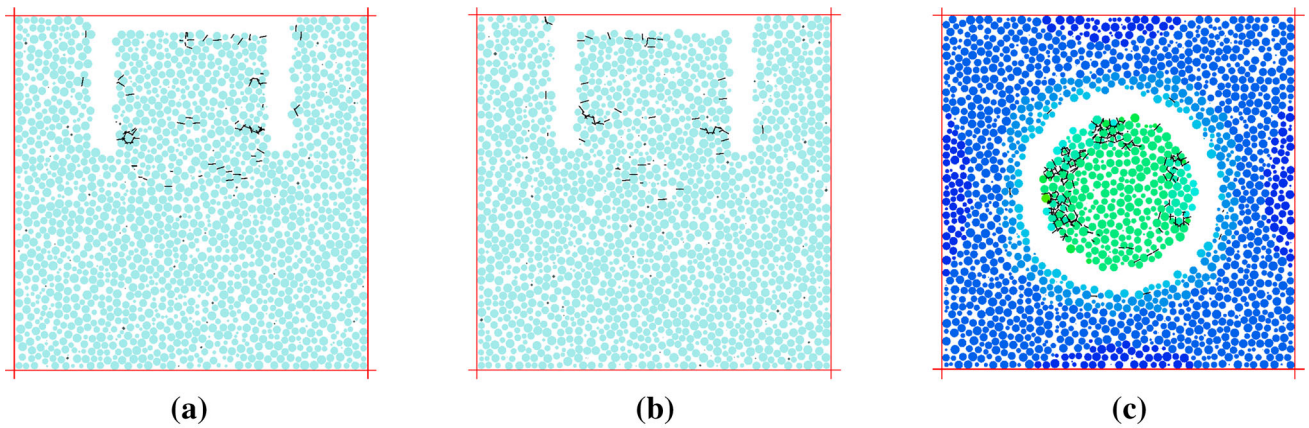

Fig. 21 Stress case (σ_x = 30MPa, σ_y = 30MPa, σ_z = 20MPa); **a** fracture morphology in sectional view along y axis, **b** fracture morphology in sectional view along x axis, **c** ball displacements and fracture morphology in sectional view along z axis

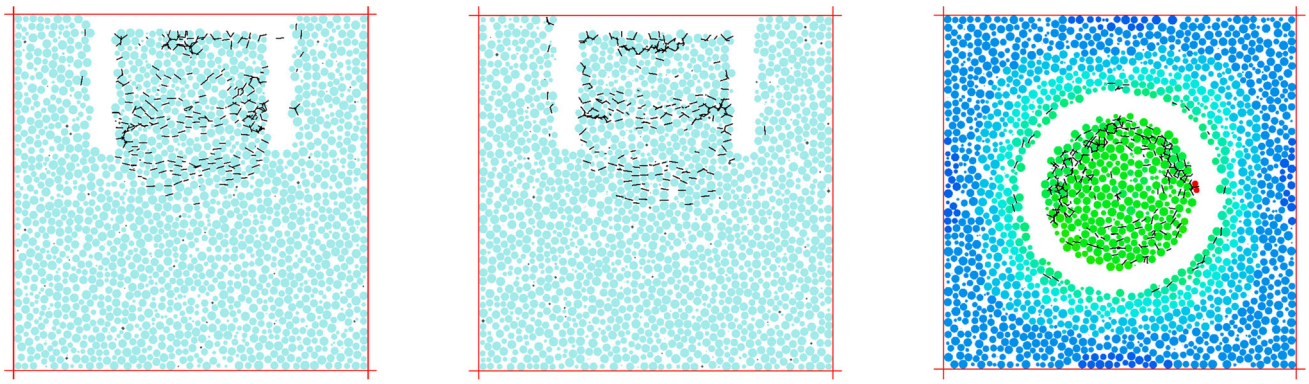

Fig. 22 Stress case ($\sigma_x = 40$MPa, $\sigma_y = 40$MPa, $\sigma_z = 20$MPa); **a** fracture morphology in sectional view along y axis, **b** fracture morphology in sectional view along x axis, **c** ball displacements and fracture morphology in sectional view along z axis

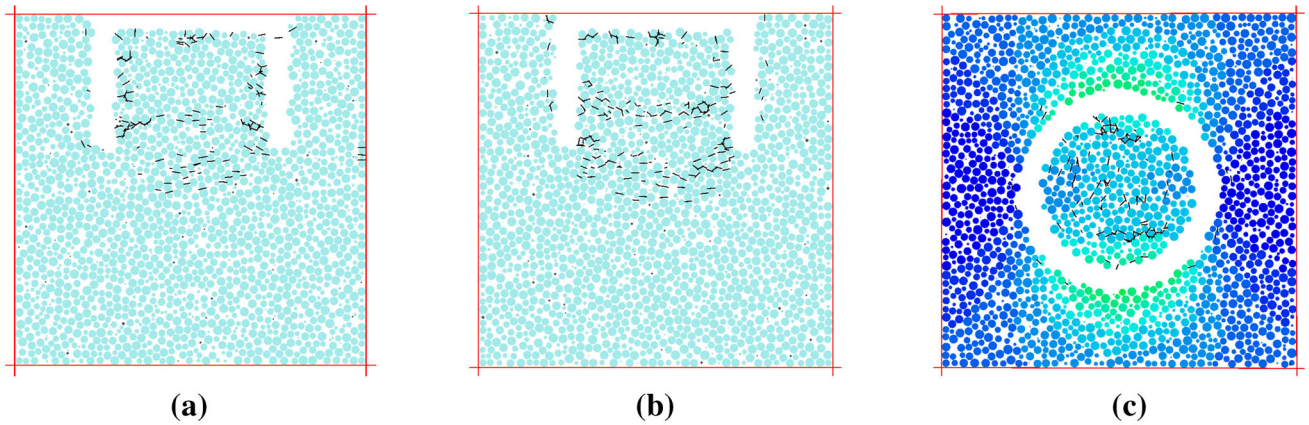

Fig. 23 Stress case ($\sigma_x = 10$MPa, $\sigma_y = 40$MPa, $\sigma_z = 10$MPa); **a** fracture morphology in sectional view along y axis, **b** fracture morphology in sectional view along x axis, **c** ball displacements and fracture morphology in sectional view along z axis

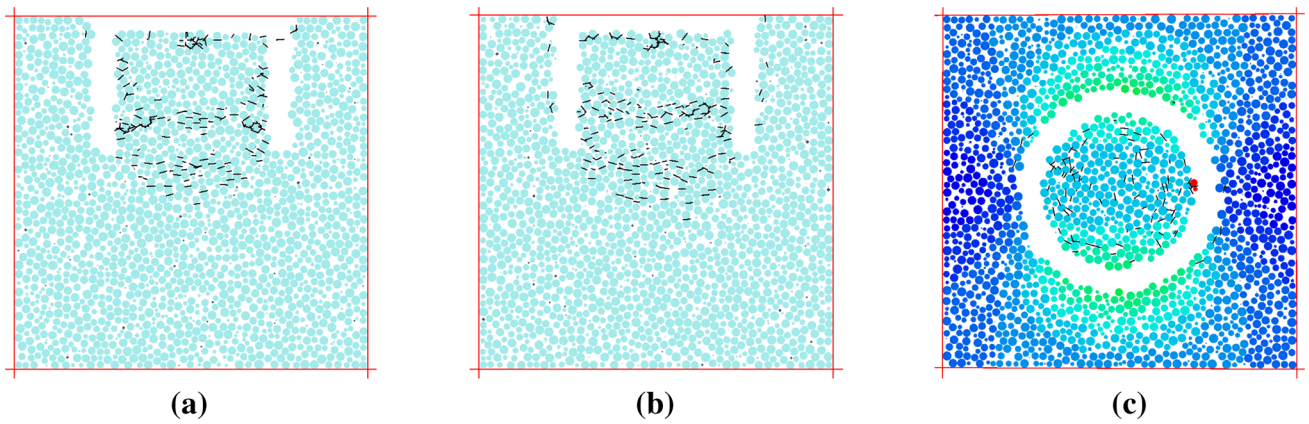

Fig. 24 Stress case ($\sigma_x = 20$MPa, $\sigma_y = 40$MPa, $\sigma_z = 10$MPa); **a** fracture morphology in sectional view along y axis, **b** fracture morphology in sectional view along x axis, **c** ball displacements and fracture morphology in sectional view along z axis

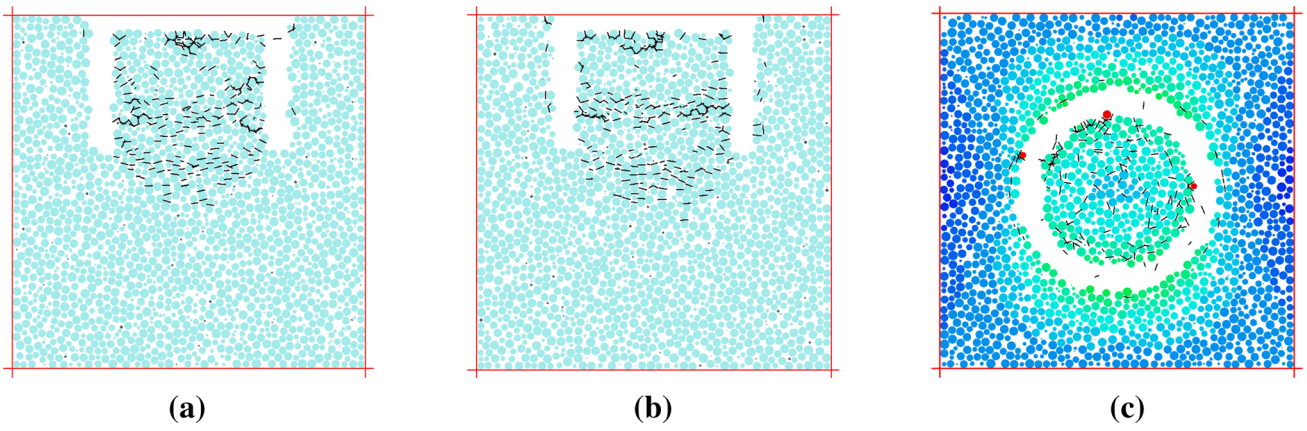

Fig. 25 Stress case ($\sigma_x = 30$MPa, $\sigma_y = 40$MPa, $\sigma_z = 10$MPa); **a** fracture morphology in sectional view along y axis, **b** fracture morphology in sectional view along x axis, **c** ball displacements and fracture morphology in sectional view along z axis

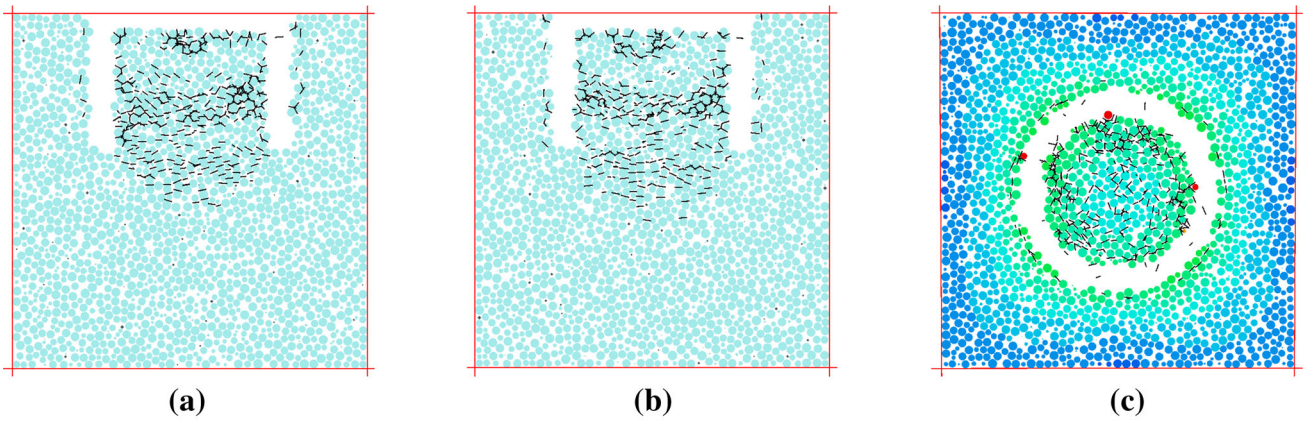

Fig. 26 Stress case ($\sigma_x = 40$MPa, $\sigma_y = 40$MPa, $\sigma_z = 10$MPa); **a** fracture morphology in sectional view along y axis, **b** fracture morphology in sectional view along x axis, **c** ball displacements and fracture morphology in sectional view along z axis

Effects of axial stress

Based on the results in Initial stress of rock core disking showing that 40 MPa is required for core disking in the simulated Indiana limestone, a horizontal stress of 40 MPa is chosen to investigate the effects of axial stress on core disking in this section. Four stress cases with ratios of axial to radial stress ranging from 0.25 to 1 are simulated. The results of the four cases are shown in Figs. 15, 16, 17, and Fig. 18. The third drilling stages are considered in this part. A sectional view along z axis is also added for a better view of whether fractures go through the axis of the core or not.

The results in Figs. 15, 16, 17, and 18 are very interesting. The fractures run through the inner center of the core when the axial stress becomes smaller and the thickness of the core disking increases as the axial stress becomes larger and, finally, the phenomenon turns to partial disking when the axial stress is equal to radial stress 40 MPa. It can be seen from the results that the core disking phenomenon gets more obvious as the ratio of radial stress to axial stress becomes lower. Or stated another way, the axial stress can impede the core disking occurrence. The result is similar to the work of Tianhui et al. (2016) who finds that the core disking weakens with the increase of the axial stress when the radial stress remains constant.

Effects of radial stresses

In three-dimensional numerical modeling, the effects of the radial stresses can be separated into two parts in this study, one is equal horizontal stresses ($\sigma_x = \sigma_y$) and the other is unequal horizontal stresses ($\sigma_x \neq \sigma_y$).

For the first case, an axial stress of 20 MPa in the vertical direction is applied in the numerical model, and 10, 20, 30 and 40 MPa are chosen as the radial stress. Ball displacements, fracture morphologies and number of

fractures are compared for the four stress situations, similar to the layout of the last section.

From Figs. 19, 20, 21, and 22, it is clear that when the axial stress remains constant, the core disking phenomenon becomes much more obvious as the radial stresses increase. The fractures turn from local concentrating in the vicinity of drilling kerf to running through the whole core. And fractures even appear under the drilling core in addition to those near the drilling kerf.

In a thrust fault stress environment, where the horizontal stresses are different, the maximum principal stress σ_H is assumed in the y direction, the intermediate principal stress σ_h is assumed in the x direction, and the minimum principal stress σ_V is in the vertical z direction aligned with the drilling axis. Here, we look at the situation where the minimum principal stress and the maximum principal stress are kept constant, while the intermediate principal stress is varied from 10 MPa to 40 MPa, as shown in Figs. 23, 24, 25, and 26. The models are cut from three different directions (two vertical slices and one horizontal slice) to have good views of the fracture morphologies. The particle displacements are also shown in the horizontal slice.

Figures 22, 23, 24, 25, and 26 show that differences in the fracture morphologies are not easy to find between the two vertical cutting sections, even though the radial stresses in the x and y directions are different. From the horizontal cross-section view, the results show that fractures and ball displacements are both higher in the larger radial stress direction. In fact, those differences are related to the shape of the core disking. A clear morphology of core disking is difficult to plot in the three-dimensional modeling as the model is not large enough and the particles are not small enough. Section view is a proper way to show the influences of different radial stresses on the shape of core disking.

Results and discussion

This paper describes the use of the 3D particle flow code to improve our understanding of fracture initiation and propagation associated with core disking. The results shown in this paper are just a small subset of the possible uses of PFC3D to study the effects of stress condition, rock material properties, and drilling parameters on core disking. The results shown in this paper specifically address the four unknowns with regard to fracture propagation associated with core disking: (1) when in the drilling process fractures initiate, (2) which part of the core the fractures initiate, (3) relationship between stress state (normal, thrust, strike-slip) and fracturing, and (4) dependence of disk thickness on stress magnitude. The results provide many insights into these problems For example, it is found that the stress to initiate core disking has a quantitative relationship with the tensile strength rather than the compressive strength. Also, this study has shown how the magnitudes of the axial and radial stresses can influence the shape, the thickness and the initiation location of core disking.

As in any numerical simulation study, some simplifications and assumptions are made in the modeling. First of all, the particle size is larger than the actual grain size of the simulated Indiana limestone. Simplifications have also been made in the simulated drilling process. Li and Schmitt (1997a, b) pointed out that the bottom-hole concentration of far field stress was influenced by the core stub length and Poisson's ratio. Variations in parameters such as Poisson's ratio have not been made, and the drilling bit weight and fluid pressure during the drilling process are not included. Overall the discrete element model is a simplified one. In spite of these simplifications, the numerical model is able to provide insight into all four of the problems mentioned above.

Compared with other core disking simulation studies that utilized a simplified form of unloading (Huang et al. 2016) or numerical studies that involved adding new layers to the core stub (Li 1997), the particle flow code method used in this paper gives a more realistic core retrieving process by deleting the rock core outer particles. Most published research is focused on stress redistribution associated with core disking rather than fracturing. However, it is the initiating, growing and coalescing of the micro-fractures that results in the core disking phenomenon.

Conclusions

Core disking has been recognized as an indicator of high in situ stress and a more detailed relationship between core disking and in situ stress was established in this paper by utilizing the discrete element method and considering the initiation and propagation of fractures. Several specific conclusions can be drawn from this work that have value both in core disking research as well as practical application in the field of in situ stress estimation.

(1) The axial stress has a negative effect on the core disking occurrence, whereas the radial stress has a positive effect.
(2) Numerical modeling results in this paper show that the initiation stress of the disking phenomenon is about 6–7 times of the tensile strength. The result agrees well with the statistical results of rock core disking initiation in URL by Lim and Martin (2010).

(3) When the drilling axis is aligned with one of the principal stress directions, the core disking is a tensile failure rather than a shear failure process, as indicated by the fact that shear fractures did not appear during the drilling process simulation.
(4) Core disk thickness decreases as the radial stress increases, which agrees with previous studies.
(5) The initiation locations of the core disking fractures are dependent on the specific stress state. The numerical simulation showed that fractures begin from the center of core rather than the drilling kerf when the drilling is under a thrust fault stress regime.

The results in this paper are simple but provide valuable insights into some of the important aspects of core disking that remain unresolved. This paper also provides guidance on the optimal method for simulating the core disking phenomena using numerical modeling software. In the future, many additional core disking simulations will be made to provide a more accurate quantitative relationship between the stress state and the occurrence of core disking. Investigation will also be made as to whether shear fracturing can occur as part of the core disking process under certain circumstances (principal stresses not aligned with the core axis, for example).

Acknowledgements The support received from Key Program of Natural Science Foundation of China (51774020) and Beijing Training Project for the Leading Talent in S & T (Z151100000315014) is gratefully acknowledged.

References

Bahrani N, Valley B, Kaiser PK (2015) Numerical simulation of drilling-induced core damage and its influence on mechanical properties of rocks under unconfined condition. Int J Rock Mech Min Sci 80:40–50. https://doi.org/10.1016/j.ijrmms.2015.09.002

Bankwitz PBE (1997) Fractographic features on joints in KTB drill cores as indicators of the contemporary stress orientation. Geol Rundsch 86:34–44

Chenghu W (2014) Brief review and outlook of main estimate and measurement methods for in situ stresses in rock mass. Geol Rev 60(5):971–995

Corthésy R, Leite MH (2008) A strain-softening numerical model of core discing and damage. Int J Rock Mech Min Sci 45:329–350. https://doi.org/10.1016/j.ijrmms.2007.05.005

Crawford BR, Smart BGD, Main IG, Liakopoulou-Morris F (1995) Strength characteristics and shear acoustic anisotropy of rock core subjected to true triaxial compression. Int J Rock Mech Min Sci 32:189–200. https://doi.org/10.1016/0148-9062(94)00051-4

Cundall PA, Strack ODL (1979) A discrete numerical model for granular assemblies. Géotechnique 29:47–65. http://dx.doi.org/10.1680/geot.1979.29.1.47

Dyke CG (1989) Core discing: its potential as an indicator of principal in situ stress directions. Rock Gt. Depth 2:1057–1064

Flottmann T, Campagna DJ, Hillis R, Warner D (2004) Horizontal microfractures and core discing in sandstone reservoirs, Coopers Basin, Australia. PESA's East Aust Basins Symp 2:689–694

Hast N (1958) The measurement of rock pressure in mines. Norstedt, Stockholm

Hast N (1979) Limits of stress measurements in the earth's crust. Rock Mech 150:143–150

Holt RM, Brignoli M, Kenter CJ (2000) Core quality: quantification of coring-induced rock alteration. Int J Rock Mech Min Sci 37:889–907. https://doi.org/10.1016/S1365-1609(00)00009-5

Holt RM, Pestman BJ, Kenter CJ (2001) Use of a discrete particle model to assess feasibility of core based stress determination. In: Rock mechanics in the national interest, pp 1361–1366

Hongwei Z, Hai R, Jun H et al (2014) Study on rock core discing mechanism based on stress and energy principle. Chin J Appl Mech 31(4):512–517

Hou F, Jia Y (1984) Stress analysis on disced rock cores. Chin J Geotech Eng 6(5):48–58

Huang H, Fan P, Li J et al (2016) A theoretical explanation for rock core disking in triaxial unloading test by considering local tensile stress. Acta Geophys 64:1430–1445. https://doi.org/10.1515/acgeo-2016-0068

Ishida T, Saito T (1989) A study on core discing with a center hole. Shigen-to-Sozai 105:603–608. https://doi.org/10.2473/shigentosozai.105.603

Ishida T, Saito T (1995) Observation of core discing and in situ stress measurements; Stress criteria causing core discing. Rock Mech Rock Eng 28:167–182. https://doi.org/10.1007/BF01020150

Itasca Consulting Group I (2015) PFC—particle flow code in 2 and 3 dimensions, Version 5.0

Jaeger JC, Coox NGW (1963) Pinching-off and disking of rocks. J Geophys Res 68(6):1759–1765

Katsuhiko S et al (1978) A study on core discing of rock. J Min Met Inst Jpn 94:797–803

Kaga N, Matsuki K, Sakaguchi K (2003) The in situ stress states associated with core discing estimated by analysis of principal tensile stress. Int J Rock Mech Min Sci 40:653–665. https://doi.org/10.1016/S1365-1609(03)00057-1

Kulander BR, Dean SL, Ward BJ (1990) Fractured core analysis-induced fractures in core. American Association of Petroleum Geologists

Li Y (1997) Drilling induced core damage and their relationship to crustal in situ stress states and rock properties. University of Alberta, Edmonton

Li Y, Schmitt DR (1997a) Effects of poisson's ratio and core stub length on bottomhole stress concentrations. Int J Rock Mech Min Sci 34:761–773. https://doi.org/10.1016/S1365-1609(97)00001-6

Li Y, Schmitt DR (1997b) Well-bore bottom stress concentration and induced core fractures. Am Assoc Pet Geol Bull 81(1997):1909–1925. https://doi.org/10.1306/3B05C668-172A-11D7-8645000102C1865D

Li Y, Schmitt DR (1998) Drilling-induced core fractures and in situ stress. J Geophys Res 103:5225–5239

Lim SS (2013) In-situ stress magnitude and core disking. University of Albert, Edmonton

Lim SS, Martin CD (2010) Core disking and its relationship with stress magnitude for Lac du Bonnet granite. Int J Rock Mech Min Sci 47:254–264. https://doi.org/10.1016/j.ijrmms.2009.11.007

Matsuki K, Hongo K, Sakaguchi K (1997a) A tensile principal stress analysis for estimating three-dimensional in situ stressed from core discing. In: Rock stress, Rotterdam, Balkema, pp 343–348

Matsuki K, Hongo K, Sakaguchi K (1997b) A tensile principal stress analysis for estimating three-dimensional in situ stresses from core discing. In: Rock Stress, Rotterdam, Balkema, pp 343–348

Matsuki K, Kaga N, Yokoyama T, Tsuda N (2003) Determination of three-dimensional directions of in situ stress from core discing.

In: Rock stress: proceedings of the third internaional symposium on rock stress, pp 237–243

Matsuki K, Kaga N, Yokoyama T, Tsuda N (2004) Determination of three dimensional in situ stress from core discing based on analysis of principal tensile stress. Int J Rock Mech Min Sci 41:1167–1190. https://doi.org/10.1016/j.ijrmms.2004.05.002

McGarr A, Gay NC (1978) State of stress in the earth's crust. Annu Rev Earth Planet Sci 6:405–436. https://doi.org/10.1146/annurev.ea.06.050178.002201

Obara Y, Kang SS, Seguchi T, Sato A (1998) a criterion of hollow core disking initiation. Shigen to Sozai 114:875–880

Obert L, Stephenson DE (1965) Stress conditions under which core discing occurs. Soc Min Eng AIME Trans 232:227–235

Shang Y, Sun Q (1991) Rock core disking mechanism analysis of TianHuangCheng power station

Stacey TR (1982) Contribution to the mechanism of core discing. J S Afr Inst Min Metall 82:269–276

Takehiro O (2001) Core disking and Rockburst in soft tuffaceous rock masses at Iwate tunnel tuffaceous. QR RTRI 42:130–135

Tianhui M, Long W, Tao X, Qun YU (2016) Mechanism and stress analysis of rock core discing. J Northeastern Univ 37(10):1491–1495

Vallejos JA, Salinas JM, Delonca A, Mas Ivars D (2016) Calibration and verification of two bonded-particle models for simulation of intact rock behavior. Int J Geomech 17:6016030. https://doi.org/10.1061/(ASCE)GM.1943-5622.0000773

Zhu W, Li G, Wang K (1985) Analyses of disking phenomenon and stress field in the region of an underground powerhouse. Rock Mech Rock Eng 18:1–15. https://doi.org/10.1007/BF01020412

Acta Geophysica (2018) 66:283–291
https://doi.org/10.1007/s11600-018-0142-1

RESEARCH ARTICLE - SOLID EARTH SCIENCES

Identifying the role of initial wave parameters on tsunami focusing

Baran Aydın[1]

Received: 1 March 2018 / Accepted: 7 April 2018 / Published online: 16 April 2018

Abstract
Unexpected local tsunami amplification, which is referred to as *tsunami focusing*, is attributed to two different mechanisms: bathymetric features of the ocean bottom such as underwater ridges and dipolar shape of the initial wave itself. In this study, we characterize the latter; that is, we explore how amplitude and location of the focusing point vary with certain geometric parameters of the initial wave such as its steepness and crest length. Our results reveal two important features of tsunami focusing: for mild waves maximum wave amplitude increases significantly with transverse length of wave crest, while location of the focusing point is almost invariant. For steep waves, on the other hand, increasing crest length dislocates focusing point significantly, while it causes a rather small increase in wave maximum.

Keywords Tsunami · Focusing · Dipolar waves · Steepness · Finite crest length

Introduction

Tsunami is a series of water waves generated after sudden displacement of ocean floor. Tsunami wave can propagate as far as thousands of kilometers and can run-up as high as tens of meters. Geophysicists and coastal engineers usually want to know details of tsunami wave field for different purposes. Scientists want to understand the dynamics of the generation and propagation mechanisms to develop or advance theories, while engineers and emergency managers want to assess impact of subsequent waves along coastlines to prevent loss of lives and property. There are several wave theories, either linear or nonlinear, dispersive or nondispersive, developed to predict height and velocity of subsequent waves, offshore and onshore. Nevertheless, some past events have proved that certain locations in the wave field may experience unpredictably large waves which could not be explained mathematically using the classical wave theories (Kânoğlu et al. 2013). This abnormality in free surface elevation is referred to as *tsunami focusing*.

Studies so far have shown that the geometrical focusing of long waves can be attributed to two mechanisms. The first is bathymetric features of the sea bed. Satake (1988) applied the idea of ray tracing for seismic surface waves to tsunamis and examined bathymetric effects along their propagation path, showing that focusing due to bathymetry can be significant for tsunamis. Pelinovsky (2006) also reviewed the mathematical theory of wave ray tracing and presented ray patterns calculated over real bathymetries for a number of historical tsunamis. In their numerical simulations for the great 26 December 2004 Indian Ocean Tsunami, Titov et al. (2005) showed that the focusing effect of the large extension of the earthquake source region was the primary factor determining directionality of the tsunami in the near field. As Berry (2007) explained using the diffraction theory, shallower regions at the ocean bottom such as underwater islands or ridges can act as lenses and focus the energy of tsunamis, having the potential of multiplying the energy tenfold over a transverse range of tens of kilometers, and making tsunamis more destructive, especially where focal regions include sections of coasts. Degueldre et al. (2015) further combined the stochastic caustic theory and the shallow-water wave dynamics and showed that small fluctuations in the measurements of ocean's bathymetry can lead to unexpectedly large fluctuations in predicted tsunami heights, with maxima several times greater than the average wave height. They, therefore, concluded that a precise knowledge of bathymetry of ocean is indispensable for successful tsunami forecasts.

✉ Baran Aydın
baydin@adanabtu.edu.tr

[1] Adana Science and Technology University, Adana, Turkey

A second mechanism that leads to tsunami focusing is a special configuration of the initial wave profile itself. Dotsenko et al. (1986) used the two-dimensional linear wave theory to demonstrate, probably for the first time, that wave energy amplification depends on whether or not the initial perturbation is dipolar, i.e. it consists of depression and elevation parts with different amplitude signs. Marchuk and Titov (1989) noticed existence of a point at which abnormal wave height is registered, hence called *focusing point*, during their numerical experiments for dipolar initial waveforms having a *finite* crest length in the transverse direction. Radiation of seismic waves from finite sources was studied in detail by Ben-Menahem (1961), who described the dominant role of finiteness of the source in the wave pattern, especially when the wavelength and the fault dimensions or the wave period and the time of rupture are of the same order. Ben-Menahem (1961) also found that azimuthal distribution of amplitudes depends strongly on the dimensions of the source, which led to the idea of a *directivity function* defined as the ratio of spectral amplitudes of waves leaving the source in opposite directions. Ben-Menahem and Rosenman (1972) further studied the relationship between seismic and tsunamigenic source parameters and expressed the far-field deep-water wave amplitudes as a function of the azimuth angle and the finite dimensions of the source, as well as other source parameters such as the dip and slip angles, the fault dislocation, and the epicentral distance. Azimuthal directivity in the far-field is later used by Okal (2003) to discriminate between earthquake- and landslide-generated tsunamis.

If the effect of source finiteness of the parent earthquake over the subsequent sea surface pattern is desired to be analyzed, then the associated hydrodynamic model must employ two spatial dimensions. Such studies are very few in the literature if (semi-)anaytical solutions are considered. Carrier and Yeh (2005) used the linear shallow-water wave framework to determine directivity of tsunami propagation from strip sources. Their mathematical formulation, however, had a number of limitations. Their assumption of initial wave distribution was quite restrictive since it was based on an axisymmetric wave and hence their solution could not be calculated for large values of spatial and temporal variables. They switched to Green's function representation to avoid this adversity, but they then ended up with an elliptic integral, which was difficult to evaluate because of singularity. They eventually replaced their solution with a fitted curve after trial-and-error inspection.

A simple two-dimensional analytical model for finite-crested sources is recently proposed by Aydın (2011). Like Carrier and Yeh (2005), Aydın (2011) also used the linear shallow-water wave equation; however, unlike Carrier and Yeh (2005), his analytical model allowed treatment of a wide class of tsunami initial conditions and analytical justification of the earlier clues on existence of focusing points presented in the numerical study of Marchuk and Titov (1989) for dipolar initial waves of finite extent, which are more appropriate initial conditions for tsunami propagation problems, when compared with waves having infinite transverse length or waves with an elevation only. Focusing from a dipolar-shaped finite crest length wave has recently been proposed as a possible explanation for controversial extreme run-ups observed during, for example, the 17 July 1998 Papua New Guinea, the 17 July 2006 Java Island (Indonesia), and the 11 March 2011 Tohoku (Japan) tsunamis (Kânoğlu et al. 2013).

In this study, we characterize focusing resulting from the initial wave configuration using the linear shallow-water wave theory. Variation of focusing point, in both amplitude and location, with geometric parameters dictating the size of the initial wave, namely its steepness and crest length, are explored by calculating and comparing maximum wave envelopes for different values of relevant parameters. For the sake of clarity, we remark that our goal here is not to assess tsunami impact at the coast, but rather to show the sole influence of certain initial wave parameters on tsunami focusing; therefore, we will use a simple wave model which neglects nonlinear and dispersive terms and effects due to the change in bathymetry.

The paper is organized as follows: we first review the analytical theory of two-dimensional wave propagation over a flat bottom and note the difference with one-dimensional theory. We then introduce initial wave types leading tsunami focusing, namely finite-crested dipolar initial waves. The results showing how steepness and transverse extent of wave crest affect amplitude and location of focusing points are given next and the paper is closed with concluding remarks.

Review of the analytical model

Propagation of tsunamis can satisfactorily be modeled using the shallow-water wave (SW) equations, which are derived from the Euler equations by neglecting vertical acceleration (Pelinovsky 2006; Stoker 1957). In two space dimensions, the SW equations consist of three first-order nonlinear partial differential equations, which, after linearization, can be combined into a single second-order partial differential equation and hence called the *linear SW equation*. If the sea bed is further assumed to be flat, the resulting equation is the classical two-dimensional wave equation:

$$\frac{\partial^2 \tilde{\eta}}{\partial \tilde{t}^2} - g\,\tilde{h}\left(\frac{\partial^2 \tilde{\eta}}{\partial \tilde{x}^2} + \frac{\partial^2 \tilde{\eta}}{\partial \tilde{y}^2}\right) = 0. \tag{1}$$

In Eq. (1), $\tilde{\eta}(\tilde{x},\tilde{y},\tilde{t})$ represents the free surface height, while $\tilde{h}$ is the undisturbed water depth and g is the gravitational acceleration. $(\tilde{x},\tilde{y})$ are the space variables and $\tilde{t}$ is time. Dimensionless quantities can be defined through

$$(x,y)=\frac{(\tilde{x},\tilde{y})}{l_0}=\frac{(\tilde{x},\tilde{y})}{\tilde{h}},\quad \eta=\frac{\tilde{\eta}}{h_0}=\frac{\tilde{\eta}}{\tilde{h}},$$
$$t=\frac{\tilde{t}}{t_0}=\tilde{t}\sqrt{\frac{g}{\tilde{h}}},$$

in which l_0, h_0, and $t_0=l_0/\sqrt{gh_0}$ are characteristic length, depth, and time scales, respectively, with $l_0=h_0=\tilde{h}$, the undisturbed water depth. The dimensionless form of Eq. (1) is then

$$\frac{\partial^2\eta}{\partial t^2}-\left(\frac{\partial^2\eta}{\partial x^2}+\frac{\partial^2\eta}{\partial y^2}\right)=0. \tag{2}$$

The initial conditions for Eq. (2) can be considered to be a pre-defined initial wave with zero initial velocity:

$$\eta(x,y,t)\big|_{t=0}=\eta_0(x,y), \tag{3a}$$

$$\frac{\partial}{\partial t}\eta(x,y,t)\big|_{t=0}=0. \tag{3b}$$

Two-dimensional spread of a given wave profile $\eta_0(x,y)$ over constant-depth ocean basin can be obtained by solving Eq. (2) subject to Eq. (3). Analytical solution of this initial value problem is a classical exercise of water wave mechanics. It is a linear problem which can be solved easily via standard techniques developed for partial differential equations. The technique which will serve our purpose of demonstrating tsunami focusing is the double Fourier transform over space variables, recently utilized by Aydın (2011):

$$\hat{\eta}(\rho,\sigma,t)=\iint_{\mathbb{R}^2}\eta(x,y,t)\,\mathrm{e}^{-\mathrm{i}(\rho x+\sigma y)}\,\mathrm{d}x\,\mathrm{d}y, \tag{4}$$

where $\mathbb{R}^2\equiv(-\infty,\infty)\times(-\infty,\infty)$ and $\mathrm{i}=\sqrt{-1}$ (the imaginary unit). Equation (4) transforms Eq. (2) into the ordinary differential equation

$$\frac{\mathrm{d}^2\hat{\eta}}{\mathrm{d}t^2}+(\rho^2+\sigma^2)\hat{\eta}=0. \tag{5}$$

Here, ρ ve σ are the wavenumbers in x- and y-directions, respectively. The Fourier transforms of the initial conditions (3) are also apparent:

$$\hat{\eta}(\rho,\sigma,t)\big|_{t=0}=\hat{\eta}_0(\rho,\sigma), \tag{6a}$$

$$\frac{\mathrm{d}}{\mathrm{d}t}\hat{\eta}(\rho,\sigma,t)\big|_{t=0}=0. \tag{6b}$$

The solution in the transform space then reads

$$\hat{\eta}(\rho,\sigma,t)=\hat{\eta}_0(\rho,\sigma)\cos\omega t, \tag{7}$$

where $\omega=\sqrt{\rho^2+\sigma^2}$. Finally the analytical solution in the physical space is obtained by inverting the Fourier transform solution (7) as

$$\eta(x,y,t)=\frac{1}{(2\pi)^2}\iint_{\mathbb{R}^2}\hat{\eta}_0(\rho,\sigma)\,\mathrm{e}^{\mathrm{i}(\rho x+\sigma y)}\cos\omega t\,\mathrm{d}\rho\,\mathrm{d}\sigma. \tag{8}$$

Below we show that the linear nondispersive wave model (2)–(3) leads to tsunami focusing when initial waves with finite crest are imposed.

Finite versus infinite crest length

It is well-known from the one-dimensional classical water wave theory assuming infinite crest length in the transverse direction that a dipolar wave of amplitude H splits into two waves having identical amplitudes of H / 2, propagating in opposite directions, called *leading-depression* and *leading-elevation* sides, in the absence of initial velocity (see Fig. 1).

In the framework of the two-dimensional theory, that is, accounting for finite crest length, propagation might become more complex, depending on the cross-section of the initial wave in the main propagation direction. More explicitly, dipolar waves such as the one in Fig. 2a produce abnormal water elevations, i.e. focusing, in some local region on the leading-depression side of the propagation (Fig. 2d). It is extremely important to understand the underlying mechanism of this phenomenon, since additional amplification of wave height can severely increase the potential damage of tsunamis, especially when focusing zone overlaps piece of land. Kânoğlu et al. (2013) speculated that, for example, the unexpected damage at the

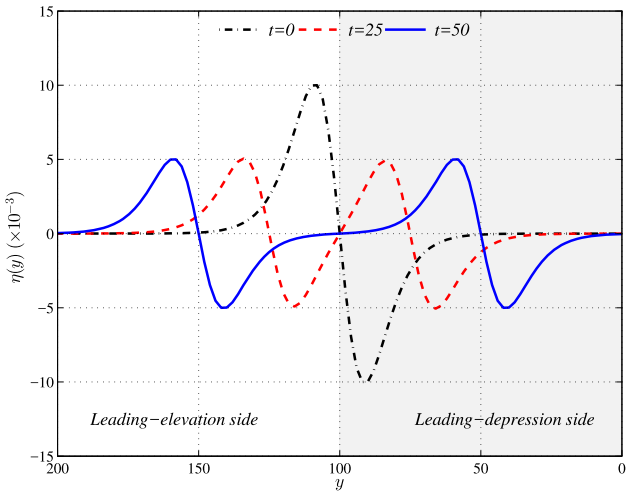

Fig. 1 Propagation of a typical N-wave in one space dimension

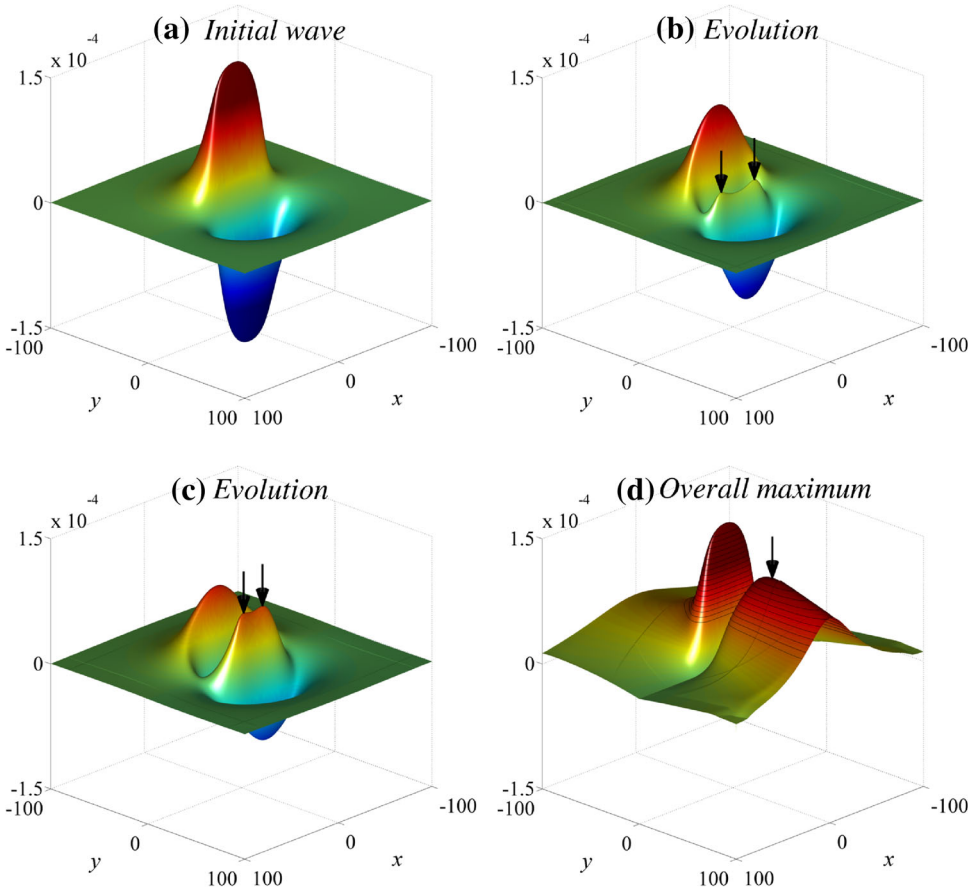

Fig. 2 Propagation and focusing of a finite-crested *N*-wave in two space dimensions: **a** Initial wave, **b, c** its evolution, and **d** its focusing in the long time (Kânoğlu et al. 2013)

Sissano Lagoon during the 17 July 1998 Papua New Guinea tsunami might be due to focusing.

Initial waveforms leading tsunami focusing

We start with an initial wave having a functional form first suggested by Carrier and Yeh (2005) for axisymmetric waves and later generalized by Aydın (2011) for any two-dimensional initial wave:

$$\eta_0(x,y) = f(x)\, g(y). \tag{9}$$

Here, the direction of decreasing y is chosen as the main propagation direction or *onshore* direction (Fig. 3), and the direction of decreasing x is the lateral or *longshore* direction (Fig. 4). So, in Eq. (9), $g(y)$ is the cross-section of the initial wave profile along the onshore direction, and $f(x)$ is the cross-section of the initial wave profile along the longshore direction.

The advantage of using the functional form (9) is two-fold: from a mathematical point of view, this functional form perfectly suits the solution technique reviewed above, as the Fourier transforms of $g(y)$ and $f(x)$ can be evaluated separately. More importantly, from a geophysical point of view, Eq. (9) allows analysis of a wide class of tsunami

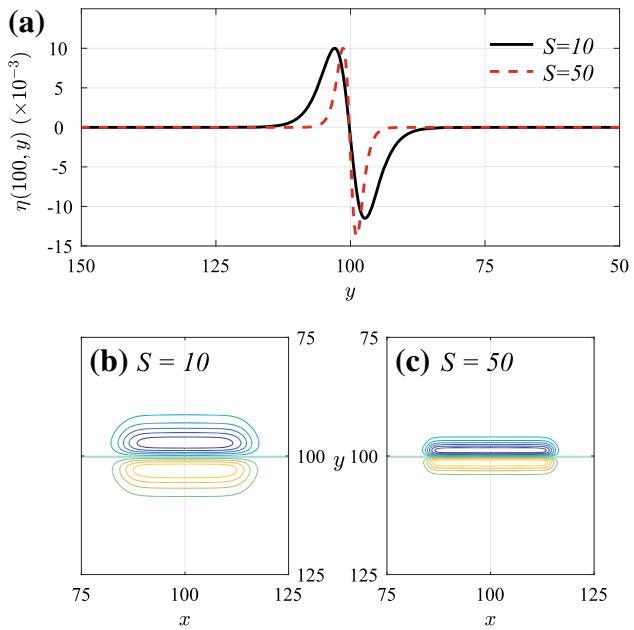

Fig. 3 **a** The function $g(y)$ given in Eq. (10) for two different values of the steepness parameter S. Note that $g(y)$ is the cross-section of the N-wave defined in Eq. (14) along the onshore (y-) direction. The crest length is taken as $L = 30$, while the other wave parameters are listed in Table 1. Contour views are also provided in **b** and **c** for $S = 10$ and $S = 50$, respectively

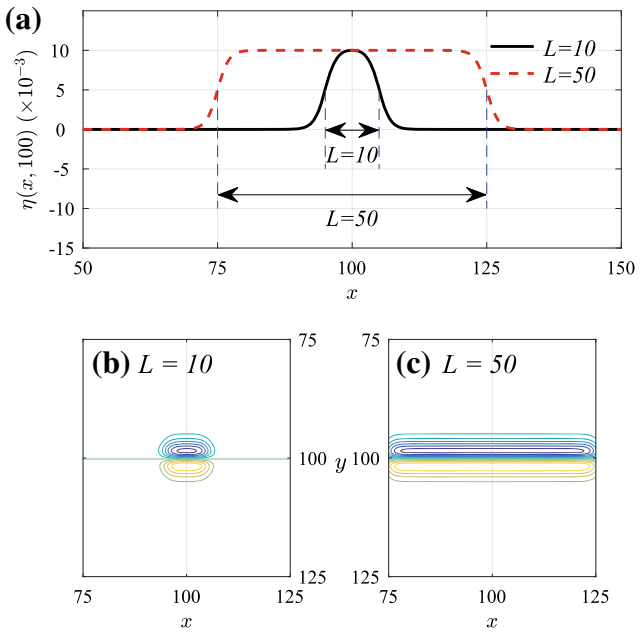

Fig. 4 **a** The function $f(x)$ given in Eq. (12) for two different values of the crest length L. Note that $f(x)$ is the cross-section of the N-wave defined in Eq. (14) along the longshore (x-) direction. The steepness parameter is taken as $S = 30$, while the other wave parameters are listed in Table 1. Contour views are also provided in **b** and **c** for $L = 10$ and $L = 50$, respectively

initial conditions, obtained by changing wave cross-sections in y- and x-directions. Besides these advantages, we should also mention the disadvantage of using Eq. (9) as initial condition that we ignore the possible physical effects of nonseparable initial disturbances.

The functions $g(y)$ and $f(x)$ are chosen appropriately so that a depression–elevation initial wave having finite crest length is imposed. Along the onshore direction we prefer using the so-called generalized N-wave profile defined as

$$g(y) = \varepsilon H\,(y - y_2)\,\mathrm{sech}^2\gamma(y - y_1). \tag{10}$$

This dipolar wave is introduced by Tadepalli and Synolakis (1994) as a more realistic initial condition for tsunamis compared to the solitary wave. In Eq. (10), y_1 and y_2 are points on the y-axis which control depression and elevation parts of the wave, H is the initial wave amplitude and γ is defined as $\gamma = \sqrt{3HS}/2$, employing a parameter S, called the *steepness parameter*, to change the extent of the initial wave's cross-section (and, therefore, its wavelength and consequently period) in the onshore direction. The significance of the steepness parameter S is that the cross-section of the initial wave in y-direction can be changed from *mild* to *steep* by increasing S (Fig. 3). In the definition of the N-wave above an additional parameter ε, called the *scaling parameter*, is necessarily introduced because, even though H is referred to as initial wave amplitude, the actual height of $g(y)$ is not exactly H without scaling it by ε. The Fourier transform of Eq. (10) is readily available (Tadepalli and Synolakis 1994):

$$\begin{aligned}\hat{g}(\sigma) = {} & \varepsilon\frac{4H\alpha^2}{\pi}\,\mathrm{e}^{-\mathrm{i}\sigma y_1} \\ & \times\left[(y_1 - y_2)\,\sigma + \mathrm{i}(1 - \alpha\,\coth\alpha\sigma)\right]\mathrm{csch}\,\alpha\sigma,\end{aligned} \tag{11}$$

where $\alpha = \pi/(2\gamma)$.

For the finite-crested cross-section in the longshore direction, on the other hand, we use the profile (Aydın 2011)

$$f(x) = \frac{1}{2}\left[\tanh\gamma(x - x_0) - \tanh\gamma(x - x_0 - L)\right]. \tag{12}$$

Starting at point $x = x_0$, this function generates a hump of unit amplitude with crest length L (finite) in the longshore (transverse) direction (Fig. 4). The Fourier transform of Eq. (12) is provided by Aydın (2011) as

$$\hat{f}(\rho) = \mathrm{i}\,\alpha(\mathrm{e}^{-\mathrm{i}\rho L} - 1)\,\mathrm{e}^{-\mathrm{i}\rho x_0}\mathrm{csch}\,\alpha\rho. \tag{13}$$

Now that the cross-sections of the initial wave in both directions are defined, we can construct the two-dimensional initial wave by multiplying $g(y)$ and $f(x)$, as in Eq. (9), and the associated Fourier transform by multiplying $\hat{g}(\sigma)$ and $\hat{f}(\rho)$. Hence, the finite-crested N-wave initial condition in the physical space is

$$\begin{aligned}\eta_0(x,y) = {} & \frac{\varepsilon H}{2}\,(y - y_2)\,\mathrm{sech}^2\gamma(y - y_1) \\ & \times\left[\tanh\gamma(x - x_0) - \tanh\gamma(x - x_0 - L)\right],\end{aligned} \tag{14}$$

and its integral transform is

$$\begin{aligned}\hat{\eta}_0(\rho,\sigma) = {} & \mathrm{i}\frac{4\varepsilon H}{\pi}\,\alpha^3\,(\mathrm{e}^{-\mathrm{i}\rho L} - 1)\,\mathrm{e}^{-\mathrm{i}(\rho x_0 + \sigma y_1)}\left[(y_1 - y_2)\,\sigma\right. \\ & \left. + \mathrm{i}\,(1 - \alpha\sigma\,\coth\alpha\sigma)\right]\mathrm{csch}\,\alpha\rho\;\mathrm{csch}\,\alpha\sigma.\end{aligned} \tag{15}$$

We will show in the next section that as the initial wave defined in Eq. (14) propagates, localized abnormal wave heights are registered, a phenomenon referred to as *tsunami focusing*.

Results

Two characteristic properties of the initial profile we consider here are the wave steepness S in y-direction and the crest length L in x-direction, as shown in Figs. 3 and 4, respectively. We, therefore, investigated the influence of S and L on focusing point through parameterization, keeping the other initial wave properties fixed. The computational domain is described in Table 1. Referring to Kânoğlu et al. (2013), the parameters other than S and

Table 1 Dimensionless initial wave parameters used in Eq. (14). The scaling parameter (ε) is not listed below since it changes with L and the grid resolution

Parameter	Value
Computational domain	$(x, y) \in [0, 200] \times [0, 200]$
Grid resolution	$\Delta x = \Delta y = 0.25$
Initial wave amplitude	$H = 0.01$
Depression parameter	$y_1 = \frac{1}{2} y_{\max} = 100$
Elevation parameter	$y_2 = 100.2$
Steepness parameter	$S \in [1, 50]$
Crest length	$L \in [2, 50]$
Point where wave crest starts	$x_0 = \frac{1}{2}(x_{\max} - L) = \frac{1}{2}(200 - L)$

L are selected to mimic the initial wave of the 1998 Papua New Guinea tsunami, to demonstrate the sole effect of the initial wave parameters on focusing, isolated from the effect due to the variation of bathymetry.

The wave field is calculated as follows: the wave parameters in Table 1 are first substituted in Eq. (15), which is then plugged in Eq. (8). After integrating Eq. (8) numerically using Gauss–Kronrod quadrature, we obtain free surface elevation at any desired spatial point (x, y) and at any time t.

We record and plot variation of amplitude and location of the *focusing point*, i.e. point with maximum wave height on the leading-depression side of the propagation (Fig. 2d), with respect to the steepness parameter (S) and the crest length (L) of the initial source. For particular values of these variables maximum wave envelopes are plotted along the bisector (i.e. along the line $x = 100$, according to Table 1) since focusing point is the point on the bisector where two positive waves from the leading-depression side of the propagation arrive simultaneously (Kânoğlu et al. 2013). Maximum envelope is obtained by registering the largest wave height at each spatial location until the initial wave leaves the computational domain. The entire time to generate a maximum envelope, therefore, depends on the size of the computational domain. Given that the wave model we use is linear, and referring to the point at which the initial wave is located in the computational domain ($y_1 = y_{\max}/2$, Table 1), the time needed to generate the maximum envelopes, in other words, the time needed for the initial waves in Figs. 5 and 6 to leave the computational domain, is at the order of $y_{\max}/2$.

Fixing the steepness parameter, in each panel of Fig. 5 we plot maximum wave envelopes for $2 \le L \le 10$ ($0.01 \le L/x_{\max} \le 0.05$, in terms of aspect ratio), corresponding to relatively small crest length of the initial source. In Fig. 6 we plot the same quantity for relatively large values, $10 \le L \le 50$ ($0.05 \le L/x_{\max} \le 0.25$). The results provide important information about the character of focusing. The left panels of Fig. 5 suggest that when the initial wave is mild (i.e. S is small, e.g. $S < 10$) there is a very small fluctuation in either amplitude or location of the focusing point. For instance, the increase in focusing amplitude from $L = 2$ to $L = 10$ is only 3% for $S = 1$ (compare with 25% for $S = 50$, see the relevant columns of Table 2). Similarly, location of focusing point slightly moves from $y = 113.25$ (for $L = 2$) to $y = 113.00$ (for $L = 10$) when $S = 1$. Consequently, amplitude and location of the focusing point are *almost* invariant when $S < 10$ and $L < 10$, as clearly seen from the left panels of Fig. 5.

When $S > 10$, on the other hand, changing crest length affects both amplitude and location of focusing point. A deeper analysis of the results shows that, while $L < 10$ reflects as a significant increase in the amplitude of focusing point, with a small variation in its location, $L \ge 10$ translates the location of focusing point significantly, with a small amount of increase in its amplitude (Compare the right columns of Figs. 5 and 6). The increase in focusing amplitude for $S = 10$ is nearly 20% when L goes from 10 to 50, while for $S = 30$ the same increase is about 10%. This result is also consistent with the above explanation that focusing develops because of the unusual wave heights at both edges of the dipolar initial wave as it propagates (arrows in Fig. 2b, c): *the longer crest length is, the farther focusing point is*. Focusing points are not indicated for the cases $S = 40$ and $S = 50$ when $L = 50$ (Fig. 6) because they do not fall into the computational domain due to large values of the parameters.

We further plot in Fig. 7 variation of the focusing amplitude (η_F) and that of the focusing location (y_F) over the ranges $S \in [1, 50]$ and $L \in [2, 50]$, respectively. We observe a monotonic increase in η_F when one of the parameters is fixed and the other is allowed to increase. A rapid increase of focusing amplitude is observed in Fig. 7b initially, when $L < 10$, especially for large values of S; the increase slows down, however, for $L \ge 10$. The location of focusing point (y_F), on the other hand, is almost fixed when $L < 10$, but decreases very quickly with S as L gets larger (Fig. 7c). Recalling that y-axis decreases as we move from left to right, decrease in y_F corresponds to a translation to the right. The situation is similar when S is fixed and L is varied. We see that y_F decreases (moves further away) very slowly for milder initial waves while it decreases very rapidly for steeper waves (Fig. 7d). Again, for $L < 10$ the location of focusing point is almost fixed, especially when $S < 10$. For $L \ge 10$, the focusing point shifts to the right very fast, particularly for large S.

Accurate calculation of the wave field is not possible, however, when the initial wave is very steep and long, as the computational domain remains too narrow for focusing to develop. Regarding our parameter set (Table 1),

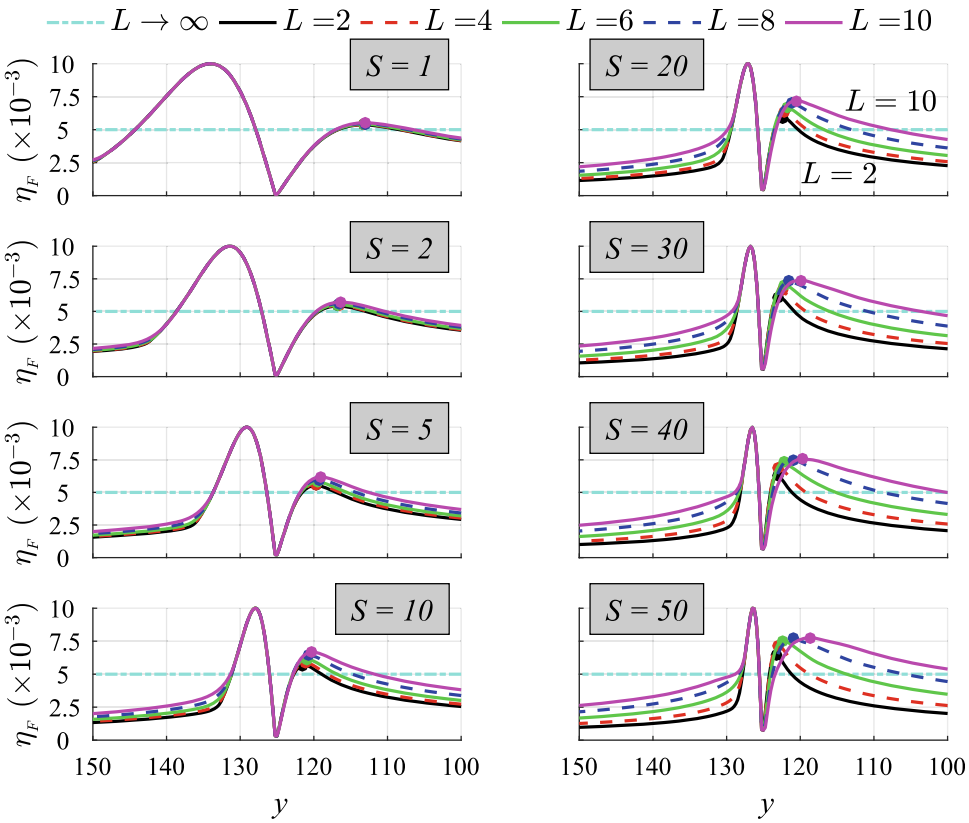

Fig. 5 Maximum wave envelopes and the variation of focusing point (shown as filled dot) with small source length (L) when steepness is fixed. The dash-dotted horizontal line shows the limiting one-dimensional case $L \to \infty$, for which the constant propagation height is H / 2

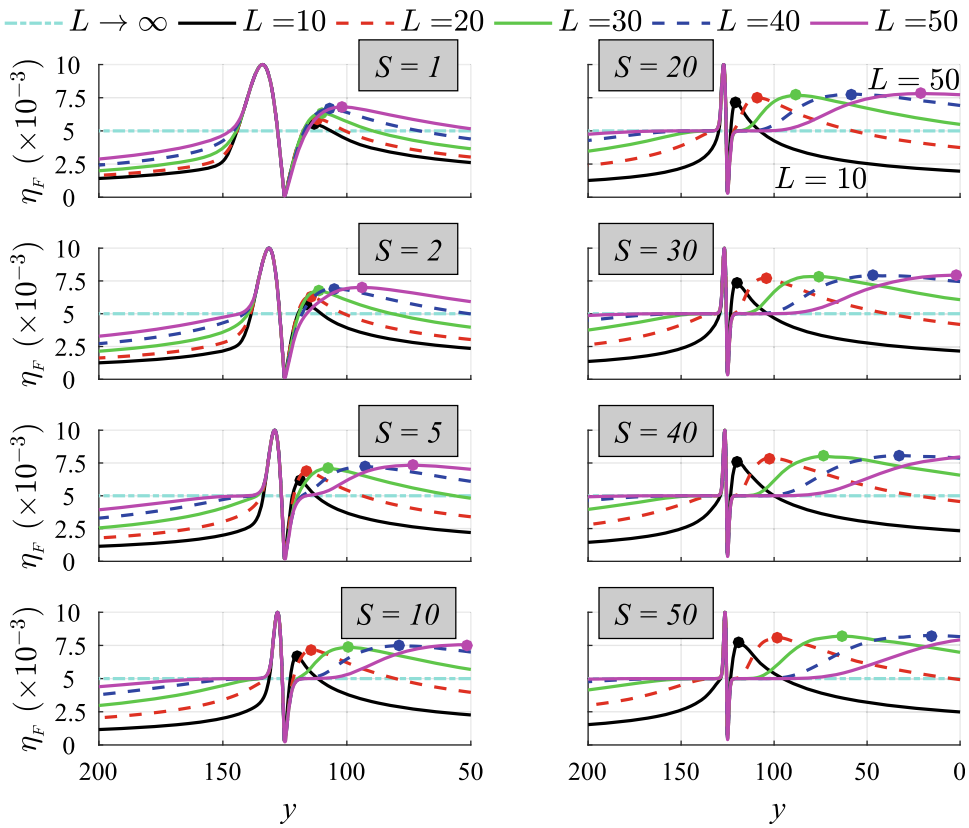

Fig. 6 As Fig. 5, but the source length (L) varies over a wider range. Note that in the right panels the initial wave is placed 50 units to the left, compared with the left panels, to include the focusing points in the computational domain. Still, the focusing points corresponding to the pairs ($S = 40$, $L = 50$) and ($S = 50$, $L = 50$) fall outside

Table 2 The amplification factor A_F (%) calculated from Eq. (16) for different values of S and L for the wave defined in Eq. (14) along the bisector, i.e. $x = 100$

Crest length	Steepness parameter							
	$S = 1$	$S = 5$	$S = 10$	$S = 20$	$S = 35$	$S = 40$	$S = 45$	$S = 50$
$L = 2$	7.16	10.59	13.48	18.43	24.54	26.04	28.20	*30.08*
$L = 6$	8.25	15.77	22.77	33.53	44.22	46.32	48.39	*50.98*
$L = 10$	10.29	23.48	33.45	43.71	50.59	50.86	52.78	*55.42*
$L = 20$	18.24	37.72	43.17	49.98	56.91	57.42	59.05	*61.80*
$L = 30$	26.76	41.59	47.04	53.66	59.68	**60.06**	**61.30**	***63.99***
$L = 50$	**36.10**	**46.47**	**51.12**	**56.38**	***59.85***	59.24	58.73	58.43

Bold numbers show the largest values for fixed S (columns) while italic numbers are the largest values for fixed L (rows). Wave parameters except for S and L are tabulated in Table 1. Note that η_{1D} in Eq. (16) is $\eta_{1D} = H/2 = 0.005$ for $H = 0.01$

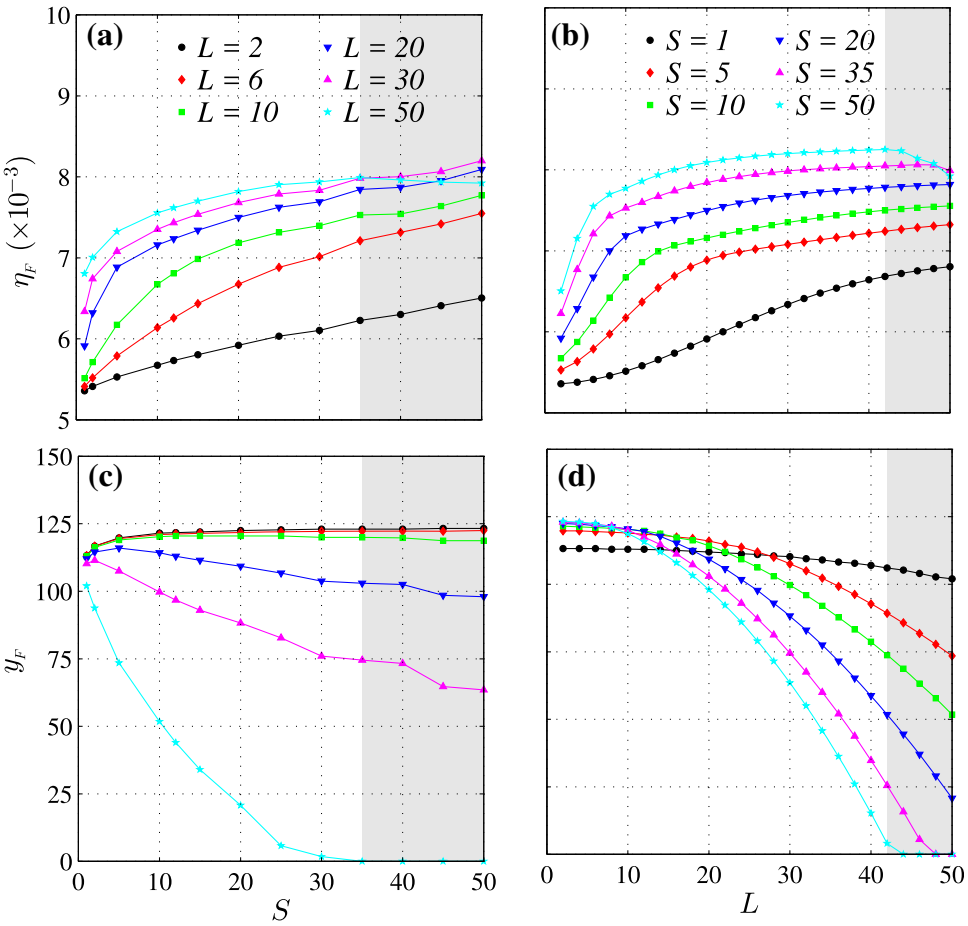

Fig. 7 Variation of **a**, **b** the focusing amplitude η_F, and **c**, **d** the focusing location y_F with the steepness parameter (left) and the crest length (right), respectively. The shaded areas to the right of the figures indicate the ranges for S or L for which focusing does not fully develop

focusing does not occur within our computational domain when the N-wave initial condition given in Eq. (14) possesses a steepness of $S \geq 35$ and a crest length of $L > 40$ (i.e. a lateral aspect ratio of $L/x_{\max} > 0.2$). As a consequence, unrealistic decreases in focusing amplitude or location are observed in Fig. 7. We, therefore, conclude that the results we generated for $S \geq 35$ and $L > 40$ should be ignored for our analysis here. The shaded strips in Fig. 7 indicate the ranges for S and L for which the resulting focusing values are unreliable.

Finally, the increase in focusing amplitude can be quantified by introducing the *amplification factor* defined as

$$A_F = \frac{\eta_F - \eta_{1D}}{\eta_{1D}} \times 100, \tag{16}$$

where η_F is the maximum wave height generated by the two-dimensional initial wave on the leading-depression side as it propagates through and leaves the computational domain, and η_{1D} is the one-dimensional propagation

height. We note that our definition of amplification factor here as the percent relative increase in focusing amplitude is quite similar to that of Berry (2007), who defines it as $A = z_{\text{foc}}/z_{\text{unfoc}}$, where z_{foc} is elevation of the tsunami as it passes through the focus and z_{unfoc} is the corresponding elevation when there is no focusing. The amplification factor defined in Eq. (16) is calculated for several values of parameters S and L and results are presented in Table 2. The results confirm our previous observations that larger focusing amplitude occurs for larger value of the crest length L in the interval $S<40$. Similar behavior is also observed for the interval $L<50$, steeper wave yields larger focusing amplitude.

Conclusions

In this paper, we studied how initial wave steepness and crest length affect the amplitude and the location of tsunami focusing. We considered finite-crested depression–elevation initial sources and we calculated and plotted maximum wave envelopes for a set of parameters ranging from mild to steep regarding the steepness parameter, and from small to large aspect ratio regarding the crest length.

Although both amplitude and location of focusing point change with both steepness and crest length, as expected, the results we obtained show that amplitude magnification is dominant for mild waves, i.e. when steepness is small, and focusing point dislocation is dominant for steep waves, i.e. when steepness is large. Furthermore, for steep initial waves the focusing point amplitude seems to reach a limiting value and not to further increase with crest length. This qualitative behavior of focusing is expected to be independent of the parameters used in this study and to remain unchanged in the framework of our linear nondispersive wave model, as far as the finite-crested dipolar form of the initial wave is preserved. The effect of dispersion on tsunami focusing would be the subject of a future study.

Acknowledgements The author acknowledges the financial support by Adana Science and Technology University Unit of Scientific Research Project Coordination through Project Number MUHDB-F.IM.2015-8.

Compliance with ethical standards

Conflict of interest The author states no conflict of interest.

References

Aydın B (2011) Analytical solutions of shallow-water wave equations. Ph.D. Thesis, Middle East Technical University, Ankara

Ben-Menahem A (1961) Radiation of seismic surface-waves from finite moving sources. Bull Seismol Soc Am 51(3):401–435

Ben-Menahem A, Rosenman M (1972) Amplitude patterns of tsunami waves from submarine earthquakes. J Geophys Res 77(17):3097–3128. https://doi.org/10.1029/JB077i017p03097

Berry MV (2007) Focused tsunami waves. Proc R Soc A 463:3055–3071. https://doi.org/10.1098/rspa.2007.0051

Carrier GF, Yeh H (2005) Tsunami propagation from a finite source. Comput Model Eng Sci 10:113–121. https://doi.org/10.3970/cmes.2005.010.113

Degueldre H, Metzger JJ, Geisel T, Fleischmann R (2015) Random focusing of tsunami waves. Nat Phys 12:259–262. https://doi.org/10.1038/NPHYS3557

Dotsenko SF, Sergeevsky BY, Cherkesov LV (1986) Spatial tsunami waves caused by a sign-changing displacement of the ocean surface. In: Tsunami Waves Researches, pp. 1–7. Academy of Sciences of the USSR (in Russian)

Kânoğlu U, Titov VV, Aydın B, Moore C, Stefanakis TS, Zhou H, Spillane M, Synolakis CE (2013) Focusing of long waves with finite crest over constant depth. Proc R Soc A. https://doi.org/10.1098/rspa.2013.0015

Marchuk AG, Titov VV (1989) Source configuration and the process of tsunami waves forming. In: Gusiakov VK (ed) Tsunamis: their science and hazard mitigation, Proceedings of international tsunami symposium, pp 11–17. Novosibirsk, USSR

Okal EA (2003) Normal mode energetics for far-field tsunamis generated by dislocations and landslides. Pure Appl Geophys 160:2189–2221. https://doi.org/10.1007/s00024-003-2426-9

Pelinovsky E (2006) Hydrodynamics of tsunami waves. In: Grue J, Trulsen K (eds) Waves in geophysical fluids: tsunamis, rogue waves, internal waves and internal tides, vol 1. Springer, NewYork, pp 1–48

Satake K (1988) Effects of bathymetry on tsunami propagation: application of ray tracing to tsunamis. Pure Appl Geophys 126(1):27–36. https://doi.org/10.1007/BF00876912

Stoker JJ (1957) Water waves: the mathematical theory with applications. Wiley, Amsterdam

Tadepalli S, Synolakis CE (1994) The run-up of N-waves on sloping beaches. Proc R Soc A 445:99–112. https://doi.org/10.1098/rspa.1994.0050

Titov V, Rabinovich AB, Mofjeld HO, Thomson RE, González FI (2005) The global reach of the 26 December 2004 Sumatra Tsunami. Science 309(5743):2045–8

Acta Geophysica (2018) 66:293–304
https://doi.org/10.1007/s11600-018-0147-9

RESEARCH ARTICLE - APPLIED GEOPHYSICS

Modeling of a historical earthquake in Erzincan, Turkey (Ms~7.8, in 1939) using regional seismological information obtained from a recent event

Shaghayegh Karimzadeh[1] · Aysegul Askan[2]

Received: 26 January 2018 / Accepted: 11 April 2018 / Published online: 20 April 2018

Abstract
Located within a basin structure, at the conjunction of North East Anatolian, North Anatolian and Ovacik Faults, Erzincan city center (Turkey) is one of the most hazardous regions in the world. Combination of the seismotectonic and geological settings of the region has resulted in series of significant seismic activities including the 1939 (Ms ~ 7.8) as well as the 1992 (Mw = 6.6) earthquakes. The devastative 1939 earthquake occurred in the pre-instrumental era in the region with no available local seismograms. Thus, a limited number of studies exist on that earthquake. However, the 1992 event, despite the sparse local network at that time, has been studied extensively. This study aims to simulate the 1939 Erzincan earthquake using available regional seismic and geological parameters. Despite several uncertainties involved, such an effort to quantitatively model the 1939 earthquake is promising, given the historical reports of extensive damage and fatalities in the area. The results of this study are expressed in terms of anticipated acceleration time histories at certain locations, spatial distribution of selected ground motion parameters and felt intensity maps in the region. Simulated motions are first compared against empirical ground motion prediction equations derived with both local and global datasets. Next, anticipated intensity maps of the 1939 earthquake are obtained using local correlations between peak ground motion parameters and felt intensity values. Comparisons of the estimated intensity distributions with the corresponding observed intensities indicate a reasonable modeling of the 1939 earthquake.

Keywords Historical earthquakes · The 1939 Erzincan (Turkey) earthquake · Ground motion simulation · Felt intensity · Ground motion prediction equations

Introduction

Study of destructive historical events without recorded ground motion data is challenging yet promising particularly if there is available intensity or damage data. Ground motion simulations can be performed for such historical events to obtain the anticipated ground motions in the corresponding meizoseismal areas. With the advance of computers and mathematical models, simulation methods have been improved to provide reliable synthetic ground motion records by modeling the earthquake source, propagation and site effects. Regarding the solution approaches as well as modeling assumptions, three main types of ground motion simulation techniques can be considered: Deterministic, stochastic as well as hybrid methods. Deterministic approach, which requires well defined seismic source and velocity models, provides numerical solutions of the wave equation (e.g., Frankel 1993; Olsen et al. 1996; Komatitsch et al. 2004; Aagaard et al. 2010). It is physical and accurate but practical only up to certain frequencies due to the minimum wavelength requirement. Stochastic approach models the ground motions as a combination of the deterministic far field S-wave spectrum and random phase angles (e.g., Boore 1983; Beresnev and

✉ Aysegul Askan
aaskan@metu.edu.tr

Shaghayegh Karimzadeh
shaghkn@metu.edu.tr

[1] Civil Engineering Department, Middle East Technical University, 06800 Ankara, Turkey

[2] Civil Engineering and Earthquake Studies Departments, Middle East Technical University, 06800 Ankara, Turkey

Atkinson 1997). It models the higher frequencies effectively despite the lack of full wave propagation and complex source effects (e.g., Castro et al. 2001; Motazedian and Moinfar 2006; Moustafa and Takenaka 2009; Askan et al. 2013, 2015; Tsereteli et al. 2016; Unal et al. 2017; Askan et al. 2017; Karimzadeh et al. 2017a, b). The whole frequency range of interest can be accurately modeled using hybrid techniques. In these techniques, the low frequency band is simulated with deterministic approaches while high frequency band is simulated using stochastic methods (e.g., Kamae et al. 1998; Hartzell and Harmsen 1999; Hisada 2008; Mai et al. 2010). Different precision levels and computation costs are acquired for alternative ground motion simulation techniques. Regardless of the simulation method, for simulation of the historical earthquakes with no records, a direct validation of the simulated data with the recorded data is not possible. Thus, indirect validations of the simulations can be performed in terms of comparisons with the shaking intensity or damage distributions as well as empirical ground motion prediction equations.

In this study, an initial attempt is presented to simulate the 1939 Erzincan earthquake (Ms ~ 7.8) which is among the most destructive events of the last century causing a surface rupture length of 360 km on five different segments on North Anatolian Fault Zone (NAFZ). The earthquake caused significant damage to about 120,000 buildings in the city and resulted in more than 30,000 fatalities (Barka 1996). In the aftermath of the event, the city was relocated towards North. The region has always been seismically active due to its tectonic nature: Historical records indicate approximately twenty large earthquakes close to Erzincan within the last ten centuries (Barka 1993). Another large earthquake occurred in Erzincan in 13 March 1992 (Mw = 6.6) which caused major structural loss and a considerable number of fatalities. However, there are only three near-field strong ground motion records from the 1992 event while no records are available from the 1939 event. It is important to simulate the ground motions from these large earthquakes to study both the physical properties of the earthquakes and obtain the records at locations where there are no stations. The recorded ground motions of the 1992 Erzincan earthquake are simulated in an initial study (e.g., Askan et al. 2013) followed by further investigations including simulations of scenario events in the region (Askan et al. 2015, 2017) as well as loss estimations using simulated motions (Karimzadeh et al. 2018). However, a quantified ground motion model of the 1939 earthquake is not available. Most of the available studies on the 1939 event are based on observations in the region in terms of the fault plane and source mechanism such as the rupture dimensions and slip values (e.g., Barka 1996; Stein et al. 1997; Askan et al. 2013; Gursoy et al. 2013). The major contribution of this study different from the previous ones is to physically and mathematically model a historical event (including source, path and site effects) for which no recorded ground motions are available. Through the simulations performed herein, the source properties of the earthquake are investigated and spatial distribution of the observed intensities is studied against the simulated intensity values. Finally, a database containing the simulated ground motions of the 1939 event at 244 nodes is formed. These motions are readily available for use in future engineering seismology and earthquake engineering studies.

In this paper, a preliminary simulation of the 1939 Erzincan earthquake is performed using the stochastic finite-fault method based on a dynamic corner frequency approach by Motazedian and Atkinson (2005). The stochastic finite-fault technique does not require the computational effort as well as the well-refined source and velocity models necessary for other simulation approaches to model particularly the higher frequencies (e.g., Motazedian and Atkinson 2005; Boore 2009; Atkinson et al. 2009; Raghukanth and Somala 2009; Ghofrani et al. 2013). In addition, the available observed intensity and damage distributions represent the rigid buildings in the region at that time with mostly lower fundamental periods. Thus, stochastic approach is chosen here to practically model the ground motion amplitudes corresponding to the frequency range of interest for this historical earthquake.

The organization of the paper is as follows: Initially, stochastic simulation of the 1939 event is performed with the region-specific path and site parameters which were previously verified with the strong motion records of the 1992 Erzincan event in study by Askan et al. (2013). Several of the parameters for the source model of the 1939 event are adopted from the studies involving field observations while others are computed from empirical relationships on source parameters (Barka 1996; Stein et al. 1997; Askan et al. 2013; Gursoy et al. 2013). There is no recorded strong motion of the event. Thus, a validation of the simulated motions against the observed records is not possible. For this reason, as the next step, the simulated motions are compared with two ground motion prediction equations. Finally, the estimated felt intensity values are obtained from the simulated peak ground motion parameters and compared against the corresponding observed intensities during the 1939 event (Altinok and Ersoy 2000).

Study region and information on the event

The most destructive earthquakes in Turkey have occurred on the NAFZ which is among the most active fault zones in the world with a dominant strike-slip character (Fig. 1a).

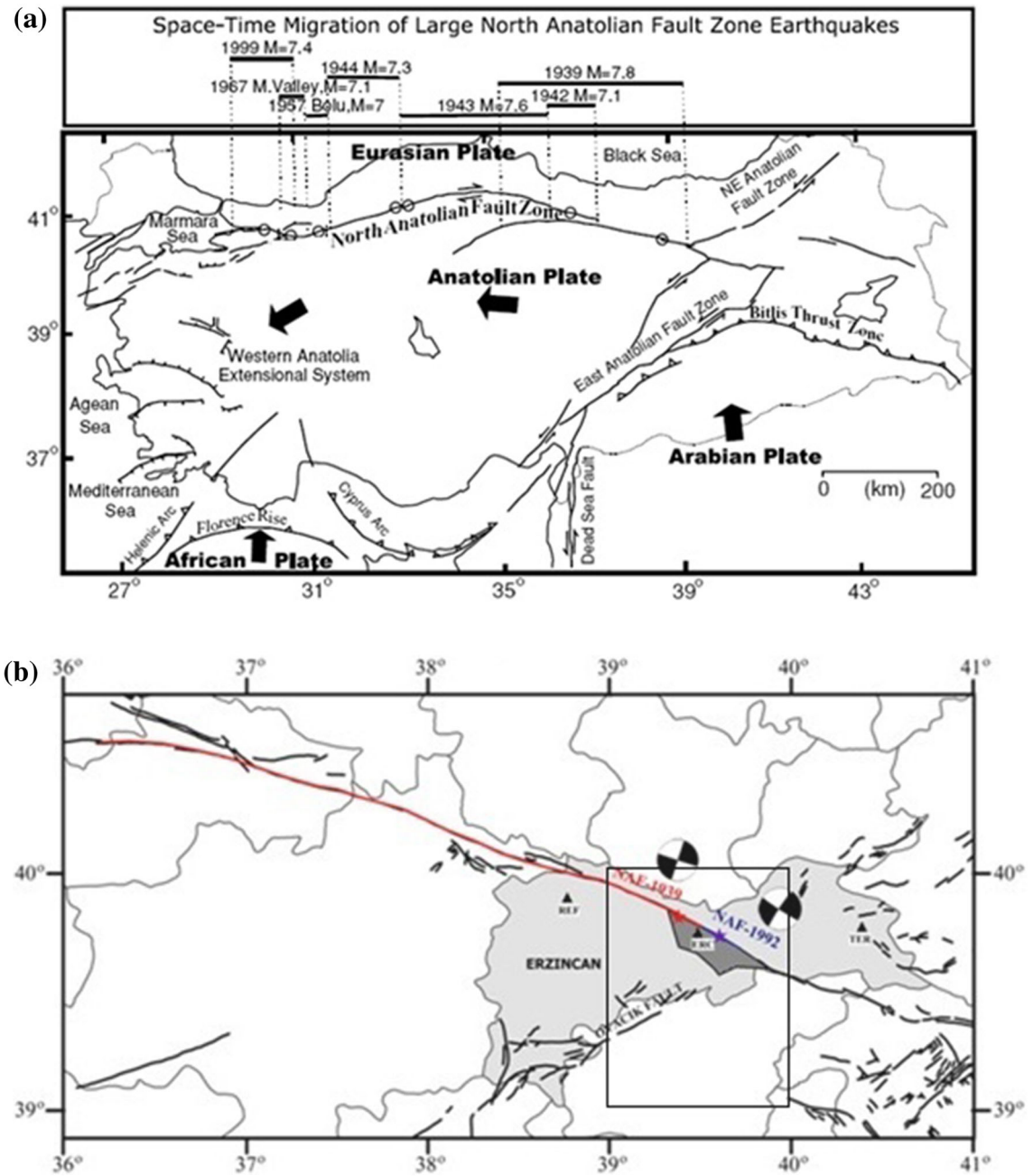

Fig. 1 **a** Main tectonic systems nearby the Anatolian plate besides the large earthquakes that occurred on the North Anatolian Fault Zone in the past century. **b** The epicenters of the 1939 and 1992 earthquakes along with the fault structures in the Erzincan area. The light gray region is the Erzincan county and the dark gray area is the Erzincan basin where the historical and the current city center is located. The rectangle box shows the study area (**a** and **b** are adapted from Utkucu et al. (2013) and Askan et al. (2013), respectively)

Throughout the last century, several major events occurred along this fault zone starting with the 1939 Erzincan (Ms ~ 7.8) event with an obvious westward migration (e.g., Ambraseys 1970; Barka 1992, 1996; Stein et al. 1997; Armijo et al. 2002). Most of the previous studies in Turkey have focused on the western parts of NAFZ due to the existing industrial facilities and residential areas. The Eastern sections are also less-densely instrumented when compared to the Western sections. Thus, the Eastern regions of NAFZ including Erzincan, should also be studied in detail due to the intense regional seismic activity. Such efforts are particularly necessary not only to investigate the past earthquakes in the region but also for risk mitigation in potential large earthquakes.

This study focuses on the Erzincan city center and its surroundings within a selected mesh bounded by 39°–40°N latitudes and 39°–40°E longitudes. The seismic activity in the study area arise from the complex tectonic regime: The

left-lateral strike-slip North East Anatolian and Ovacik Faults meet the right-lateral strike-slip North Anatolian Fault at the northern and southern edge of the Erzincan Basin, respectively (e.g., Bernard et al. 1997; Avsar et al. 2013) as shown in Fig. 1b. Erzincan city center is currently located on an alluvium pull-apart basin of size 50 km × 15 km (e.g., Tatar et al. 2013; Sarp 2015). The soil conditions within the basin vary from stiffer soils in the Northwestern regions to softer soils in the central and Southern regions (Askan et al. 2015). Before the 1939 event, the city center was within the same basin yet located about 4 km South of the current center.

Simulation of the 1939 Erzincan (Ms~7.8) earthquake

The fundamental ground motion simulation methods include deterministic, stochastic and hybrid models details of which are explained in the Introduction section. In this study, among these methods, stochastic approach is preferred where a deterministic theoretical amplitude spectrum is combined with a stochastic phase spectrum to yield acceleration spectra. This is mostly because there is neither a detailed source model nor any recorded seismograms of the 1939 Erzincan earthquake which would be required for a more rigorous simulation approach. For the simulation of the 1939 Erzincan event, a recent form of stochastic finite-fault modeling, which was shown to provide realistic broadband frequencies for engineering purposes, is used (Motazedian and Atkinson 2005).

Stochastic finite-fault method used in this study models ground motions radiating from a rectangular finite-fault plane which is discretized into smaller subfaults. Each subfault is treated as a stochastic point-source using an ω^{-2} spectrum. In this technique, propagation of rupture is supposed to start radially with a constant rupture velocity from the hypocenter. Each subfault is triggered once the rupture arrives at the center of that subfault. Appropriate time delays are considered to add up the contribution of the subfaults. In the dynamic corner frequency approach, the total released energy from the fault plane is preserved irrespective of the assumed size for each subfault. In this study, the stochastic finite-fault method based on the dynamic corner frequency approach is used as introduced within the computer program EXSIM (Motazedian and Atkinson 2005).

In the dynamic corner frequency approach, $A_{ij}(f)$ of the ijth subfault indicates the acceleration spectrum as follows (Motazedian and Atkinson 2005):

$$A_{ij}(f) = CM_{0ij}H_{ij}\frac{(2\pi f)^2}{\left[1+\left(\frac{f}{f_{c_{ij}}}\right)^2\right]}e^{-\frac{\pi f R_{ij}}{Q(f)\beta}}G(R_{ij})A(f)e^{-\pi\kappa f}, \quad (1)$$

where $C = \frac{\Re^{\theta\varphi}\cdot\sqrt{2}}{4\pi\rho\beta^3}$, $\Re^{\theta\varphi}$, and H_{ij} indicate the source constant, radiation pattern, and a high-frequency conservation scaling factor, respectively. The terms ρ and β represent the density and shear wave velocity, respectively. The seismic moment is expressed by $M_{0_{ij}} = \frac{M_0 S_{ij}}{\sum_{k=1}^{nl}\sum_{l=1}^{nw} S_{kl}}$, where S_{ij} is the relative slip weight; n_l and n_w are the number of subfaults along the length and width of the fault plane, respectively. The dynamic corner frequency of ijth subfault is stated by $f_{c_{ij}}(t) = N_R(t)^{-1/3}4.9\times10^6\beta\left(\frac{\Delta\sigma}{M_{0_{\text{ave}}}}\right)^{1/3}$. Here, $N_R(t)$ is the cumulative number of subfaults that are ruptured when time is t, $M_{0_{ave}} = M_0/N$ is the mean magnitude of subfaults, and $\Delta\sigma$ stands for the stress drop. The term R_{ij} corresponds to the distance of $ijth$ subfault from the observation point. Quality factor is shown with $Q(f)$. The geometric spreading term is expressed by $G(R_{ij})$. Finally, $A(f)$ stands for the site amplification factor, while $e^{-\pi\kappa f}$ represents the decay of the spectrum at high frequencies. This effect is modeled in this study using the κ factor of soils (Anderson and Hough 1984). Stochastic approach models the ground motions as a combination of the deterministic far field S-wave spectrum given in Eq. 1 and random phase angles (Boore 1983).

In this study, among the source parameters, fault geometry (dimensions and angles) is taken from previous studies on the 1939 Erzincan earthquake including Barka (1996), Stein et al. (1997) and Gursoy et al. (2013). In these reference studies, the magnitude of the 1939 event is reported in Ms scale rather than Mw scale. However, in the simulations Mw value is required. Rather than Ms–Mw conversions; in this study, a physical source property is preferred to estimate the Mw value directly. Thus, the moment magnitude Mw of the earthquake is estimated using an empirical relationship by Wells and Coppersmith (1994) that relates Mw to the Surface Rupture Length (SRL). Employing SRL = 360 km for the 1939 earthquake as reported in Barka (1996), a moment magnitude value of Mw = 8.0 is obtained. Another important source property, the stress drop of the earthquake is computed to be 120 bars via an empirical correlation between stress drop and fault width proposed by Mohammadioun and Serva (2001). Random slip distributions are assumed on the fault. The path parameters in Erzincan region shown in Table 1 were validated in past studies mostly using the ground motion records of the 1992 earthquake (Askan et al.

Table 1 Input parameters employed in the simulation of the 1939 Erzincan event

Parameter	Value
Moment magnitude	8.0
Location of hypocenter	39.8°N, 39.38°E
Depth of hypocenter	11.25 km
Depth to the top of the fault plane	0 km (360 km of surface rupture was observed)
Orientation of the fault plane	Strike: 108°, dip: 90°
Dimensions of the fault plane	Length: 360 km, width: 25 km
Crustal shear wave velocity	3700 m/s
Rupture velocity	3000 m/s
Crustal density	2800 kg/m^3
Stress drop	120 bar
Quality factor	$Q = 122f^{0.68}$
Geometrical spreading	$R^{-1.0}$
Duration model	$T = T_0 + 0.05\,R$
Windowing function	Saragoni–Hart
Kappa factor	Regional kappa model ($K_0 = 0.066$)
Site amplification factors	Corresponding site amplifications at each node (Askan et al. 2015; Boore and Joyner 1997)

2013, 2015, 2017). Finally, amplifications at each site of interest are considered through the site amplification factors suggested by (Boore and Joyner 1997). At each simulation node, available information on site classes (Askan et al. 2015) is used to model the corresponding site amplification factors. Since the regional geology does not change in 100 years, path and site parameters are still valid in 1992 event. Table 1 presents all of the input parameters employed in the simulation of the1939 Erzincan event.

Simulated ground motions are obtained at 244 nodes within the study area bounded by 39°–40°N latitudes and 39°–40°E longitudes. Among these nodes, 123 of them are selected within a close vicinity of the Erzincan city center as presented in Fig. 2a. At 9 nodes within the city center (nodes 116–129 represented with green squares), detailed shear wave velocity models from a microtremor array study are available (Askan et al. 2015). At nodes 1 to 115, since there is no detailed information regarding the local soil conditions, the soil velocity model of the closest node with available information is used in simulations. Among these 115 nodes, the black triangles correspond to the current Erzincan district centers while the red circular ones represent the regular nodes with 1 km grid spacing in both directions. Finally, at nodes 124–244 which remain in a larger region outside of the city center with a lack of soil velocity models, a coarser mesh employed with 10 km grid spacing (Fig. 2b). At these nodes, generic soil amplification factors of Boore and Joyner (1997) for site class C are used in the simulations consistent with the geology of the region (Senel 1997).

Results and validations

Since it is not possible to demonstrate the simulated time histories at all nodes, the results of the simulations are expressed in terms of peak ground velocity (PGV), peak ground acceleration (PGA), and 5% damped pseudo-spectral acceleration (PSA) maps at selected spectral periods within the study area, as shown in Fig. 3. The results reveal that the historical city center experience much higher ground motion levels compared to the surrounding Northern and Southern regions. This is expected due to the closer distances from the fault plane as well as softer soil conditions in the historical city center. The historical city, which was located about 4 km south of the current city center, is exposed to a PGA of 1.26 g, PGV of 145 cm/s, PSA at $T = 0.33$ s of 3.14 g, PSA at $T = 1$ s of 0.54 g and PSA at $T = 2$ s of 0.64 g. These very high values definitely contain modeling errors yet the amplitudes in general explain the widespread damage in the region. The PGA, PGV, PSA ($T = 0.33$ s), PSA ($T = 1$ s) and PSA ($T = 2$ s) values in the current city center are mostly lower than those in the old city center and are estimated as 1.12 g, 91 cm/s, 2.82 g, 0.8 g, 0.51 g, respectively. The acceleration time histories, velocity time histories along with the Fourier amplitude spectra (FAS) of acceleration and pseudo acceleration response spectrum (PSA up to 4 s) at these two selected nodes are displayed in Figs. 4 and 5. Large ground motion amplitudes are observed in both acceleration and velocity time series at both nodes. In addition, FAS and PSA also indicate high spectral values at

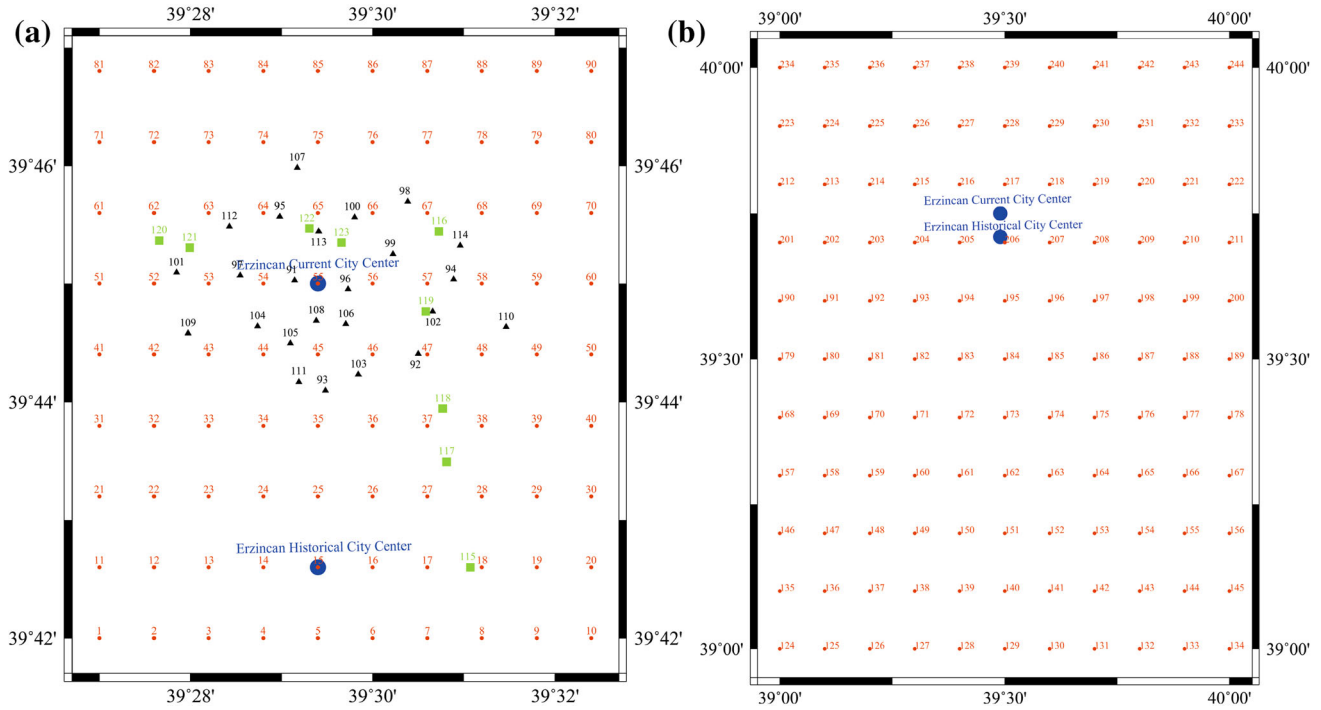

Fig. 2 Distribution of the selected nodes **a** within **b** outside the Erzincan city center

most frequencies/periods. The multiple wave packages on both acceleration time histories indicate finite-fault source effects radiating from the large fault plane.

Next, attenuation of the simulated peak ground motion values is compared against the ground motion prediction equations (GMPEs) by Boore and Atkinson (2008) as well as Akkar and Cagnan (2010) in Fig. 6. These equations were previously shown to represent the attenuation characteristics in Eastern Turkey (Akansel et al. 2014). It is observed in Fig. 6 that the simulated motions remain within $\pm 1\sigma$ of both GMPEs, indicating effectiveness of the simulations. Simulated data of the 1939 Erzincan earthquake show a more similar trend to the GMPE by Boore and Atkinson (2008).

Since a direct validation of the simulation results is not possible due to lack of recorded motions from the 1939 Erzincan event, comparisons of the estimated intensity distribution with the observed one are presented. For this purpose, anticipated intensity values are computed at the nodes shown in Fig. 2b using local correlations between modified Mercalli intensity (MMI) with PGA and PGV. These correlations are derived from felt intensity and ground motion databases of Turkey. The damage patterns monitored in the past earthquakes in Turkey reveal the importance of using local intensity models in terms of PGA and PGV for stiff and flexible structures, respectively (Erberik 2008a, b; Bilal and Askan 2014). To account for all types of structures in the region, the simulated PGA and PGV values at each node are used as inputs to the following simple linear relationships proposed by Bilal and Askan (2014):

$$\mathrm{MMI} = 0.132 + 3.884 * \log(\mathrm{PGA}), \quad (2)$$

$$\mathrm{MMI} = 2.673 + 4.340 * \log(\mathrm{PGV}). \quad (3)$$

Figure 7a displays the observed intensity distribution collected in the field after the 1939 event in Medvedev–Sponheuer–Karnik (MSK) scale. It is known that the large intensity values in MSK and MMI scales correspond to the same felt intensity levels (Musson et al. 2010). Thus, the comparisons in MSK and MMI scales are considered to contain negligible error. Figure 7b and c displays the estimated MMI values for the 1939 earthquake from Eqs. (2) and (3) using simulated motions, respectively. Comparison of the estimated and observed intensity values in the region reveals the consistency among them regardless of the relationship used. This consistency is much more obvious for both historical and current Erzincan city centers. However, it is noted that the MMI–PGA relationship (Fig. 7b) gives even a closer intensity distribution to the observed map. This is due to the fact that the buildings in the region at that time were mostly rigid masonry structures whose damage is better correlated with PGA than PGV (Erberik 2008a, b). Figure 7b and c indicates a slight overestimation of the observed intensity values in the Southern regions. This discrepancy could arise from the modeling errors in both simulations and MMI–PGA/PGV relationships. Despite this small

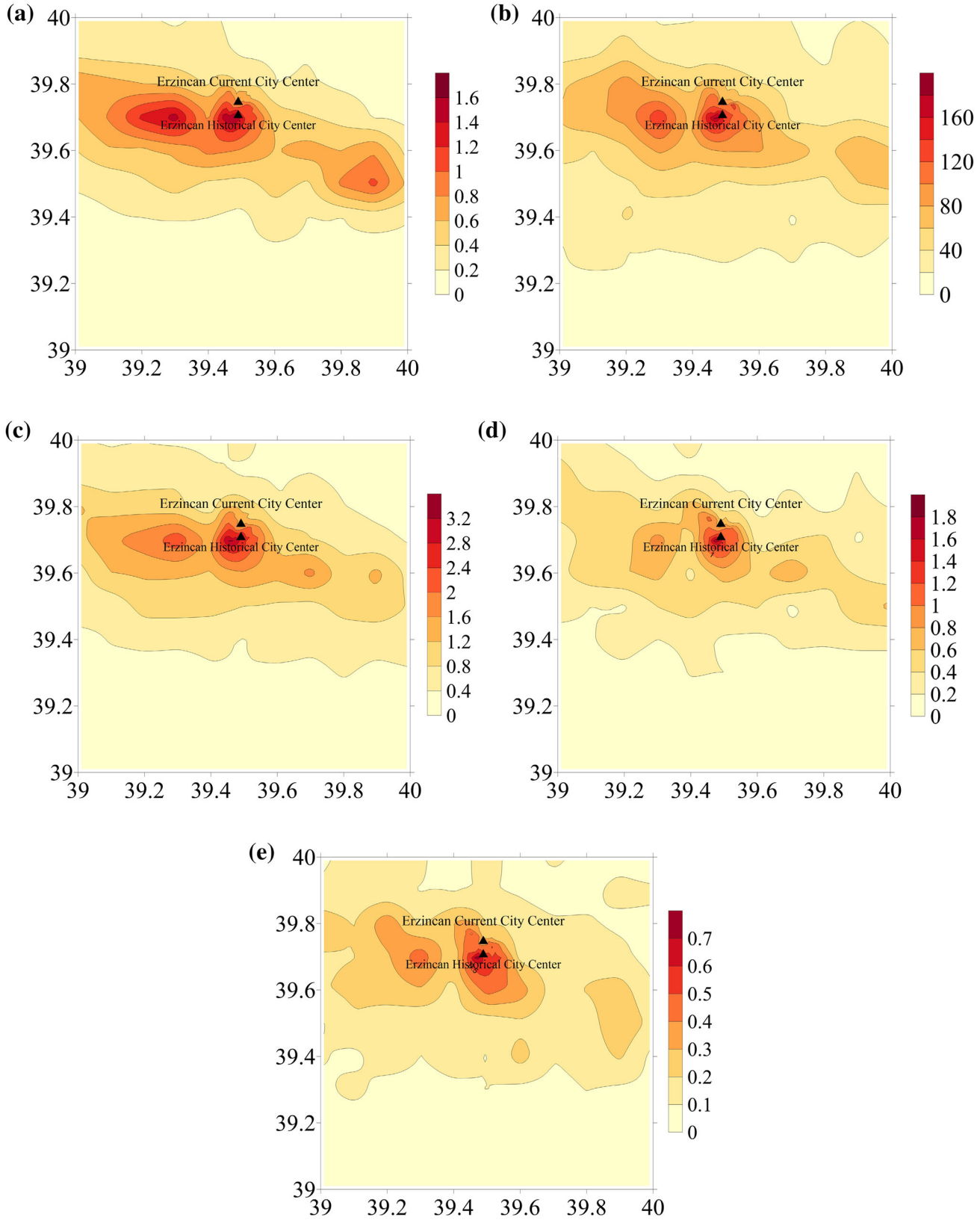

Fig. 3 Maps of simulated **a** PGA (g), **b** PGV (cm/s), **c** PSA ($T = 0.3$ s) (g), **d** PSA ($T = 1$ s) (g), **e** PSA ($T = 2$ s) (g) values of the 1939 Erzincan earthquake

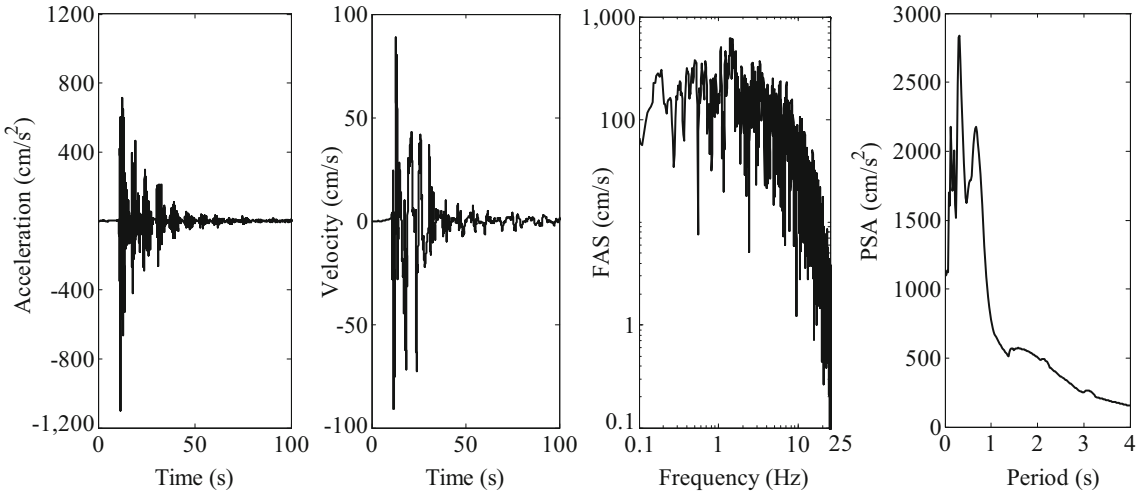

Fig. 4 Simulated acceleration and velocity time histories, FAS and PSA in the current Erzincan city center (ERC station) during the 1939 earthquake

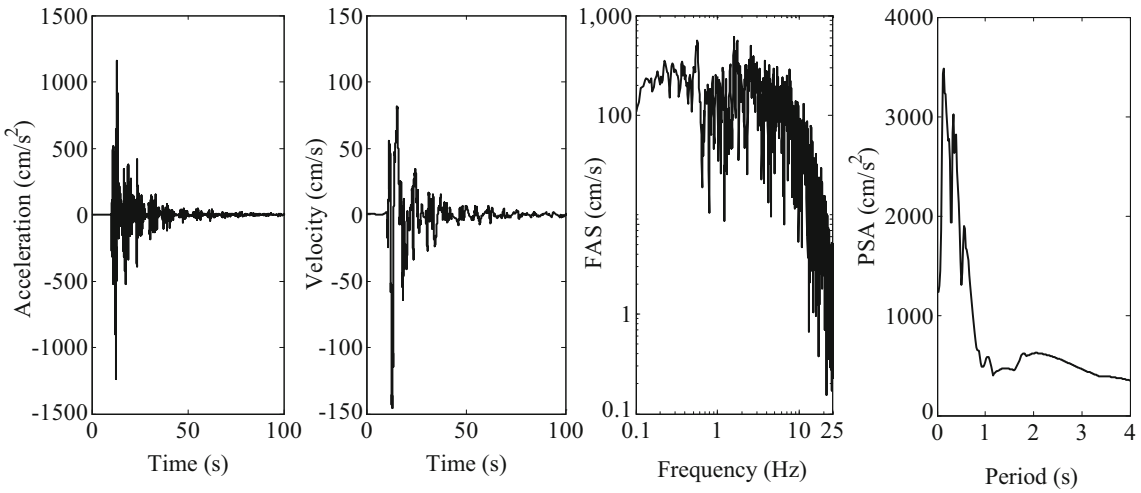

Fig. 5 Simulated acceleration and velocity time histories, FAS and PSA in the historical Erzincan city center during the 1939 earthquake

discrepancy, the pattern of the simulated intensity distribution in Fig. 7b matches the observed one closely. This indicates a physically reasonable source, propagation and site modeling in spite of the existing uncertainties and lack of data. In general, simulated motions are considered to conservatively estimate the anticipated ground motions of the 1939 Erzincan earthquake. In summary, the numerical results indicate that the anticipated ground motion levels and seismic intensity values are excessively large which explain the extent of the damage and number of fatalities during the 1939 Erzincan earthquake.

Conclusions

In this paper, the 1939 Erzincan (Ms ~ 7.8) earthquake is studied using stochastic finite-fault ground motion simulations. The source parameters are estimated using empirical relationships and previous studies including observations on the fault plane and surface rupture. The path and site parameters are adapted from past studies in the region validated mostly with data from the 1992 Erzincan earthquake. In the simulations, 244 nodes are considered in an area covering the historical and current Erzincan city centers. The simulation results yield PGA and PGV values that exceed 1 g and 100 cm/s, respectively at several nodes within the study area including the old and current city centers. The high amplitudes and spatial distribution of the simulated ground motions are consistent with the widespread damage observed during the 1939

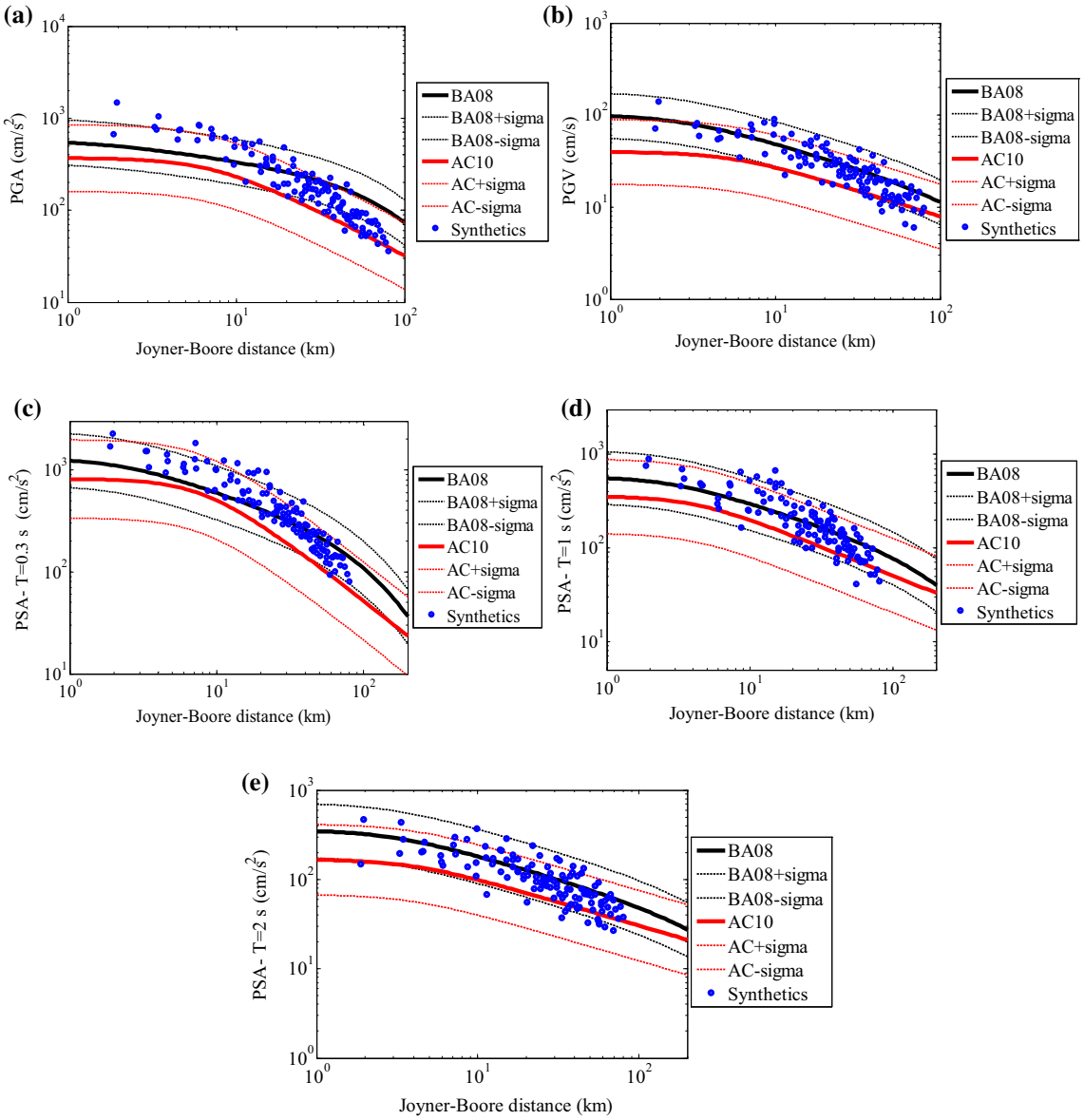

Fig. 6 Attenuation of the simulated **a** PGA, **b** PGV, **c** PSA ($T = 0.3$ s), **d** PSA ($T = 1$ s), **e** PSA ($T = 2$ s) values at the selected nodes in comparison with the selected GMPEs by Boore and Atkinson (2008) as well as Akkar and Cagnan (2010) denoted with BA08 and AC10, respectively

event. There is no ground motion record from this event for a direct validation of the simulations. Thus, to validate the simulations indirectly, observed intensity map prepared after the earthquake is compared with the estimated ones. The estimated intensities are obtained using local empirical conversion relationships between MMI and peak ground motion parameters (PGA and PGV). The following main conclusions are derived from the numerical results of this study:

- The amplitudes and the pattern of the estimated intensities closely match the observed values. In particular, the anticipated intensity map obtained with MMI–PGA relationship yields better results. It is believed that this is because buildings in the region in 1939 were mostly rigid masonry structures with damage patterns consistent with PGA than PGV (Erberik 2008a, b).
- The consistency between observed and simulated MMI values indicates a physically reasonable source, propagation and site modeling of the 1939 Erzincan earthquake despite the existing uncertainties and lack of data. In general, simulated ground motions and estimated intensities seem to well explain the extent of the observed damage and losses in this historical event. This finding indicates that it is possible to study

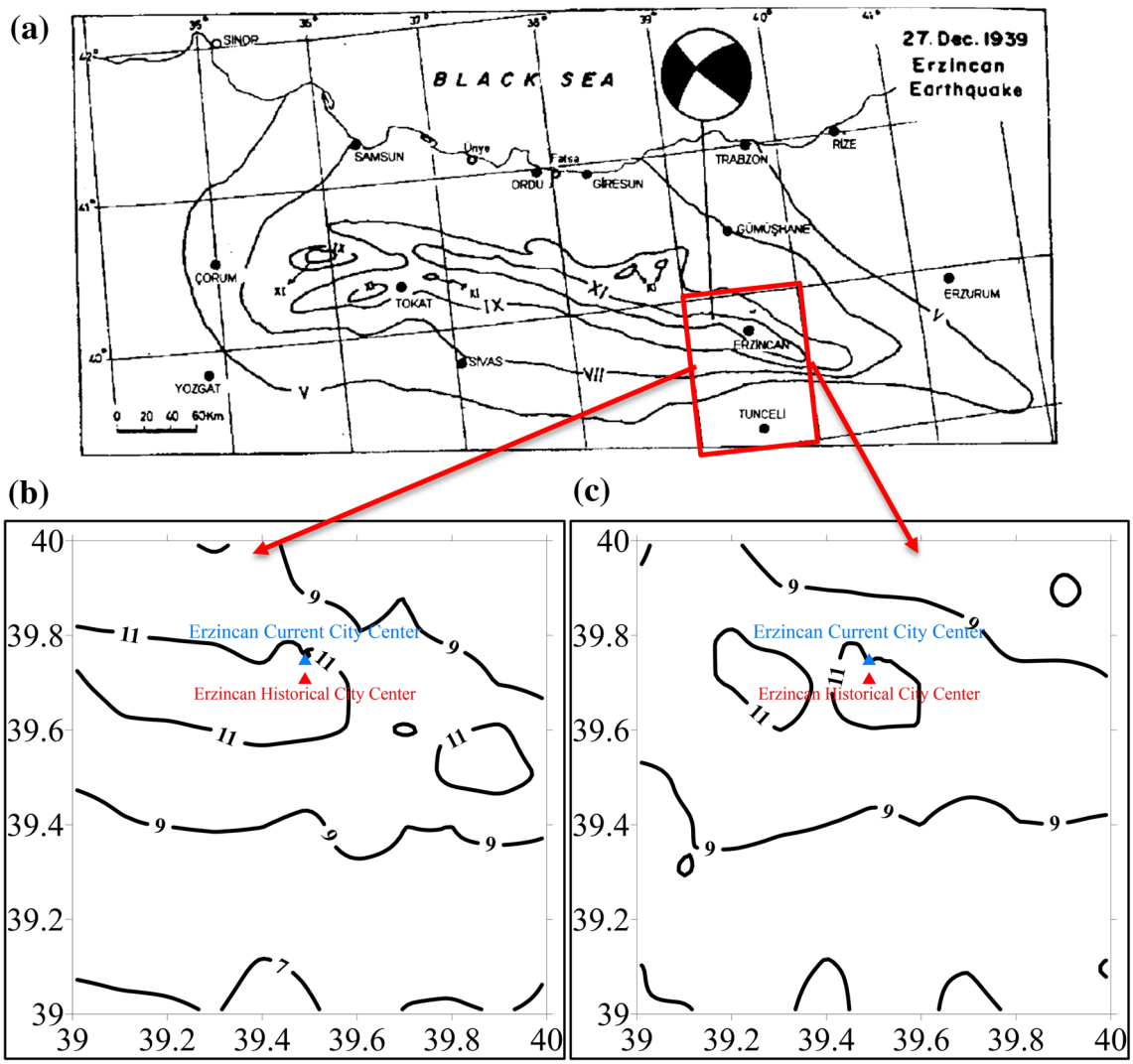

Fig. 7 **a** Observed seismic intensity map of the 1939 Erzincan earthquake (Altinok and Ersoy, 2000); estimated intensity distribution using. **b** MMI–PGA correlation given in Eq. (2), **c** MMI–PGV correlation given in Eq. (3). The red box in (**a**) shows the study area as plotted in (**b**) and (**c**)

historical events with careful selection of model parameters despite existence of certain modeling assumptions and the corresponding errors.

- Despite the inherent limitations such as simple source and propagation models, stochastic simulation methods with validated model parameters provide accurate results that could be employed for practical engineering applications similar to the one presented in this study.
- Finally, relatively lower ground motion amplitudes and intensities are observed in the current city center as compared to those in the historical one. This could also explain why the Erzincan city was relocated to the North after the 1939 event. Yet, after 53 years, the 1992 Erzincan (Mw = 6.6) earthquake occurred on NAFZ, this time close to the current city center, causing again widespread damage and losses. This points out the importance of good construction practice in addition to an effective city planning that considers interdisciplinary knowledge for risk mitigation purposes.

Acknowledgements This study is partially funded by JICA-SATREPS through the MarDiM project entitled "Earthquake and Tsunami Disaster Mitigation in the Marmara Region and Disaster Education in Turkey".

References

Aagaard BT, Graves RW, Schwartz DP, Ponce DA, Graymer RW (2010) Ground-motion modeling of Hayward fault scenario earthquakes, part i: construction of the suite of scenarios. Bull Seismol Soc Am 100:2927–2944. https://doi.org/10.1785/0120090324

Akansel V, Ameri G, Askan A, Caner A, Erdil B, Kale O, Okuyucu D (2014) The 23 October 2011 M W 7.0 Van (Eastern Turkey) earthquake: interpretations of recorded strong ground motions and post-earthquake conditions of nearby structures. Earthq Spectra 30:657–682. https://doi.org/10.1193/012912EQS020M

Akkar S, Cagnan Z (2010) A local ground-motion predictive model for Turkey, and its comparison with other regional and global ground-motion models. Bull Seismol Soc Am 100:2978–2995. https://doi.org/10.1785/0120090367

Altinok Y, Ersoy S (2000) Tsunamis observed on and near the Turkish coast. Nat Hazards 21:185–205

Ambraseys NN (1970) Some characteristic features of the North Anatolian Fault Zone. Tectonophysics 9:143–165. https://doi.org/10.1016/0040-1951(70)90014-4

Anderson J, Hough S (1984) A model for the shape of the Fourier amplitude spectrum of acceleration at high frequencies. Bull Seismol Soc Am 74:1969–1993

Armijo R, Meyer B, Navarro S, King G, Barka A (2002) Asymmetric slip partitioning in the Sea of Marmara pull-apart: a clue to propagation processes of the North Anatolian Fault. Terra Nova 14:80–86. https://doi.org/10.1046/j.1365-3121.2002.00397.x

Askan A, Sisman FN, Ugurhan B (2013) Stochastic strong ground motion simulations in sparsely-monitored regions: a validation and sensitivity study on the 13 March 1992 Erzincan (Turkey) earthquake. Soil Dyn Earthq Eng 55:170–181. https://doi.org/10.1016/j.soildyn.2013.09.014

Askan A, Karimzadeh S, Asten M, Kılıç N, Şişman FN, Erkmen C (2015) Assessment of seismic hazard in Erzincan (Turkey) region: construction of local velocity models and evaluation of potential ground motions. Turk J Earth Sci 24:529–565. https://doi.org/10.3906/yer-1503-8

Askan A, Karimzadeh S, Bilal M (2017) Seismic intensity maps for North Anatolian Fault Zone (Turkey) based on recorded and simulated ground motion data. In: Cemen Ibrahim, Yilmaz Yucel (eds) Neotectonics and earthquake potential of the Eastern Mediterranean Region, in active global seismology: neotectonics and earthquake potential of the Eastern Mediterranean Region. Wiley, Hoboken

Atkinson G, Assatourians K, Boore DM (2009) A guide to differences between stochastic point-source and stochastic finite-fault simulations. Bull Seismol Soc Am 99:3192–3201. https://doi.org/10.1785/0120090058

Avsar U, Turkoglu E, Unsworth M, Caglar I, Kaypak B (2013) Geophysical images of the North Anatolian Fault Zone in the Erzincan Basin, Eastern Turkey, and their tectonic implications. Pure Appl Geophys 170:409–431. https://doi.org/10.1007/s00024-012-0521-5

Barka A (1992) The North Anatolian Fault Zone. Ann Tecton 6:164–195

Barka A (1993) The tectonics of Erzincan basin and 13 March 1992 Erzincan earthquake. In: Proceedings of the 2nd Turkish national earthquake engineering conference, 259–270, Istanbul Technical University Structures and Earthquake Applications-Research Center, (in Turkish)

Barka A (1996) Slip distribution along the North Anatolian fault associated with the large earthquakes of the period 1939 to 1967. Bull Seismol Soc Am 86:1238–1254

Beresnev I, Atkinson G (1997) Modeling finite-fault radiation from the ωn spectrum. Bull Seismol Soc Am 87:67–84

Bernard P, Gariel JC, Dorbath L (1997) Fault location and rupture kinematics of the magnitude 6.8, 1992 Erzincan earthquake, Turkey, from strong ground motion and regional records. Bull Seismol Soc Am 87:1230–1243

Bilal M, Askan A (2014) Relationships between felt ıntensity and recorded ground-motion parameters for Turkey. Bull Seismol Soc Am 104:484–496. https://doi.org/10.1785/0120130093

Boore DM (1983) Stochastic simulation of high-frequency ground motions based on seismological models of the radiated spectra. Bull Seismol Soc Am 73:1865–1894

Boore DM (2009) Comparing stochastic point-source and finite-source ground-motion simulations: SMSIM and EXSIM. Bull Seismol Soc Am 99:3202–3216. https://doi.org/10.1785/0120090056

Boore DM, Atkinson GM (2008) Ground-motion prediction equations for the average horizontal component of PGA, PGV, and 5% damped PSA at spectral periods between 0.01 sand 10.0s. Earthquake Spectra 24:99–138. https://doi.org/10.1193/1.2830434

Boore DM, Joyner WB (1997) Site amplifications for generic rock sites. Bull Seismol Soc Am 87:327–341

Castro RR, Rovelli A, Cocco M, Di Bona M, Pacor F (2001) Stochastic simulation of strong-motion records from the 26 September 1997 (Mw 6), Umbria–Marche (central Italy) earthquake. Bull Seismol Soc Am 91:27–39. https://doi.org/10.1785/0120000011

Erberik MA (2008a) Generation of fragility curves for Turkish masonry buildings considering in-plane failure modes. Earthq Eng Struct D 37:387–405. https://doi.org/10.1002/eqe.760

Erberik MA (2008b) Fragility-based assessment of typical mid-rise and low-rise RC buildings in Turkey. Eng Struct 30:1360–1374. https://doi.org/10.1016/j.engstruct.2007.07.016

Frankel A (1993) Three-dimensional simulations of the ground motions in the San Bernardino valley, California, for hypothetical earthquakes on the San Andreas fault. Bull Seismol Soc Am 83:1020–1041

Ghofrani H, Atkinson GM, Goda K, Assatourians K (2013) Stochastic finite-fault simulations of the 2011 Tohoku, Japan, earthquake. Bull Seismol Soc Am 103:1307–1320. https://doi.org/10.1785/0120120228

Gursoy H, Tatar O, Akpınar Z, Polat A, Mesci L, Tunçer D (2013) New observations on the 1939 Erzincan Earthquake surface rupture on the Kelkit Valley segment of the North Anatolian Fault Zone, Turkey. J Geodyn 6:259–271. https://doi.org/10.1016/j.jog.2012.06.002

Hartzell S, Harmsen S (1999) Calculation of broadband time histories of ground motion: comparison of methods and validation using strong-ground motion from the 1994 Northridge earthquake. Bull Seismol Soc Am 89:1484–1504

Hisada Y (2008) Broadband strong motion simulation in layered half-space using stochastic Green's function technique. J Seismol 12:265–279

Kamae K, Irikura K, Pitarka A (1998) A technique for simulating strong ground motion using hybrid Green's function. Bull Seismol Soc Am 88:357–367

Karimzadeh S, Askan A, Yakut A, Ameri G (2017a) Assessment of alternative simulation techniques in nonlinear time history analyses of multi-story frame buildings: a case study. Soil Dyn Earthq Eng 98:38–53. https://doi.org/10.1016/j.soildyn.2017.04.004

Karimzadeh S, Askan A, Yakut A (2017b) Assessment of simulated ground motions for their use in structural engineering practice; a case study for Duzce (Turkey). Pure Appl Geophys. https://doi.org/10.1007/s00024-017-1602-2

Karimzadeh S, Askan A, Erberik MA, Yakut A (2018) Seismic damage assessment based on regional synthetic ground motion dataset: a case study for Erzincan. Nat Hazards, Turkey. https://doi.org/10.1007/s11069-018-3255-6

Komatitsch D, Liu Q, Tromp J, Süss P, Stidham C, Shaw JH (2004) Simulations of ground motion in the Los Angeles basin based upon the spectral-element method. Bull Seismol Soc Am 94:187–206. https://doi.org/10.1785/0120030077

Mai P, Imperatori W, Olsen K (2010) Hybrid broadband ground-motion simulations: combining long-period deterministic synthetics with high-frequency multiple S-to-S backscattering. Bull Seismol Soc Am 100:2124–2142. https://doi.org/10.1785/0120080194

Mohammadioun B, Serva L (2001) Stress drop, slip type, earthquake magnitude, and seismic hazard. Bull Seismol Soc Am 91(4):694–707. https://doi.org/10.1785/0120000067

Motazedian D, Atkinson GM (2005) Stochastic finite-fault modeling based on a dynamic corner frequency. Bull Seismol Soc Am 95:995–1010. https://doi.org/10.1785/0120030207

Motazedian D, Moinfar A (2006) Hybrid stochastic finite fault modeling of 2003, M 6.5, Bam, earthquake (Iran). J Seismol 10:91–103

Moustafa S, Takenaka H (2009) Stochastic ground motion simulation of the 12 October 1992 Dahshour earthquake. Acta Geophys 57:636–656. https://doi.org/10.2478/s11600-009-0012-y

Musson RMW, Grünthal G, Stucchi M (2010) The comparison of macroseismic intensity scales. J Seismol 14:413–428. https://doi.org/10.1007/s10950-009-9172-0

Olsen KB, Archuleta RJ, Matarese JR (1996) Three-dimensional simulation of a magnitude 7.75 earthquake on the San Andreas fault. Science 270:1628–1632

Raghukanth S, Somala S (2009) Modeling of strong-motion data in northeastern India: Q, stress drop, and site amplification. Bull Seismol Soc Am 99:705–725. https://doi.org/10.1785/0120080025

Sarp G (2015) Tectonic controls of the North Anatolian Fault System (NAFS) on the geomorphic evolution of the alluvial fans and fan catchments in Erzincan pull-apart basin; Turkey. J Asian Earth Sci 98:116–125. https://doi.org/10.1016/j.jseaes.2014.11.017

Senel M (1997) Geological maps of Turkey in 1: 250 000 scale: Erzincan sheet, mineral research and exploration directions of Turkey (MTA), Ankara, Turkey

Stein RS, Barka A, Dieterich JH (1997) Progressive failure on the North Anatolian fault since 1939 by earthquake stress triggering. Geophys J Int 128:594–604. https://doi.org/10.1111/j.1365-246X.1997.tb05321.x

Tatar O, Akpinar Z, Gursoy H, Piper JDA, Kocbulut F, Mesci BL, Polat A, Roberts AP (2013) Palaeomagnetic evidence for the neotectonic evolution of the Erzincan Basin North Anatolian Fault Zone, Turkey. J Geodyn 65:244–258. https://doi.org/10.1016/j.jog.2012.03.009

Tsereteli N, Askan A, Hamzehloo H (2016) Hybrid-empirical ground motion estimations for Georgia. Acta Geophys 64:1225–1256. https://doi.org/10.1515/acgeo-2016-0048

Unal B, Askan A, Selcuk-Kestel AS (2017) Simulation of large earthquakes and its implications on earthquake insurance rates: a case study in Bursa region (Turkey). Nat Hazards 85:215–236. https://doi.org/10.1007/s11069-016-2578-4

Utkucu M, Nalbant SS, McCloskey J, Steacy S, Alptekin O (2013) Slip distribution and stress changes associated with the 1999 November 12, Duzce (Turkey) earthquake (Mw = 7.1). Geophys J Int 153:229–241. https://doi.org/10.1046/j.1365-246X.2003.01904.x

Wells D, Coppersmith K (1994) New empirical relationships among magnitude, rupture length, rupture width, rupture area, and surface displacement. Bull Seismol Soc Am 84:974–1002

Acta Geophysica (2018) 66:305–316
https://doi.org/10.1007/s11600-018-0149-7

RESEARCH ARTICLE - APPLIED GEOPHYSICS

Influence of seismic diffraction for high-resolution imaging: applications in offshore Malaysia

Yasir Bashir[1] · Deva Prasad Ghosh[1] · Chow Weng Sum[1]

Received: 26 November 2017 / Accepted: 12 April 2018 / Published online: 20 April 2018

Abstract
Small-scale geological discontinuities are not easy to detect and image in seismic data, as these features represent themselves as diffracted rather than reflected waves. However, the combined reflected and diffracted image contains full wave information and is of great value to an interpreter, for instance enabling the identification of faults, fractures, and surfaces in built-up carbonate. Although diffraction imaging has a resolution below the typical seismic wavelength, if the wavelength is much smaller than the width of the discontinuity then interference effects can be ignored, as they would not play a role in generating the seismic diffractions. In this paper, by means of synthetic examples and real data, the potential of diffraction separation for high-resolution seismic imaging is revealed and choosing the best method for preserving diffraction are discussed. We illustrate the accuracy of separating diffractions using the plane-wave destruction (PWD) and dip frequency filtering (DFF) techniques on data from the Sarawak Basin, a carbonate field. PWD is able to preserve the diffraction more intelligently than DFF, which is proven in the results by the model and real data. The final results illustrate the effectiveness of diffraction separation and possible imaging for high-resolution seismic data of small but significant geological features.

Keywords Seismic diffraction · Resolution · Preservation · Plane-wave destruction · Frequency

Introduction

Malaysian Basin

Malaysian basin is geologically complex because of the evaluation through various phases of continental accretion, mountain building and rifting. The geology of the Malay Basin is much older than the other part of Sarawak and Sabah (Madon 1999). The geophysical challenges includes but not limited to: imaging thin sands, often beyond seismic resolution; imaging below gas clouds and below carbonates; diffraction imaging; imaging basement internal architecture; understanding wave propagation in effective media and related anisotropy; velocity analysis and anisotropy; Gas cloud imaging using full waveform inversion; and multiple elimination (Ghosh et al. 2010). The main focus of research in this region is to image the fracture and karst using diffraction imaging as shown in Fig. 1.

Sarawak Basin

Diffraction separation analyses were performed on the Sarawak Basin, which lies NW of Borneo and forms the southern boundary of the Oligocene-Recent South China Sea basin; its tectonic evolution has been nearly matched to rifting and sea-floor spreading in the South China Sea marginal basin (Madon et al. 2013). The majority of the Sarawak Basin, including that part in Malaysia, is comprised of carbonate build-up, thus making seismic imaging challenging. The pre-carbonate deposit of the late Oligocene to early Miocene and later terrestrial deposit in-filled the accommodation zone in Cycle I and Cycle II. The cycles are described as follows: Cycle I and II (Upper Eocene to Lower Miocene age) was interpreted as channel sands, overbank clays and coal deposited. Cycle III (Lower-Middle Miocene age) contains shale with thin

✉ Yasir Bashir
Yasir.bashir@utp.edu.my; yasir.bashir@live.com

[1] Department of Petroleum Geoscience, Centre for Seismic Imaging (CSI), Universiti Teknologi PETRONAS, Darul Ridzuan, Seri Iskandar, Perak, Malaysia

limestone and sandstone, Cycle IV (Middle Miocene age) is composed of limestone with minor quantity of mixed clastics, Cycle V (middle to upper Miocene) is recognized as limestone, Cycle VI to Cycle VIII (Upper Miocene to Pleistocene age) is composed of open marine to coastal clays and sand, respectively. The prograding sediments of Cycle VI to Cycle VIII have stifled the extensive carbonate buildups progressively until the present day. In Central Luconia, carbonate deposition began in the early Miocene (Cycle III) and grew extensively in Cycles IV and V, during the middle to late Miocene (Janjuhah et al. 2017). The structure is dominated by a phase of E–W extension that resulted in intensive but simple N–S trending faults. These faults affected deposition within Cycles I and II and acted as foci for the development of Cycles IV and V carbonate reefs and build-up. The domination of the intensive pre-carbonate structuration has thus resulted in poor seismic imaging quality.

Diffraction

Diffraction patterns frequently occur in seismic sections, especially in carbonate reservoirs, due to abrupt lateral changes in impedance contrast and the discontinuity of subsurface layers. However, a very serious objection to the application of classical theory has argued that stacked seismic data are not true zero-separation data, since it is not at all obvious that the results of stacking the data recorded over a wide range of source receiver separations will reasonably approximate the results of true zero-separation recording, insofar as diffraction amplitudes are concerned (Berryhill 1977). Berryhill also explained the concept and compared zero-separation theory with nonzero-separation source-geophone distance, concluding that diffraction amplitudes at nonzero source-receiver separation are well ordered almost completely by the location of the source-receiver midpoint.

As is well known regarding wave-propagation and geometric paths, a point diffractor gives rise to a hyperbolic pattern on the stacked section. The hyperbola is explained as a symmetrical open curve formed by the intersection of a circular cone with a plane at a smaller angle with its axis than the sides of the cone. Diffraction can only be considered hyperbolic, if the overburden is homogeneous, which is not a very natural assumption to make. The curvature of the diffraction hyperbola is dependent on the velocity of the medium, with the apex as an indicator of fault location. Imaging of diffractions is a challenge in seismic processing and adopted by a workflow using common-reflection-surface by (Krey 1952; Dell and Gajewski 2011; Schwarz and Gajewski 2017).

In reflection seismology applied to exploration geophysics, such wave propagation phenomena are employed to estimate the properties of the Earth's subsurface reflector. Furthermore, the diffraction phenomenon is also concerned with reflection because of the properties of the subsurface as defined above. The acoustic (seismic) impedance, $Z = V\rho$, where V is the seismic wave velocity and ρ is density.

Although seismic migration is now one of the primary imaging tools employed in the field, the earliest analogue seismic records took the form of simple single-fold illustration (Khaidukov et al. 2004; Decker et al. 2013; Klokov and Fomel 2013; Madon et al. 2013). These records were characterised by diffracted energy and random noise, but still provided a useful interpretation of the Earth's subsurface. Later, mechanical migration removed the structural misrepresentation of early seismic data, with CMP stacks condensing the amount of random noise when diffracted energy is preserved.

Seismic reflection and diffraction waves are essentially different physical phenomena. Most seismic processors tune and image by enhancing seismic reflection data, and do not deliberate the diffracted waves present in the processed data, which carry most of the information regarding minor yet important subsurface events (Bashir et al. 2017a, b). Such small-scale subsurface events (such as faults, fractures, channels, karsts and edges of salt bodies) present themselves in seismic data as diffracted waves, which can be captured during reservoir production as fluid flow and as fluid presence in well production (Kozlov et al. 2004; Landa and Keydar 1998).

The plane-wave destruction (PWD) filter was initially introduced by Claerbout (1992) for the characterisation of seismic images using the superposition of local plane waves. This PWD filter was based on the plane-wave differential equation, after the original plane-wave destruction filter with the same approximation was found to exhibit poor performance when applied to spatially aliased data in comparison with frequency–distance (F–X) prediction-error filters (Spitz 1991). In contrast, the dip frequency filtering approach is applied in the f–k domain. Here we employ the Fourier transform to convert data from the time to the frequency domain, with a filter then designed that can eliminate reflections based on wave cycles per kilometre.

In the presented paper, we develop a workflow with which to capture these small-scale events through diffractions separated on the basis of the smoothness and continuity of the local event slope that corresponds to the reflection event. We compare the two different techniques of dip frequency filtering and plane-wave destruction filtering, before integrating the two approaches and performing comparative analysis regarding the optimum preservation of diffractions.

Diffraction imaging and resolution

Diffraction imaging and resolution have a direct relationship with each other, while the frequency of the seismic wave also affects the final seismic image, with a high frequency providing a high-resolution image. The relationship between the seismic wave frequency and penetration, resolution, wavelength and diffraction hyperbolic curve is presented in Table 1 (Bashir et al. 2016, 2017a, b).

Seismic data resolution is typically around $\lambda/4$, which means that high frequency waves illuminate a small object; however, as increasing the frequency will also have an effect on the depth of penetration, it is generally defined according to the research objective. Seismic studies usually use lower frequencies for subsurface imaging. As a result, seismic images have a slightly lower resolution ($\lambda/4$ to $\lambda/8$ depend on the data quality) but deeper penetration (10's of kilometres) than those produced via biomedical imaging, which require a lower depth of penetration (in feet) but higher resolution ($\lambda/200$ depends on acquired frequency of data) (Table 2).

Diffraction imaging in depth and time

Although numerous studies have been carried out regarding diffractions based on both the depth and time domains, the latter does not provide an exact indication of the discontinuity of the subsurface feature examined in the present work. In the depth domain, the existence of diffraction is a frequent indicator of strong complexity and a powerfully inhomogeneous trend (Berkovitch et al. 2009). As a consequence, pre stack depth imaging methods are more labour- and computation-intensive than those involving time imaging (Moser and Howard 2008). In addition, the success of identifying and isolating diffraction in the depth domain depends on the accuracy of the velocity model employed to provide the full-wave depth image.

Multi-focusing diffraction imaging (MFDI) is a new move-out time correction technique that effectively describes diffraction events, with the ideal summation of the diffracted events and the attenuation of specular reflections enabling the creation of an image comprising mostly diffraction energy. The time correction, which is based on the multi-focusing method, depends on two parameters, the emergent angle and radius of the curvature of the diffracted wavefront. The above parameters are calculated from the pre-stack seismic traces (Berkovitch et al. 2009). The outcome of MFDI is thus a full-azimuth high-resolution seismic image that contains optimally stacked diffraction events. The diffraction section contains important data regarding local heterogeneities and discontinuities in the subsurface geology, which can be used to enhance horizontal drilling and establish the optimum location of exploration wells.

The multi-focusing diffraction imaging method helps to:

- Identify naturally fractured reservoirs.
- Avoid possible unwanted fluid pathways.
- Map sources of velocity anisotropy.
- Contour faults and salt bodies.

Table 1 Relationship between seismic wave frequency and other parameters

High frequency	Low frequency
Lower depth of penetration	Higher depth of penetration
High resolution	Low resolution
Small wavelength	Large wavelength
Lower diffraction response	Higher diffraction response

Table 2 Seismic acquisition parameters used for synthetic seismic data acquisition

Acquisition parameters	
X	1000 m
Z	2000 m
Source distance (dxs)	10 m
Receiver distance (dxr)	10 m
Dt	2 ms
No. of sources	1001
Frequency	50 Hz
Sampling interval	2 ms

Methods

Geological model building

A geological model was developed based on one of the producing fields in the Malay Basin. The model contains four superimposed layers of different velocity/density, with major faulting due to uplifting of the sublayers during tectonic activity. Synthetic seismic data were obtained using the finite difference wave equation modelling technique as described in the following section. A zero-offset recording survey design was chosen for the finite difference modelling and the parameters optimised for data quality as follows:

Finite difference modelling

Finite difference methods (FDM) are widely used in seismic modelling and migration. In the present paper, a conventional FDM was used for modelling, with the model input being velocity and density values, and model output the seismic data. Finite difference methods (FDM) are numerical methods for solving differential equation by approximating them with difference equations, in which finite difference approximate the derivatives. In the seismic wave modelling, FD methods are used to propagate the wave into the subsurface. This method has no dip limitations and produces all the events associated with the wave equation such as multiple reflections, head waves and when the elastic wave equation is used, anisotropic effects and model conversion of the data (Gray et al. 2001). Therefore, F-D wave equation modelling is the ideal way to produce the seismic synthetic data. Although, the ultimate goal of the migration is to get the image of the real earth using the seismic data, which is difficult to test the accuracy of the migration methods with the desired results. In the case of seismic inversion, the input comprises the traces and the output the structural image. For this purpose, the quantities below must be calculated (Bleistein 1986):

$\emptyset$ Propagation angle
τ Travel time
β Incident angle from source or receiver
$\partial\beta/\partial x$ Geometrical spreading parameter

For each source or receiver, the above quantities must satisfy the equations (Bleistein 1986) in "Appendix".

Dip frequency filtering (DFF)

The wavelength to frequency equation can be defined as

$$f = \frac{v}{\lambda}, \tag{1}$$

where f is the frequency, v is the velocity and λ is the wavelength.

The wave number is the total number of complete wave cycles and is related to the wavelength as follows:

$$k = \frac{1}{\lambda}, \tag{2}$$

As reflection seismology is concerned with both reflection and diffraction phenomena, in the present research work we developed an algorithm using frequency filtering in the f–k domain to achieve our objective (Dell et al. 2017). The workflow proceeds as follows:

1. Input stack data.
2. Apply Fourier transform to observe the spectrum.
3. Develop the filter on the basis of the reflector dip in the (dt/dx) plane.
4. Carry out frequency filtering to remove the horizontal reflectors depending on the slope.
5. Apply inverse Fourier transforms to move the results back into the seismic diffraction section.

This workflow is a complete procedure that can separate diffraction and reflection in stack seismic data. Depending on the dip filtering, one can separate either the reflection or diffraction sections. However, in the present paper we separate the diffraction section only, as our objective was to study diffraction phenomena to detect faults and fractures with high dip angles in complex geological conditions, thereby improving imaging results.

Plane-wave destructors (PWD)

The plane-wave destruction filter is originated from the local plane-wave model for characterizing the seismic data. This filter works in time domain (T–X) such as time–distance and can be extended to the frequency domain. The PWD is constructed with the help of an implicit finite-difference scheme for the local plane-wave equation as described (Fomel 2002).

For the characterisation of several plane waves, it is possible to cascade several filters similar to that of the following equation:

$$A(Z_x) = \left(1 - \frac{Z_x}{Z_1}\right)\left(1 - \frac{Z_x}{Z_2}\right)\ldots\left(1 - \frac{Z_x}{Z_N}\right), \tag{3}$$

where Z_1, Z_2,…, Z_N are the zeroes of the polynomial. The Taylor series method (equating the coefficients of the Taylor series expansion about the zero frequency) yields the expression

$$B_3(Z_t) = \frac{(1-\sigma)(2-\sigma)}{12} Z_t^{-1} + \frac{(2+\sigma)(2-\sigma)}{6} + \frac{(1+\sigma)(2+\sigma)}{12} Z_t. \tag{4}$$

For a three-point centred filter B_3 (Z_t)

$$B_5(Z_t) = \frac{(1-\sigma)(2-\sigma)(3-\sigma)(4-\sigma)}{1680} Z_t^{-2} + \frac{(4-\sigma)(2-\sigma)(3-\sigma)(4+\sigma)}{420} Z_t^{-1} + \frac{(4-\sigma)(3-\sigma)(3+\sigma)(4+\sigma)}{280} + \frac{(4-\sigma)(2+\sigma)(3+\sigma)(4+\sigma)}{420} Z_t + \frac{(1+\sigma)(2+\sigma)(3+\sigma)(4+\sigma)}{1680} Z_t^2. \tag{5}$$

For a five-point centred filter B_5 (Z_t), the derivation of Eqs. (4) and (5) can be found in Fomel (2002).

The filter used in the present work is a modified version of filter A (Z_t, Z_x):

$$C(Z_t, Z_x) = A(Z_t, Z_x)B\left(\frac{1}{Z_t}\right) = B\left(\frac{1}{Z_t}\right) - Z_x B(Z_t) \quad (6)$$

This filter avoids the requirement of a polynomial partition. In the case of the three-point filter Eq. (4) and the 2-D filter Eq. (5), there are six coefficients comprised of two columns; in each column there are three coefficients and the second column is a reverse copy of the first.

Slope estimation

Slope estimation is a necessary step in applying the finite-difference plane-wave filters to real data (Fomel 2000), although estimating different dual slopes, σ_1 and σ_2, in the available data is more complicated than estimating a single slope (Fomel 2002).

The regularisation condition should thus be applied to both $\Delta\sigma_1$ and $\Delta\sigma_2$ as follows:

$$\varepsilon D\Delta\sigma_1 \approx 0, \quad (7)$$

$$\varepsilon D\Delta\sigma_2 \approx 0. \quad (8)$$

The above equations' solutions are dependent on the initial values of slope 1 and slope 2, which should not be equal, but can be extended to the number equation with respect to the data set grid number. However, this equation is here used to calculate the slopes for the given data set.

In the present study we used a modified and improved version of the plane-wave destruction method for the separation of the seismic diffractions based on Claerbout (1992). Figure 3 shows the generalized workflow of the diffraction separation used in this paper.

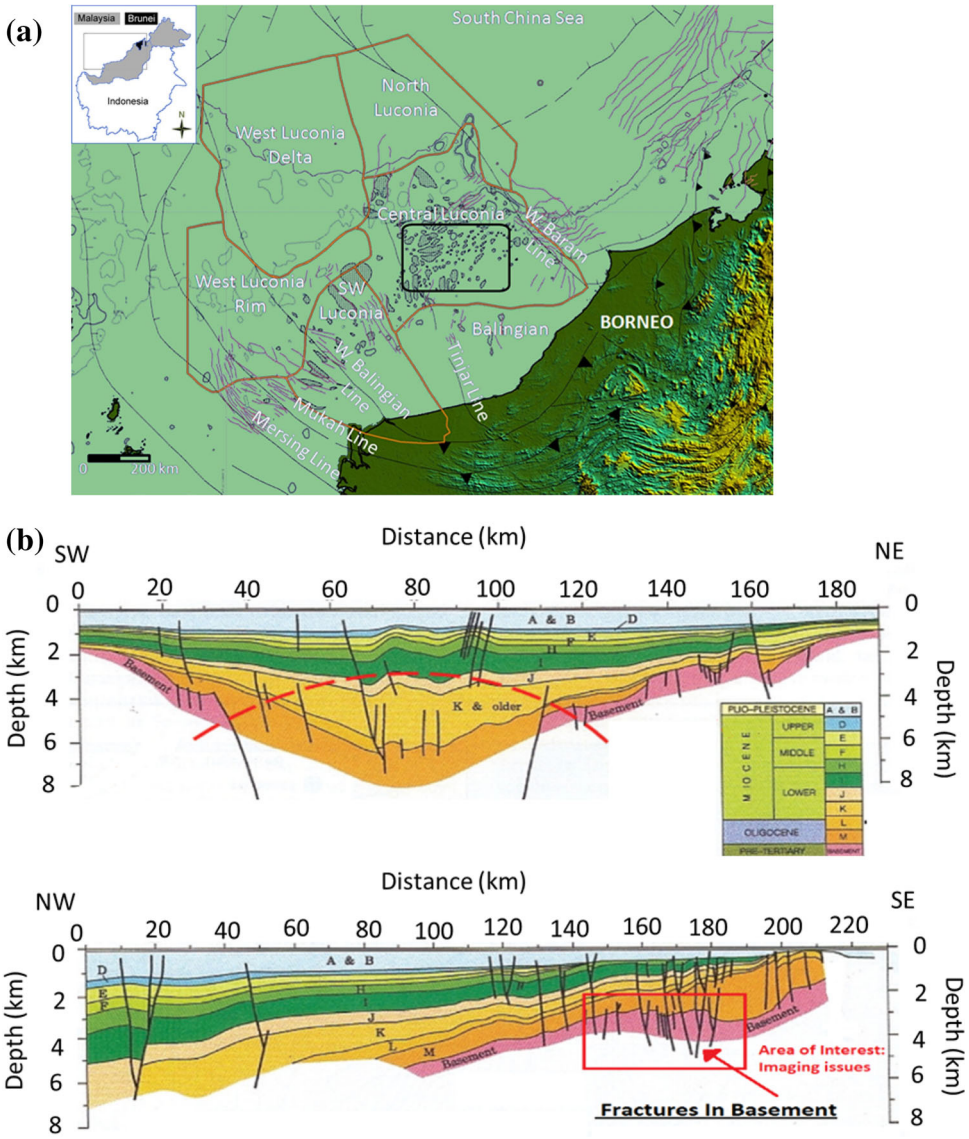

Fig. 1 **a** Geographical representation of the Malaysian Basin (Janjuhah et al. 2017) and **b** Malay Basin subsurface structure with cross-section view. Fractured basement can be seen at a depth of 2–5 km, varying with lateral extension (Ghosh et al. 2010)

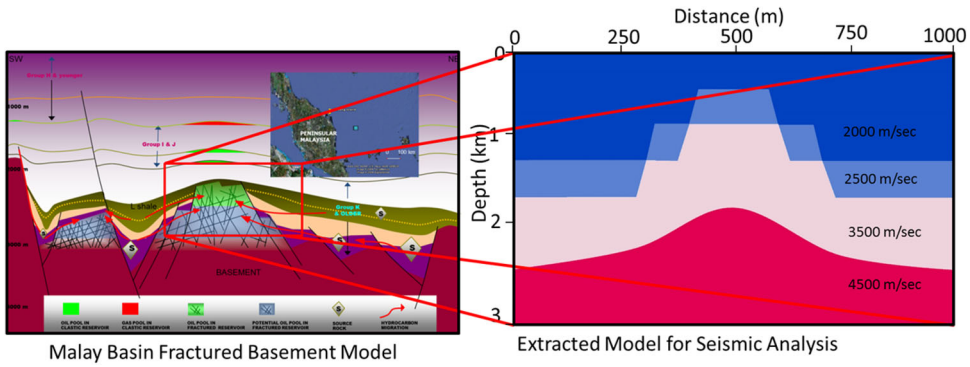

Fig. 2 **a** Geological model of the Malay Basin field (Kadir, 2010) and **b** extracted velocity model with highly dipping faults

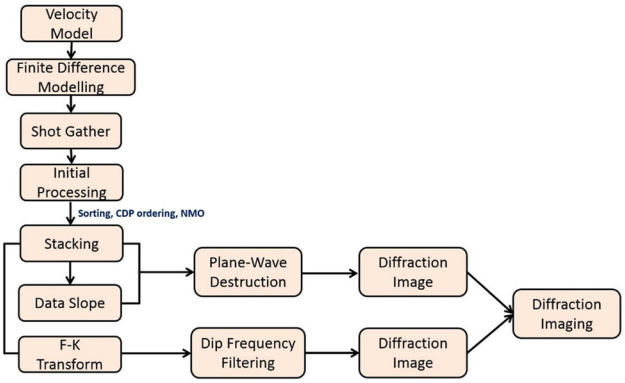

Fig. 3 Generalised workflow

Results and discussions

The first example is shown in Fig. 4, which displays results based on the Malay Basin fracture model shown earlier in Fig. 2 (Yasir et al. 2016). The highly dipping faults present in the basin are associated with typical illumination problems in reflection data imaging. First, an attempt was made to remove the reflection of reflectors 1, 2 and 3 as shown in Fig. 4a. Since the dip (dt/dx) of the wave is near to zero in the t–x plane, we designed a filter that could remove the energy from zero dip in the f–k plane (Fig. 3).

The workflow described above in the methodology section in this case involved a double Fourier transform in the t and x directions to create the f–k spectrum shown in Fig. 4b.

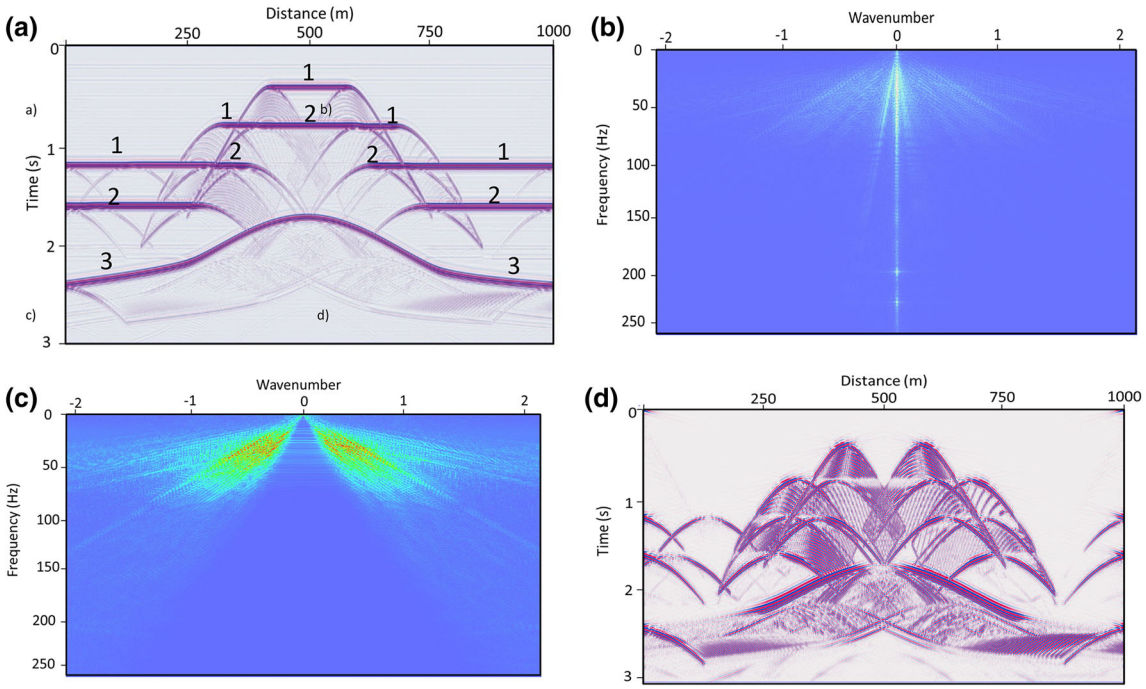

Fig. 4 Steps involved in diffraction preservation carried out via dip frequency filtering (DFF): **a** zero-offset section containing a set of faults, with the numbers indicating the different layers; **b** f–k spectrum of the seismic data, showing the horizontal reflection energy at minimum wave number; **c** after filtering the wave frequency of reflectors 1, 2 and 3, diffraction energy is distributed and enhanced; and **d** separated seismic diffraction section after dip frequency filtering

In the displayed spectrum, one can observe that reflectors 1, 2 and 3 are all located around zero in the t–x plane.

Figure 4c shows the f–k spectrum after applying the filter on the basis of slopes that are not quantified, while Fig. 4d displays the output obtained after filtering data, showing the diffraction section only.

The accuracy of the plane-wave destruction method introduced by Claerbout depends on slope identification and the texture display used to quickly assess fault surfaces. Figure 5a displays the zero-offset section of the model data after finite difference modelling. Diffractions are caused by the irregular fault boundaries and are preserved in the section. The calculation of slopes in the data was performed using the slope estimation method, with the results shown in Fig. 5b. The corresponding texture display providing an indication of surface discontinuities is elaborated in Fig. 5c. These texture plots permit us to access the ability of the destruction filters to characterize the main locally plane features in the given data. Finally, Fig. 5d displays the separated diffraction response obtained after the implementation of PWD and suppression of the reflected seismic data.

Synthetic data comparison: faulted model

Before application of the proposed algorithm on real field data we have tested on the synthetic data, which is discussed in this section. Figure 6a, b shows the separated diffraction sections produced using the DFF and PWD methods, respectively, with the red arrows indicating the reflections suppressed from the given data. Although both filtering techniques are able to eliminate upper straight reflection, analysis of the flanks below the anticline reveals that DFF eliminated those reflections that did not originally belong to the diffraction data. In contrast, the PWD filtering technique is able to remove these reflections but preserve the diffractions, with this method based on the slope estimation of the given data as shown in Fig. 5b.

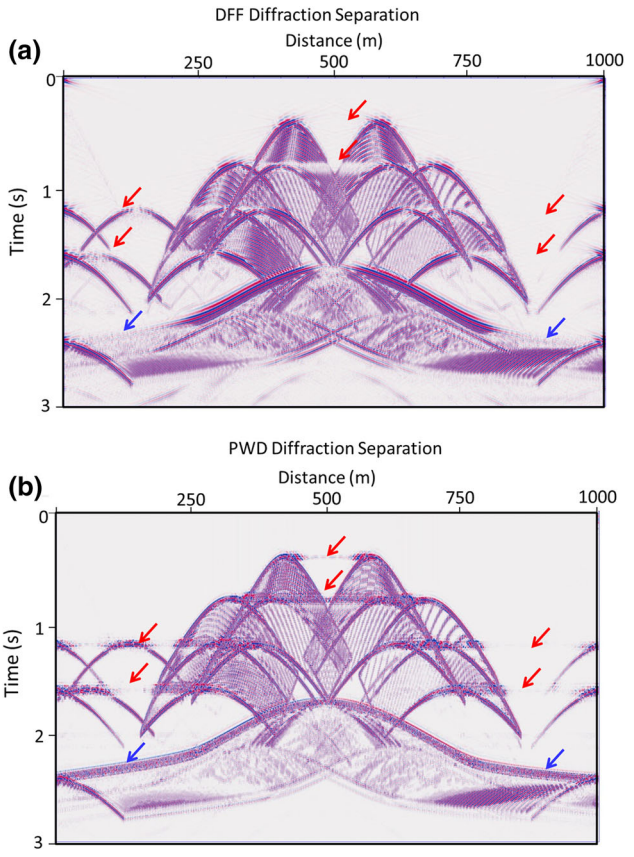

Fig. 6 Comparison of the two different methods used for diffraction preservation: **a** dip frequency filtering in the f–k domain (DFF), **b** plane-wave destruction filtering (PWD)

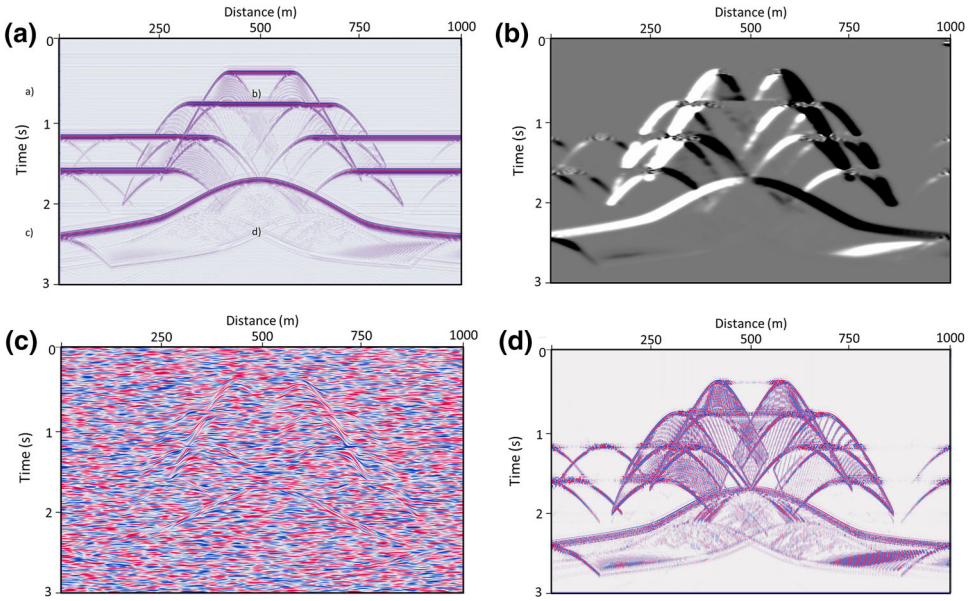

Fig. 5 Application of diffraction separation to the fracture model: **a** input zero-offset seismic data; **b** estimated corresponding dip of faults and fracture; **c** corresponding texture display highlighting the locations of probable local plane waves; and **d** separated diffraction response obtained using the plane-wave destruction method

2D synthetic data example: the Complex Marmousi Model

The proposed approach was then extended to a complex data set comprising the 2D synthetic Marmousi model in order to separate diffractions and carry out imaging for the delineation of faults and subsurface structure. Figure 7a shows the model input obtained using the finite difference modelling (FDM) technique, with 3 of the synthetic shot-gathered data calculated as shown in Fig. 7b. Initial processing was performed to the data in order to improve the signal to noise ratio, involving sorting, NMO correction, and stacking, etc. Figure 7c displays the stack section of the Marmousi data set, while Fig. 7d shows the estimated slope of the diffraction section, illustrating the positive to the negative slope of the data. Figure 7e shows the corresponding texture (Claerbout and Brown 1999) display of the convolved field numbers, with the inverse of the plane-wave destruction filters applied to obtain the texture display to show the discontinuities. Application of the plane-wave destruction is applied to the stack data to preserve the diffractions which are shown in Fig. 7f.

Figure 8a, b shows the separated diffractions obtained via the DFF and PWD methods, respectively. Analysis of the highlighted red circles above 0.5 s vertical time reveals that the DFF results contain planer waves along with the preserved diffractions at time 0.5 s, and that the PWD method eliminated all local planer waves efficiently and preserved only the diffractions. The latter results thus reflect the major slopes in the data, with three major faults interpreted in the slope section (Fig. 9). A frequency spectrum comparison between two proposed method is plotted (Fig. 10), as PWD preserves the lower and higher frequencies rather than DFF.

Real seismic data example from the Malaysian (Sarawak) Basin

Seismic pre-migrated offset gather was provided for this project. Initial processing, including sorting from offset

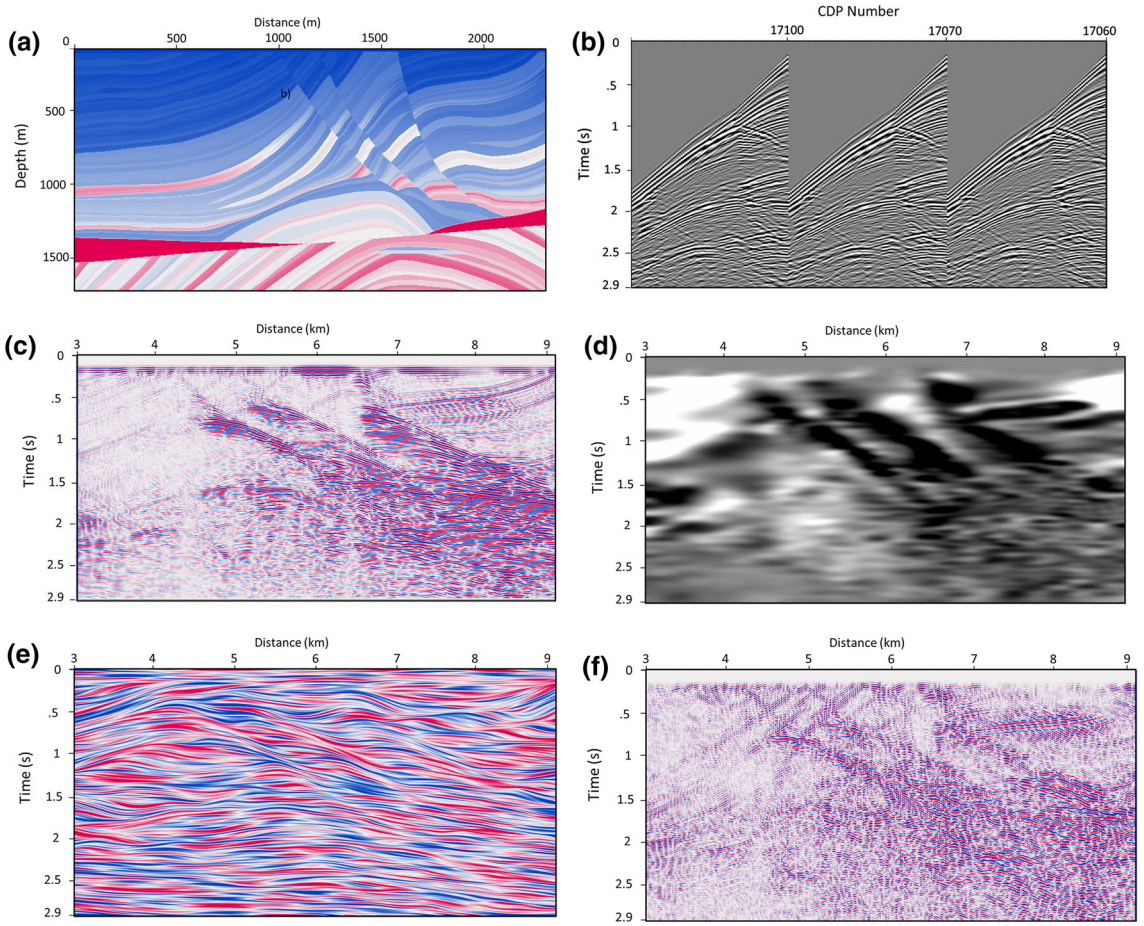

Fig. 7 Finite difference modelling of shot-gathered data for seismic analysis and diffraction separation: **a** the complex Marmousi velocity model; **b** shot-gathered data after finite difference modelling; **c** stacked data after sorting, CDP ordering and NMO correction; **d** dip component of the modelled data after corresponding estimation; **e** texture display of input data for local plane estimation; and **f** separated diffraction after plane-wave destruction filtering

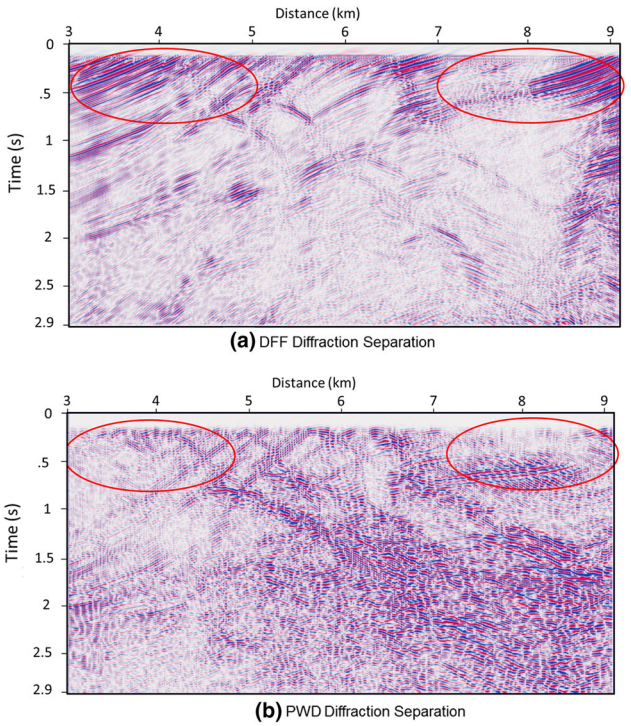

Fig. 8 Comparison of the two different approaches used for diffraction preservation: **a** dip frequency filtering (DFF) in the *f*–*k* domain, and **b** plane-wave destruction (PWD)

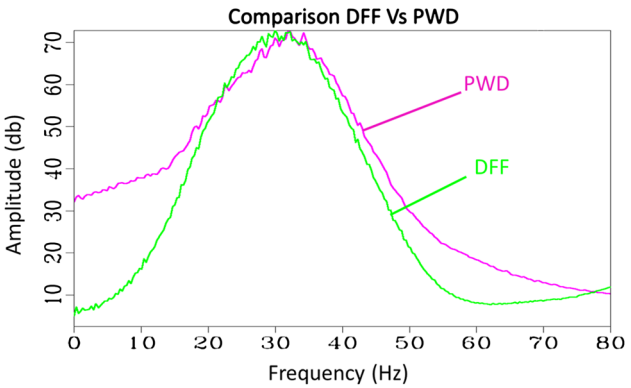

Fig. 9 Frequency spectrum of the separated diffraction data, and enhancement of the amplitude is shown to form 0–10 Hz frequency as well as 50–70 Hz frequency energy has been improved

gather to CMP, was then performed in order to obtain the stack seismic section. Figure 10a shows the offset gather data provided, with the following procedure adopted for sorting purposes:

1. Select a window around the structure with the maximum diffraction response.
2. Extract the inline and crossline for the 3D data to obtain a single 2D line.
3. The inline was constant over the full length; 810 traces were extracted from the crossline.

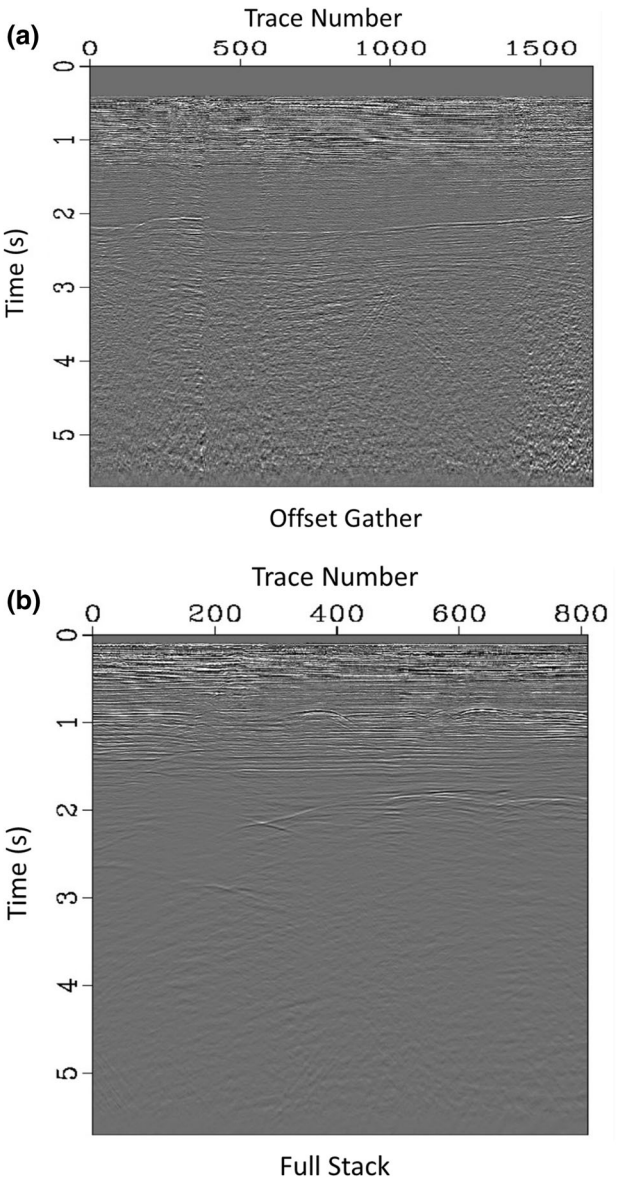

Fig. 10 Input real seismic data from Malaysian Basin. **a** Offset gather data and **b** stack data before migration: Sarawak Basin, carbonate build-up structure

4. Perform NMO correction and velocity analysis.
5. Perform offset dependent diffraction enhancement analysis.
6. Stack the data for diffraction analysis in the full stack data set.
7. Estimate dip components from the data using Eqs. (5) and (6).
8. Remove the reflections and preserve the diffractions via PWD filtering.

Figure 10b shows 2D stacked pre-migrated seismic data from the Sarawak Basin carbonate field (Bashir et al. 2018). The diffraction separation method was then extended to

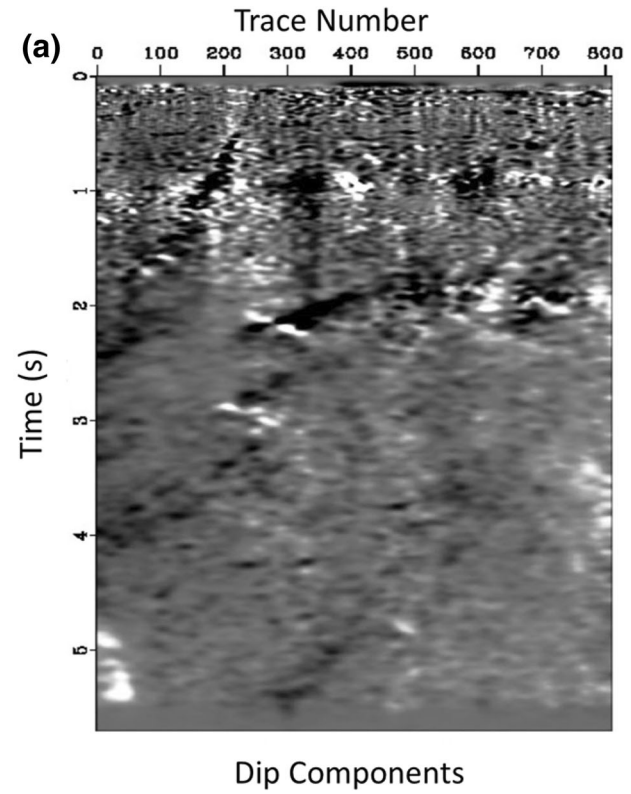

Fig. 11 **a** Estimated dip field of data shown in Fig. 10, **b** texture computed by convolving field number with the inverse of plane-wave destruction filters

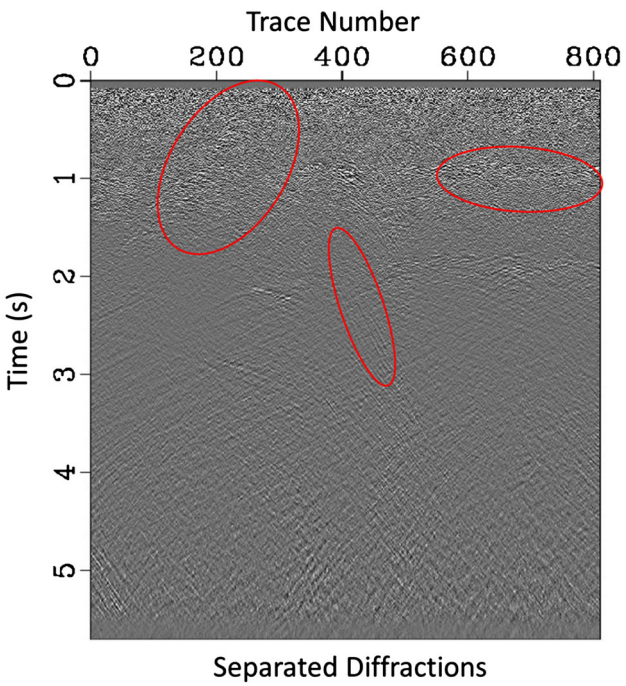

Fig. 12 Preserved diffractions after plane-wave destruction of zero-offset data. Red circle shows the a series of preserved diffraction response

preserve the diffractions in the real data. Figure 10a shows the estimated dip components of the data, which help to identify the dipping faults and pinch outs, while Fig. 11b shows the corresponding texture (Claerbout and Brown 1999) obtained by convolving a field of random numbers with the inverse of the plane-wave destruction filters, the latter constructed using helical filtering techniques (Claerbout 1998; Fomel and Claerbout 2003). The advantage of this type of texture display is that the user can visualise local plane features in the data, with the dip field then calculated via the linearization method outlined in the previous section. As use of seismic diffraction to complement the seismic reflection is essential for small-scale features in the seismic data. Figure 12 shows the separated diffraction data using proposed PWD diffraction separation algorithm. In the red circle the preserved series of diffractions can be observed that shows the continuity of the fault and highly dipping feature in the subsurface. Further, the stacking of these diffractions with the accurate velocity provides a better interpretation of these features to the interpreter.

Conclusions

In this paper we have presented and developed two studies of diffraction preservation in seismic data with the aim of helping to improve imaging results, especially for fractures and small-scale discontinuities. The proposed method is

illustrated through examples of different data sets: two synthetic (one simple and one complex) and one real data set from the Malaysian Basin. For both methods we assume accurate filtering was carried out during the processing of the seismic data that was sufficient to enable optimally focused full-wave post stack diffraction separation. The plane-wave destruction filtering and dip frequency filtering methods are powerful tools with which to separate diffraction events from reflection seismic data. However, dip frequency filtering suffers from a lack of separation in the case of complex structures, such as dipping reflectors, unconformities and anticlinal structures. As a result, filtering and separation of diffractions based on DFF can cause the removal of reflections by considering them as diffractions. In contrast, plane-wave destruction filtering is more robust in separating diffractions for both simple and complex geologies. PWD is able to handle the horizontal, inclined and curved features of seismic data more effectively, while its preservation of diffractions is precise due to accurate slope estimation. A frequency spectrum of the both separated diffraction data demonstrates the improvement in energy from 0–10 Hz as well as 50–70 Hz. Experiments were initially performed on synthetic data, with the results satisfying the predefined requirements; further testing of the algorithm was then applied to real production data, successfully confirming the accuracy of the method. The produced diffraction images can be a great help in the interpretation of structural features, such as small-scale faults, pinch-outs and carbonate build-up structures.

Although the above methods were successfully carried out based on finite difference synthetic modelling, we did not investigate the effect of diffraction in low signal-to-noise ratios in pre-stack data. Testing of the proposed algorithm is also in progress for low-rank modelling, in which a high signal-to-noise ratio of the full-wave effect with frequency variation will be explained for both pre-stack and post-stack imaging conditions.

Acknowledgements We are thankful to Universiti Teknologi PETRONAS (UTP), Geoscience department and the Centre of Seismic Imaging (CSI) for providing the facilities for this research. In this work, we have used Seismic Unix from CSM and Madagascar.We would like to thanks Sergey Fomel and Luke Decker from University of Texas at Austin's and Texas Consortium for Computational Seismology for their valuable suggestions which really help me to progress my research, and esteem thanks goes to reviewers of Acta Geophysica for their suggestions and comments to improve the manuscript for publication.

Appendix

$$\left(\frac{\partial\tau}{\partial x}\right)^2+\left(\frac{\mathrm{d}\tau}{\mathrm{d}x}\right)^2=\frac{1}{v^2(x,z)}, \tag{9}$$

$$\sin\emptyset=v\frac{\mathrm{d}\tau}{\mathrm{d}x}, \tag{10}$$

$$\frac{\partial\sigma}{\partial x}\frac{\partial\tau}{\partial x}+\frac{\partial\sigma}{\partial z}\frac{\partial\tau}{\partial z}=1, \tag{11}$$

$$\frac{\partial\beta}{\partial x}\frac{\partial\tau}{\partial x}+\frac{\partial\beta}{\partial z}\frac{\partial\tau}{\partial z}=1, \tag{12}$$

$$\frac{\partial}{\partial z}\left(\frac{\partial\beta}{\partial x}\right)+\frac{\partial}{\partial x}\left[\mu(x,z)\frac{\partial\beta}{\partial x}\right]=0, \tag{13}$$

where $v(x, z)$ is the velocity and

$$\mu(x,z)=\frac{\partial\tau}{\partial x}\left[\frac{\partial\tau}{\partial z}\right]^{-1}.$$

Equation (9) is the eikonal equation, Eqs. (11) and (12) are derived from Pusey and Vidale (1991) and Eq. (13) follows from Eq. (11).

References

Bashir Y, Ghosh DP, Alashloo SYM, Sum CW (2016) Effect of frequency and migration aperture on seismic diffraction imaging. In: IOP conference series: earth and environmental science. IOP Publishing, p. 12001

Bashir Y, Ghosh D, Sum C (2017a) Preservation of seismic diffraction to enhance the resolution of seismic data. In: SEG Technical Program Expanded Abstracts 2017. Society of Exploration Geophysicists, pp. 1038–1043

Bashir Y, Ghosh DP, Sum CW (2017b) Diffraction amplitude for fractures imaging & hydrocarbon prediction. J Appl Geol Geophys 5:50–59

Bashir Y, Ghosh DP, Weng Sum C, Janjuhah HT (2018) Diffraction enhancement through pre-image processing: applications to field data, Sarawak Basin, East Malaysia. Geosciences 8:74

Berkovitch A, Belfer I, Hassin Y, Landa E (2009) Diffraction imaging by multifocusing. Geophysics 74:WCA75–WCA81

Berryhill JR (1977) Diffraction response for nonzero separation of source and receiver. Geophysics 42:1158–1176. https://doi.org/10.1190/1.1440781

Bleistein N (1986) Two- and-one-half dimensional in-plane wave propagation*. Geophys Prospect 34:686–703. https://doi.org/10.1111/j.1365-2478.1986.tb00488.x

Claerbout JF (1992) Earth soundings analysis: processing versus inversion, vol 6. Blackwell Scientific Publications, London

Claerbout J (1998) Multidimensional recursive filters via a helix. Geophysics 63:1532–1541

Claerbout J, Brown M (1999) Two-dimensional textures and prediction-error filters. In: 61st EAGE conference and exhibition

Decker L, Klokov A, Fomel S (2013) Comparison of seismic diffraction imaging techniques: Plane wave destruction versus

apex destruction. In: SEG technical program expanded abstracts 2013. Society of exploration geophysicists, pp. 4054–4059
Dell S, Gajewski D (2011) Common-reflection-surface-based workflow for diffraction imaging. Geophysics 76:S187–S195
Dell S, Abakumov I, Kashtan B, Gajewski D (2017) Utilizing diffractions in full-wave inversion for a detailed model building. In: SEG technical program expanded abstracts 2017. Society of exploration geophysicists, pp. 1033–1037
Fomel S (2000) Three-dimensional seismic data regularization (Doctoral dissertation, Stanford University)
Fomel S (2002) Applications of plane-wave destruction filters. Geophysics 67:1946–1960
Fomel S, Claerbout JF (2003) Multidimensional recursive filter preconditioning in geophysical estimation problems. Geophysics 68:577–588
Ghosh D, Halim MFA, Brewer M, Viratno B, Darman N (2010) Geophysical issues and challenges in Malay and adjacent basins from an E & P perspective. The Leading Edge 29(4):436–449
Gray SH, Etgen J, Dellinger J, Whitmore D (2001) Seismic migration problems and solutions. Geophysics 66(5):1622–1640
Janjuhah HT, Gamez Vintaned JA, Salim AMA, Faye I, Shah MM, Ghosh DP (2017) Microfacies and depositional environments of miocene isolated carbonate platforms from Central Luconia, Offshore Sarawak, Malaysia. Acta Geol Sin 91:1778–1796 **(English Ed.)**
Kadir MB (2010) Fractured basement exploration case study in Malay Basin. In: PGCE 2010
Khaidukov V, Landa E, Moser TJ (2004) Diffraction imaging by focusing-defocusing: an outlook on seismic superresolution. Geophysics 69:1478–1490
Klokov A, Fomel S (2013) Seismic diffraction imaging, one migration dip at a time. In: SEG technical program expanded abstracts 2013. Society of exploration geophysicists, pp. 3697–3702
Kozlov E, Barasky N, Korolev E, Antonenko A, Koshchuk E (2004) Imaging scattering objects masked by specular reflections. In: SEG technical program expanded abstracts 2004. Society of exploration geophysicists, pp. 1131–1134
Krey T (1952) The significance of diffraction in the investigation of faults. Geophysics 17:843–858
Landa E, Keydar S (1998) Seismic monitoring of diffraction images for detection of local heterogeneities. Geophysics 63:1093–1100
Madon MH (1999) Malay basin. Petronas: The Petroleum Geology and Resources of Malaysia
Madon M, Kim CL, Wong R (2013) The structure and stratigraphy of deepwater Sarawak, Malaysia: implications for tectonic evolution. J Asian Earth Sci 76:312–333
Moser TJ, Howard CB (2008) Diffraction imaging in depth. Geophys Prospect 56:627–641
Pusey LC, Vidale JE (1991) Accurate finite-difference calculation of WKBJ travel times and amplitudes. In: SEG technical program expanded abstracts 1991. Society of exploration geophysicists, pp. 1513–1516
Schwarz B, Gajewski D (2017) Accessing the diffracted wavefield by coherent subtraction. Geophys J Int 211:45–49
Spitz S (1991) Seismic trace interpolation in the FX domain. Geophysics 56:785–794
Yasir B, Ghosh DP, Moussavi Alashloo SY, Sum CW (2016) Seismic modeling and imaging using wave theory for fault and fracture identification. In: Offshore technology conference Asia. Offshore technology conference

Acta Geophysica (2018) 66:317–318
https://doi.org/10.1007/s11600-018-0144-z

REVIEW ARTICLE - SPECIAL ISSUE

Introduction to the special issue on "hydro-meteorological time series analysis and their relation to climate change"

Javier Estévez[1] · Amanda García Marín[1] · Julián Báez Benitez[2] · M. Carmen Casas Castillo[3] · Luciano Telesca[4]

Received: 28 March 2018 / Accepted: 10 April 2018 / Published online: 16 April 2018

Observed changes in the climate system are unequivocal: atmosphere and ocean warming, sea level rising, amounts of snow and ice diminution and extreme weather events increasing are some examples (IPCC 2014). The impact of these phenomena on eco-hydrological processes is being studied all over the world (Tahir et al. 2011; Willems and Vrac 2011; Ficklin et al. 2016; Wu et al. 2016). Under this context, the study of hydro-meteorological time series is crucial to understand and characterize the behaviour of important variables such as rainfall and its related patterns and consequences (droughts and floods episodes), river flow, temperature, etc. Recent works show that small changes in temperature, precipitation and snow can have a large impact at the basin scale, being these variables the most affected by climate change (Wang et al. 2014; Zarenistanak et al. 2014; Faiz et al. 2017).

Considering the need to deeply know the evolution of hydrological series, it is important to note that water scarcity is one of the most significant challenges that society has to face today and in the coming years, being the key resource for socio-economic development and the natural ecosystems sustainability (Machiwal and Jha 2012). Due to unbridled urbanization and industrialization and the global growth of the population, the water demand is progressively growing in different locations around the world (UNESCO 2009; Grafton and Hussey 2011).

With the idea of modelling climate behaviour and forecasting more accurately certain meteorological variables, the use of different techniques can be found in the scientific literature. In this sense, many methods can be applied to detect trends and break points, to obtain scale properties and other characterization parameters. From the identification of significant cyclical components of solar irradiance and temperature (Boland 1995) using Fourier transform (spectral analysis) to the detection of long-range correlations in nonstationary hydro-meteorological time series using multifractal approach (Kalamaras et al. 2017; Krzyszczak et al. 2017), numerous techniques have been used to describe in detail the relevant natural processes. They range from the classical deterministic models such as Box–Jenkins approach or ARIMA to the most current ones using Artificial Neural Networks, Wavelet analysis, Support Vector Machine or Genetic Algorithms (Bărbulescu 2016).

To guarantee the reliability of the results obtained from time series analysis, it is necessary to work with validated data sets. Thus, different quality control procedures should be previously applied to hydro-meteorological series, identifying incorrect values, gaps or inconsistent records (Estévez et al. 2011; Fiebrich et al. 2010; López-Lineros et al. 2014).

Since hydro-meteorological variables exhibit a widely different behaviour in time and space, a detailed analysis of historical data series in different places of the world is needed. It is then a challenge for scientists to be able to understand how climate change is affecting hydro-meteorological datasets or vice versa, how the different behaviour of these variables can impact on the actual and future climate. This special issue aims at contributing to the understanding of such relationship, providing the most recent results in the analysis of time series of temperature, rainfall, drought, river flow, recorded worldwide and investigated with various statistical methods to disclose deep dynamical climate-linked properties and patterns.

✉ Luciano Telesca
luciano.telesca@imaa.cnr.it

[1] University of Cordoba, Córdoba, Spain

[2] Catholic University of Asuncion, Asunción, Paraguay

[3] Universitat Politècnica de Catalunya, Barcelona, Spain

[4] Institute of Methodologies for Environmental Analysis, National Research Council of Italy, Tito, Italy

References

Bărbulescu A (2016) Mathematical methods applied for hydro-meteorological time series modeling. In: Studies on time series applications in environmental sciences. Intelligent systems reference library, vol 103. Springer, Cham

Boland J (1995) Time-series analysis of climatic variables. Sol Energy 55(5):377–388

Estévez J, Gavilán P, Giráldez JV (2011) Guidelines on validation procedures for meteorological data from automatic weather stations. J Hydrol 402:144–154

Faiz MA, Liu D, Fu Q, Qamar MU, Dong S, Khan MI, Li T (2017) Complexity and trends analysis of hydrometeorological time series for a river streamflow: a case study of Songhua River Basin, China. River Res Appl 34:101–111

Ficklin DL, Robeson SM, Knouft JH (2016) Impacts of recent climate change on trends in baseflow and stormflow in United States watersheds. Geophys Res Lett 43:5079–5088

Fiebrich CA, Morgan CR, McCmbs AG, Hall-Jr PK, McPherson RA (2010) Quality assurance procedures for mesoscale meteorological data. J Atmos Ocean Technol 27:1565–1582

Grafton RQ, Hussey K (eds) (2011) Water resources planning and management. Cambridge University Press, Cambridge, p 777

IPCC (2014) Climate Change 2014: Synthesis Report. In: Core Writing Team, Pachauri RK, Meyer LA (eds) Contribution of Working Groups I, II and III to the Fifth Assessment Report of the Intergovernmental Panel on Climate Change. IPCC, Geneva, Switzerland

Kalamaras N, Philippopoulos K, Deligiorgi D, Tzanis CG, Karvounis G (2017) Multifractal scaling properties of daily air temperature time series. Chaos Solitons Fractals 98:38–43

Krzyszczak J, Baranowski P, Zubik M, Hoffmann H (2017) Temporal scale influence on multifractal properties of agro-meteorological time series. Agric For Meteorol 239:223–235

López-Lineros M, Estévez J, Giráldez JV, Madueño A (2014) A new quality control procedure based on non-linear autoregressive neural network for validating raw river stage data. J Hydrol 510:103–109

Machiwal D, Jha MK (2012) Introduction. Hydrologic time series analysis: theory and practice. Springer, Dordrecht

Tahir AA, Chevallier P, Arnaud Y, Neppel L, Ahmad B (2011) Modeling snowmelt-runoff under climate scenarios in the Hunza River basin, Karakoram Range, Northern Pakistan. J Hydrol 409(1):104–117

UNESCO (2009) The 3rd United Nations World Water Development Report: Water in a Changing World. World Water Assessment Program. UNESCO, Paris

Wang X, Yang X, Liu T, Li F, Gao R, Duan L, Luo Y (2014) Trend and extreme occurrence of precipitation in a mid-latitude Eurasian steppe watershed at various time scales. Hydrol Process 28:5547–5560

Willems P, Vrac M (2011) Statistical precipitation downscaling for small-scale hydrological impact investigations of climate change. J Hydrol 402(3):193–205

Wu F, Wang X, Cai Y, Li C (2016) Spatiotemporal analysis of precipitation trends under climate change in the upper reach of Mekong River basin. Quat Int 392:137–146

Zarenistanak M, Dhorde AG, Kripalani RH, Dhorde AA (2014) Trends and projections of temperature, precipitation, and snow cover during snow cover-observed period over southwestern Iran. Theor Appl Climatol 122:421–440

Acta Geophysica (2018) 66:319–328
https://doi.org/10.1007/s11600-018-0128-z

RESEARCH ARTICLE - SPECIAL ISSUE

Spatio-temporal analysis of annual rainfall in Crete, Greece

Emmanouil A. Varouchakis[1] · Gerald A. Corzo[2] · George P. Karatzas[1] · Anastasia Kotsopoulou[1]

Received: 8 October 2017 / Accepted: 16 March 2018 / Published online: 31 March 2018

Abstract
Analysis of rainfall data from the island of Crete, Greece was performed to identify key hydrological years and return periods as well as to analyze the inter-annual behavior of the rainfall variability during the period 1981–2014. The rainfall spatial distribution was also examined in detail to identify vulnerable areas of the island. Data analysis using statistical tools and spectral analysis were applied to investigate and interpret the temporal course of the available rainfall data set. In addition, spatial analysis techniques were applied and compared to determine the rainfall spatial distribution on the island of Crete. The analysis presented that in contrast to Regional Climate Model estimations, rainfall rates have not decreased, while return periods vary depending on seasonality and geographic location. A small but statistical significant increasing trend was detected in the inter-annual rainfall variations as well as a significant rainfall cycle almost every 8 years. In addition, statistically significant correlation of the island's rainfall variability with the North Atlantic Oscillation is identified for the examined period. On the other hand, regression kriging method combining surface elevation as secondary information improved the estimation of the annual rainfall spatial variability on the island of Crete by 70% compared to ordinary kriging. The rainfall spatial and temporal trends on the island of Crete have variable characteristics that depend on the geographical area and on the hydrological period.

Keywords Rainfall · Spectral analysis · Geostatistics · North Atlantic Oscillation · Crete

Introduction

Reliable hydrological modeling and soil hydrology projects require accurate information on the temporal variations and spatial distribution of precipitation. Many hydrological and soil projects involve precipitation data at the local scale to calculate runoff and evapotranspiration or to predict flooding events (Grillakis et al. 2010; Kalogeropoulos and Chalkias 2013; Masih et al. 2010; Skøien and Blöschl 2007; Vozinaki et al. 2015), while there are dynamic approaches that combine surface waters, soil properties, and groundwater level to determine groundwater level variations (Bierkens et al. 2001; Knotters and Bierkens 2000; Varouchakis et al. 2016b). The accurate information of rainfall temporal and spatial behavior plays a key role in these cases. On the island of Crete, Greece such projects have been considered necessary to examine the effect of the potential forthcoming climate variations.

Investigation of the rainfall information for the island of Crete, Greece has demonstrated that the most extreme dry hydrological year (month October onwards) was 1950/1951 followed by 1989/1990, while the wettest year was 2002/2003 followed by 1977/1978. Further investigation of the data revealed important correlations between precipitation in the western and eastern parts of the island. A spatial pattern was also detected with the spatially averaged annual precipitation being significantly higher in the west than in the east. Moreover, surface elevation was determined as an important factor strongly correlated with rainfall (Koutroulis et al. 2013).

In 2003, the temporal and spatial variation of the annual rainfall on the island of Crete was presented (Naoum and Tsanis 2003) based on 30 year data. Frequency analysis of the rainfall records was used to estimate the real rainfall on the island for return periods of 2, 5, and 10 years. Most rainfall records showed a decrease in rainfall over a

✉ Emmanouil A. Varouchakis
varuhaki@mred.tuc.gr

[1] School of Environmental Engineering, Technical University of Crete, 73100 Chania, Greece

[2] IHE Institute for Water Education, Westvest 7, 2611 AX Delft, The Netherlands

30-year period with higher negative rainfall gradients at higher elevations. In addition, Regional Climate Models (RCMs) for the island of Crete determined a negative trend for annual precipitation rates on the island up to the year 2010 and also projected a decreasing behavior during the period 2010–2040 (Giorgi and Lionello 2008; Lelieveld et al. 2012).

Precipitation variability in the eastern Mediterranean and Greece has been associated with the North Atlantic Oscillation (NAO) phenomena (Eshel and Farrell 2000; Hurrell and Van Loon 1997; Nastos et al. 2013). Particularly, it was demonstrated that decadal precipitation variations at basin scale on the island of Crete (Maas and Macklin 2002) were associated with NAO. Besides, the precipitation decline over the Mediterranean region during the last decades of the past century was interpreted by the positive trend of NAO (Krichak and Alpert 2005). Strong positive phases of NAO are associated with below normal precipitation over southern and central Europe. Opposite patterns are observed during strong NAO negative phases (Drake 2014; Hertig and Jacobeit 2014).

This paper deals with the spatio-temporal analysis of annual rainfall on the island of Crete since 1981. The objectives of this work are the interpretation of the temporal variations of rainfall and the spatial analysis of the rainfall distribution. This work examines seasonality, frequency, return periods as well as geographical properties of the annual rainfall based on measurements obtained from monitoring stations. Finally, the temporal rainfall variation is examined in relation with global climatic phenomena such as North Atlantic Oscillation index.

Materials and methods

Description of the study area

The island of Crete is located in the eastern Mediterranean basin. Crete is the largest island in Greece (Fig. 1) and the fifth largest in the Mediterranean. It is located 160 km south of the Greek mainland, representing the southernmost part of the EU, and it is surrounded by numerous small islands. The total area of the island is 8335 km^2, with a length of 260 km, width ranging from 12 to 57 km, and a coastline of 1306 km. The island is characterized by rough terrain and four major mountain ranges with many common characteristics. The soil distribution rates in the plain, hilly, and mountainous areas are 22.7, 27.9, and 49.4%, respectively. The fertile parts of the island are formed at the foot of the mountainous areas and at the plains. The surface waters of Crete are determined by rainfall and topography, while another important element is the composition of the rock formations. Roughly, 45–50% of the area of Crete is covered by carbonate rocks clustered in four major mountains, which are the main water catchers. The fact that the carbonate rocks allow water flow, combined with the tectonic structures displayed on Crete (ruptures, discontinuities, etc.), leads to high rainwater infiltration rates into the aquifers (Special water secretariat of Greece 2015).

The study of precipitation patterns is very useful and has been the object of study in many disciplines. The conclusions concerning the qualitative and quantitative assessments, the identification of areas affected by drought due to their geographical position, the investigation of the existence of statistically significant trends in precipitation, and the rainfall distribution maps are some of the most significant contributions of this work. The application of statistical and geostatistical analysis was based on monthly observational data sets, provided by the Department of Water Resources Management of the Region of Crete, from 52 rainfall stations randomly distributed over the four prefectures of Crete (Fig. 1) during the 1981–2014 period.

Data from nearby stations were compared as well as with data from other nearby stations not included in the data set with shorter time series available, so that values and date of occurrence are similar. The aforementioned procedure was applied as a data quality check (Sungmin et al. 2018).

Most stations are located at altitudes between 200 and 500 m, while only six stations are located between 500 and 800 m and 11 stations at altitudes below 200 m. In the following, the two prefectures located in the western part of the island will be referred to as the western part of Crete, whereas the other two as the eastern part.

According to the Special Water Secretariat of Greece (2015), the average annual rainfall has been determined equal to 927 mm, which corresponds to 7.69 billion cubic meters of precipitation annually. More specifically, the rainfall ranges between 300 and 700 mm in low areas and areas along the coast, between 700 and 1000 mm in the plains of the mainland, and is up to 2000 mm in the mountainous areas. More than one-third of the total rainfall occurs along the northern coast of the island, where the White Mountains and Mountains Idi and Dikti are located (Fig. 1). Despite the fact that the island receives high amounts of precipitation, it was estimated that 62% is lost to evapotranspiration and 10% is lost as runoff to the sea. Thus, only 28% of the precipitation becomes groundwater recharge (Special water secretariat of Greece 2015).

The water district of Crete is divided into 91 aquifer systems. According to the recent water resources management plan (Special water secretariat of Greece 2015), 81 of these aquifer systems have considerable groundwater resources, but 10 of them have been considerably depleted as the average level has fallen below certain, locally

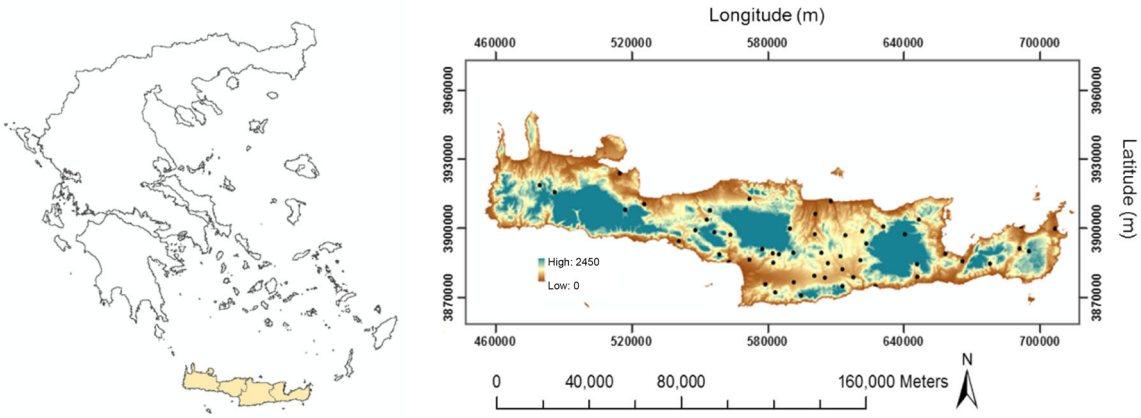

Fig. 1 Location of the island of Crete, its four prefectures, and spatial distribution of rainfall stations (black dots) on a Digital Elevation Map of the island. Maps were created using ArcGIS 10.2 (ESRI 2014) (http://www.esri.com/software/arcgis/arcgis-for-desktop)

significant, limits (Fig. 2). Considering the quantitative characteristics of these aquifers, all of them require special attention in terms of groundwater resources management. Thus, the potential of recharge from rainfall was also discussed in this work.

Methodological tools

The statistical analysis of the temporal rainfall variations was based on descriptive statistics and spectrum analysis. In this work, the temporal course of precipitation from 1981 to the most recent data is presented for the entire island, eastern and western part, during wet and dry periods. A spectrum analysis of the inter-decadal variability of the presented rainfall trends provides useful information regarding its return periods. Important periodicities in the rainfall inter-decadal variability can be identified using spectral analysis. The periodogram tool of spectral analysis, using the respective function and appropriately developed code in Matlab® (MATLAB 2010) environment, was applied to identify the dominant frequencies-periods of a time series. To identify clearly the dominant return periods in each case of rainfall temporal variability previously presented, the mean rainfall value is subtracted as in similar cases to concentrate on rainfall fluctuations (Musial et al. 2011; Vamos and Craciun 2012).

The spatial analysis was based on geostatistical analysis principles using ordinary kriging (OK) and regression kriging (RK) by employing secondary information (Cressie 1993; Deutsch and Journel 1992; Kitanidis 1997). Geostatistics is a set of spatial statistics methods aimed at estimating physical variables distributed in space using existing measurements. The geostatistical analysis methods involve two stages. The statistical parameters that determine the spatial distribution (variogram) are estimated in the first stage. The spatial model is used to derive estimates at locations, where measurements are not available in the second stage. One of the main objectives of this paper is to

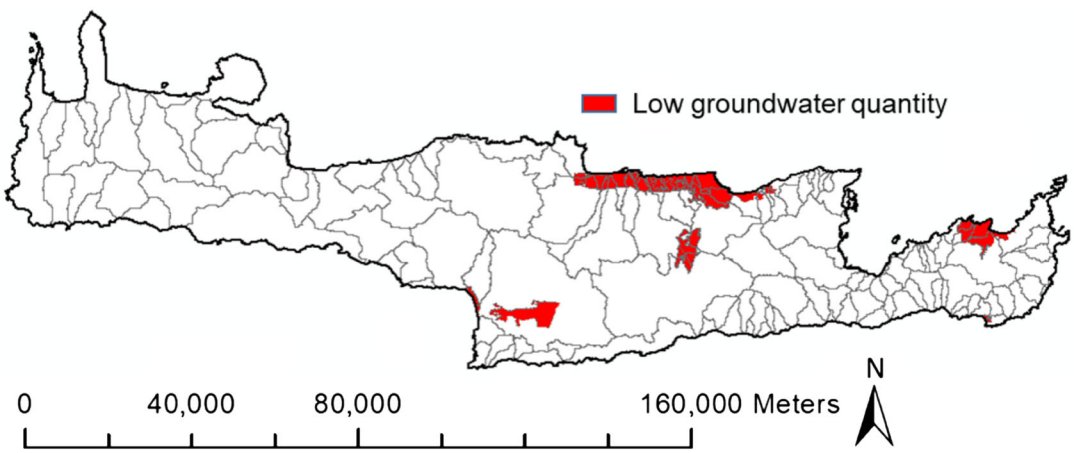

Fig. 2 Map of hydrological basins of Crete presenting aquifers of poor quantity (Special water secretariat of Greece 2015). Map was created using ArcGIS 10.2 (ESRI 2014) (http://www.esri.com/software/arcgis/arcgis-for-desktop)

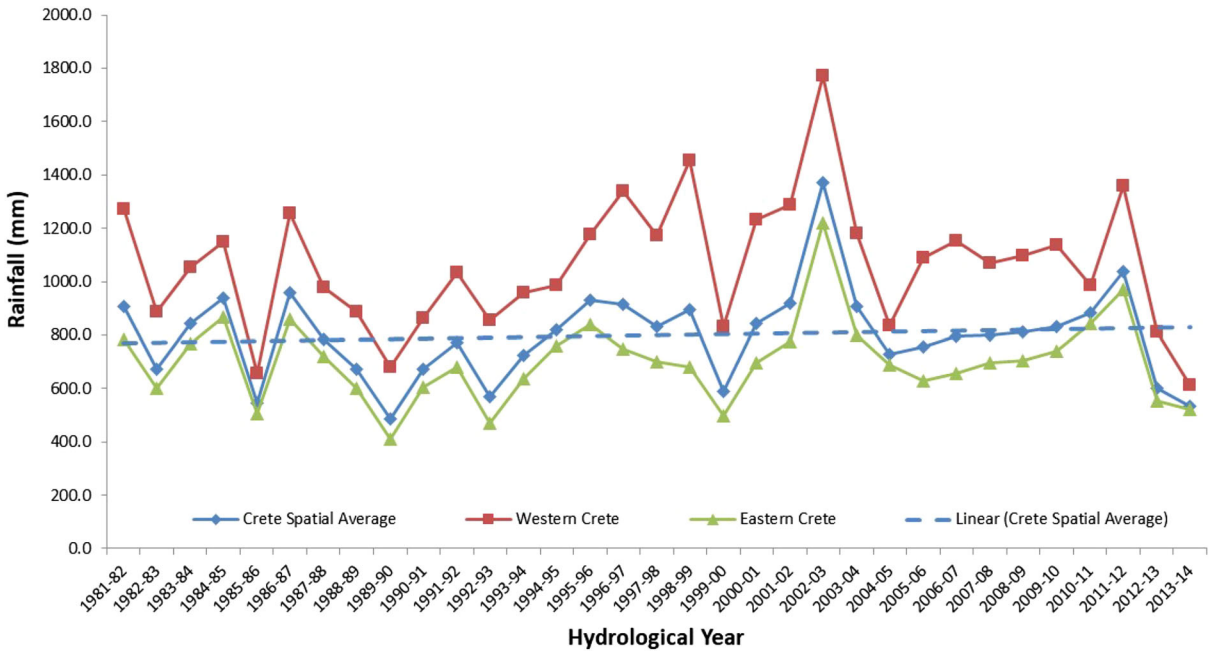

Fig. 3 Spatial average of the total annual rainfall on Crete Island, Eastern Crete and Western Crete

reproduce the spatial distribution of precipitation on the island, based also on data from a 50 × 50 m digital elevation map of Crete (Fig. 1). Therefore, the average annual rainfall of the island is studied. Geostatistical Matlab® (2010) codes (Varouchakis 2012) and the regression kriging package (Hastik and Cammerer 2012) developed for ArcGis (ESRI 2014) were applied for the geostatistical analysis. Two geostatistical spatial interpolation techniques were tested: the OK method and the RK method. Auxiliary information can be incorporated in the interpolation procedure using the RK method. Previous studies have shown that incorporating such auxiliary information in the trend function improves the accuracy of the spatial interpolation and that the use of auxiliary variables generally improves the accuracy of kriging estimation (Goovaerts 1999; Rivest et al. 2008; Varouchakis and Hristopulos 2013; Varouchakis et al. 2016a).

For the implementation of each method, different variograms were tested in a Matlab® environment, and the one that provided the most accurate cross-validation results was used to build the corresponding rainfall display map. The following theoretical variogram models were tested (Goovaerts 1997): Gaussian, spherical, exponential, and Matérn. Based on the comparative analysis of the results for the OK and RK methods, RK provided the most reliable representation of precipitation spatial variability on the island of Crete. RK was applied through the ArcGis software using the optimal variogram. The RK package developed for ArcGis was selected to produce the spatial representation of the rainfall variability to exploit the information of the digital elevation map. Thus, to estimate the rainfall distribution in the island boundaries using the surface elevation as an auxiliary variable.

Results and discussion

The annual rainfall in Crete shows an upward trend especially towards the end of the time series, between hydrological years 2004 and 2012, while exhibits a random pattern without clear return periods (Fig. 3). The latter also applies to the eastern and western parts of the island (Fig. 3).

In addition, Fig. 3 shows that, as expected, there is a strong gradient between rainfall in the western and in the eastern parts of the island. In particular, in some hydrological years, the rainfall in the western and eastern parts differ significantly, such as in 1999/2000 when it was estimated at 830.5 and 496.1 mm, respectively.

For our study period and data, the average annual rainfall on the island was calculated at 798.3 mm, 80% of which is from rainfall during the wet season (October–March) (Fig. 4), while the dry season (April–September) contributes only 20% (Fig. 4). Finally, the correlation between rainfall and the altitude of the location of each station was examined. It became apparent that stations located at altitudes over 660 m received three times the amount of water received by stations located at very low altitudes.

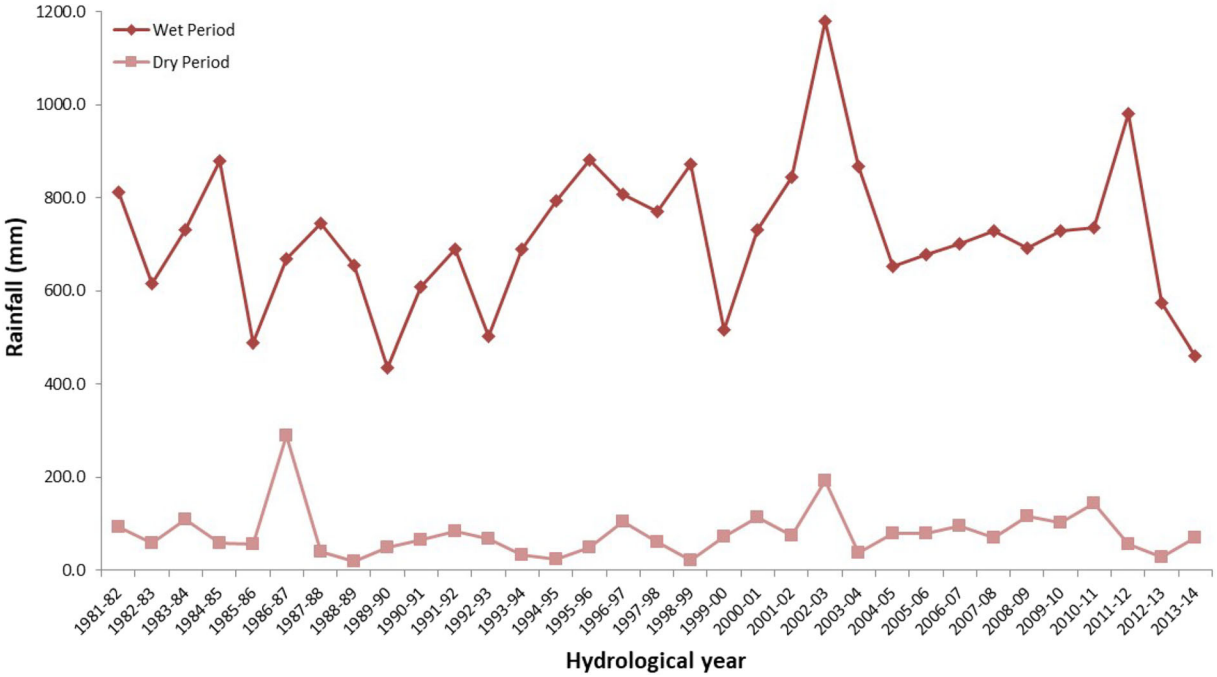

Fig. 4 Spatial average of the total rainfall on Crete Island during the wet and the dry hydrological periods

A very interesting observation from the rainfall data analysis is that the inter-annual rainfall variation on the island of Crete for the period 1981–2014 has an increasing trend (Fig. 3). This trend corresponds to an annual rainfall increase rate of 1.84 mm/year. The nonparametric Mann–Kendall test commonly applied in hydrological series analysis (Jing et al. 2017; Kisi and Ay 2014; Yue et al. 2002) confirmed a slightly significant increasing trend in the time series, $S = 130$, tau = 0.245, p value = 0.036 at 0.05 significance level. In addition, the parametric t test shows that the slope coefficient of the fitted linear regression is significantly different from zero (Longobardi and Villani 2010), t statistic = 2.25 with p value = 0.0316 at 0.05 significance level. Both statistical tests provide marginal significance of the trend, which still though confirms an increasing rainfall tendency for the period of study or at least that overall the annual rainfall remains stable for the given period.

This finding is in contrast to the estimations of models for the region of Crete and the Eastern Mediterranean. According to the specific field measurements and for the specific period of study, rainfall rates have not decreased as expected. Lately, there are works that discuss similar results (Deidda et al. 2013; Jacob et al. 2007). The specific finding led to further investigation of the available rainfall data. It became apparent that what has changed significantly in terms of rainfall behavior on the island of Crete is the number of rainy days throughout the year. A very important observation is that compared to the early 1980s the percentage of rainy days in the late 2000s has decreased by around 15%, while the intensity of rainfall has increased. The average number of rainy days during the early 1980s was 95 days, while during the late 2000s was around 80 days. A similar conclusion has been reached in a recent drought analysis for Greece, which concluded that the number of rainy days show a downward trend (Nastos et al. 2013).

The periodogram application (Fig. 5) provides useful and important information regarding rainfall return periods in Crete for the examined time series. A significant observation from the periodograms of the total annual, wet period and western part of Crete rainfall data is a dominant cycle of 25 years. However, due to the time series extend, i.e., 33 years the latter is probably not applicable for this data set analysis. On the other hand, the interpretation of the individual periodograms provides the significant rainfall cycles of every case examined. The total annual rainfall variability on the island of Crete presents a major cycle almost every 8 years (e.g., 1/0.13) and two more cycles of similar magnitude one almost every 4 years and another one almost every 2 years. The wet periods, that mainly contributes to the total annual rainfall, follow the same dominant cycle, while the second significant cycle appears almost every 3 years. In contrast, the dry periods have a major cycle almost every 3 years and a minor of similar magnitude every 5 years, denoting that the dry periods in Crete are quite similar. Regarding the western and eastern parts of the island, where significant differences in annual

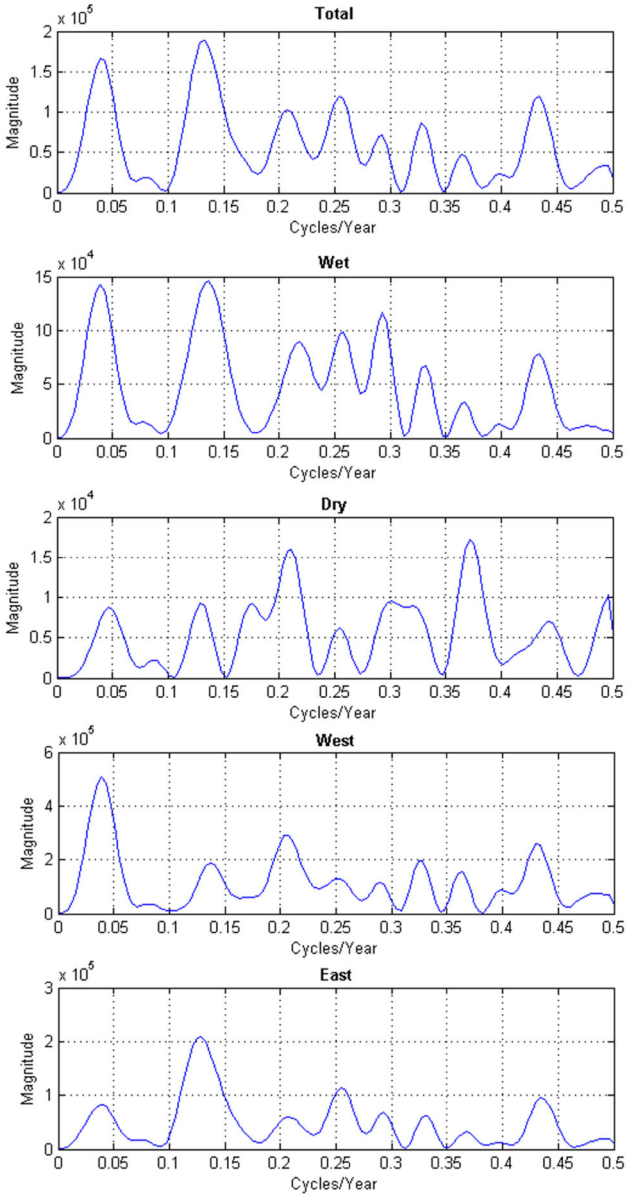

Fig. 5 Periodograms of inter-decadal rainfall variability on the island of Crete for the period 1981–2014. The figure presents the periodograms of the total annual rainfall, the wet and dry periods, and at the western and eastern parts of the island. The unit of the power spectral density (PSD) estimates on the *y*-axis is the unit of the time series data squared, i.e., mm^2. The figure was created using a Matlab® (2010) environment (https://www.mathworks.com/)

rainfall values have been recorded, the eastern part has a major return period every 8 years, similar to the total annual and to wet period rainfall variability, and two minor return periods every 4 and 2 years, respectively. The western part shows return periods of the same low magnitude almost every 5 years and almost every 2 years similar to the eastern part. The findings for the western part of Crete were pretty much expected due to the high rainfall rates that it receives.

Regarding the North Atlantic Oscillation index (Delworth et al. 2016; Hurrell and National Center for Atmospheric Research Staff 2017), its inter-decadal trend, for the examined period in terms of hydrological years, follows an opposite compared to rainfall trend on the island of Crete (Fig. 6). Rainfall appears to be below normal from the mid-1980s to the mid-1990s, followed by above normal rainfall during the following decade, while close to but above normal between mid-2000s and early 2010. Similarly, the NAO index has an increasing trend during the first reference decade, a decreasing trend follows through the next decade and finally the index decreases again during the last reference period. The correlation coefficient between the two variables is -0.505 with a p value equal to 0.0027 denoting that the result is significant both at 0.01 and 0.05 significance levels. This result declares that there is a negative correlation between the rainfall variability in Crete and the NAO index at annual scale in terms of a hydrological year. Thus, the rainfall variability in the island of Crete is affected by the NAO index variability.

The NAO index has been used to interpret the rainfall variability in many cases. Rainfall in the Mediterranean areas has been mostly identified to be negatively correlated with the NAO index (Brandimarte et al. 2011). Similar works have resulted to similar outcomes regarding negative correlation between NAO index and rainfall in the Mediterranean region testing the significance of these correlations using the 0.01 and 0.05 significance levels, e.g., (Brandimarte et al. 2011; Fernández-González et al. 2012; Ferrari et al. 2013). In Brandimarte et al. (2011), negative correlation of NAO index and rainfall in southern Italy was identified. A value of -0.49 for the whole southern Italy was determined statistically significant for p value < 0.01. Recently, a similar work for a hydrological basin in the Mediterranean area identified a negative correlation between rainfall and winter NAO index of -0.50 characterizing it a good correlation that could be useful for future winter precipitation and runoff tendencies (Corona et al. 2018). The statistically significant correlation of annual rainfall variation with the NAO index identified in this work helps to improve the current understanding of the inter-annual variability of rainfall on the island of Crete, and confirms the findings of the previous works mentioned in the text and extents future research to be focused on longer time series and shorter time scales such as the winter period.

The results of the spatial analysis (OK, RK) are obtained using originally developed codes in Matlab® environment and are presented in Table 1 in terms of mean absolute error (MAE), mean absolute relative error (MARE), and root mean square error (RMSE) (Goovaerts 1997; Leuangthong et al. 2004). The Matérn variogram yielded the most accurate cross-validation results for both kriging

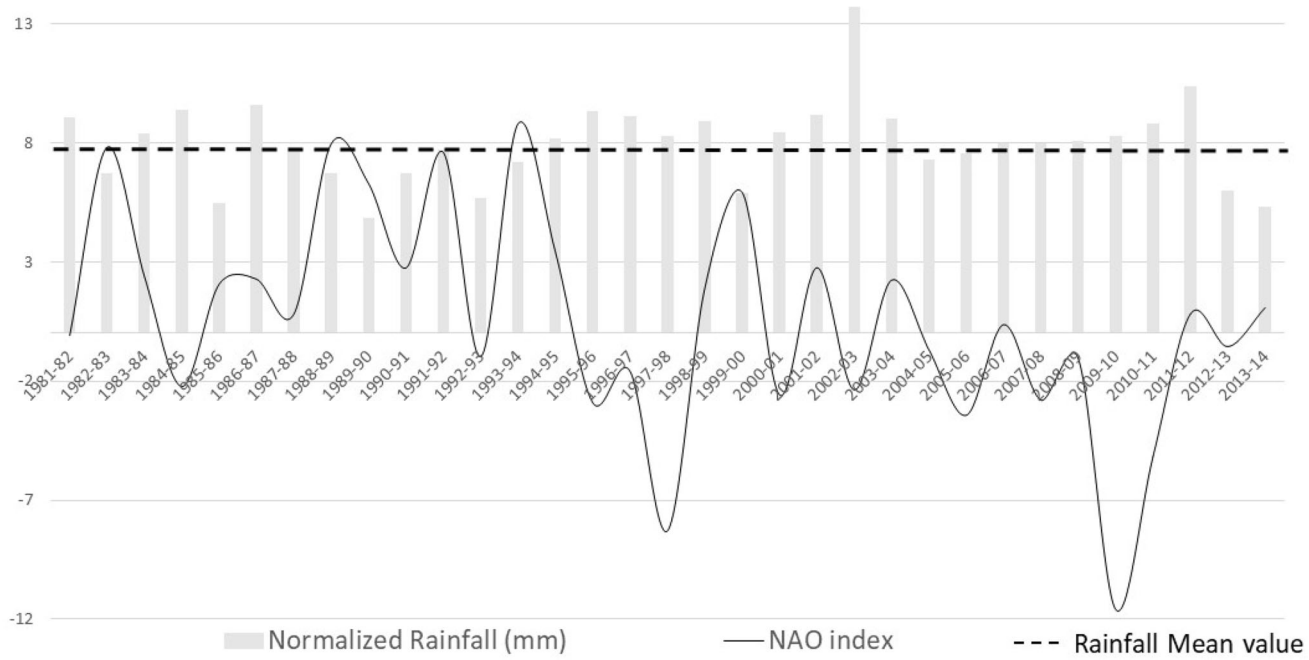

Fig. 6 Inter-annual variability of normalized rainfall in the island of Crete and of NAO index

Table 1 Cross-validation results for ordinary (OK) and regression (RK) kriging

Average annual rainfall data				
Method/variogram	Matérn	Spherical	Exponential	Gaussian
RK	MAE = 42 mm	MAE = 56 mm	MAE = 50 mm	MAE = 58 mm
	MARE = 0.15	MARE = 0.19	MARE = 0.17	MARE = 0.20
	RMSE = 54 mm	RMSE = 69 mm	RMSE = 59 mm	RMSE = 76 mm
OK	MAE = 63 mm	MAE = 68 mm	MAE = 71 mm	MAE = 73 mm
	MARE = 0.26	MARE = 0.28	MARE = 0.30	MARE = 0.31
	RMSE = 77 mm	RMSE = 83 mm	RMSE = 88 mm	RMSE = 89 mm

techniques, while RK resulted in the highest interpolation accuracy. The respective parameter of the residual variogram is: variance: $\sigma^2 = 574$ m^2, correlation length: 22,160 m, smoothness parameter: $\nu = 0.66$. Figure 7 shows the experimental variogram of the residuals, after the trend removal, along with the optimal theoretical model fit. The spatial distribution of the average annual rainfall on the island of Crete along with the associated estimation uncertainty using RK is presented in Fig. 8.

As can be observed from the rainfall distribution map, the western part of Crete receives the highest rainfall rates. On the other hand, the eastern part receives the lowest rates. There is also an increasing trend from south to north, especially in the eastern part of the island. A similar trend also exists in the western part of the island, but it is not clearly represented in the figure due to the small number of available measurements. A successful geostatistical analysis can reliably provide the spatial distribution of rainfall at unvisited locations. Therefore, hydrological modeling

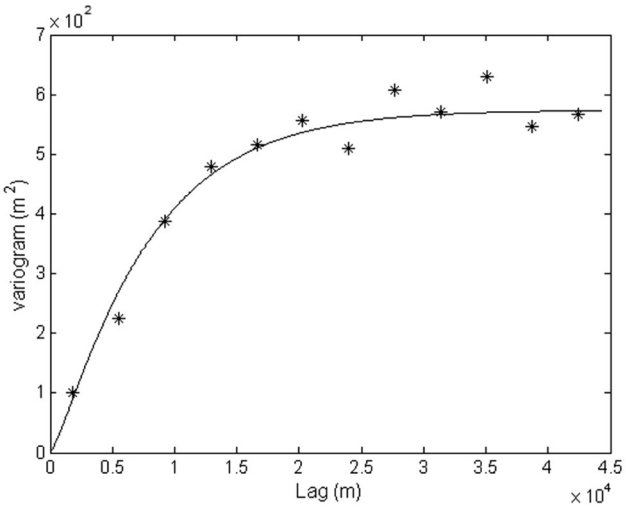

Fig. 7 Fit of the theoretical variogram (line) to the experimental variogram (asterisks) of the residuals after the trend removal. Figure was created using the Matlab® (2010) environment (https://www.mathworks.com/)

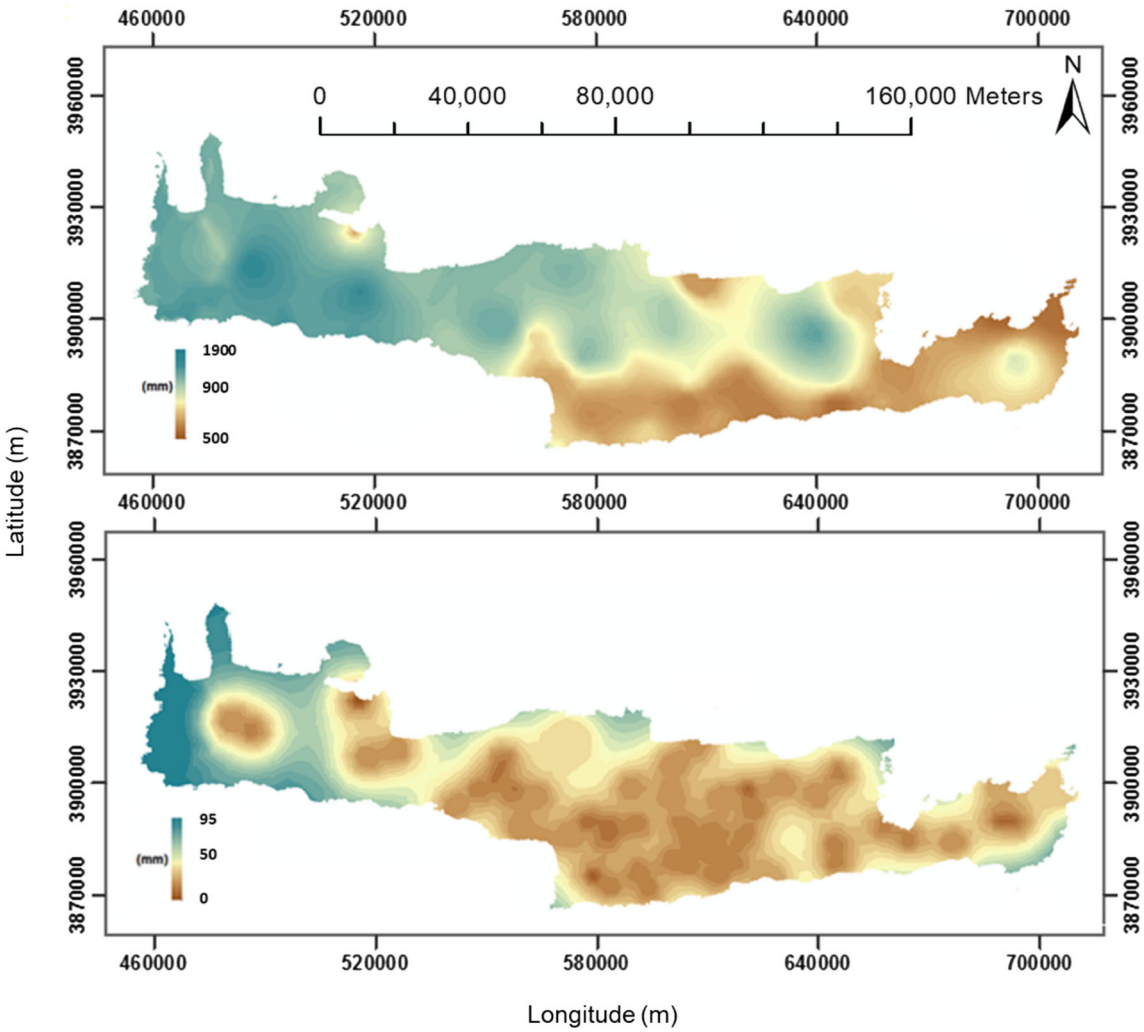

Fig. 8 Spatial distribution of the average annual rainfall (top) and the associated estimation uncertainty (bottom) on the island of Crete. Maps were created using ArcGIS 10.2 (ESRI 2014) (http://www.esri.com/software/arcgis/arcgis-for-desktop)

studies at basin scale can then be applied or large-scale climate models can be calibrated at the local scale to predict future rainfall variations accurately. Figure 9 presents the hydrological basins of Crete along with the rainfall spatial variability, where the findings of this work will be useful.

In addition, useful observations can be extracted regarding the ten poor quantity aquifers (Fig. 2). All of these aquifers belong to the eastern part of the island, and according to the rainfall maps they are located in the areas that receive low-to-lowest rainfall rates. Moreover, these aquifers have very low levels of groundwater table. Therefore, infiltration is inadequate to increase the aquifer levels. The vulnerable aquifers located in the southern part of the island are of high agricultural productivity, whereas those located in the northern part are in highly touristic areas, where high pumping occurs to cover the necessary water demand. On the other hand, as can be seen from the rainfall distribution map, the rainfall rates in these areas are not sufficient to recharge the aquifers. Before this study, only point rainfall information was available for the island of Crete for the specific time period. This work provides the average spatial distribution of rainfall on the island with increased reliability, providing authorities with the capability to make the necessary decisions to manage the water resources in vulnerable areas.

Conclusion

The descriptive statistical analysis of the rainfall data on the island of Crete presents the temporal variation of the rainfall identifying key hydrological years that led to drought (1989/1990) or excess rainfall (2002/2003). In addition, it was identified that the western part of Crete receives more rainfall compared to the eastern part. Unlike

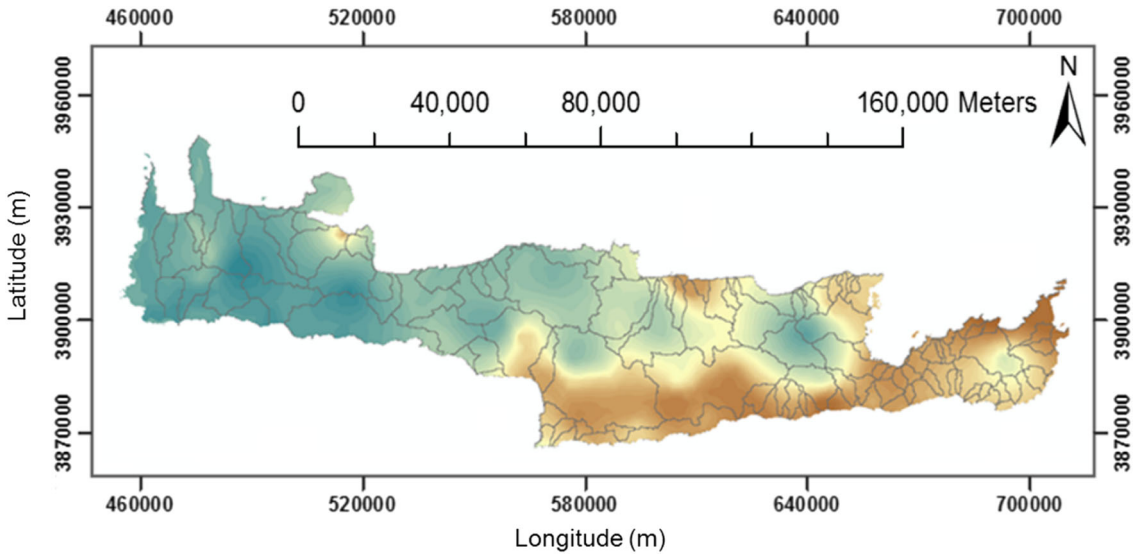

Fig. 9 Spatial distribution of the average annual rainfall along with the hydrological basins of the island of Crete. Map was created using ArcGIS 10.2 (ESRI 2014) (http://www.esri.com/software/arcgis/arcgis-for-desktop)

climate studies that predicted a decreasing trend of rainfall on the island of Crete, the rainfall trend for the specific data set on an annual basis seems to increase since 1981, but the number of rain days has decreased. Significant cycles in rainfall variability were identified from the data statistical analysis in terms of average annual variability, hydrological periods, and geographical areas on the island of Crete. In addition, the rainfall variability in Crete was found to be related to the NAO index variability. Such results help to interpret the rainfall behavior on the island and to aid decision support systems regarding water resources management.

Regression kriging using ground surface elevation as auxiliary information provided more accurate results compared to OK. Overall, RK provided the spatial distribution of precipitation on the island of Crete with a 15% MARE. The involvement of auxiliary information provided improved results for the rainfall spatial distribution on the island of Crete that could help significantly in water resources management, evapotranspiration, or soil infiltration estimation studies. The reliable spatial representation of the rainfall distribution provides local authorities and stakeholders useful information about the areas that require irrigation infrastructure because of low rainfall rates.

Acknowledgements The authors would like to thank the Department of Water Resources Management of the Region of Crete for making the rainfall data available for public use through its website.

Author contributions EAV written and edited the manuscript, performed the statistical and geostatistical analysis and the interpretation of the results, GAC contributed to the statistical interpretation, GPK contributed with his expertise to the results interpretation, and AK performed data management.

Compliance with ethical standards

Conflict of interest The authors declare no competing financial interests.

References

Bierkens MFP, Knotters M, Hoogland T (2001) Space-time modeling of water table depth using a regionalized time series model and the Kalman filter. Water Resour Res 37:1277–1290

Brandimarte L, Di Baldassarre G, Bruni G, D'Odorico P, Montanari A (2011) Relation between the North-Atlantic Oscillation and hydroclimatic conditions in Mediterranean areas. Water Resour Manag 25:1269–1279. https://doi.org/10.1007/s11269-010-9742-5

Corona R, Montaldo N, Albertson JD (2018) On the role of NAO-driven interannual variability in rainfall seasonality on water resources and hydrologic design in a typical Mediterranean basin. J Hydrometeorol 19:485–498

Cressie N (1993) Statistics for spatial data (revised ed.). Wiley, New York

Deidda R et al (2013) Regional climate models' performance in representing precipitation and temperature over selected Mediterranean areas. Hydrol Earth Syst Sci 17:5041–5059. https://doi.org/10.5194/hess-17-5041-2013

Delworth TL, Zeng F, Vecchi GA, Yang X, Zhang L, Zhang R (2016) The North Atlantic Oscillation as a driver of rapid climate change in the Northern Hemisphere. Nat Geosci 9:509–512. https://doi.org/10.1038/ngeo2738

Deutsch CV, Journel AG (1992) GSLIB. Geostatistical software library and user's guide. Oxford University Press, New York

Drake JB (2014) Climate modeling for scientists and engineers. SIAM, Philadelphia

Eshel G, Farrell BF (2000) Mechanisms of eastern Mediterranean rainfall variability. J Atmos Sci 57:3219–3232

ESRI (2014) ESRI, ArcGIS release 10.2.2. Environmental Systems Research Institute, Redlands

Fernández-González S, del Río S, Castro A, Penas A, Fernández-Raga M, Calvo AI, Fraile R (2012) Connection between NAO, weather types and precipitation in León, Spain (1948–2008). Int J Climatol 32:2181–2196. https://doi.org/10.1002/joc.2431

Ferrari E, Caloiero T, Coscarelli R (2013) Influence of the North Atlantic Oscillation on winter rainfall in Calabria (southern Italy). Theor Appl Climatol 114:479–494. https://doi.org/10.1007/s00704-013-0856-6

Giorgi F, Lionello P (2008) Climate change projections for the Mediterranean region. Glob Planet Change 63:90–104

Goovaerts P (1997) Geostatistics for natural resources evaluation. Oxford University Press, New York

Goovaerts P (1999) Geostatistics in soil science: state-of-the-art and perspectives. Geoderma 89:1–45

Grillakis MG, Tsanis IK, Koutroulis AG (2010) Application of the HBV hydrological model in a flash flood case in Slovenia. Nat Hazards Earth Syst Sci 10:2713–2725

Hastik R, Cammerer H (2012) Regression kriging for ArcGIS 10. Institute of Geography, University of Innsbruck

Hertig E, Jacobeit J (2014) Variability of weather regimes in the North Atlantic-European area: past and future. Atmos Sci Lett 15:314–320. https://doi.org/10.1002/asl2.505

Hurrell J, National Center for Atmospheric Research Staff (Eds) (2017) The Climate Data Guide: Hurrell North Atlantic Oscillation (NAO) Index (station-based), Retrieved from https://climatedataguide.ucar.edu/climate-data/hurrell-north-atlantic-oscillation-nao-index-station-based. Accessed 12 May 2017

Hurrell JW, Van Loon H (1997) Decadal variations in climate associated with the North Atlantic oscillation. Clim Change 36:301–326. https://doi.org/10.1023/a:1005314315270

Jacob D et al (2007) An inter-comparison of regional climate models for Europe: model performance in present-day climate. Clim Change 81:31–52. https://doi.org/10.1007/s10584-006-9213-4

Jing L et al (2017) Effects of hydrological regime on development of Carex wet meadows in East Dongting Lake, a Ramsar Wetland for wintering waterbirds. Sci Rep 7:41761. https://doi.org/10.1038/srep41761

Kalogeropoulos K, Chalkias C (2013) Modelling the impacts of climate change on surface runoff in small Mediterranean catchments: empirical evidence from Greece. Water Environ J 27:505–513

Kisi O, Ay M (2014) Comparison of Mann–Kendall and innovative trend method for water quality parameters of the Kizilirmak River, Turkey. J Hydrol 513:362–375. https://doi.org/10.1016/j.jhydrol.2014.03.005

Kitanidis PK (1997) Introduction to geostatistics. Cambridge University Press, Cambridge

Knotters M, Bierkens MFP (2000) Physical basis of time series models for water table depths. Water Resour Res 36:181–188. https://doi.org/10.1029/1999wr900288

Koutroulis AG, Tsanis IK, Daliakopoulos IN, Jacob D (2013) Impact of climate change on water resources status: a case study for Crete Island, Greece. J Hydrol 479:146–158. https://doi.org/10.1016/j.jhydrol.2012.11.055

Krichak SO, Alpert P (2005) Signatures of the NAO in the atmospheric circulation during wet winter months over the Mediterranean region. Theor Appl Climatol 82:27–39. https://doi.org/10.1007/s00704-004-0119-7

Leuangthong O, McLennan JA, Deutsch CV (2004) Minimum acceptance criteria for geostatistics realizations. Nat Resour Res 13:131–141

Lelieveld J, Hadjinicolaou P, Kostopoulou E, Chenoweth J, El Maayar M, Giannakopoulos C et al (2012) Climate change and impacts in the Eastern Mediterranean and the Middle East. Clim Change 114(3):667–687

Longobardi A, Villani P (2010) Trend analysis of annual and seasonal rainfall time series in the Mediterranean area. Int J Climatol 30:1538–1546. https://doi.org/10.1002/joc.2001

Maas GS, Macklin MG (2002) The impact of recent climate change on flooding and sediment supply within a Mediterranean mountain catchment, southwestern Crete, Greece. Earth Surf Proc Land 27:1087–1105. https://doi.org/10.1002/esp.398

Masih I, Uhlenbrook S, Maskey S, Ahmad MD (2010) Regionalization of a conceptual rainfall–runoff model based on similarity of the flow duration curve: a case study from the semi-arid Karkheh basin, Iran. J Hydrol 391:188–201. https://doi.org/10.1016/j.jhydrol.2010.07.018

MATLAB (2010) MATLAB, 7.10 (R2010a) edn. The MathWorks Inc., Natick

Musial JP, Verstraete MM, Gobron N (2011) Technical note: comparing the effectiveness of recent algorithms to fill and smooth incomplete and noisy time series. Atmos Chem Phys 11:7905–7923. https://doi.org/10.5194/acp-11-7905-2011

Naoum S, Tsanis IK (2003) Temporal and spatial variation of annual rainfall on the island of Crete, Greece. Hydrol Process 17:1899–1922. https://doi.org/10.1002/hyp.1217

Nastos PT, Politi N, Kapsomenakis J (2013) Spatial and temporal variability of the Aridity Index in Greece. Atmos Res 119:140–152

Rivest M, Marcotte D, Pasquier P (2008) Hydraulic head field estimation using kriging with an external drift: a way to consider conceptual model information. J Hydrol 361:349–361

Skøien JO, Blöschl G (2007) Spatiotemporal topological kriging of runoff time series. Water Resour Res 43:W09419. https://doi.org/10.1029/2006WR005760

Special water secretariat of Greece (2015) Integrated management plans of the Greek watersheds. Ministry of Environment & Energy, Athens

Sungmin O, Foelsche U, Kirchengast G, Fuchsberger J (2018) Validation and correction of rainfall data from the WegenerNet high density network in southeast Austria. J Hydrol 556:1110–1122. https://doi.org/10.1016/j.jhydrol.2016.11.049

Vamos C, Craciun M (2012) Automatic trend estimation. Springer Publishing Company, Incorporated

Varouchakis EA (2012) Geostatistical analysis and space-time models of aquifer levels: application to mires hydrological basin in the prefecture of Crete. PhD Thesis, Technical University of Crete

Varouchakis EA, Hristopulos DT (2013) Improvement of groundwater level prediction in sparsely gauged basins using physical laws and local geographic features as auxiliary variables. Adv Water Resour 52:34–49

Varouchakis EA, Kolosionis K, Karatzas GP (2016a) Spatial variability estimation and risk assessment of the aquifer level at sparsely gauged basins using geostatistical methodologies. Earth Sci Inform 9:437–448. https://doi.org/10.1007/s12145-016-0265-3

Varouchakis EA, Spanoudaki K, Hristopulos DT, Karatzas GP, Corzo Perez GA (2016b) Stochastic modeling of aquifer level temporal fluctuations based on the conceptual basis of the soil-water balance equation. Soil Sci 181:224–231. https://doi.org/10.1097/ss.0000000000000157

Vozinaki A-E, Karatzas G, Sibetheros I, Varouchakis E (2015) An agricultural flash flood loss estimation methodology: the case study of the Koiliaris basin (Greece), February 2003 flood. Nat Hazards 79:899–920. https://doi.org/10.1007/s11069-015-1882-8

Yue S, Pilon P, Cavadias G (2002) Power of the Mann–Kendall and Spearman's rho tests for detecting monotonic trends in hydrological series. J Hydrol 259:254–271. https://doi.org/10.1016/S0022-1694(01)00594-7

Acta Geophysica (2018) 66:329–343
https://doi.org/10.1007/s11600-018-0118-1

RESEARCH ARTICLE - SPECIAL ISSUE

Detection of trends and break points in temperature: the case of Umbria (Italy) and Guadalquivir Valley (Spain)

Pascual Herrera-Grimaldi[1] · Amanda García-Marín[1] · José Luís Ayuso-Muñoz[1] · Alessia Flamini[2] · Renato Morbidelli[2] · José Luís Ayuso-Ruíz[1]

Received: 15 November 2017 / Accepted: 6 February 2018 / Published online: 10 February 2018

Abstract
The increase of air surface temperature at global scale is a fact with values around 0.85 °C since the late nineteen century. Nevertheless, the increase is not equally distributed all over the world, varying from one region to others. Thus, it becomes interesting to study the evolution of temperature indices for a certain area in order to analyse the existence of climatic trend in it. In this work, monthly temperature time series from two Mediterranean areas are used: the Umbria region in Italy, and the Guadalquivir Valley in southern Spain. For the available stations, six temperature indices (three annual and three monthly) of mean, average maximum and average minimum temperature have been obtained, and the existence of trends has been studied by applying the non-parametric Mann–Kendall test. Both regions show a general increase in all temperature indices, being the pattern of the trends clearer in Spain than in Italy. The Italian area is the only one at which some negative trends are detected. The presence of break points in the temperature series has been also studied by using the non-parametric Pettit test and the parametric standard normal homogeneity test (SNHT), most of which may be due to natural phenomena.

Keywords Trend · Temperature · Break points · Homogeneity tests

Introduction

According to the Fifth Assessment Report from the Intergovernmental Panel on Climate Change (IPCC 2014), there is no doubt about the climate warming, with many changes without precedents observed since 1950 clearly influenced by anthropogenic emissions of greenhouse gases. For the Northern Hemisphere, the warmest period of the last millennium took place from 1983 to 2012, with a globally surface increase of temperature over the period 1880 to 2012 of 0.85 °C. Surface temperature is projected to rise over the twenty-first century under all assessed emission scenarios. It is very likely that heat waves will occur more often and last longer.

There are many studies that evidence the increase in the average values of temperature at local or regional scale (Hu et al. 2012; Piccarreta et al. 2015; Feidas 2016; Caloiero et al. 2017) and global (Tank and Können 2003; Klok and Klein-Tank 2009; del Río et al. 2011). The varying reference periods and places of different research groups are indications of the robustness of the results (Gonzalez-Hidalgo et al. 2015). The Mediterranean region is one with the highest increase in temperature but also with spatial variability in temperature trends (e.g. Brunet et al. 2005, 2006, 2007; Morales et al. 2005; Brunetti et al. 2006; Martínez et al. 2010; del Río et al. 2012; Gonzalez-Hidalgo et al. 2015; Piccarreta et al. 2015) that may be affected by local factors.

When dealing with long time data series it is important to assess their quality and correct their possible errors. Within this processes, the detection of in-homogeneity caused by non-climatic factors (changes in instruments, station locations, observation routines, …) is crucial in

✉ Amanda García-Marín
amanda.garcia@uco.es

[1] Área de Proyectos de Ingeniería, Departmento de Ingeniería Rural, Universidad de Córdoba, Edificio Leonardo Da Vinci, Campus de Rabanales, Carretera Nacional IV Km 396, Córdoba, Spain

[2] Department of Civil and Environmental Engineering, University of Perugia, Via G. Duranti, 93, Perugia, Italy

order to obtain accurate information about climate variability or trends. Many statistical methods can be applied to detect inhomogeneity in either original or previously validated data series. Some of them, such as the Standard Normal Homogeneity Test (Alexandersson 1986) and the Pettit test (Pettit 1979), can identify even the date of the homogeneity break points and are known as location-specific tests (e.g. Wijngaard et al. 2003). Not all inhomogeneities existing in data series are of non-climatic origin but originate from "real" climate changes (Morozova and Valente 2012) like volcanic eruptions, changes in atmospheric composition and circulation, etc.

In this work, previously validated data series have been analysed in two regions of Italy and Spain. The main objective is to study the trends and changes in temperature in two different Mediterranean areas in order to analyse the evolution patterns of this variable, and their relation with climate change origin.

Study areas and data

Two different areas have been considered in this study: the Umbria region (Italy) and the Guadalquivir Valley (Spain). The Umbria region (8456 km^2) is located in an inland zone of Central Italy (Fig. 1) characterized by a complex orography along the eastern board, where the Apennine Mountains exceed 2000 m a.s.l., and mainly hilly in the central and western areas, with elevation ranging from 100 to 800 m a.s.l.

The climate of the region is different from zone to zone with mean annual rainfall of about 900 mm and ranging between 650 and 1450 mm. Higher monthly rainfall values generally occur during the autumn–winter period, together with floods caused by widespread rainfalls. Mean annual air temperature ranges between 3.3 and 14.2 °C with maximum values during the month of July and minimum in January.

A wide percentage of the study area is included in the Tiber River basin. In fact the Tiber River crosses the region from North to South-West receiving water from many tributaries, mainly located on the hydrographic left side.

The Guadalquivir Valley (Fig. 2) is located in Andalusia (southern Spain), a Mediterranean Climate area where some geographic factors as altitude and the mountainous relief establish different bioclimatic areas. One of them is the Guadalquivir Valley, characterized by high temperatures, irregular rainfall pattern and high sunshine hours, but with Atlantic humid influence. The continental characteristics increase along the Valley, especially in the upper catchment. The mean annual temperature ranges between 17 and 18 °C, being the range of the annual Daily Temperature Range (DTR) from 18 to 20 °C. With a number of

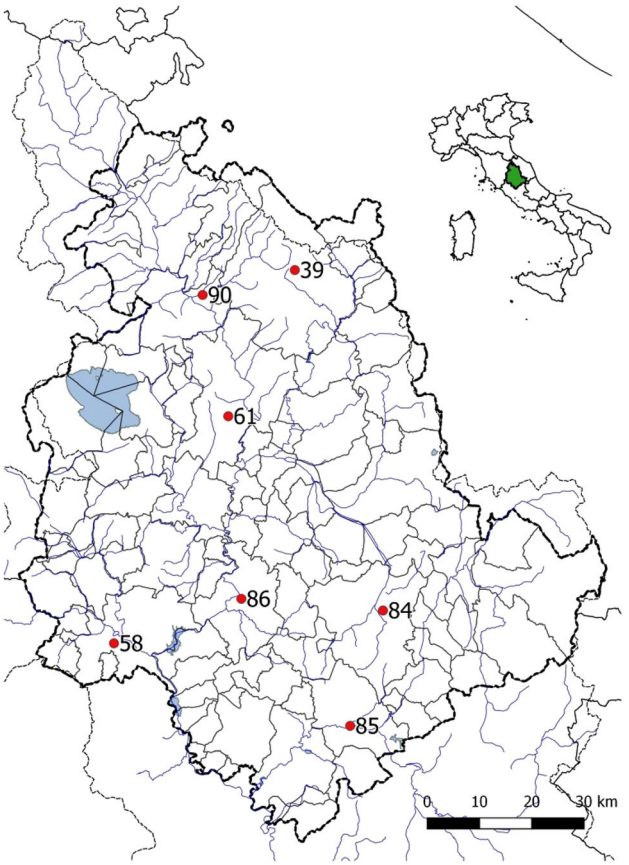

Fig. 1 Location of the Umbria region in central Italy and the seven weather stations considered

rainy days per year of 75–100, and a dry period of almost 5 months, the mean annual rainfall varies from 500 to 700 mm.

The behavior of daily temperature data series have been analyzed in both areas described above. For the Umbria region, seven meteorological stations have been considered (red circles in Fig. 1) spanning the 1924–2015 period (Table 1). Only stations with less than 15% missing data have been retained. The original dataset was provided by the National and the Regional Hydrographic Services. The thermometers used in the Italian observation network are approved and normalized by the National Hydrographic Service which provides the instruments and guaranteed their uniformity. The data represent observations of daily maximum surface air temperature, T_{max}, and daily minimum surface air temperature, T_{min}. In addition to data availability, the quality and homogeneity of the temperature time series have been previously tested. More specifically, the main goal of the quality procedure was to reduce errors in data recording and processing in accordance with Aguilar et al. (2003) and Brunet et al. (2006) in terms of gross errors checks, temporal and spatial coherency, tolerance tests and internal consistency. Furthermore, the

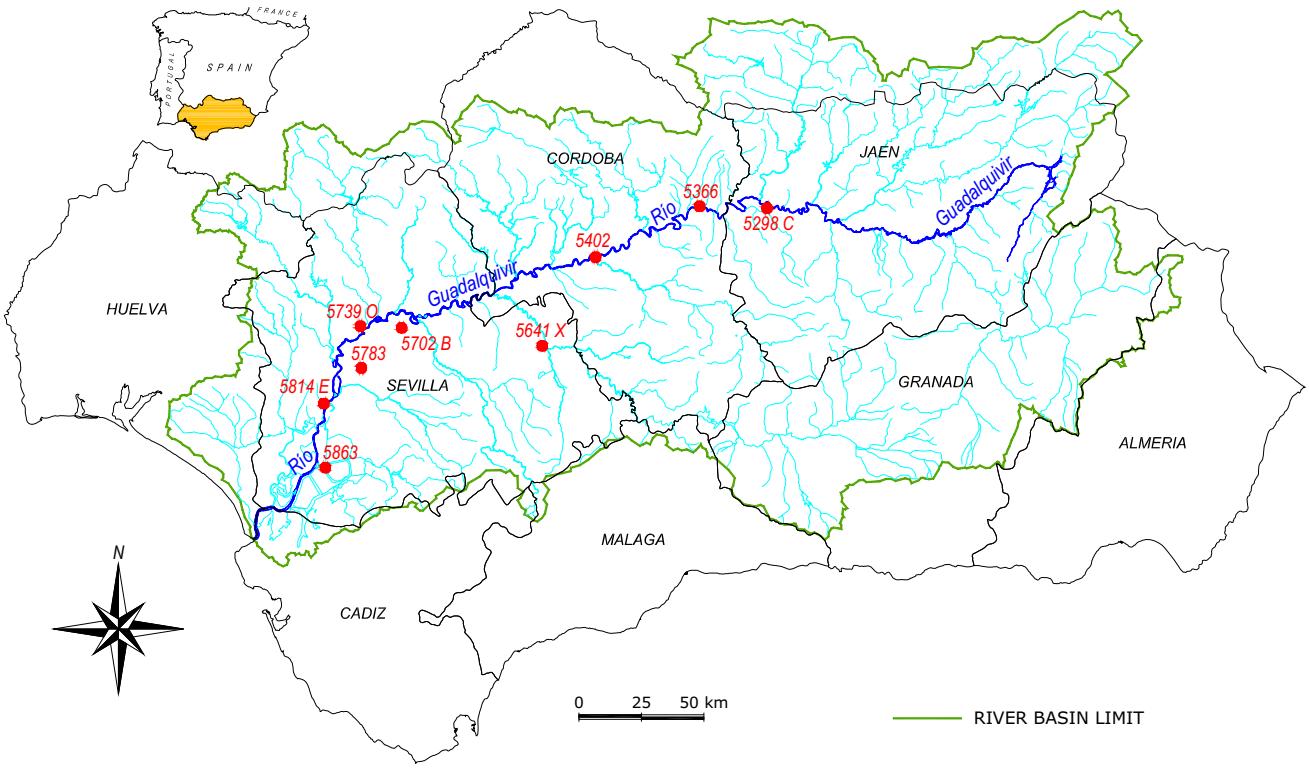

Fig. 2 Location of the Guadalquivir Valley in Andalusia (southern Spain) and the nine weather stations considered

Table 1 Detailed information about the stations used at Umbria region (Italy)

ID	Station	Altitude (m.a.s.l.)	UTM33 X (m)	UTM33 Y (m)	Available data period	Series length (years)	Missing value (%)
39	Gubbio	471	302789	4802329	1947–2015	68	14
58	Orvieto	311	263178	4733559	1948–2015	67	12
61	Perugia	440	288087	4775349	1924–2015	89	5
84	Spoleto	353	314952	4736152	1950–2015	65	9
85	Terni	123	307123	4714603	1947–2015	68	3
86	Todi	329	288089	4740319	1934–2015	80	3
90	Umbertide	305	284867	4798836	1955–2015	60	14

metadata of all the stations have been acquired in order to keep information on possible sensor and location changes. The stations of Orvieto and Todi have been always in the same location and in invariant environmental conditions. The stations of Umbertide and Spoleto were moved to a different location at the end of 90's, that of Gubbio at the end of 80's (around the year 1988), and that of Terni starting from the year 2004. As regard Perugia, a different location of the station was identified in 2001.

For the Guadalquivir Valley, nine meteorological stations (Fig. 2) have been considered mainly located in the central area (Table 2). All of the data used were obtained from the Monthly Temperature Dataset of Spain (MOTEDAS) (Gonzalez-Hidalgo et al. 2015), developed from the total amount of data digitalized by the Spanish Meteorological Agency (Agencia Estatal de Meteorología, AEMET), after a detailed quality control of data and the reconstruction of series from neighbouring stations. Sixty-one years (from 1950 to 2010) of data were considered for all the station.

Methods

Six temperature indices (three annual and three monthly) of mean, average maximum and average minimum temperature have been considered for each site in both Umbria and Guadalquivir Valley regions (Table 3). For each index,

Table 2 Detailed information about the stations used at Guadalquivir Valley (Spain)

ID	Station	Latitude	Longitude	Altitude (m.a.s.l.)
5298C	Andújar	380.264	− 40.728	200
5366	Montoro C. de A.	380.278	− 43.811	195
5402	Córdoba (Airport)	378.444	− 48.506	91
5641X	Écija	375.167	− 50.839	130
5702B	Carmona	375.686	− 57.228	50
5739°	Alcalá del Río	375.667	− 59.103	20
5783	Sevilla (Airport)	374.239	− 59.036	26
5814E	Coria del Río	372.889	− 60.575	30
5863	Cabezas de S. juan	370.583	− 60.422	3

Table 3 Temperature indices analyzed in this work

Index	Definitions	Units
TMy	Mean annual of daily average temperature	°C
TMXy	Mean annual of daily maximum temperature	°C
TMNy	Mean annual of daily minimum temperature	°C
TMm	Mean monthly of daily average temperature	°C
TMXm	Mean monthly of daily maximum temperature	°C
TMNm	Mean monthly of daily minimum temperature	°C

three tests have been performed: the Mann–Kendall test to analyse trends, the Pettit test and the standard normal homogeneity test (SNHT), to detect changes in the pattern of the temperature data series. The last two tests are known as location-specific tests, because they are capable of locate the year where a break is likely. There are some differences between SNHT and Pettit test. SNHT is sensitive in detecting the breaks near the beginning and the end of the series. Pettit test is more sensitive to breaks in the middle of the series. Besides, the SNHT assumes that the series is normally distributed, whereas Pettit test does not need this assumption because it is a non-parametric rank test (Wijngaard et al. 2003). Both tests can give information on the year of the break.

The Mann–Kendall test

This non parametric and rank-based test, was proposed by Mann (1945) and improved by Kendall (1975) and evaluate the significance of a trend. It is widely used to detect the trends in hydro-climatic data series (Yue et al. 2002; Kahya and Kalayci 2004; Jung et al. 2011; Shadmani et al. 2012; Rougé et al. 2013). The null hypothesis H0 establishes that a sample of data ($X1$, $X2$,…, Xn) is independent and identically distributed. The alternative hypothesis H1 (of a two-sided test), establishes that there is a monotonic trend in X. The test is based on S statistics. Each pair of values observed x_i, x_j ($i < j$) of the random variable is inspected to find out if $x_i > x_j$ or $x_i < x_j$, thus defining S as (Yu et al. 1993; Douglas et al. 2000; Hamed 2008),

$$S = \sum_{i=1}^{n-1} \sum_{j=1+1}^{n} \operatorname{sign}\left(x_j - x_i\right) \tag{1}$$

where x_i, x_j are the sequential data, n is the total number of data of the time series, and sign $(x_j - x_i)$ is 1 for $(x_j - x_i) > 0$; 0 for $(x_j - x_i) = 0$, and − 1 for $(x_j - x_i) < 0$. When $n \geq 8$, the statistical S is approximately normally distributed. When there are no repeated data values, the mean and the variance are expressed by,

$$E(S) = 0 \tag{2}$$

$$\operatorname{Var}(S) = \frac{n(n-1)(2n+5)}{18} \tag{3}$$

When some data of the series are tied, the variance can turn out to be,

$$\operatorname{Var}(S) = \frac{n(n-1)(2n+5) - \sum_{j=1}^{m} t_j\left(t_j - 1\right)\left(2t_j + 5\right)}{18} \tag{4}$$

where m is the number of the tied data groups, each with t_j tied observations. For $n > 10$ the standardized test statistic, Z, is calculated by,

$$Z = \begin{cases} \dfrac{S-1}{\sqrt{\operatorname{Var}(S)}} & S > 0 \\ 0 & S = 0 \\ \dfrac{S+1}{\sqrt{\operatorname{Var}(S)}} & S < 0 \end{cases} \tag{5}$$

This statistic, Z, follows the standard normal distribution with a mean of zero and variance unity, and it is used to detect a significant trend. If $Z > 0$, this indicates an increasing trend, and if $Z < 0$ this indicates a decreasing trend in the time series analyzed. Consequently, the null hypothesis H_0 is rejected at the significance level α (the probability that the test will detect a trend when there is none) if $|Z| > Z_{1-\alpha/2}$, where $Z_{1-\alpha/2}$ is the critical value of Z according to the standard normal distribution. For the

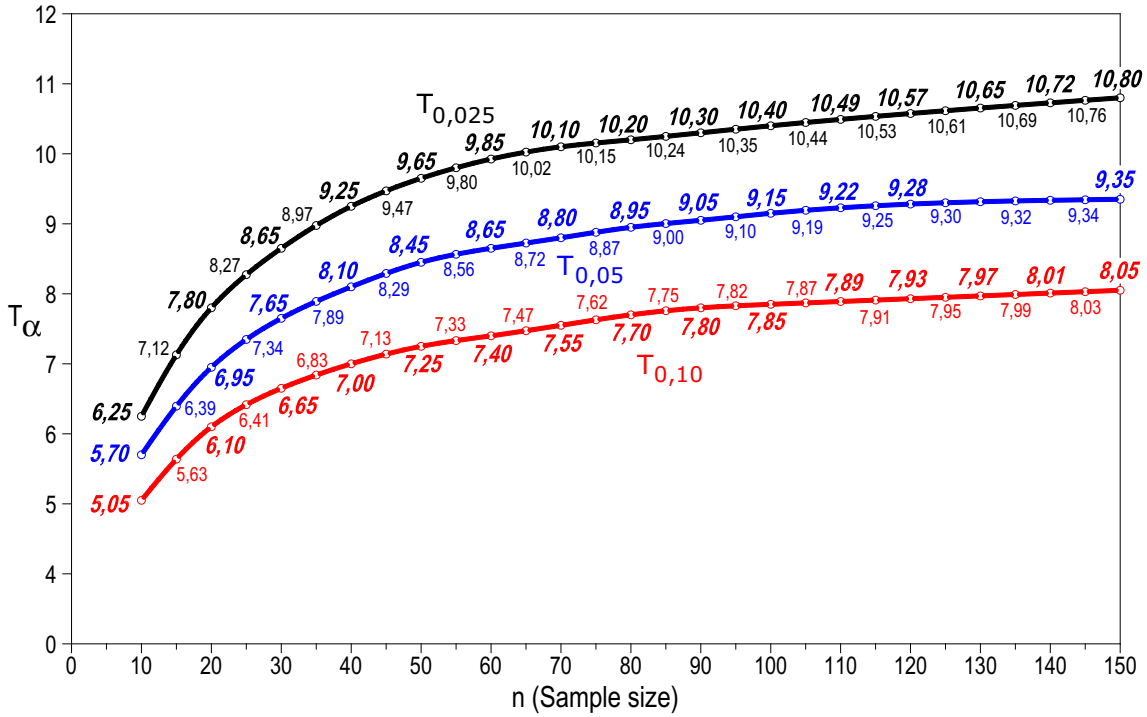

Fig. 3 Critical values of SNHT statistic T obtained from Alexandersson (1986)

Table 4 Significant trend values (°C/decade) for the Umbria region

Station	Jan	Feb	Mar	Apr	May	Jun	Jul	Aug	Sep	Oct	Nov	Dec	Annual
TMm													TMy
Gubbio						− 0.04			− 0.37				− 0.08
Orvieto			0.22		0.18		0.18	0.26					0.11
Perugia	0.21		0.20	0.20	0.28	0.21	0.24	0.3		0.23			0.19
Spoleto	0.50		0.36	0.37	0.40	0.35	0.46	0.47	0.25	0.46	0.35	0.31	0.35
Terni			0.17				0.18	0.32		0.25		0.25	0.16
Todi	0.22				0.23	0.25	0.23	0.15		0.23	0.17	0.15	0.17
Umbertide				0.24				0.23		0.24			0.15
TMXm													TMXy
Gubbio						0.02	− 0.04		− 0.36				− 0.05
Orvieto					0.25								
Perugia	0.22		0.26	0.22	0.31	0.24	0.26	0.33		0.25			0.19
Spoleto	0.36		0.26	0.28	0.32	0.37	0.38	0.46		0.36	0.30	0.25	0.28
Terni													
Todi	0.20				0.20	0.22	0.19	0.30		0.18			0.16
Umbertide													
TMNm													TMNy
Gubbio		− 0.25							− 0.25				− 0.11
Orvieto							0.21	0.33					0.11
Perugia	0.21		0.20	0.18	0.26	0.20	0.19	0.29		0.22			0.18
Spoleto	0.44		0.39	0.42	0.44	0.40	0.53	0.48	0.27	0.53	0.40	0.40	0.40
Terni	0.23		0.32	0.33	0.35	0.33	0.43	0.57	0.22	0.43	0.30	0.28	0.30
Todi	0.25				0.25	0.29	0.25	0.37	0.15	0.29	0.24	0.20	0.21
Umbertide				0.26	0.25	0.21		0.29	0.22	0.47	0.25		0.23

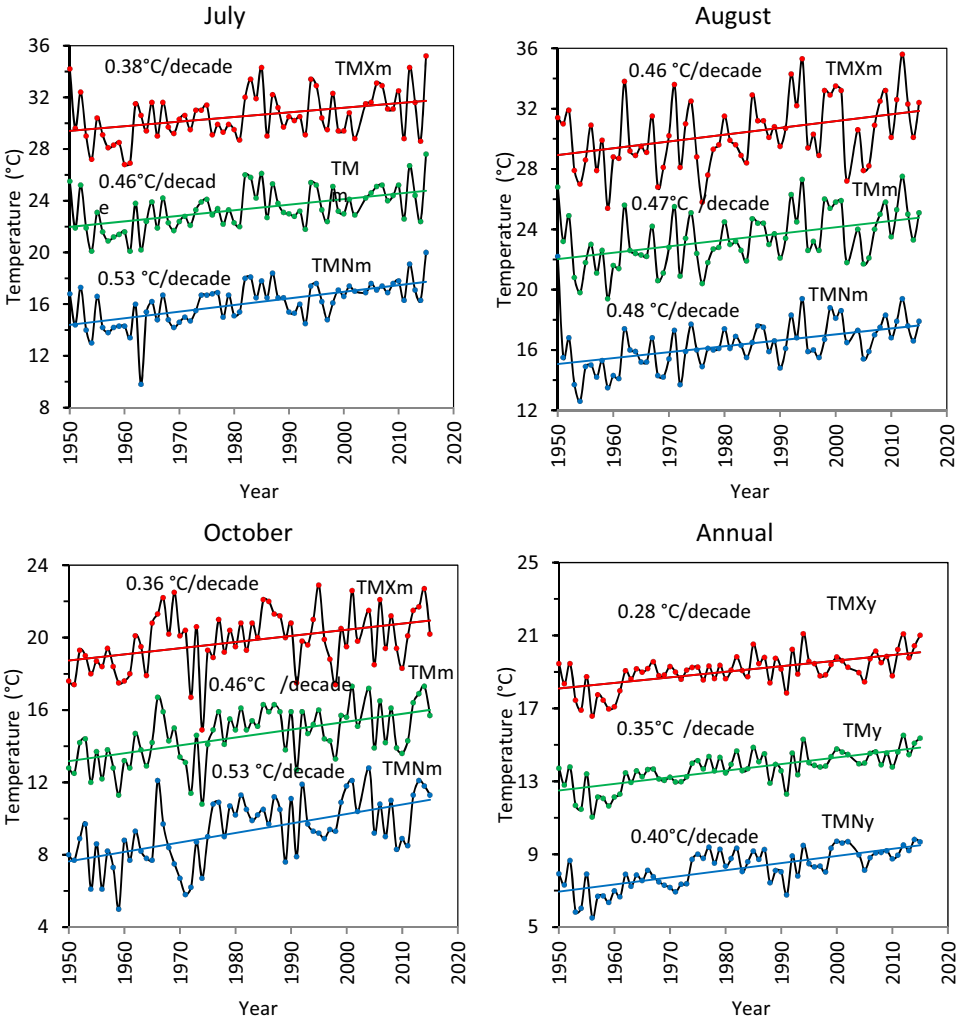

Fig. 4 Values of significant trends (°C/decade) detected in Spoleto for mean annual and monthly (July, August and October) temperature

level of significance of 5%, the value of $Z_{1-\alpha/2}$ is 1.9604. Values of $Z > 1.9604$ imply increasing trends, whereas values of $Z < -1.9604$ show decreasing trends.

The Pettit test

The Pettit test (Pettit 1979) is widely used to detect significant break points in temporal data series. This non-parametric test is very useful when the position of the break point is unknown. The null hypothesis (H_0) (no break point existence) states that a series is independent and has identically distributed random quantities, and the alternative hypothesis (H_1) is the existence of stepwise shift in the mean. Given a data series ($x1$, x_2, …, x_n) the ranks r_1, r_2, …, r_n are used to obtain the statistic U_k (Wijngaard et al. 2003),

$$U_k = 2\sum_{i=1}^{k} r_i - k(n+1) \quad k = 1, 2, \ldots, n \tag{6}$$

The tests statistic is calculated as,

$$K = \max_{1 \le k \le N} |U_k| \tag{7}$$

If a break occurs in year K, then the statistic is maximal or minimal near the year $k = K$. So, if the break occurs, then $U_K = \max U_k$. In order to probe the statistical significance of a detected break point, the obtained value of K is compared to its theoretical value for a α probability level, given by,

$$K_\alpha = \left[\frac{-\ln \alpha(n^3 + n^2)}{6}\right]^{1/2}. \tag{8}$$

For a certain α value (i.e. 0.05) the null hypothesis H_0 is rejected when $K > K\alpha$. If a break point exists, the series is divided into two around the break point.

The standard normal homogeneity test (SNHT)

The SNH test (Alexandersson 1986) can be used for the detection of abrupt breaks in the homogeneity of meteorological data series (Pandžic and Likso 2010). The test

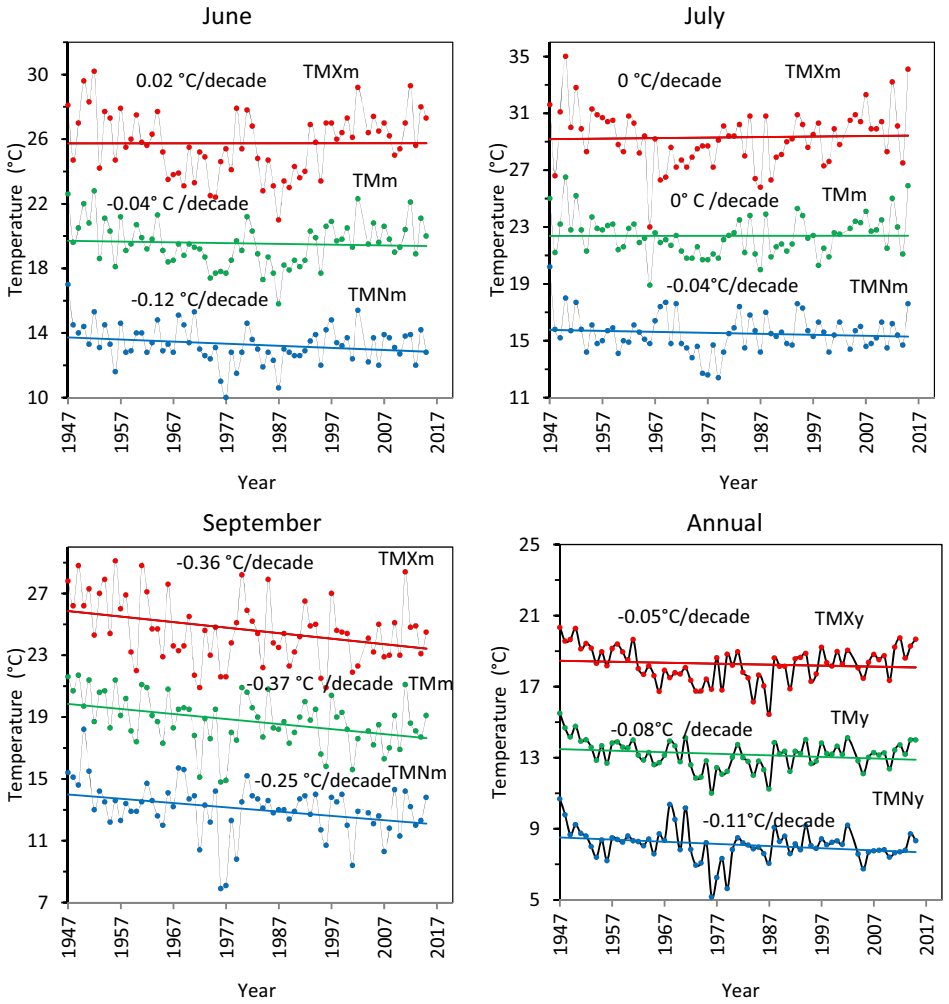

Fig. 5 Values of significant trends (°C/decade) detected in Gubbio for mean annual and monthly (June, July and September) temperature

assumes that the data series follows a normal distribution, and defines two hypotheses. The null hypothesis (H_0) states that the whole series is homogeneous and that any part follows a normal distribution. The alternative hypothesis implies that the series is inhomogeneous at year K, so that there is a mean for the first K years, and a different one for the following $n - K$ years.

Let's consider a data series with xi data (x_1, x_2, x_3,…, x_n,), being i the year from 1 to n, with an average value of $\bar{x}$ and a standard deviation s. Following Alexandersson (1986) the statistic $T(k)$ can be used to compare the average for the first K years to the one from the last $n - k$ years.

$$T(k) = k\bar{z}_1^2 + (n-k)\bar{z}_2^2 \quad k = 1, 2, \ldots, n-1 \tag{9}$$

Being,

$$\bar{z}_1 = \frac{1}{k}\frac{\sum_{i=1}^{k}(x_i - \bar{x})}{s} \tag{10}$$

$$\bar{z}_2 = \frac{1}{n-k}\frac{\sum_{i=k+1}^{n}(x_i - \bar{x})}{s} \tag{11}$$

If a break of a change exists at year K, then $T(k)$ become maximum near $k = K$. The statistic T_0 can then be defined as,

$$T_0 = \max_{1 \le k < n} T(k) \tag{12}$$

If T_0 is above the critical value (that depends on the sample size) of a certain critical level (e.g. 95%), then the null hypothesis of homogeneity can be rejected at the corresponding significance level (i.e. 5%). Critical values of SNHT statistic T_0 for various sample sizes obtained from Alexandersson (1986) are shown in Fig. 3. For different significance levels and bigger sample sizes, detailed information can be found in Khaliq and Ouarda (2007).

Results and discussion

For each site in both study areas, the Mann–Kendall test was applied to the six temperature indices shown in Table 3. For the Umbria region the results of trend analysis

Table 5 Significant trend values (°C/decade) for the Guadalquivir Valley

Station	Jan	Feb	Mar	Apr	May	Jun	Jul	Aug	Sep	Oct	Nov	Dec	Annual
TMm													TMy
Andújar			0.33			0.47	0.33	0.43					0.23
Montoro						0.50	0.31	0.47					0.19
Córdoba			0.30			0.37	0.31	0.37		0.22			0.20
Écija		0.19	0.32	0.19		0.31	0.22	0.29					0.18
Carmona		0.28	0.25	0.26		0.38	0.36	0.32					0.20
Alcalá del Río		0.25	0.32	0.19		0.31	0.24	0.28				0.24	0.22
Sevilla		0.24	0.33	0.27	0.25	0.45	0.37	0.38					0.26
Coria del Río			0.29			0.26	0.27	0.26					0.19
Cabezas S.J.			0.29	0.23		0.32	0.20	0.21					0.19
TMXm													TMXy
Andújar			0.41			0.45	0.24	0.27					0.18
Montoro			0.39			0.55	0.32	0.47					0.17
Córdoba		0.29	0.46			0.39		0.30					0.18
Écija	0.17	0.25	0.50			0.36	0.28	0.23				0.15	0.18
Carmona		0.29	0.33			0.30	0.29						0.15
Alcalá del Río		0.27	0.41			0.33	0.21					0.14	0.16
Sevilla		0.25	0.43			0.38	0.21	0.23					0.17
Coria del Río		0.32	0.43									0.14	0.16
Cabezas S.J.		0.20	0.43										0.11
TMNm													TMNy
Andújar				0.21	0.30	0.54	0.46	0.58	0.24	0.22			0.28
Montoro					0.21	0.50	0.33	0.46	0.23				0.23
Córdoba					0.25	0.41	0.45	0.44	0.27	0.35			0.23
Écija						0.29	0.18	0.33		0.22			0.19
Carmona				0.29	0.37	0.48	0.46	0.44	0.38	0.34			0.31
Alcalá del Río			0.22	0.22	0.24	0.29	0.26	0.33	0.34	0.31			0.24
Sevilla			0.25	0.29	0.38	0.52	0.50	0.50	0.37	0.33			0.35
Coria del Río						0.28	0.35	0.35	0.30				0.19
Cabezas S.J.					0.26	0.35	0.31	0.40	0.32	0.35			0.25

of annual temperature are shown in Table 4. Increases of temperature have been found for all the stations except for Gubbio, that showed a decreasing trend (Mann–Kendal statistic $Z < 0$) for the annual mean of daily minimum temperature (TMNy) with a value of -0.11 degrees centigrade per decade (°C/decade). A positive trend (values of Mann–Kendal statistic $Z > 0$) in the annual mean of daily average (TMy), maximum (TMXy) and minimum (TMXy) temperature appears for the stations of Perugia, Todi and Spoleto. For Perugia and Todi, the increase in temperature is similar, being 0.19 and 0.17 °C/decade for the annual mean of daily average temperatures, 0.19 and 0.16 °C/decade for TMXy, and 0.18 and 0.21 °C/decade for TMNy. Spoleto is the place with the highest values of trends detected, being 0.35 °C/decade for TMy, and 0.28 and 0.40 for TMXy and TMNy, respectively (see also Fig. 4). For the rest of stations analysed (Orvieto, Terni and Umbertide) there is no trend (nor positive neither negative) in TMXy. Positive trends are found for both TMy (0.11, 0.16 and 0.15) and TMNy (0.11, 0.30 and 0.23).

The trends in monthly temperature have been also analysed for the Italian region. As shown in Table 4 all the stations show an increase in any temperature index for some months, except Gubbio. This last site, as happened for the annual behaviour, presents a significant negative trend in September for the indexes TMm, TMXm and TMNm, equal to -0.37, -0.36 and -0.25 °C/decade, respectively. A decrease in TMNm is also found for the same station in February (-0.25 °C/decade), while no significant trends are present in the other months (see also Fig. 5).

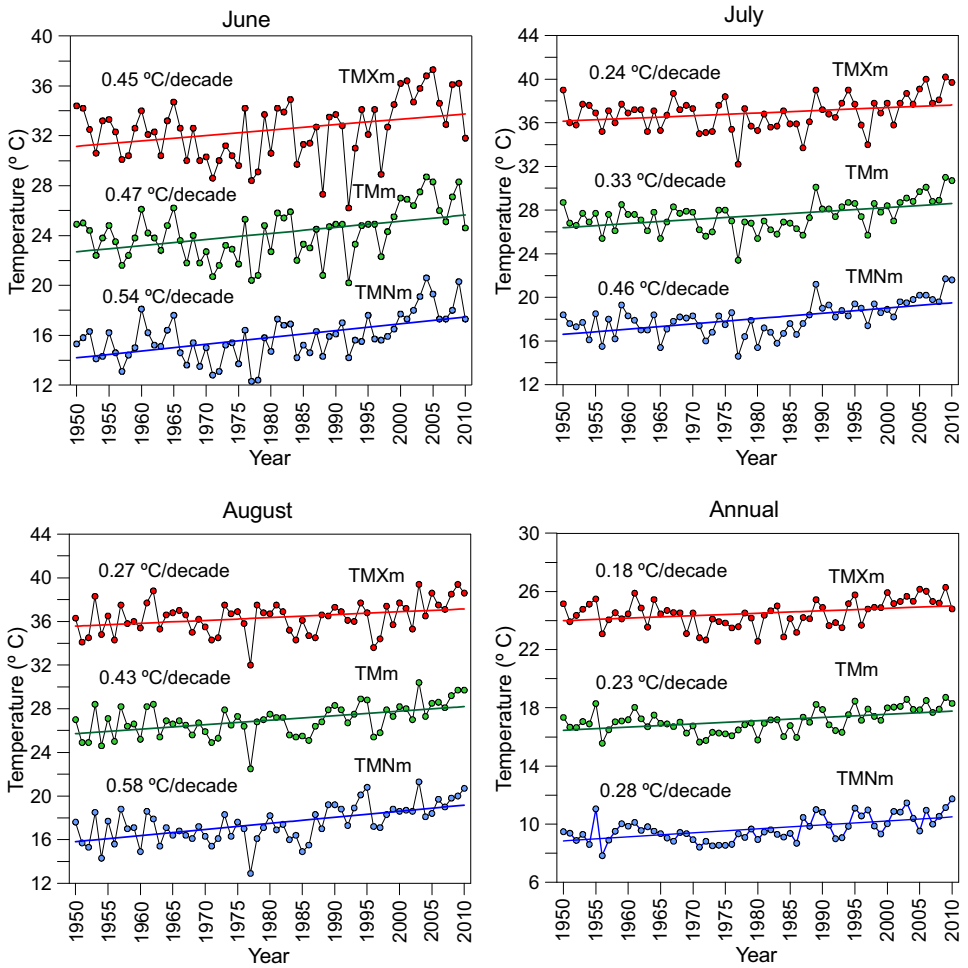

Fig. 6 Values of significant trends (°C/decade) detected in Andujar for mean annual and monthly (June, July and August) temperature

Focusing in the TMm, similar behaviour can be found for the stations of Perugia and Spoleto during January, March to August, and October. For all these months, increases of TMm higher than 0.20 °C/decade can be found, being the values for Spoleto higher than those for Perugia (almost double). A general increase on TMm is found in Spoleto for all the months except February. In fact, no trend is found for any temperature index (TMm, TMXm and TMNm) in February (Table 4). From May to August, TMm for Todi behaves similar to Perugia. Positive trend is also found from October to January.

For the values of monthly mean of daily maximum temperature (TMXm) Spoleto shows positive trend for all the months except for February and September, with values that range from 0.25 °C/decade in December to 0.46 °C/decade in August. Spoleto is followed by Perugia that presents an increase in TMXm for the same months except November and December, when no trend has been detected. The values of TMXm are also increasing during the central months (from May to August) for Todi with values around 0.20 °C/decade also for October and January. No trend is detected in the values of TMXm for Terni and Umbertide. Almost the same happens in Orvieto, which only shows an increase of 0.25 °C/decade in May.

From Table 4 it can also be seen a general increase in the monthly mean of daily minimum temperature (TMNm), with positive trends even found in sites with no trends in TMm or TMXm, like Terni and Umbertide. The only site with a negative trend in TMNm is again Gubbio, as stated before. After Gubbio, Orvieto is the place where fewer changes in TMNm are found.

All the results shown above are in agreement with those preciously found in Italy based on the analysis of mean values of climatological variables. As an example, Brunetti et al. (Brunetti et al. 2000a, b) analysed monthly mean values of daily maximum, mean and minimum temperatures available from about 40 stations covering Italy. They divided the series long more than 100 years into two groups corresponding to Northern Italy (the continental region) and Central-Sothern Italy (the peninsular region including Umbria) due to climatic differences. They found positive trends, in the range 0.04–0.07 °C/decade on annual temperature indexes in both series subgroups with values greater in the Central-Southern Italy; on a seasonal

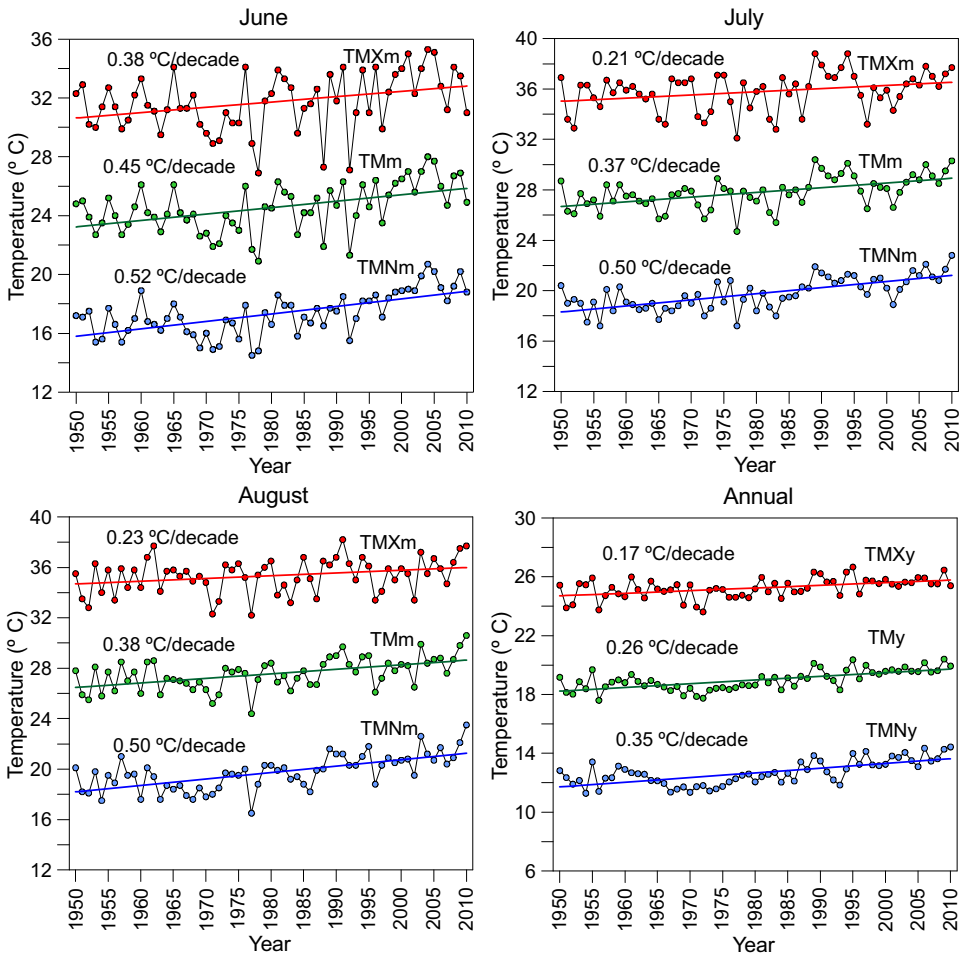

Fig. 7 Values of significant trends (°C/decade) detected in Sevilla for mean annual and monthly (June, July and August) temperature

basis positive trends were observed for all the four seasons in the Central-Southern Italy and for three seasons (autumn, springer, winter) in the Northern Italy. Furthermore, evidences of significant increases of temperature in the period 1920–1950 and then starting from 1985 are also reported. In addition, a variety of studies addressing the effects of the global climate change on specific areas of Italy are also available. Viola et al. (2014) provided evidence of a general warming in Sicily region (in the Southern Italy) with a strong rising of temperature observed in the last years of the past century with average annual temperature increase of about 0.19 °C/decade, significantly higher than that observed in other Italian regions. Tomozeiu et al. (2006) observed positive trends in seasonal minimum and maximum temperatures, the increase being more pronounced in maximum temperature with values up to 0.40 °C/decade in summer, winter and spring.

Table 5 shows the results of Mann–Kendall test for the nine stations analysed within the Guadalquivir Valley. The statistic Z adopts values bigger than 1 for TMy, TMXy and TMNy in all the stations, with increases usually higher than 0.20 °C/decade for the annual mean of daily average and minimum temperatures, and a little lower than 0.20 °C/decade for the annual mean of daily maximum temperature. Then, it can be said that in the Guadalquivir valley the annual mean of daily temperatures is increasing, whereas for the Umbria region this general pattern is not clearly found. In fact, no trends were found in this last region for some stations in the annual mean of daily temperatures (Table 4), or if found, it was a negative trend (− 0.11, − 0.05 and − 0.08 °C/decade in Gubbio for TMNy, TMXy and TMy, respectively). This general increase in the temperature of the Guadalquivir Valley can be seen in Figs. 6 and 7 that shows the results of Mann–Kendall test for the stations of Andujar and Sevilla, respectively. Focusing in the results for these two sites, even though the increase in TMXy is almost similar, Sevilla (Fig. 7) gives higher values of Z for both TMy and TMNy.

The monthly results of Mann–Kendall test for the Guadalquivir Valley (Table 5) give a general pattern of increasing temperatures during the summer (June, July and August) for all the stations for TMm, TMXm and TMNm. This last monthly temperature also shows positive trends during the last summer (September) for all the sites except

Table 6 Break points detected by Pettit and SNH tests (year Pettit/year SNHT) for Umbria region

Station	Jan	Feb	Mar	Apr	May	Jun	Jul	Aug	Sep	Oct	Nov	Dec	Annual
TMm													TMy
Gubbio			/49			65/53			71/71		73/73		62/53
Orvieto	51/51	51/51		97/97	92/92	96/96	94/94	91/91		99/99			94/93
Perugia	70/70		89/89	98/06	98/91	93/98	82/04	85/85		85/85	94/08		85/96
Spoleto	70/70	74/66	74/74	81/61	92/64	93/96	82/82	85/85	73/	76/76	63/63	75/75	74/79
Terni	69/			06/06	/47		/49	70/70		79/79	/08	75/48	78/12
Todi	70/70			/06	85/92	93/93	82/82	81/		81/83	57/57	76/	87/86
Umbertide				97/05	97/	96/98		91/98		98/99	94/02	93/	94/06
TMXm													TMXy
Gubbio				65/54		96/53	64/		67/59				62/62
Orvieto		51/51		97/97	92/92	93/93	04/04						94/93
Perugia	98/98		89/89	98/06	98/91	93/98	82/04	85/87		85/85	94/94		85/92
Spoleto	70/69	/66	72/72	06/06	92/63	93/93	82/82	85/85		65/65	63/63	75/	82/67
Terni	/40			/06							/49	75/	60/51
Todi	70/58			/06	92/	93/93	82/82	85/87		85/85	57/57		87/86
Umbertide				98/06		98/98						93/	97/06
TMNm													TMNy
Gubbio				72/72	/49	72/72	/48	/49	72/52		73/73		72/72
Orvieto	59/59	51/51	00/00	98/98	97/97	96/96	94/94	92/92					94/93
Perugia	69/48	57/57	72/89	98/06	98/91	93/96	82/82	85/85		76/76	/12		80/42
Spoleto	70/70		74/74	81/98	74/66	96/96	74/74	80/80	73/73	76/76	92/60	75/75	74/79
Terni			74/47	81/47	68/47	88/47	82/49	71/62	81/47	79/79	58/57	75/49	80/53
Todi	70/			83/	83/83	90/93	82/82	80/85	81/	79/79	90/92	76/	81/80
Umbertide	88/			94/97	94/97	96/96	72/	97/94	97/	98/98	00/00		94/94

for Ecija, and even at the early autumn (October) everywhere except in Montoro and Coria del Rio. The increase in the monthly mean of daily minimum temperature (TMNm) starts in March for Alcalá del Rio and Sevilla, in April for Andújar and Carmona, and in May for Montoro, Cordoba and Cabezas de San Juan.

While the increase of TMNm according to Mann–Kendall test results are concentrated from late spring to early autumn, values of $Z > 0$ are also found during the months of February and March for TMm and TMXm. The increases in March are found for all the sites except for the TMm in Montoro. TMXm increases in February in all the sites except in Andujar and Montoro, whereas the increases in TMm are found in the central stations of the Guadalquivir Valley (Ecija, Carmona, Alcalá del Río y Sevilla). Isolated values of $Z > 0$ are also found for TMm in October (in Ecija) and December (in Alcalá del Río), and for TMXm in January (in Ecija) and December (Ecija, Alcalá del Río and Coria del río).

The increases of temperature from year 1959 to year 2010 in the stations of Andujar and Sevilla for the main months that showed positive values of Mann–Kendall statistic (June, July and August) are shown in Figs. 6 and 7. In general, the increase of temperature is always higher in Andujar than in Sevilla, except in July for TMm and TMNm, when the values in Sevilla (0.37 and 0.50 °C/decade) are a bit higher than in Andujar (0.33 and 0.46 °C/decade).

All the results found in this work in the Guadalquivir Valley, are in agreement with those previously found by other authors all over Spain (e.g. Del Río et al. 2011, 2012) or Andalusia (e.g. Sousa et al. 2007; Llorente 2012). The general finding is that the temperature has increased in mainland Spain during the 20th century, with an evident increase during spring and summer (Gonzalez-Hidalgo et al. 2015).

Once the existence of any trends in the temperature data series analysed in both Umbria and Guadalquivir Valley regions was studied, the existence of any possible break points in the same data series was investigated by applying the Pettit and the NSH tests. The null hypothesis assumes that no break exists, whereas under the alternative hypothesis, they assume that a break in the mean is present.

Table 7 Break points detected by Pettit and SNH tests (year Pettit/year SNHT) for Guadalquivir Valley

Station	Jan	Feb	Mar	Apr	May	Jun	Jul	Aug	Sep	Oct	Nov	Dec	Annual
TMm													TMy
Andújar			86/86	94/94		93/98	88/88	88/88				75/	86/93
Montoro			80/86		85/	80/93	88/88	87/87					80/84
Córdoba			86/86	94/94	85/	93/93	83/88	87/87		93/93			75/93
Écija		/56	86/86	94/94	85/	88/98	88/88	87/87				/75	75/86
Carmona			86/86	83/86	85/	88/88	83/87	87/87				75/75	80/86
Alcalá del Río			80/86	80/94	85/	78/93	85/83	87/87				75/75	80/86
Sevilla			86/86	91/94	85/85	88/93	87/87	87/87	76/76			75/73	86/86
Coria del Río			86/86	94/94		78/97	87/88	87/87				75/75	78/83
Cabezas S.J.			79/93	94/94		93/97	/03	/08				75/73	94/94
TMXm													TMXy
Andújar			86/86	94/94		97/98	88/01	97/02					93/93
Montoro			80/80			80/93	87/87	84/84					80/79
Córdoba			80/86			93/98	88/	87/87				73/73	80/93
Écija		88/	80/80	91/		88/98	88/					73/73	79/79
Carmona		87/06	80/80	83/		88/	83/	87/87	92/			73/	80/80
Alcalá del Río		88/	80/80			78/93	83/87	/08				76/73	79/79
Sevilla		88/	80/80	90/		78/97	87/87	87/				73/73	88/88
Coria del Río		88/	80/86	91/91		88/98	88/					76/76	86/87
Cabezas S.J.		77/	80/80			93/97			91/			73/73	93/93
TMNm													TMNy
Andújar			88/89	95/95	91/94	94/99	87/87	86/88	77/	84/85			86/86
Montoro			88/	94/94	85/91	80/93	88/88	87/88	79/79	84/			84/93
Córdoba				94/95	85/91	80/94	84/84	86/86	79/79	84/84			86/94
Écija			88/88	94/95	85/91	93/97	87/88	86/86	76/	93/93			86/94
Carmona		/06	86/86	80/95	85/85	89/89	85/86	86/86	79/79	82/82		75/	84/86
Alcalá del Río			89/88	95/95	85/85	93/93	84/85	86/86	76/76	84/93		75/75	84/86
Sevilla			88/88	94/95	85/95	93/93	86/86	86/87	77/76	93/93		74/74	86/86
Coria del Río					89/89	78/78	86/86	78/78	76/76				76/76
Cabezas S.J.			95/95	95/95	93/93	93/97	83/83	86/86	77/77	93/00			94/94

For the seven stations available at the Umbria region, Table 6 shows the break points detected for the temperature data series by applying the Pettit and the NSH tests. Focusing on the annual mean of daily average (TMy), maximum (TMXy) and minimum (TMNy) temperature, changes are found for all the stations with both tests applied. The year of the break is identical for both tests only at Gubbio (for TMXy and TMNy), and Umbertide (for TMNy). For the monthly mean temperatures TMm, TMXm and TMNm, several break points have been detected at all the stations. Both tests applied gave the same year for the 50.97% of the breaks detected. If only a year of difference is considered, the percentage increases to 54.19%. For 31 breaks detected out of the total (186) only one test gave information of a break point: 7 breaks detected with NSH test and 24 with the Pettit test.

By the analysis of Table 6, the breaks found in data series by applying homogeneity tests cannot be ascribed to changes in station sensors or locations because they occur in different periods. Only in the case of Umbertide station some monthly or annual temperature indexes exhibit breakpoints near the station repositioning year (at the end of 90's). In addition, it's possible to notice that, even if the breakpoints involve a wide range of years through the selected stations, two specific periods recur: the first part of 80's and the first half of 90's. The inhomogeneities detected for years close to these two periods can probably be related to effects of climate change on temperature indexes in the region along the lines of other results available in literature (Brunetti et al. 2000a, b).

Table 7 shows the break points analysis for the stations at the Guadalquivir Valley. If Tables 5 and 7 are compared,

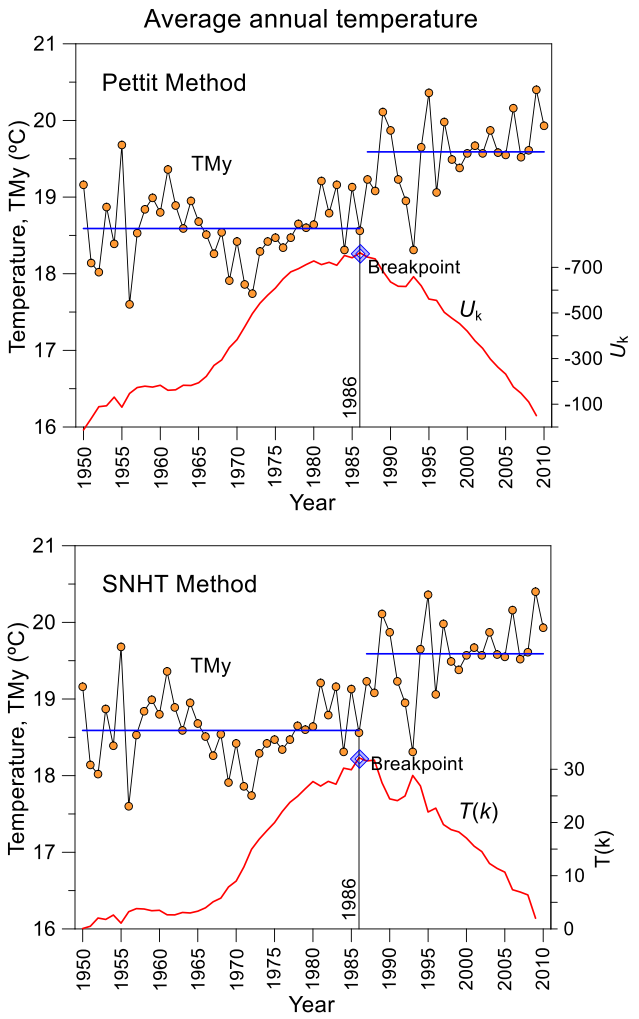

Fig. 8 Break points detected by Pettit and SNHT method for Sevilla (Guadalquivir Valley)

a similar pattern can be observed according to the location and months, and TMm, TMXm and TMNm series. Attending to the break points results, similar years were detected by Pettit and NSH tests in 58.14% of the total detections 172. If a difference of only 1 year is considered, the percentage is then a 66.28%. For some months, only one test detected a break point being mainly given by Pettit test. Figure 8 shows the break point detected with both Pettit and SNH tests for annual data in Sevilla (Guadalquivir Valley). The mean annual average temperature before and after the break point detected in 1986 and the statistics' behaviour of each method are also represented.

The breaks found in data series by applying homogeneity tests like the one in this work, would be usually due to changes in sensors or in the weather station location. For the results shown in Table 7, these motives can be discarded because of two main reasons. First of all, the data base used was preciously put through a high quality control by Gonzalez-Hidalgo et al. (2015). Secondly, it is very unlikely to find the same break points at the same time for all the stations, like occurs for TMm, TMxm and TMNm (Table 7). In consequence, the break points detected for the Guadalquivir Valley stations, should be attributed to natural phenomena, like volcanic eruptions (e.g. Martínez et al. 2010). All the inhomogeneities detected for years close to periods 1982–1984 and 1991–1994, can then be related to periods of strong eruptions over the world (e.g. Morozova and Valente 2012). The majority of break points detected for the stations in the Guadalquivir Valley are around these ranges.

Conclusions

Although climate change and its effects on the increase of global surface temperature is widely known, in order to analysis the local effects, we present in this work a regional analysis of six temperature indices over two different regions in the Mediterranean area.

Working with previously validated monthly temperature data led us to find representative results at each area. The Mann–Kendall test showed the presence of significant trends in both areas. For the Spanish area (the Guadalquivir Valley) all the trends detected were positive, showing increases of temperature that ranges from 0.11 °C/decade for the mean annual of daily maximum temperature (TMXy) to 0.58 °C/decade for the mean monthly of daily minimum temperature (TMNm). The same pattern of trends was detected for all the stations in the region, with higher temperatures in summer and an increase in the minimum values from late spring to early autumn. For the Italian area (the Umbria region) positive trends were also found for all the sites except for one at which different temperature indices seem to be descending in February, June, July and September. The different geographical characteristics of this station may be the reason of this different behaviour. Although a general positive trend pattern was found in both Umbria and Guadalquivir Valley, no clear pattern in the months with increases in temperature can be defined in the former region. For instance, some sites showed no trends in the mean annual of daily maximum temperature, and at those sites with increases in temperature indices they are distributed along the year.

Therefore, although the temperature indices studied showed the general increasing trend of global surface temperature, some differences were found among regions and long the year, with sites or months even with no trends detected.

The Pettit and SNH tests were then applied in order to detect any change or break points in the data series analysed. Since the quality of all the series had been previously checked, the breaks found gave information related

basically to climate processes. Again, the results were more homogeneous for the Guadalquivir Valley at which several dates of the detected break points were similar for both tests and stations, and as happened with the trends, they were concentrated in certain months or periods. For the Umbria region, there was no clear pattern again in the breaks detected, but if found, they were also mainly similar for both tests.

All the results of this work show the importance of develop a local analysis of monthly temperature data before approach any study that may depend on them. Even when the general increase of temperature is worldwide present, the local behaviour may be different due to geographical, human or natural phenomena.

Acknowledgements The authors want to acknowledge the kindness and help of Jose Carlos González-Hidalgo with providing the temperature data of the Guadalquivir Valley stations from the database MOTEDAS.

Compliance with ethical standards

Conflict of interest On behalf of all authors, the corresponding author states that there is no conflict of interest.

References

Aguilar E, Auer I, Brunet M, Peterson TC, Wieringa J (2003) Guidelines in climate metadata and homogenization. WCDMP No. 53, WMO-TD No. 1186. WMO. Geneva. Switzerland

Alexandersson H (1986) A homogeneity test applied to precipitation data. J Climatol 6:661–675

Brunet M, Sigro J, Saladie O, Aguilar E, Jones P, Moberg A, Walther A, Lopez D (2005) Spatial patterns of long-term Spanish temperature change. Geophys Res Abstr 7:04007

Brunet M, Saladie O, Jones PD, Sigro J, Aguilar E, Moberg A, Lister DH, Walther A, Lopez D, Almarza C (2006) The development of a new dataset of Spanish daily adjusted temperature series (SDATS) (1850–2003). Int J Climatol 26:1777–1802

Brunet M, Jones P, Sigro J, Saladie O, Aguilar E, Moberg A, Della-Marta PM, Lister D, Walther A, Lopez D (2007) Temporal and spatial temperature variability and change over Spain during 1850–2005. J Geophys Res 112:D12117

Brunetti M, Maugeri M, Nanni T (2000a) Variations of temperature and precipitation in Italy from 1866 to 1995. Theor Appl Climatol 65:165–174

Brunetti M, Buffoni L, Maugeri M, Nanni T (2000b) Trends of minimum and maximum daily temperatures in Italy from 1865 to 1996. Theor Appl Climatol 66:49–60

Brunetti M, Maugeri M, Monti F, Nannia T (2006) Temperature and precipitation variability in Italy in the last two centuries from homogenised instrumental time series. Int J Climatol 26:345–381

Caloiero T, Coscarelli R, Ferraric E, Sirangelod B (2017) Trend analysis of monthly mean values and extreme indices of daily temperature in a region of southern Italy. Int J Climatol. https://doi.org/10.1002/joc.5003

del Río S, Herreo L, Pinto-Gomes C, Penas A (2011) Spatial analyses of mean temperature trends in Spain over the period 1961–2006. Glob Planet Change 78:65–75

del Río S, Cano-Ortiz A, Herrero L, Penas A (2012) Recent trends in mean maximum and minimum air temperatures over Spain (1961–2006). Theor Appl Climatol 109:605–626

Douglas EM, Vogel RM, Kroll CN (2000) Trends in floods in low flows in the United States: impact of spatial correlation. J Hydrol 240:90–105

Feidas H (2016) Trend analysis of air temperature time series in Greece and their relationship with circulation using surface and satellite data: recent trends and an update to 2013. Theor Appl Climat. https://doi.org/10.1007/s00704-016-1854-2

Gonzalez-Hidalgo JC, Peña-Angulo D, Brunetti M, Cortesi C (2015) MOTEDAS: a new monthly temperature database for mainland Spain and the trend in temperature (1951–2010). Int J Climatol 35:4444–4463

Hamed KH (2008) Trend detection in hydrologic data: the Mann–Kendall trend test under the scaling hypothesis. J Hydrol 349:350–363

Hu Y, Maskey S, Uhlenbrook S (2012) Trends in temperature and rainfall extremes in the Yellow River source region, China. Clim Change 110:403–429

IPCC (2014) Climate change 2014: synthesis report. Fifth Assessment report, Ginebra, Suiza

Jung IW, Baeand DH, Kim G (2011) Recent trends of mean and extreme precipitation in Korea. Int J Climatol 31:359–370

Kahya E, Kalayci S (2004) Trend analysis of streamflow in Turkey. J Hydrol 289:128–144

Kendall MG (1975) Rank correlation methods. Ed, Charles Griffin, London

Khaliq MN, Ouarda TBMJ (2007) Short Communication on the critical values of the standard normal homogeneity test (SNHT). Int J Climatol 27:681–687

Klok EJ, Klein-Tank AMG (2009) Updated and extended European dataset of daily climate observations. Int J Climatol 29:1182–1191

Llorente M (2012) Tendencias españolas de variables agrometeorológicas en los últimos 30 años. Departamento de Producción Vegetal, Universidad Politécnica de Madrid, ETSIA, p 99

Mann HB (1945) Non parametric test against trend. Econometrica 13:245–259

Martínez MD, Serra C, Burgueño A, Lana X (2010) Time trends of daily maximum and minimum temperatures in Catalonia (NE Spain) for the period 1975–2004. Int J Climatol 30:267–290

Morales CG, Ortega MT, Labajo JL, Piorno A (2005) Recent trends and temporal behavior of thermal variables in the region of Castilla–Leon (Spain). Atmosfera 18:71–90

Morozova AL, Valente MA (2012) Homogenization of Portuguese long-term temperature data series: Lisbon, Coimbra and Porto. Earth Syst Sci Data 4:187–213

Pandžić K, Likso T (2010) Homogeneity of average air temperature time series for Croatia. Int J Climatol 30:1215–1225

Pettit AN (1979) A non-parametric approach to the change-point problem. Appl Stat 28:126–135

Piccarreta M, Lazzari M, Pasini A (2015) Trends in daily temperature extremes over the Basilicata region (southern Italy) from 1951 to 2010 in a Mediterranean climatic context. Int J Climatol 35:1964–1975

Rougé C, Ge Y, Cai X (2013) Detecting gradual abrupt changes in hydrological records. Adv Water Resour 53:33–44

Shadmani M, Marofiand S, Roknian M (2012) Trend analysis in reference evapotranspiration using Mann–Kendall and Spearman's Rho tests in Arid Regions of Iran. Water Resour Manage 26:211–224

Sousa A, García-Barrón L, Jurado V (2007) Climate change in Andalusia: trends and environmental consecuences. Consejería de Medio Ambiente. Junta de Andalucía

Tank AMGK, Können GP (2003) Trends in indices of daily temperature and precipitation extremes in Europe, 1946–99. J Clim 16:3665–3680

Tomozeiu R, Pavan V, Cacciamani C, Amici M (2006) Observed temperature changes in Emilia-Romagna: mean values and extremes. Clim Res 31(2–3):217–225

Viola F, Liuzzo L, Noto LV, Lo Conti F, La Loggia G (2014) Spatial distribution of temperature trends in Sicily. Int J Climatol 34:1–17

Wijngaard JB, Klein Tank AMG, Konnen GP (2003) Homogeneity of 20th century European daily temperature and precipitation series. Int J Climatol 23:679–692

Yu YS, Zou S, Whittemore D (1993) Nonparametric trend analysis of water quality data of rivers in Kansas. J Hydrol 150:61–80

Yue S, Pilon P, Phinney B, Cavadias G (2002) The influence of autocorrelation on the ability to detect trend in hydrological series. Hydrol Processes 16:1807–1829

Acta Geophysica (2018) 66:345
https://doi.org/10.1007/s11600-018-0145-y

CORRECTION

Correction to: Detection of trends and break points in temperature: the case of Umbria (Italy) and Guadalquivir Valley (Spain)

Pascual Herrera-Grimaldi[1] · Amanda García-Marín[1] · José Luís Ayuso-Muñoz[1] · Alessia Flammini[2] · Renato Morbidelli[2] · José Luís Ayuso-Ruíz[1]

Published online: 13 April 2018

Correction to: Acta Geophysica
https://doi.org/10.1007/s11600-018-0118-1

In the original authors list there was a mistake with the surname of Professor Alessia Flammini. The corrected authors list is:

Pascual Herrera-Grimaldi, Amanda García-Marín, José Luís Ayuso-Muñoz, Alessia Flammini, Renato Morbidelli, José Luís Ayuso-Ruíz.

The original article can be found online at https://doi.org/10.1007/s11600-018-0118-1.

✉ Amanda García-Marín
amanda.garcia@uco.es

[1] Área de Proyectos de Ingeniería, Departmento de Ingeniería Rural, Universidad de Córdoba, Edificio Leonardo Da Vinci, Campus de Rabanales, Carretera Nacional IV Km 396, Córdoba, Spain

[2] Department of Civil and Environmental Engineering, University of Perugia, Via G. Duranti, 93, Perugia, Italy

Acta Geophysica (2018) 66:347–360
https://doi.org/10.1007/s11600-018-0116-3

RESEARCH ARTICLE - SPECIAL ISSUE

Trend detection in river flow indices in Poland

Mikołaj Piniewski[1,2] · Paweł Marcinkowski[1] · Zbigniew W. Kundzewicz[2,3]

Received: 15 November 2017 / Accepted: 1 February 2018 / Published online: 7 February 2018

Abstract
The issue of trend detection in long time series of river flow records is of vast theoretical interest and considerable practical relevance. Water management is based on the assumption of stationarity; hence, it is crucial to check whether taking this assumption is justified. The objective of this study is to analyse long-term trends in selected river flow indices in small- and medium-sized catchments with relatively unmodified flow regime (semi-natural catchments) in Poland. The examined indices describe annual and seasonal average conditions as well as annual extreme conditions—low and high flows. The special focus is on the spatial analysis of trends, carried out on a comprehensive, representative data set of flow gauges. The present paper is timely, as no spatially comprehensive studies (i.e. covering the entire Poland or its large parts) on trend detection in time series of river flow have been done in the recent 15 years or so. The results suggest that there is a strong random component in the river flow process, the changes are weak and the spatial pattern is complex. Yet, the results of trend detection in different indices of river flow in Poland show that there exists a spatial divide that seems to hold quite generally for various indices (annual, seasonal, as well as low and high flow). Decreases of river flow dominate in the northern part of the country and increases usually in the southern part. Stations in the central part show mostly 'no trend' results. However, the spatial gradient is apparent only for the data for the period 1981–2016 rather than for 1956–2016. It seems also that the magnitude of increases of river flow is generally lower than that of decreases.

Keywords River flow · Trend detection · High flows · Low flows · Poland

Introduction

The issue of trend detection in long time series of river flow records is a very important task of vast theoretical interest and considerable practical relevance (Kundzewicz et al. 2005). The former statement reflects the search for impacts of the ongoing climate change. Climate change track is easy to find in records of increasing temperature, but the situation is far more complex in precipitation and even more so in river flow records. The latter statement reflects the fact that water management is based on the assumption of stationarity, that is, constancy of statistical properties of the river flow record. Hence, it is crucial to find whether the statistical properties of the record can be regarded as approximately stationary, recognizing that stationarity is only a convenient idealization (Milly et al. 2008, 2015). For instance, flood risk reduction is based on the concept of design flood, with the probability of exceedance in any one year being, depending on the area, 0.01, 0.05, 0.1, etc. River flow corresponding to a given probability of exceedance is the parameter of importance for people responsible for flood preparedness, both from the viewpoint of general natural disaster risk reduction and climate change adaptation, as flood risk tends to increase in the warming climate, with more room for water vapour is the warmer atmosphere (Hanson et al. 2007).

No research known to the authors convincingly demonstrates a regionally ubiquitous and uniform change in river flow at any larger scale (global, continental, regional, national). There exist several contributing (and partly compensating) factors affecting the river flow process.

✉ Mikołaj Piniewski
m.piniewski@levis.sggw.pl

[1] Department of Hydraulic Engineering, Warsaw University of Life Sciences – SGGW, Warsaw, Poland

[2] Potsdam Institute for Climate Impact Research, Potsdam, Germany

[3] Institute for Agricultural and Forest Environment, Polish Academy of Sciences, Poznań, Poland

As noted by Kundzewicz and Robson (2004), data are indeed the backbone of change detection in hydrological records; hence, conditions that have to be fulfilled by the data are quite demanding. A series of records should be sufficiently long (in relation to the natural variability of the process) for a change to be detected with adequate reliability. The choice of river gauging stations to be used typically reflects such criteria as the length of the time series of good-quality records as well as the currency of records that should extend through to a recent past. Missing values and gaps in data are complicating factors. It is advantageous to seek a representative geographical coverage, while avoiding the inclusion of many neighbouring (and possibly correlated) gauging stations in the data set. Also, catchment size is of relevance, with priority given to smaller catchments which are more likely to have less strong anthropogenic influence in comparison to larger catchments. Selection of stations to use in a climate change impact study is particularly important (cf. Kundzewicz and Robson 2004). River flow is the integrated result of natural factors, such as precipitation, catchment storage and evaporation, as well as catchment management practices and river engineering that alter the river conveyance system over time. This complicates the problem of detecting a climate change signature in river flow data (Kundzewicz et al. 2005). To assess climatically forced hydrological changes, data should be taken, to the extent possible, from near-pristine drainage basins that are not largely affected by human activities (urbanization, deforestation, reservoirs, drainage systems, water abstraction, river engineering, etc.). Catchments featuring significant changes during the interval of records, related to land use and land cover or river regulation are not appropriate.

The objective of this study is the analysis of long-term trends in selected river flow indices describing annual and seasonal average conditions as well as annual extreme conditions in small- and medium-sized catchments with relatively unmodified flow regime (semi-natural catchments) in Poland. The special focus is on the spatial analysis of trends, carried out on a comprehensive, representative data set of flow gauges used in this study.

Climate change in Poland manifests itself in the most pronounced way in observed temperature records, particularly heat indices (Graczyk et al. 2017). To interpret the change in river flow, it is important to examine the results of change detection studies in precipitation (therein also intense precipitation and snow-related characteristics), where weaker, although apparent trends, were detected, e.g. in precipitation-based drought indices by Somorowska (2016). Pińskwar et al. (2018a) analysed changes in observed daily precipitation records in Poland from 1951 to 2015. Trends were detected, but mostly weak and statistically insignificant. Yet, there are regionally consistent seasonal changes and precipitation increase in spring and winter dominates. Pińskwar et al. (2018b) examined precipitation extremes in Poland, showing that daily maximum precipitation for the summer half-year (Apr.–Sept.) increased for many stations and there were more positive changes during the summer half-year than those in the winter half-year (Oct.–March). The number of days with intense precipitation ($\geq$ 10 mm per day) increased especially in the north-western part of Poland. Szwed et al. (2017) examined the variability of the characteristics of snow cover in Poland. They found that the observed time series of snow-related variables have complex and not easily interpretable behaviour. Yet, a statistical link between the North Atlantic Oscillation (NAO) index and the snow cover depth, as well as the number of snow cover days was found.

Although a substantial amount of studies on trend detection of different types of hydrological indices were published in the Polish language (see, e.g. a review of such studies by Pociask-Karteczka 2011), very few are available for a wider international audience in the English language. Those available ones typically used time series ending in the 1990s (Strupczewski et al. 2001) or early 2000s (Kaczmarek 2003). More recent studies usually focused on single catchments (e.g. Banasik et al. 2013; Ilnicki et al. 2014; Kędra 2017; Miler 2015; Somorowska 2017) or small regions (Niedźwiedź et al. 2015; Ruiz-Villanueva et al. 2016; Sen and Niedzielski 2010), with one notable exception of Wrzesiński and Sobkowiak (2018) who analysed long-term changes (but not trends) in flow regime of 159 flow gauges with a good geographical coverage in Poland. Polish rivers were not included in several pan-European (Hannaford et al. 2013; Stahl et al. 2010) or global (Hodgkins et al. 2017) studies on trend detection, perhaps due to restrictive data sharing policy (Kundzewicz et al. 2017). In summary, a need for a comprehensive trend detection study for Polish river flows is well motivated.

Materials and methods

River flow data

Many countries (e.g. Canada, UK, USA) possess networks of gauges with long and uninterrupted river flow records from catchments with minimal anthropogenic activity—sometimes referred to as reference hydrometric networks, RHNs (Burn et al. 2012). Such networks are usually subsets of national hydrometric networks and are particularly useful for detecting and attributing trends in river flow indices. Data sets of gauging stations with RHN-like characteristics were also created for large parts of Europe

(Stahl et al. 2010) or for the Alpine region in central Europe (Bard et al. 2015). Although Poland does not maintain its RHN, in this study we have used a data set of gauging stations with RHN-like features.

In his study of classification of natural flow regimes in Poland, Piniewski (2017) analysed a large observation data set of long time series of river flow records, covering the whole country. Flow data were acquired from the Institute of Meteorology and Water Management, National Research Institute (IMGW-PIB). To select data suitable for this analysis, Piniewski (2017) sought gauging stations in river cross sections terminating small to medium catchments with relatively unmodified flow regime. Selected catchments were characterized by a good geographical coverage taking into account spatial climatic and physiographic variability as well as the length of the available river flow record (Piniewski 2017). Gauges with catchment area of more than 10,000 km^2 were excluded, as at this scale flow disturbance is almost unavoidable (Leasure et al. 2016). A comprehensive analysis of available GIS data was carried out to exclude catchments suspected to have a moderate or high degree of flow regime disturbance (cf. Piniewski 2017). For example: (1) all catchments containing reservoirs with capacity above 5 million m^3 were excluded; (2) catchments containing cities with population above 200,000 inhabitants were all excluded. Daily hydrographs for all gauges were inspected to identify dubious patterns. It is acknowledged that some, unavoidable, level of human-induced flow alteration is still present in most of the selected catchments; however, some degree of disturbance has to be tolerated (cf. Murphy et al. 2013), and furthermore the work done represented best effort to select the subset of least human-impacted gauges in Poland.

The original set of data consists of 147 stations. In the present study, it was decided to analyse two subsets of the complete data set (Fig. 1). One subset (A) comprised 57 gauges with daily data available for 61 years (1956–2016), while the other subset (B) comprised 144 gauges with daily river flow data available over the time interval of 36 years (1981–2016). Note that data for hydrological years (1 November–31 October) were used here. This decision to divide the original data set into subsets reflects the trade-off of having a set of longer time series for a smaller set of stations or a set of shorter time series for a larger set of stations. The subset (A) was selected to maximize the duration of the time series of records, while the subset (B) was selected to maximize the station count and geographical coverage. Stations with data gaps longer than 1 year were avoided, i.e. the maximum length of data gaps for each station in subsets (A) and (B) was 1 year. As shown in Fig. 1, only four stations in subset (A) and ten stations in subset (B) had 1-year-long data gaps, whereas several further stations had much shorter gaps (mean value 15 days). Data infilling was carried out using a simple interpolation method for short gaps (provided that no larger flood events were noted in the neighbouring stations) or regression from donor catchments for short periods with flood events and for all longer periods. However, since the fraction of missing records in the entire studied data set was very low [0.4% in subset (A) and 0.3% in subset (B)], it is believed that the infilling procedure did not have any tangible effect on the analyses.

As shown in Fig. 1, geographical coverage of catchments is good, albeit some regions known for their lower human impact (e.g. NE Poland) have a stronger representation. Table 1 presents the basic properties of the selected catchments. The median of catchment areas is equal to 557 km^2. The catchments present large variability in climatic parameters (precipitation and temperature), elevation and land cover. Huge variability is also present for hydrological parameters which demonstrate that the catchments are indeed well representative for Polish conditions.

River flow indices

The indices describing average annual, average seasonal, as well as characteristics of low and high river flow commonly used in water resources management and engineering are examined here. As this study is supposed to serve as a preliminary one in this subject, simple indices were preferred over the more complex ones. For describing average annual and seasonal conditions, the time series of mean annual (denoted as Q_MEAN) and seasonal (denoted as Q_DJF, Q_MAM, Q_JJA and Q_SON for winter, spring, summer and autumn, respectively) flows were calculated. For extreme low flow conditions, the annual minima of 7 day averaged daily flows (denoted as Q7_MIN) were calculated. Finally, as the index of high extremes, the annual maxima of daily flows (Q_MAX) were used. All indices were calculated in $m^3\ s^{-1}$.

To permit comparisons between catchments and analysis of spatial patterns of trend magnitudes, the annual time series of indices listed in Table 2 were first standardized (i.e. values were subtracted from the mean and divided by the standard deviation).

Trend detection

As in many other studies on trend detection in river flow indices (Kundzewicz and Robson 2004; Stahl et al. 2010; Burn et al. 2012; Hannaford et al. 2013), in this study we also used the non-parametric rank-based Mann–Kendall (MK) test for monotonic trend (Kendall 1975). The test is applicable for non-normally distributed data and data

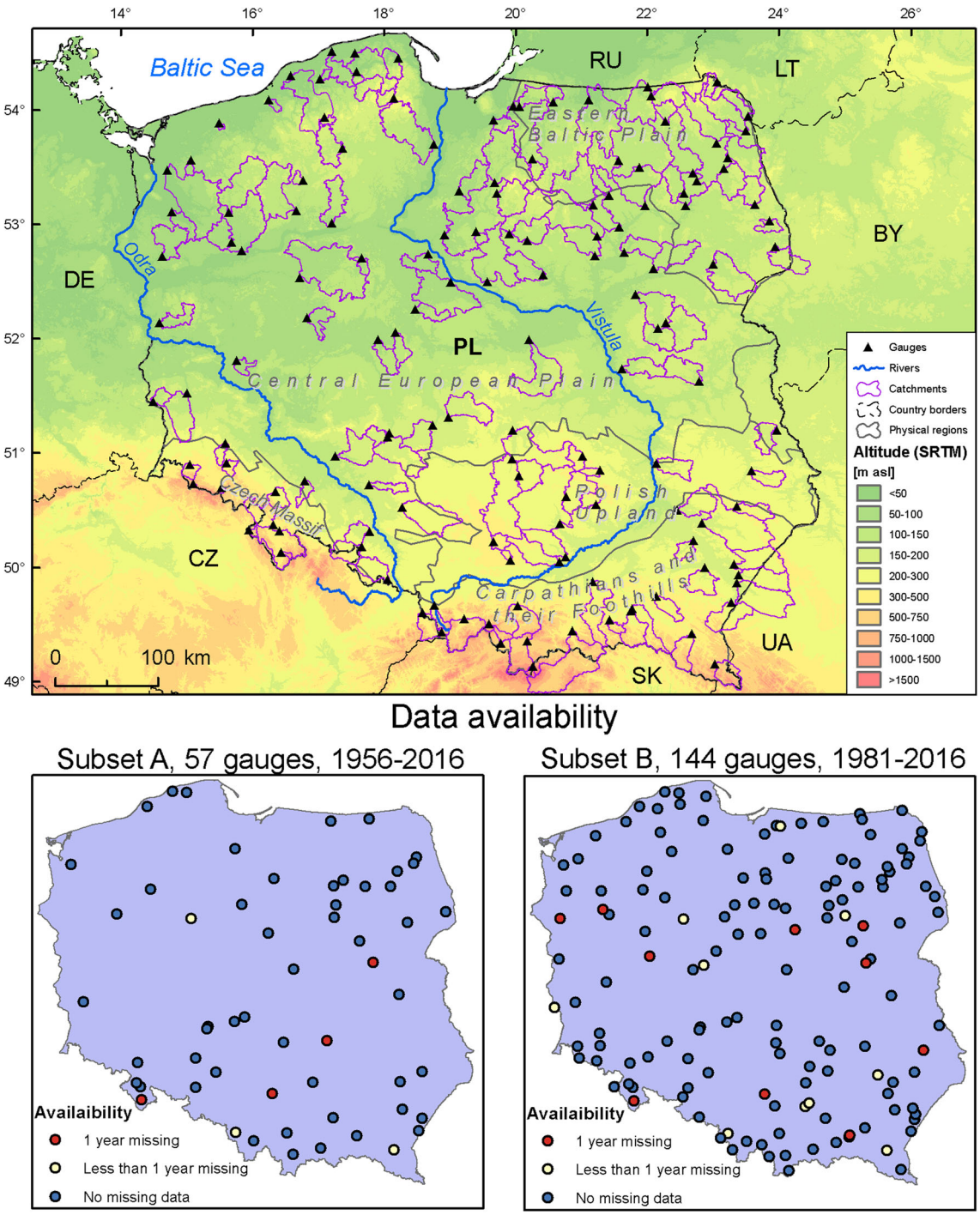

Fig. 1 Gauging stations and catchments used in the present study (adapted from Piniewski 2017) as well as flow data availability for two subsets of gauges within two time periods: 1956–2016 and 1981–2016

containing outliers or non-linear trends (Stahl et al. 2010). The MK statistic, Z, is a rank sum standardized by its variance and follows the standard normal distribution with a mean of zero and variance of one. The reader is directed to literature for more details on trend calculation (cf. Kundzewicz and Robson 2004).

Due to controversies around testing statistical significance of changes in river flow indices using the MK test, we have decided to focus on direction and magnitudes of trends and their spatial patterns rather than significance. A frequent presence of auto-correlation in hydrological time series (the Polish ones are no exception here) has a direct

Table 1 Statistics of selected parameters describing 144 catchments used in this study

Parameter	Unit	Minimum	1st quartile	Median	Mean	3rd quartile	Maximum
Catchment area	km^2	6	236	557	867	1034	6818
Annual total precipitation	mm/year	587	660	695	760	781	1385
Winter total precipitation	mm/year	102	128	136	152	170	320
Summer total precipitation	mm/year	213	236	248	265	267	456
Annual mean temperature	°C	0.2	7.0	7.5	7.4	7.9	8.9
Winter mean temperature	°C	− 7.6	− 2.7	− 2.2	− 2.1	− 1.3	− 0.1
Summer mean temperature	°C	8.1	16.4	16.9	16.6	17.3	17.9
Mean elevation	m asl	54.6	130.2	170.6	263.8	283.8	1647.2
Percent of forests	%	2.5	22.0	33.1	37.2	48.9	100.0
Percent of agricultural land use	%	0.0	46.0	62.6	58.6	74.2	93.4
Annual mean flow	m^3/s	0.3	1.4	3.0	5.4	6.8	37.0
Coefficient of variation of daily flows	–	0.25	0.65	1.02	1.06	1.36	3.37
Mean annual specific runoff	mm/year	45	128	172	246	266	1581

Table 2 List of river flow indices used in this study

Index	Abbreviation	Category
Mean annual flow	Q_MEAN	Average conditions
Winter season mean flow	Q_DJF	Seasonal conditions
Spring season mean flow	Q_MAM	Seasonal conditions
Summer season mean flow	Q_JJA	Seasonal conditions
Autumn season mean flow	Q_SON	Seasonal conditions
Annual minimum of 7-day mean flows	Q7_MIN	Extreme conditions
Annual maximum daily flow	Q_MAX	Extreme conditions

effect on MK test significance (Hamed and Rao 1998; Yue and Wang 2002). Streamflow time series are also known to exhibit what is called a long-term persistence (LTP; Cohn and Lins 2005; Koutsoyiannis and Montanari 2007), which violates the assumptions of the MK test. Furthermore, significance levels usually have an arbitrary nature (Hannaford et al. 2013).

Sen slopes (Sen 1968) were calculated for estimation of trend magnitudes for each index and station. They are calculated using a simple, non-parametric, procedure, as the median of slopes of all possible ordered pairs of time series values. Sen slopes are more robust to outliers than parametric tests such as linear regression. Since slopes are calculated based on standardized time series, they are expressed in standard deviations of a given index value per year. It should be also noted that the existence of autocorrelation does not affect the estimated value of the Sen slope, unlike the p value of the MK test (Yue et al. 2002).

Results

Mean annual flow

For both studied periods and corresponding station subsets, decreasing trends in mean annual flow are prevailing in observation records in Poland (Fig. 2). An important feature of the larger subset of stations is a clear division of the country into three latitudinal zones: (1) northern part, in which decreasing trends dominate (particularly strong in its central part); (2) central part, in which trends are very weak; (3) southern part, in which Q_MEAN increases for the majority of gauges. In contrast, for the time interval 1956–2016, for approximately half of gauging stations scattered around Poland, no trends were identified.

Mean seasonal flows

Mean seasonal flows are characterized by fairly similar changes as mean annual flows, i.e. between-season differences are not very large (Fig. 3). Overall, decreasing trends are more common than increasing trends for all seasons. Trend slopes are lower for the smaller subset of stations

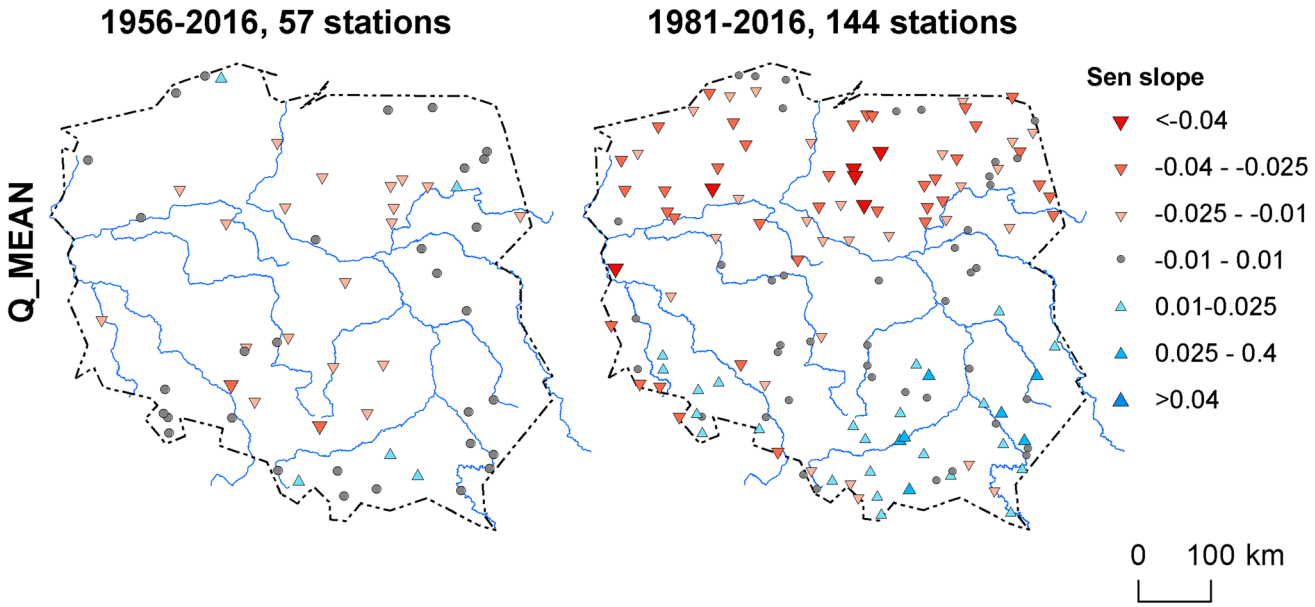

Fig. 2 Trend magnitudes (described by Sen slope) of mean annual flow (Q_MEAN) time series for two time periods: 1956–2016 [subset (A), 57 flow gauges] and 1981–2016 [subset (B), 144 gauges]

possessing data for a longer period than for the larger subset and shorter period. In the latter case, latitudinal pattern of change can be observed for every season (as for Q_MEAN), with seasonal flow decreases dominating in the northern part, increases prevailing in the southern part, and low trend slopes for stations in the central part of Poland. The highest decreases can be noted for Q_MAM in the northern part of Poland, but only for the subset (B). Since the river flow maxima, typically of snowmelt origin, are usually reached in the spring season in this region of Poland, it is expected that similar decreases will be obtained for Q_MAX.

Low flows and floods

Figure 4, describing spatial variability of trend slopes in Q7_MIN and Q_MAX, supports previous findings from Figs. 2 and 3 that absolute values of the Sen slope are higher for shorter time intervals. As in the case of mean annual and seasonal flows, decreases in minimum and maximum river flow indices in the time interval 1981–2016 are the highest in the northern part of Poland. The spatial pattern in the southern part of Poland has a more mixed nature, with a considerable number of stations undergoing increases, decreases, or little changes. It is worthy of stating that decreases of Q7_MIN are observed in areas where the mean river flow is low, in general. Hence, the problems related to streamflow drought are likely getting exacerbated.

Summary of trends

As presented in Table 3, the time period 1981–2016 for which a larger gauging station data set was available is characterized by a higher level of agreement between the studied river flow indices. Only for Q_SON, the autumn season average flow, only 58% of stations have a negative trend, while for the remaining six indices it ranges between 66 and 68%. For the longer period 1956–2016, in one case, for Q_DJF, more stations show increasing than decreasing trends. In contrast, in the case of annual maximum flow (Q_MAX), only 21% of gauges show increasing trends. It should be noted though that trend magnitudes for the longer period were generally lower (Figs. 2, 3, 4).

Inter-annual variability in river flow indices

In addition to studying trends in river flow indices, it is important to track their inter-annual variability (Fig. 5). Since, as shown in Table 3, for all indices there are stations showing either increasing or decreasing trends, Fig. 5 uses a selection of stations, of which one always shows a negative trend (left column) and the other shows a positive trend (right column). Example flow gauges were selected for each index separately, in such a manner that they represented a region in which most of the stations showed trends in a similar direction. Thus, the majority of stations showing negative trends are located in the northern part of Poland, whereas most of the stations showing positive trends are situated in the southern part. Plotted trend lines

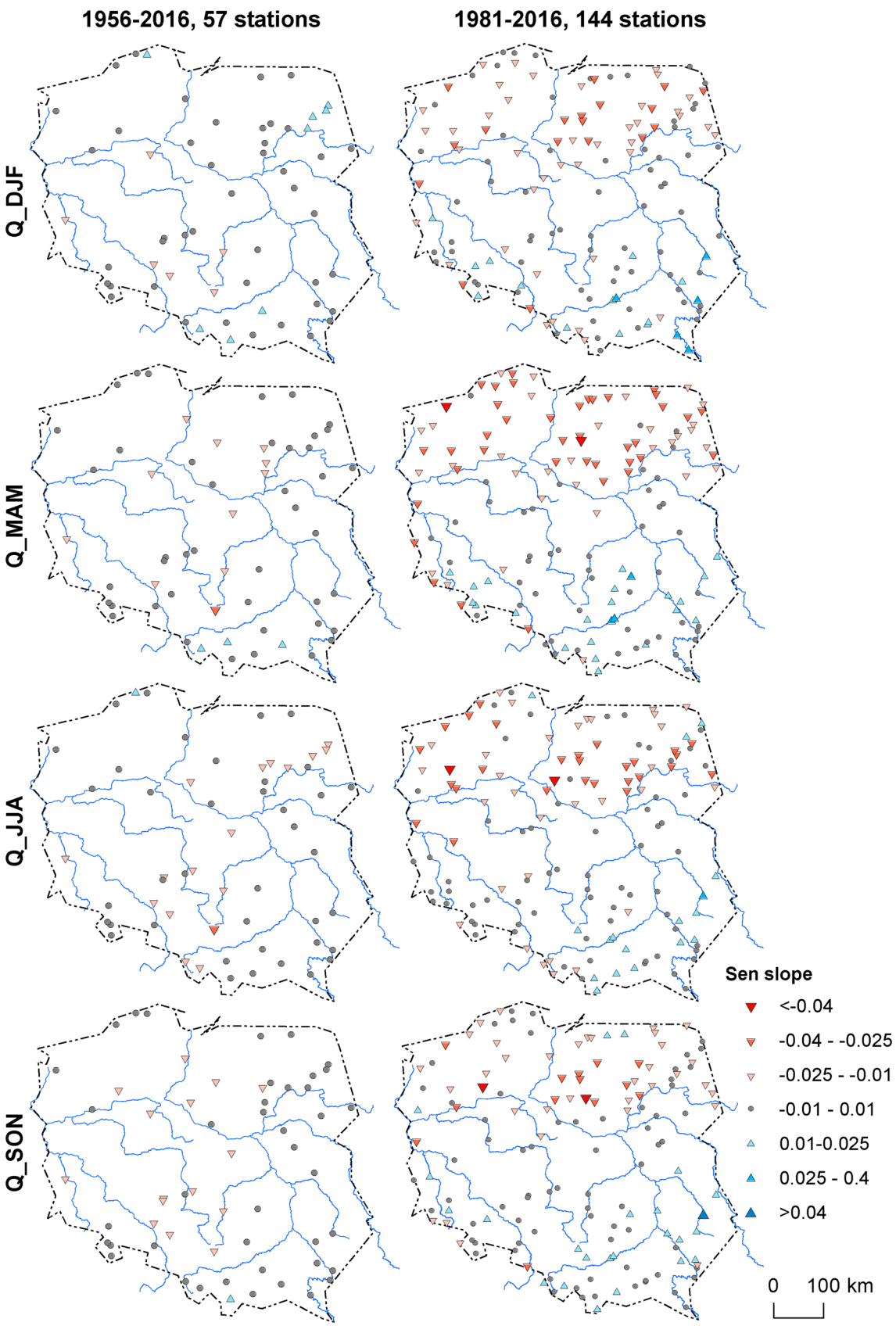
1956-2016, 57 stations
1981-2016, 144 stations
Q_DJF
Q_MAM
Q_JJA
Q_SON
Sen slope
<-0.04
-0.04 - -0.025
-0.025 - -0.01
-0.01 - 0.01
0.01-0.025
0.025 - 0.4
>0.04
0 100 km

◀**Fig. 3** Trend magnitudes (described by Sen slope) of mean seasonal flow (winter, spring, summer and autumn, denoted as Q_DJF, Q_MAM, Q_JJA and Q_SON, respectively) time series for two time periods: 1956–2016 [subset (A), 57 flow gauges] and 1981–2016 [subset (B), 144 gauges]

using Sen slopes are drawn for the two studied periods: 1956–2016 and 1981–2016, which means that only stations from the less abundant subset (A) of longer duration of record were selected.

Trend slopes for two studied periods can be quite different, as for example in the case of River Orzyc at Maków

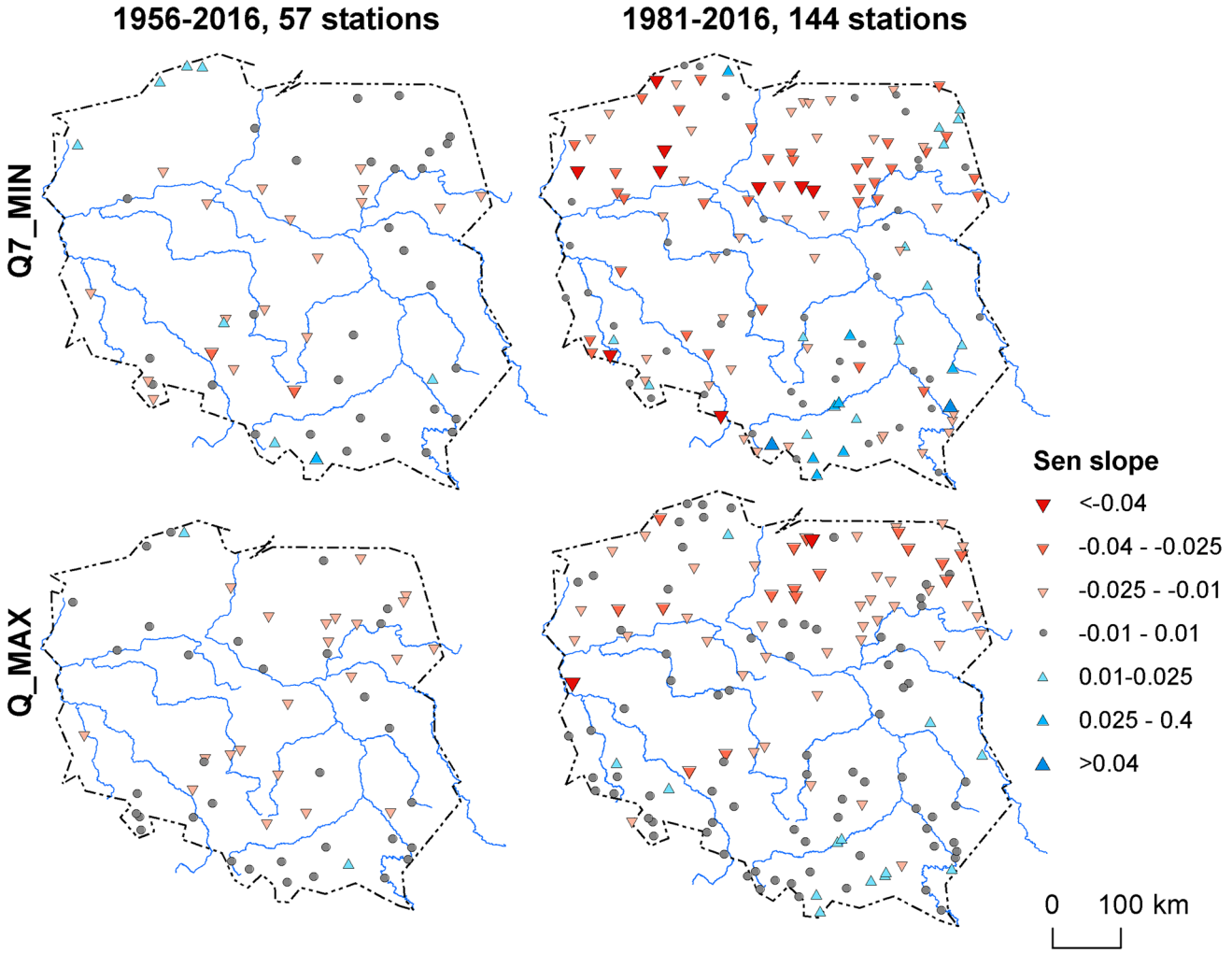

Fig. 4 Trend magnitudes (described by Sen slope) of annual minimum of 7-day average flows (Q7_MIN) and annual maximum flow (Q_MAX) time series for two time periods: 1956–2016 (subset (A), 57 flow gauges) and 1981–2016 (subset B, 144 gauges)

Table 3 Summary of trend directions for different river flow indices and two analysed subsets

Index	1956–2016 (57 stations)		1981–2016 (144 stations)	
	Increase (%)	Decrease (%)	Increase (%)	Decrease (%)
Q_MEAN	26	74	34	66
Q_DJF	54	46	33	67
Q_MAM	32	68	33	67
Q_JJA	25	75	34	66
Q_SON	26	74	42	58
Q7_MIN	39	61	32	68
Q_MAX	21	79	33	67

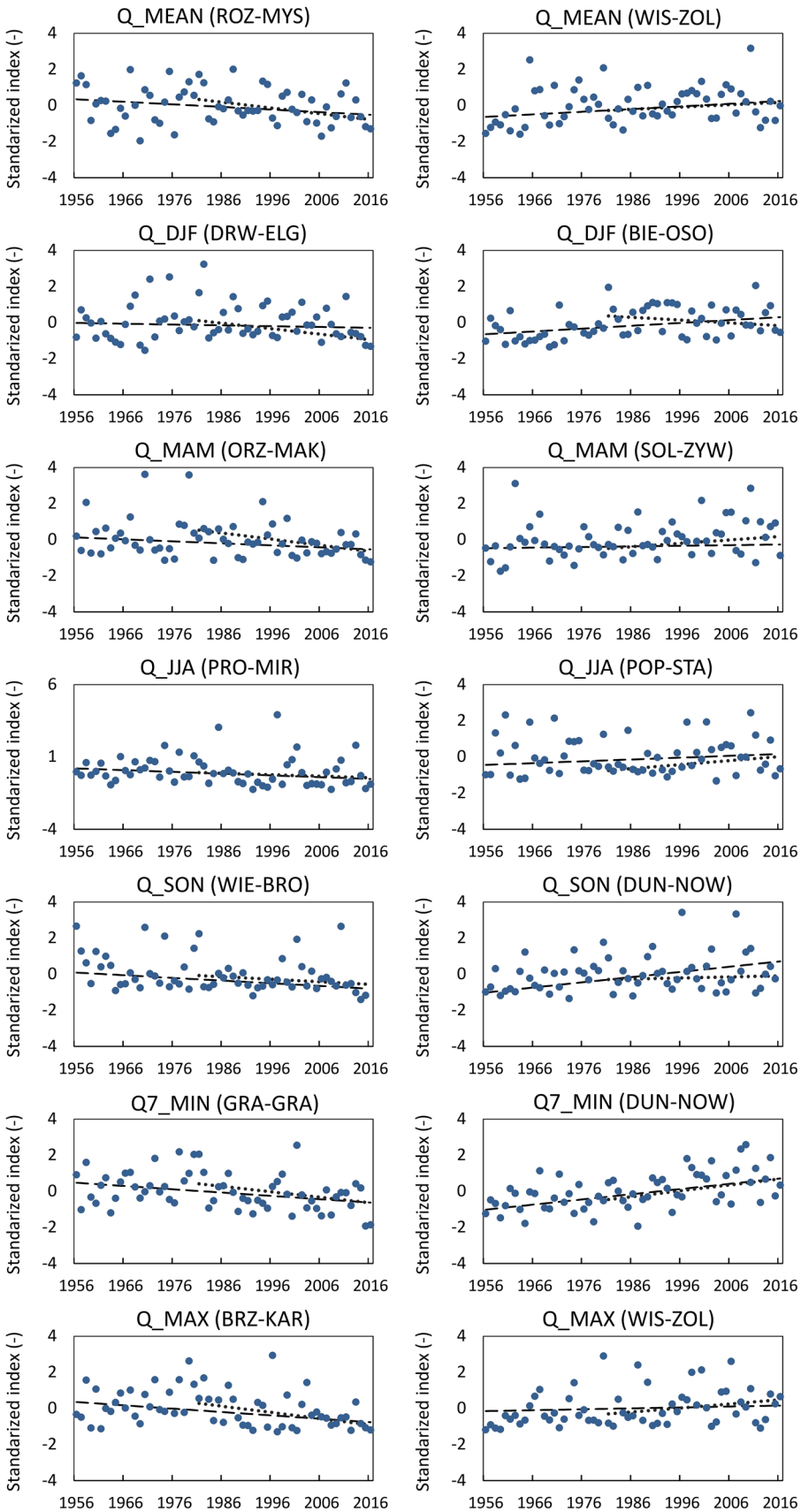

Fig. 5 Inter-annual dynamics of selected river flow indices (standardized values) in selected catchments. Black dashed and dotted lines denote trends obtained using Sen slope for 1956–2016 and 1981–2016, respectively. For each index, two example gauges are shown. River-gauge codes are: ROZ-MYS (River Rozoga at Myszyniec), WIS-ZOL (Wisłoka at Żółków), DRW-ELG (Drwęca at Elgiszewo), BIE-OSO (Biebrza at Osowiec), ORZ-MAK (Orzyc at Maków Mazowieski), PRO-MIR (Prosna at Mirków), POP-STA (Poprad at Stary Sącz), WIE-BRO (Wierzyca at Brody), DUN-NOW (Dunajec at Nowy Targ), GRA-GRA (Grabia at Grabno), BRZ-KAR (Brzozówka at Karpowicze)

Mazowiecki, for which Q_MAM undergoes a more rapid decrease in the period 1981–2016 than in the period 1956–2016 (Fig. 5). Such a situation is most often the case; however, sometimes the longer period exhibits higher magnitudes of slopes (increases in the River Dunajec at Nowy Targ for Q_SON), and sometimes nearly the same magnitudes are visible for both periods (decreases for the River Prosna at Mirków for Q_JJA).

Relationship between streamflow and catchment characteristics

Piniewski (2017) calculated a number of climatic, physiographic and hydrological catchment properties for all gauging stations used in this study. We now used the former database of catchment properties to examine possible correlations between them and the trend slopes estimated in the present study. Four example linear regression plots for those combinations of river flow indices and catchment properties that achieved the highest correlations show that, in general, Q_MAM and Q_MEAN had the highest mean correlation across all seven indices (reaching $R^2 = 0.17$), whereas the lowest correlation was obtained for Q7_MIN (equal to 0.05) (Fig. 6).

Comparison of calculated R^2 values across all seven river flow indices suggests that some of the catchment properties had much higher correlation with river flow indices than others. The strongest predictor of Sen slope was the parameter called LOC_DistCoast, denoting distance from the geographical centre of the catchment from the (Baltic Sea) coast. This is in line with Figs. 2, 3 and 4, demonstrating a clear divide of the country into two or three zones, depending on the latitude and distance from the coast. The lower the distance from the coast, the more pronounced is the decrease in river flow indices, for example in Q_MAM for which the correlation was the highest (Fig. 6). The ratio of outwash sands and gravels (GEO_outsand) was another good predictor of trend slope magnitude, with catchments rich in this type of bedrock having generally more pronounced decreasing trends, particularly in Q_SON. A similar relationship was present between the ratio of lakes (HYD_Lake) and Q_DJF (but not other indices). Finally, the coefficient of variation of daily flows (Q_CV) was positively correlated with the Sen slope magnitude for several indicators, in particular with Q_MEAN as shown in Fig. 6. It is also noteworthy that other possibly important catchment properties such as drainage area or some temperature and precipitation indices had lower correlation values than those shown in Fig. 6.

Discussion

In the light of the objective of this study mentioned in "Introduction", the special focus was on the spatial analysis of trends, carried out on a comprehensive, representative data set of river flow used in this study. This paper addresses a visible need for a comprehensive trend detection study for Polish river flows.

The results of trend detection in different indices of river flow in Poland presented in this paper show that there exists a spatial divide that seems to hold quite generally for various indices that were examined. Decreases of river flow were found to dominate in the northern part, while increases dominate in the southern part. The central part, extending around a central parallel over Poland, being a transition zone between the north and the south, is frequently characterized by the majority of 'no trend' results. It should be noted, though, that this spatial gradient is apparent only for the results based on the larger subset of stations having data available for the period 1981–2016, and not really for the longer period 1956–2016, with a lower number of stations. This is in accordance with the study of Ilnicki et al. (2014) which observed that trends in mean annual discharge of the River Warta were going in opposite directions (positive in 1950–1980 and negative in 1981–2010). Furthermore, the magnitude of increases is generally lower than that of decreases. The results also show that one of the indicators of geographical location, distance of catchment centroid from the coast, is a very good predictor of trend slopes for all but one index. The highest correlation occurred between the location from the coast and the spring season average flow. This finding is quite similar to the one reported by Kriaučiūnienė et al. (2012), who mentioned that moderate decreases in spring flows can be noted in the western, maritime regions of the Baltic States, while they are absent in eastern, continental regions. In the Polish case, the distance from the coast is on one hand correlated with climatic indices (maritime vs. continental climate), but also with some of the physiographic catchment properties, which is connected to the glacial legacy of Polish landscape. The surface slope basically declines northwards (with some exceptions), but geomorphic properties, e.g. the type of prevailing postglacial deposits on the vast Polish plain, also exhibit clear spatial trends.

Dominating downward trends in river flow indices detected in this study for rivers situated on the Polish plain are supported by publications of other authors (Banasik et al. 2013; Somorowska 2017). Upward trends in mean winter and spring season flows found in this study for numerous stations located in the southern part of Poland were also found by Kędra (2017) for the River Soła located

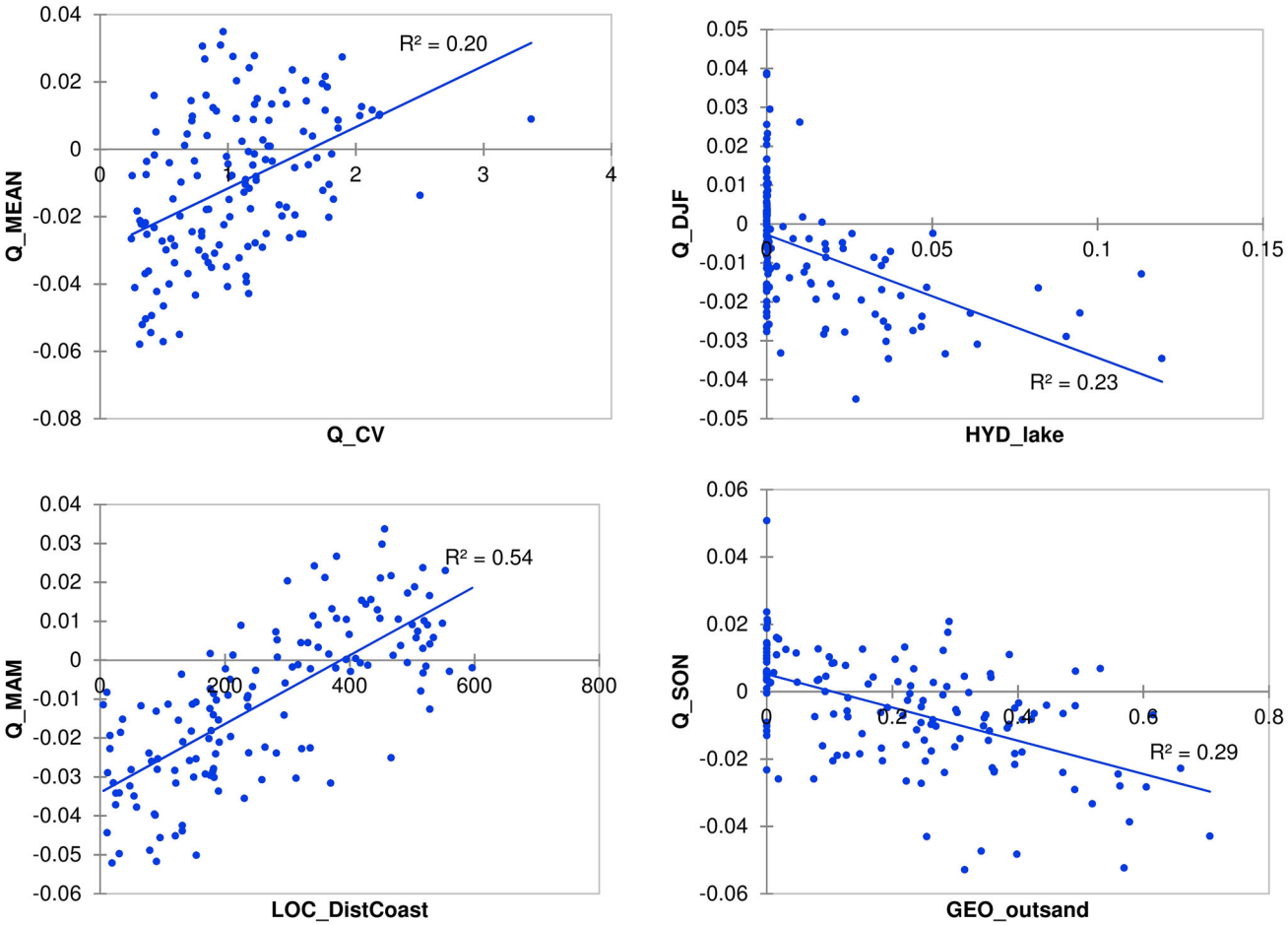

Fig. 6 Linear regression between Sen slopes for selected river flow indices (Q_MEAN, Q_DJF, Q_MAM and Q_SON) for subset (B) (144 stations) and selected catchment properties (*Q_CV* coefficient of variation of daily flows, *HYD_lake* ratio of lakes, *LOC_DistCoast* distance from coast, *GEO_outsand* ratio of outwash sands and gravels). See Piniewski (2017) for more details on calculated catchment properties

in the Carpathians. The results of a multi-temporal trend analysis performed for annual maximum flows by Ruiz-Villanueva et al. (2016) for rivers in the Dunajec catchment demonstrated that trend direction depends on the analysis period. While increasing trends were prevailing for periods starting in the 1960s and ending in the 1990s, the opposite direction of trends was noted for later periods, i.e. starting in the 1980s and ending in the 2000s. Kaczmarek (2003) reported decreasing trends in snowmelt-induced floods in four major Polish rivers: Vistula, Odra, Warta and Bug, which partly corroborates our findings on decreases in Q_MAX and Q_MAM, especially in northern Poland. Pociask-Karteczka (2011) analysed trends in mean annual flows of the Vistula and Odra rivers concluding that "statistically significant increase or decrease in river discharge in Poland as a response to climate changes in Poland has not been observed". Our study shows that in Polish rivers whose drainage areas are two to five orders of magnitude lower than those of the Vistula and Odra (10^0–10^3 vs. 10^5 km^2), certain trends can be detected, although the picture is rather complex. Stonevicius et al. (2014) detected strong upward trends in winter flows in Lithuanian rivers. This result is different from the one obtained in the present study for rivers situated in NE Poland, in close proximity to the Lithuanian border. Bormann and Pinter (2017) evaluated trends in low flows in Germany, presenting maps illustrating strong upward trends in southern and central Germany, and non-significant or downward trends in its northern part. The pattern observed for Polish rivers in this study was quite similar. It should be noted though that rivers in the study of Bormann and Pinter (2017) were influenced by water management, which can perturb natural climate-driven trends for near-pristine drainage basins, as demonstrated in a study of Marcinkowski and Grygoruk (2017). Wrzesiński and Sobkowiak (2018) demonstrated that the largest changes in the flow regime of Polish rivers

in the time interval 1951–2010 took place in catchments with the strongest human influence, which partly explains rather weak and unequivocal trends detected in this study for semi-natural catchments.

No research known to the authors convincingly demonstrates a regionally ubiquitous and uniform change in river flow at any larger scale (global, continental, regional, national). Gerten et al. (2012) identified statistically significant changes in average annual discharge across Europe between 1901–1970 and 1971–2002 and proposed attribution of changes. However, the resultant map of changes is complex and heterogeneous. Over Poland, their results differ from those presented in the present study and this is understandable for several reasons (selection of different time horizons of analysis, use of model-based simulations over all grids in contrast to raw observation data on catchments in Poland that were found not to be heavily modified).

To interpret the change in river flow it is important to examine the results of change detection studies in precipitation (therein also intense precipitation) and snow cover. However, even if trends were detected, they were mostly weak and statistically insignificant. Yet, there are regionally consistent seasonal changes and precipitation increase in spring and winter dominates. Pińskwar et al. (2018b) showed that daily maximum precipitation for the summer half-year (Apr.–Sept.) increased for many stations and there were more positive changes during the summer half-year than those in the winter half-year (Oct.–March). Szwed et al. (2017) found that observed tendencies in time series of snow-related variables is complex and not easy to interpret. Yet, statistical relations between the North Atlantic Oscillation (NAO) index and the snow cover depth, as well as the number of snow cover days were found. Quasi-cyclic variability in some of the river flow indices can also be noted in Fig. 6; however, investigation of correlation between NAO (or similar indices) and trend results presented herein was beyond the scope of this study. We refer the reader to other studies devoted to this phenomenon, e.g. Rutkowska et al. (2017), Pociask-Karteczka (2006), Wrzesiński (2011) and a recent review article of Steirou et al. (2017).

Comparison of results of trend detection with river flow projections shows that projections build a far more spatially homogeneous map than the observation records and this is not surprising. By construction, projections (cf. Piniewski et al. 2017b, c) are based on smooth information from climate models (subject to empirical–statistical or dynamical downscaling and bias correction). Moreover, projections show likely increases of mean annual and seasonal flows (cf. Piniewski et al. 2017b) as well as indices of low and high flows (cf. Piniewski et al. 2017c), which are driven by projected increases in precipitation, particularly in winter and spring seasons (Piniewski et al., 2017a). Hence, there are many places in Poland where the direction of change of river flow does not correspond between observations and projections, rendering interpretation a considerable conceptual dilemma. Although much effort has been undertaken to select flow gauges free of visible human pressure, there is a risk that at least for some of the catchments other effects could play their role.

It is important to stress that time series of annual maximum and annual minimum (7-day) flows, analysed in this study, convey information on some river discharge extremes only. This broadly used approach is straightforward and well established. However, in years with more than one high-flow episode, only one flood event per year is selected, while in years with no large flows at all, a non-flood (medium or even low) flow, in absolute terms, could have been extracted as the annual maximum. An alternative is a peak-over-threshold (POT) approach, where all independent floods above a certain threshold (i.e. possibly several events in one year and none in another year) are considered (Kundzewicz et al. 2005). Likewise, in generally wet years, the annual minimum does not have to be a low flow in absolute terms.

Conclusion

This study analysed long-term trends in selected river flow indices over two time intervals (1956–2016 and 1981–2016) in small- and medium-sized catchments with relatively unmodified flow regime (semi-natural catchments) in Poland. The examined indices describe annual and seasonal average conditions as well as annual extreme conditions—low and high flows. Geographical coverage of catchments in this study is good, albeit some regions known for their lower human impact (e.g. NE Poland) have a stronger representation. Two selected time windows demonstrate the sensitivity of the river flow process to the selection of the study period. The more recent period, however, is of more practical interest for water managers.

Altogether, there is a strong random component in the river flow process, the changes are weak and the spatial pattern is complex. For both studied periods and for two station subsets (providing longer time series at fewer stations or shorter time series at more stations), decreasing trends in mean annual flow are prevailing in observation records in Poland. Yet, the results of trend detection in different indices of river flow in Poland show, for 1981–2016, the existence of a spatial divide that seems to hold quite generally for various indices (annual, seasonal, as well as low and high flow). Decreases of river flow dominate in the northern part of the country, while increases usually dominate in the southern part. At stations

in the central part changes are mostly very weak. It seems that the magnitude of increases of river flow is generally lower than that of decreases. In contrast, for the time interval 1956–2016, for approximately half of gauging stations scattered around Poland, no trends were identified. It is worthy of stating that decreases of low flow are observed in areas where the mean river flow is low, in general. Hence, the problems related to streamflow drought have likely been exacerbated.

It was found that some catchment properties have a fairly strong correlation with river flow indices. The strongest predictor of the Sen slope was the distance from the geographical centre of the catchment from the Baltic Sea coast. In this context, one can interpret the existence of a clear divide of the country into two or three zones, depending on the latitude and distance from the coast.

Trend detection in long time series of river flow records is an activity of vast theoretical interest and considerable practical relevance. The former statement reflects the search for impacts of the ongoing climate change and for adaptation needs. Climate change track is easy to find in records of overwhelmingly increasing temperature, but the situation is far more complex for precipitation and even more so for river flow records, where several contributing (and partly compensating) factors play a role. The latter statement reflects the fact that water management is based on the assumption of stationarity, that is, constancy of statistical properties of the river flow record. Hence, it is crucial to check, on a regular basis and using updated records, whether taking this assumption is justified, i.e. whether the statistical properties of the record can be regarded as approximately stationary. For instance, flood risk reduction is based on the concept of design flood; hence, river flow corresponding to a given probability of exceedance is the parameter of importance for people responsible for flood preparedness, both from the viewpoint of general natural disaster risk reduction and climate change adaptation, as flood hazard is expected to increase in the warming climate, with more room for water vapour in the warmer atmosphere.

Acknowledgements The support of the projects CHASE-PL (Climate Change Impact Assessment for Selected Sectors in Poland) of the Polish–Norwegian Research Programme operated by the National Centre for Research and Development (NCBiR) under the Norwegian Financial Mechanism 2009–2014 in the frame of Project Contracts No. Pol Nor/200799/90/2014 is gratefully acknowledged. The first author thanks the Alexander von Humboldt Foundation and the Ministry of Science and Higher Education for the financial support. The Institute of Meteorology and Water Management, National Research Institute (IMGW-PIB) is kindly acknowledged for providing the hydrometeorological data used in this work. All authors are thankful to the two anonymous referees who provided a number of insightful comments that helped to improve the manuscript.

Compliance with ethical standards

Conflict of interest On behalf of all authors, the corresponding author states that there is no conflict of interest.

References

Banasik K, Hejduk L, Hejduk A, Kaznowska E, Banasik J, Byczkowski A (2013) Long-term variability of runoff from a small catchment in the region of the Kozienice Forest. Sylwan 158:578–586

Bard A, Renard B, Lang M, Giuntoli I, Korck J, Kobolsching G, Janza M, d'Amico M, Volken D (2015) Trends in the hydrologic regime of Alpine rivers. J Hydrol 529:1823–1837

Bormann H, Pinter N (2017) Trends in low flows of German rivers since 1950: comparability of different low-flow indicators and their spatial patterns. River Res Appl 33:1191–1204

Burn DH, Hannaford J, Hodgkins GA, Whitfield PH, Thorne R, Marsh T (2012) Reference hydrologic networks II. Using reference hydrologic networks to assess climate-driven changes in streamflow. Hydrol Sci J 57(8):1580–1593

Cohn TA, Lins HF (2005) Nature's style: naturally trendy. Geophys Res Lett 32(23):L23402

Gerten D, Lucht W, Kundzewicz ZW (2012) Detection and attribution of changes in water resources. In: Kundzewicz ZW (ed) Changes in flood risk in Europe, Special Publication No. 10. IAHS Press, Wallingford, pp 422–434

Graczyk D, Pińskwar I, Kundzewicz ZW, Hov Ø, Førland EJ, Szwed M, Choryński A (2017) The heat goes on—changes in indices of hot extremes in Poland. Theor Appl Climatol 129(1–2):459–471

Hamed KH, Rao AR (1998) A modified Mann-Kendall trend test for autocorrelated data. J Hydrol 204:182–196

Hannaford J, Buys G, Stahl K, Tallaksen LM (2013) The influence of decadal-scale variability on trends in long European streamflow records. Hydrol Earth Syst Sci 17:2717–2733

Hanson CE, Palutikof JP, Livermore MTJ, Barring L, Bindi M, Corte-Real J, Durao R, Giannakopoulos C, Good P, Holt T, Kundzewicz ZW, Leckebusch GC, Moriondo M, Radziejewski M, Santos J, Schlyter P, Schwarb M, Stjernquist I, Ulbrich U (2007) Modelling the impact of climate extremes: an overview of the MICE project. Clim Change 81:163–177. https://doi.org/10.1007/s10584-006-9230-3

Hodgkins GA, Whitfield PH, Burn DH, Hannaford J, Renard B, Stahl K, Fleig AK, Madsen H, Mediero L, Karhonen J, Murphy C, Wilson D (2017) Climate-driven variability in the occurrence of major floods across North America and Europe. J Hydrol 552:704–717

Ilnicki P, Farat R, Górecki K, Lewandowski P (2014) Impact of climatic change on river discharge in the driest region of Poland. Hydrol Sci J 59(6):1117–1134

Kaczmarek Z (2003) The impact of climate variability on flood risk in Poland. Risk Anal 23:559–566

Kędra M (2017) Long-term trends in river flow: a case study of the Soła River (Polish Carpathians). In: E3S Web of Conferences, vol 19. https://doi.org/10.1051/e3sconf/20171902012

Kendall MG (1975) Rank correlation methods. Griffin, London

Koutsoyiannis D, Montanari A (2007) Statistical analysis of hydroclimatic time series: uncertainty and insights. Water Resour Manag 43:W05429. https://doi.org/10.1029/2006WR005592

Kriaučiūnienė J, Meilutytė-Barauskienė D, Reihan A, Koltsova T, Lizuma L, Šarauskienė D (2012) Variability in temperature, precipitation and river discharge in Baltic States. Boreal Environ Res 17:150–162

Kundzewicz ZW, Robson AJ (2004) Change detection in river flow records—review of methodology. Hydrol Sci J 49(1):7–19

Kundzewicz ZW, Graczyk D, Maurer T, Pińskwar I, Radziejewski M, Svensson C, Szwed M (2005) Trend detection in river flow series: 1. Annual maximum flow. Hydrol Sci J 50(5):797–810

Kundzewicz ZW, Førland EJ, Piniewski M (2017) Challenges for developing national climate services—Poland and Norway. Clim Serv 8:17–25

Leasure DR, Magoulick DD, Longing SD (2016) Natural flow regimes of the Ozark-Ouachita interior highlands region. River Res Appl 32:18–35

Marcinkowski P, Grygoruk M (2017) Grygoruk M (2017) Long-term downstream effects of a dam on a lowland river flow regime: case study of the Upper Narew. Water 9:783

Miler AT (2015) Variability of the Warta River water discharge in the city of Poznań as influenced by the Jeziorsko reservoir. Arch Environ Prot 41(3):53–59

Milly PCD, Betancourt J, Falkenmark M, Hirsch RM, Kundzewicz ZW, Lettenmaier DP, Stouffer RJ (2008) Stationarity is dead: whither water management? Science 319:573–574

Milly PCD, Betancourt J, Falkenmark M, Hirsch RM, Kundzewicz ZW, Lettenmaier DP, Stouffer RJ, Dettinger MD, Krysanova V (2015) On critiques of "Stationarity is dead: whither water management?". Water Resour Res 51(9):7785–7789

Murphy C, Harrigan S, Hall J, Wilby RL (2013) Climate-driven trends in mean and high flows from a network of reference stations in Ireland. Hydrol Sci J 58(4):755–772

Niedźwiedź T, Łupikasza E, Pińskwar I, Kundzewicz ZW, Stoffel M, Małarzewski Ł (2015) Variability of high rainfalls and related synoptic situations causing heavy floods at the northern foothills of the Tatra Mountains. Theor Appl Climatol 119(1–2):273–284

Piniewski M (2017) Classification of natural flow regimes in Poland. River Res Appl 33:1205–1218. https://doi.org/10.1002/rra.3153

Piniewski M, Mezghani A, Szcześniak M, Kundzewicz ZW (2017a) Regional projections of temperature and precipitation changes. Robustness and uncertainty aspects. Met Zeit 26(2):223–234

Piniewski M, Szcześniak M, Huang S, Kundzewicz ZW (2017b) Projections of runoff in the Vistula and the Odra river basins with the help of the SWAT model. Hydrol Res. https://doi.org/10.2166/nh.2017.280

Piniewski M, Szcześniak M, Kundzewicz ZW, Mezghani A, Hov Ø (2017c) Changes in low and high flows in the Vistula and the Odra basins: model projections in the European-scale context. Hydrol Process 31(12):2210–2225

Pińskwar I, Choryński A, Graczyk D, Kundzewicz ZW (2018a) Observed changes in precipitation in Poland. Geografie (in review)

Pińskwar I, Choryński A, Graczyk D, Kundzewicz ZW (2018b) Observed changes in extreme precipitation in Poland: 1991–2015 versus 1961–1990. Theor Appl Climatol. https://doi.org/10.1007/s00704-018-2372-1

Pociask-Karteczka J (2006) River hydrology and the North Atlantic Oscillation: a general review. Ambio 35(6):312–314

Pociask-Karteczka J (2011) River runoff response to climate changes in Poland (East-Central Europe). IAHS Publication No. 344, pp 182–187

Ruiz-Villanueva V, Stoffel M, Wyżga B, Kundzewicz ZW, Czajka B, Niedźwiedź T (2016) Decadal variability of floods in the Northern foreland of the Tatra Mountains Reg. Environ Change 3:603–615

Rutkowska A, Willems P, Onyutha C, Młocek W (2017) Temporal and spatial variability of extreme river flow quantiles in the Upper Vistula River basin, Poland. Hydrol Process 31:1510–1526

Sen PK (1968) Estimates of the regression coefficient based on Kendall's tau. J Am Stat Assoc 63(324):1379–1389. https://doi.org/10.2307/2285891

Sen AK, Niedzielski T (2010) Statistical characteristics of riverflow variability in the Odra River Basin, Southwestern Poland. Pol J Environ Stud 19(2):387–397

Somorowska U (2016) Changes in drought conditions in Poland over the past 60 years evaluated by the Standardized Precipitation-Evapotranspiration Index. Acta Geophys 64(6):2530–2549

Somorowska U (2017) Climate-driven changes to streamflow patterns in a groundwater-dominated catchment. Acta Geophys 65:789–798

Stahl K, Hisdal H, Hannaford J, Tallaksen LM, van Lanen AJ, Sauquet E, Demuth S, Fendekova M, Jodar J (2010) Streamflow trends in Europe: evidence from a dataset of near-natural catchments. Hydrol Earth Syst Sci 14:2367–2382

Steirou LG, Gerlitz L, Apel H, Merz B (2017) Links between large-scale circulation patterns and streamflow in Central Europe: a review. J Hydrol 549:484–500

Stonevicius E, Valiuškevicius G, Rimkus E E, Kazys J (2014) Climate induced changes of Lithuanian rivers runoff in 1960–2009. Water Resour 41:592–603

Strupczewski WG, Singh VP, Mitosek HT (2001) Non-stationary approach to at-site flood-frequency modelling. Part III. Flood analysis of Polish rivers. J Hydrol 248:152–167

Szwed M, Pińskwar I, Kundzewicz ZW, Graczyk D, Mezghani A (2017) Changes of snow cover in Poland. Acta Geophys 65:65–76. https://doi.org/10.1007/s11600-017-0007-z

Wrzesiński D (2011) Regional differences in the influence of the North Atlantic Oscillation on seasonal river runoff in Poland. Quaest Geogr 30(3):127–136

Wrzesiński D, Sobkowiak L (2018) Detection of changes in flow regime of rivers in Poland. J Hydrol Hydromech 66(1):55–64

Yue S, Wang C (2002) The Mann–Kendall test modified by effective sample size to detect trend in serially correlated hydrological series. Water Resour Manag 18:201–218

Yue S, Pilon P, Phinney B, Cavadias G (2002) The influence of autocorrelation on the ability to detect trend in hydrological series. Hydrol Process 16:1807–1829

Acta Geophysica (2018) 66:361–367
https://doi.org/10.1007/s11600-018-0141-2

RESEARCH ARTICLE - SPECIAL ISSUE

Scaling properties of rainfall records in some Mexican zones

Fercia Angulo-Fernández[1] · Israel Reyes-Ramírez[2] · Elsa Leticia Flores-Márquez[3]

Received: 13 November 2017 / Accepted: 2 February 2018 / Published online: 21 April 2018

Abstract
Since the 1990 decade, it has been suggested that atmospheric processes associated with rainfall could be a self-organized critical (SOC) phenomenon similar, for example, to seismicity. In this sense, the rain events taken as the output of the complex atmospheric system (sun's radiation, water evaporation, clouds, etc.) are analogous to earthquakes, as the output of a relaxation process of the earth crust. A clue on this possible SOC behavior of rain phenomenon has been the ubiquitous presence of power laws in rain statistics. In the present article, we report the scaling properties of rain precipitation data taken from meteorological stations located at six zones of Mexico. Our results are consistent with those that assert that rainfall is a SOC phenomenon. We also analyze the Hurst exponent, which is appropriate to measure long-term memory of time series.

Keywords SOC systems · Precipitation processes · Scaling laws

Introduction

During the first half of twentieth century, several empirical relationships in seismology were established, such as the Gutenberg–Richter, Utsu and Omori laws (Gutenberg and Richter 1944; Richter 1958; Scholz 1992; Kanamori and Anderson 1974; Utsu and Seki 1954). These relations were elaborated from seismic catalogs by means of statistical methods. The mathematical expressions corresponding to these empirical relations are power laws, that is, they have the form $N(M) \sim M^{\beta}$, where $N(M)$ is the number of events with magnitude larger than M and β is a scaling exponent. The Gutenberg–Richter laws for the energy and the frequency of earthquakes in terms of their magnitudes were explained on the basis of physical principles in the decade of 80s of the past century. In 1987, Bak, Tang and Weinselfeld (BTW) (Bak et al. 1987, 1988) coined the concept of self-organized critical systems, which are open systems, that is, they can exchange matter and energy with their surroundings. These systems are formed by a very large number of constituents which do not have a characteristic size, and between them predominate short-range interactions. Since its publication, the concept of self-organized criticality (SOC) became a paradigm to explain the dynamics of a variety of complex systems. BTW introduced these ideas using the sand pile model, which consists of adding sand grains one by one over a plane surface. As the grains accumulate, a pile is formed which, upon reaching a certain critical angle of inclination, begins to have a complex behavior in the sense that as more grains are added, avalanches of any size are generated. Interestingly, the statistical distribution of the avalanche sizes is analogous to the Gutenberg–Richter law of seismicity. The sand pile self-organizes to reach a critical state. The original BTW model was a computer simulation using cellular automata. However, later the model was experimentally implemented (Grumbacher et al. 1993) obtaining a similar behavior. In 1992, Olami, Feder and Christensen (OFC) proposed a spring-block model to explain in a first approximation the seismic dynamics (Olami et al. 1992). OFC reproduced a Gutenberg–Richter law for the synthetic seismicity generated by means of this model. Nowadays, the idea that the earth's crust is a SOC system has gained

✉ Fercia Angulo-Fernández
ferciaa@gmail.com

[1] Posgrado en Ciencias de la Tierra, Centro de Ciencias de la Atmósfera, UNAM, Circuito Institutos s/n, Ciudad Universitaria, 04510 Mexico City, Mexico

[2] Instituto Politécnico Nacional-UPIITA, Av. IPN 2580, 07340 Mexico City, Mexico

[3] Instituto de Geofísica, UNAM, Circuito Institutos s/n, Ciudad Universitaria, 04510 Mexico City, Mexico

terrain (Geller et al. 1997). According to Fraedrich and Lander (1993), "the dynamic relevant to atmospheric phenomena may be characterized by a wide range of scales which exhibit scale invariance or scaling behavior; that is, fluctuations at small scale, are related to larger ones by the same scaling law without showing any preferred mode". However, for the case of frequency–magnitude relationship of seisms (Gutenberg–Richter law), it is well established that there exists a crossover between the scaling of small and large earthquakes for a magnitude around $M = 7.5$ (Pacheco et al. 1992). Later, we will see that an analog crossover is observed in the scaling relationships corresponding to the rainfall statistics.

On the other hand, since 1990 it has been proposed that the registers of rain intensities in meteorologic stations can be interpreted within the context of SOC theories, that is, the different stages of the rain phenomenon, mainly in the precipitation phase, interpreted as the water relaxation in the troposphere, could be an indication of self-organized criticality (Andrade et al. 1998; Peters et al. 2002; Peters and Christensen 2002; García-Marín et al. 2008; Svensson et al. 1996). Interestingly, Peters and Christensen (2002) suggest an analogy between earthquakes and rain events as SOC phenomena. This analogy is as follows: (a) for the crust of Earth the energy source are the convective currents of the mantle, and for the atmosphere is the Sun; (b) for the Earth's crust the energy storage is the tension and for the atmosphere is the evaporated water; (c) for the Earth's crust the threshold is friction and for the atmosphere is saturation; (d) for the Earth's crust the release of energy is by means of earthquakes and for the atmosphere is through rain events.

According to Andrade et al. (1998), an important consequence of SOC models could be to improve the managing of early warning, protection, adaptation, etc. for the case of disasters detonated by geophysical forces. One of the main sources of catastrophes affecting the human kind are the climatic variability and extreme hydrological events. According to these authors (Andrade et al. 1998), extending the SOC concept to the analysis of meteorologic phenomena such as droughts, big storms and floods (Lovejoy and Schertzer 1991) can be of great usefulness. Recently, Andrade et al. (1995) analyzed historical registers of surface temperatures of the south Pacific ocean and they found that the EL NIÑO phenomenon is an example of SOC behavior in the climatic context.

On the other hand, according to Mandelbrot's ideas, many of the scale invariance properties associated with fractals did not have their own physical sense. However, by linking these properties with the power laws derived from some physical phenomena such as annual river discharges or seismicity, the physical sense of fractality was understood. Hurst studied the river Nile flows and reservoir modeling (Mandelbrot 1977; Mandelbrot and Hudson 2004), discovering a major empirical law concerning long-range dependence in geophysics, using what is now called the Hurst exponent (H). The H exponent is computed using rescaled range analysis (R/S), which has been introduced in the study of climate time series, such as precipitation data. As shown by Schepers et al. (1992) and later used by Andrade et al. (1995), a good estimate of H for a given time series can be obtained from the relation $H = \beta - 1/2$ where β is the absolute value of the exponent in the Fourier amplitude spectrum, which is very important to determine the SOC nature of some complex phenomena (Bak et al. 1987, 1988).

Some efforts to study the climatic conditions have been made by several authors such as Rangarajan and Sant (2004) that used the fractal analysis in data series of some regions of India, and Rehman and El-Gebeily (2009), who used H exponent to compute a climate predictability index based on barometric pressure and temperature series analysis.

In the present work, we use rain intensity (in mm/day) data obtained from meteorological stations in six different zones in Mexico. We report data from stations located at several zones of Mexico. The studied zones are north of Baja California state (Z1); Hermosillo in Sonora state (Z2); Guasave municipality in Sinaloa state (Z3); Mexico city north (Z4); Mexico city south (Z5) and Tuxtla Gutierrez at Chiapas state (Z6) (see the map in Fig. 1). The data cover periods larger than two decades of registers. The analysis of the data suggests the SOC behavior reported by other authors (Fraedrich and Lander 1993; Andrade et al. 1998; Peters et al. 2002; Peters and Christensen 2002) for rain intensities. Additionally, we present a study of the Hurst exponent for the six mentioned zones. The connection of H with the spectral exponent β leads to β-values consistent with a SOC behavior of the rain events. The article is

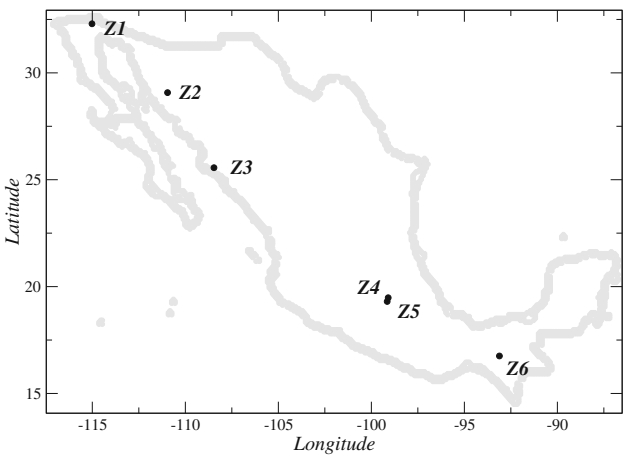

Fig. 1 Location of the six studied Mexican zones

organized in the following manner: the next section is dedicated to the employed data followed by which our methodology and results are shown, and finally the conclusions are presented.

Data

In the present study of rain intensities in Mexico, we use data obtained from the web page of CONAGUA (http://www.conagua.gob.mx), which is a government agency in charge of water management in Mexico. This work started focusing on the municipality of Guasave which has a warm-desert climate, where we take data from seven weather stations (defined as Z3, see Fig. 1) located in Sinaloa state in northwestern Mexico. The data available for these stations range from 1962 to 2015. To improve the statistics, we pooled the data under the assumption that all these stations are from the same region, resulting in more than 6000 points for the analysis. In Fig. 2 (Z3), we show the time series corresponding to the weather station Guasave-25038, which is representative of this municipality. Subsequently, we add five zones of other climatic regions of Mexico. The typical climate of the other five studied zones are the following ones: Z1 and Z2 have a warm-desert climate; Z4 and Z5 have climates ranging from temperate to humid cold alpine tundra and Z6 has a climate warm subhumid with rains in the summer. In Fig. 2, we show six time series corresponding to one representative station of each of the six zones. In each zone, we analyze a number of stations in the following way: in Z1 two stations (9003, 9009; ranging from 1945 to 2003), in Z2 three stations (26138, 26139, 26179; ranging from 1965 to 2016), in Z3 seven stations (25013, 25027, 25038, 25039, 25048, 25080, 25178; ranging from 1962 to 2015), in Z4 two stations (9003, 9029; ranging from 1933 to 2015), in Z5 three stations (9014, 9024, 9070; ranging from 1961 to 2015) and in Z6 three stations (7165, 7176, 7202; ranging from 1951 to 2016). For the six zones we pooled the data of the meteorological stations of each zone, the minimum number of data points is 1012 corresponding to Z1, and the maximum number is 12772 for Z6. However, due to the old registration technology used by these stations (it comes from the 50 s of the past century), the low-intensity values have great uncertainties. We remark that we are analyzing precipitation events, all data points that report zero

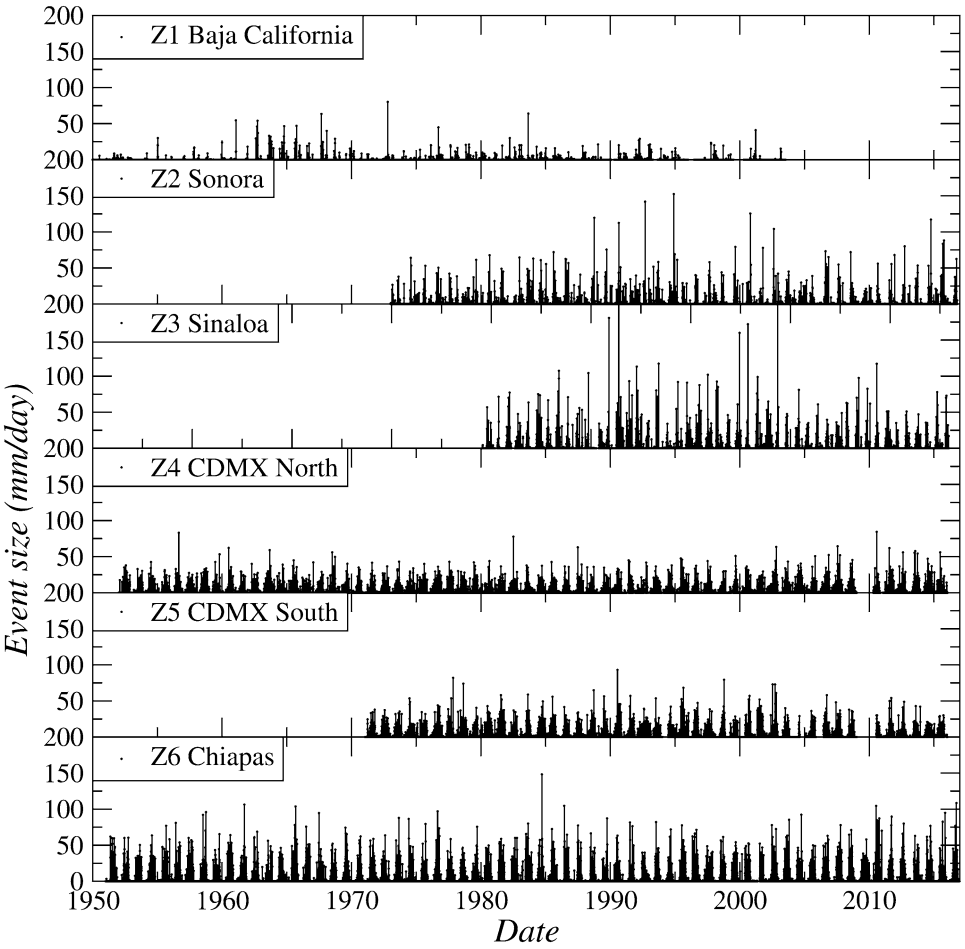

Fig. 2 Time series of rain intensities in mm/day for six representative meteorological stations of each zone. The studied data were the result of pooling all the stations of each zone. The time period and the number of points n (after removing zero values) for each zone are, respectively, the following ones: Z1 (1945–2003, $n_1 = 1012$), Z2 (1965–2016, $n_2 = 2699$), Z3 (1962–2015, $n_3 = 6619$), Z4 (1933–2015, $n_4 = 12407$), Z5 (1961–2015, $n_5 = 9171$) and Z6 (1951–2016, $n_6 = 12772$)

precipitation are removed from the statistics, such as it was made in Olami et al. (1992).

Methods and results

As we said in the "Introduction", we are looking for evidence that the statistical behavior of rain intensities in six Mexican zones supports the previously reported idea that the rain can be seen as a SOC phenomenon. To study the available data we will use two approaches: a frequency-size distribution and the Hurst exponent.

Frequency-size distribution

Many complex systems and processes cannot be characterized by means of one or few space and time scales. On the contrary, behind complex system behavior underlies a large variety of scales, described in general by power laws, which are of the form

$$p(x) \propto x^{-\tau}, \tag{1}$$

where τ is a parameter of the probability distribution $p(x)$ called the scaling exponent. The SOC systems are characterized by hyperbolic distributions of several quantities (Andrade et al. 1995). One of them is the relative frequency n of avalanches releasing energy (or mass), with a power law of the form

$$n(x) \propto x^{-\tau}. \tag{2}$$

As asserted by Andrade et al. (1998), the overall balance of water content in the atmosphere is governed by evaporation from subtropical oceans and transport within the atmosphere. After a certain residence time in the atmosphere and throughout the water cycle, the water is released by rainfall in avalanche-like events. This behavior suggests a SOC-type dynamics. Since long time ago, the most used procedure to register the intensity of precipitation of rainwater has been simply to collect the water in a container and measuring the amount of water after a certain time (hours or days). Despite the imprecision of this method it is able to capture the global statistical behavior of the rain. According to Peters et al. (2002), avalanches in a pile of grains or earthquakes do not look very different to rain, that is, the three phenomena are of the SOC type reaching for themselves a stationary critical state. For the case of rain events, these represent fluctuations of the water content in the atmosphere, hence with avalanches (Peters et al. 2002; Peters and Christensen 2002). Here, we use the cumulative distribution function $C(x)$ of the power law distribution given by the following equation:

$$C(x) = \int_x^M n(x)\mathrm{d}x, \tag{3}$$

where $n(x)$ is the number of events with size x and M is the maximum event in the data set. Eq. (3) gives

$$R(x) = \frac{C(x)}{x} \propto \frac{x^{-\tau}}{\tau - 1}\left[1 - \left(\frac{x}{M}\right)^{\tau-1}\right]. \tag{4}$$

When we plot $log(R(x))$ versus $log(x)$ for the rain data from the six Mexican zones studied, we obtain a behavior as those shown in Fig. 3. The six curves have a bimodal behavior with a crossover x_c between small and large rain intensities. For Z3, we found for $x < 30$ mm/day a slope of $\tau_1 = 1.34$ and for $x > 30$ mm/day a $\tau_2 = 3.72$, that is, there exists a crossover in $x_c = 30$ mm/day. A similar behavior was found for the other five zones (see Table 1).

All the values of τ_1 corresponding to $x < x_c$ are not so far from the $\tau_1 = 1.36$ found by Peters et al. (2002) and Peters and Christensen (2002) using high-resolution data collected with a compact vertically pointing Doppler radar at the Baltic coast Zingst with a resolution of minutes. On the other hand, our results for τ_1 are in reasonable agreement with those reported by Andrade et al. (1998) which are $\tau_1 = 1.1$ for Paris and $\tau_1 = 1.58$ for Karwar, and by García-Marín et al. (2008) for Cordoba (Spain) which is $\tau_1 = 1.17$. As asserted in Andrade et al. (1998) and García-Marín et al. (2008), Eq. (4) fits very well the bimodal curves of rain intensities for the cases of Paris (Andrade et al. 1998) and Cordoba (Spain) (García-Marín et al. 2008). In Fig. 3 we observe that for the six Mexican studied zones also bimodal curves of rain intensities are found using Eq. (4).

The fact that experimental data of rain intensities satisfy Eq. (4) is taken as a support of the SOC nature of the rain phenomenon (Andrade et al. 1998; García-Marín et al. 2008). According to Andrade et al. (1998), the ratio $\sigma =$

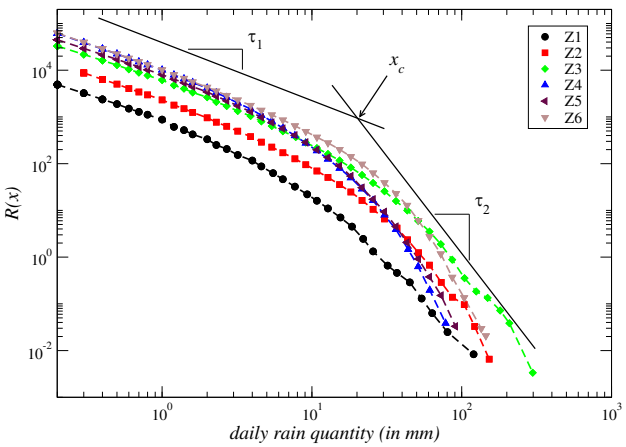

Fig. 3 Log–log plot of the distribution function $R(x)$ (Eq. 4) against x for the six zones

Table 1 Second column: τ_1 values; third column: τ_2 values; fourth column: crossover point x_c for each zone; fifth column: σ values; sixth column; Hurst exponent values

Zone	τ_1	τ_2	x_c (mm)	σ	H
Z1	1.37	3.23	25	2.35	0.57
Z2	1.44	3.94	25	2.73	0.60
Z3	.134	3.72	30	2.77	0.60
Z4	1.46	4.87	20	3.33	0.65
Z5	1.38	4.51	20	3.26	0.64
Z6	1.39	5.22	36	3.75	0.65

τ_2/τ_1 can give information on the specific interplay between the so-called large-scale and convective precipitation at a given location. For the case of tropical and subtropical regions, where convective precipitations abound, σ is in the range 2–3. In Table 1 we observe that for Z1, Z2 and Z3, the values of σ are $\sigma_1 = 2.35$, $\sigma_2 = 2.73$ and $\sigma_3 = 2.77$, respectively, which are in the interval 2–3 reported by Andrade et al. (1998) for tropical and subtropical regions, which is the case of Z1, Z2 and Z3. Interestingly, for Z4, Z5 and Z6, which are very rainy regions, the corresponding σs are $\sigma_4 = 3.33$, $\sigma_5 = 3.26$ and $\sigma_6 = 3.76$, respectively, which are in the range of $\sigma = 3.62$ reported for the case of Paris (Andrade et al. 1998), which also is a very rainy location.

In summary, the distribution of the number of rain intensities by size is reminiscent of the frequency–magnitude relationship for earthquakes (the GR law). Both distributions present a crossover between small and large scales reflecting a finite-size effect which for the case of seismicity has been explained by Pacheco et al. (1992) in terms of the width of the seismogenic layer. This finite-size effect is also evident in the synthetic seismicity modeled by SOC spring-block simulations made using cellular automata (Olami et al. 1992). It would be very interesting to investigate the cause of the finite-size effect in rain intensities. On the other hand, the values found for τ_1 are not so far from the characteristic scaling exponents appearing in other SOC phenomena (Olami et al. 1992; Angulo-Brown and Muñoz-Diosdado 1999).

Hurst exponent

In 1951, Hurst introduced the rescaled-range R/S analysis to study temporal correlations in annual Nile river discharges (Hurst et al. 1965). This method is appropriate to measure long-term memory of time series. To calculate the amount R/S first the mean of each nth segment of length T is obtained:

$$\langle x \rangle_{n,T} = \frac{1}{T} \sum_{i=(n-1)T+1}^{nT} x_i. \tag{5}$$

The standard deviation $S_{n,t}$ of the nth segment of length T is defined as

$$S_{n,T} = \left[\left(\frac{1}{T} \right) \sum_{i=(n-1)T+1}^{nT} (x_i - \langle x \rangle_{n,T})^2 \right]^{1/2}. \tag{6}$$

For each point i in the time series, it is calculated,

$$y_{i,n,T} = \sum_{k=(n-1)T+1}^{i} (x_i - \langle x \rangle_{n,T}), \tag{7}$$

for $(n-1)T + 1 < i < nT$. The range $R_{n,T}$ in the nth segment is then calculated by subtracting the smallest value of $y_{i,n,T}$ from the largest value of $y_{i,n,T}$. The range is divided by the standard deviation to determine the rescaled range and define an average rescaling range as

$$(R/S)_T = \frac{1}{N(T)} \sum_{n=1}^{N(T)} (R_{n,T})/(S_{n,T}). \tag{8}$$

The rescaled range is calculated for different time durations T, and the logarithm of $(R/S)_T$ against the logarithm of T is plotted. The slope of this graph is H, the so-called Hurst exponent. The exponent H takes values in the interval (0,1). The value $H = 0.5$ corresponds to a R/S local dependence and it suggests that observations sufficiently distant from each other in time are statistically independent. In fact, for a series of Gaussian random variables (white noise) the value of H should be 0.5 (Siu-Ngan Lam 1993). On the other hand, $H \neq 0.5$ corresponds to a R/S-global dependence (Mandelbrot 2002), when $\frac{1}{2} < H < 1$, the difference between consecutive values of the time series are said to be persistent, that is, increases at one time are more likely to be followed by increases at later times, and decreases at one time are more likely to be followed by decreases at later times. On the other hand, when $0 < H < 0.5$, the time series behavior is antipersistent, that is, increases at one time are more likely to be followed by the decreases at later times, and decreases at one time are more likely to be followed by increases at later times (Liebovicitch 1998).

Another common method to investigate correlations in time series is the detrended fluctuation analysis (DFA) (Peng et al. 1994). The DFA scaling exponent α is nearly related to the Hurst exponent (Kantelhardt 2008) (see below).

According to Mandelbrot (2002), typically in geophysics $H > 0.5$. However, in a recent paper, López-Lambraño et al. (2017) presented an extensive compilation

of H values for precipitation time series around the world, including some cases where $H < 0.5$, as, for example, in Tamil Nadu, India (Rehman and El-Gebeily 2009) with a tropical steppe climate, $H = 0.21$. Other cases with $H \leq 0.5$ are some places at the south Baltic sea in Europe (Domino et al. 2014). For example, in Kolobrzeg $H = 0.45$, that is, a case of negative autocorrelations and in Swinoujscie $H = 0.49$, that is, near a white noise type behavior with no correlations.

In Fig. 4, we depict a double log plot of R/S against lag for the six Mexican zones under study. The corresponding values of H are shown in Table 1, and they are $H_1 = 0.57$, $H_2 = 0.60$, $H_3 = 0.60$, $H_4 = 0.65$, $H_5 = 0.64$ and $H_6 = 0.65$, that is, all these values correspond to persistent time series. These results of H correspond to around 1.5 decades in the T-axis (lags from 6 days to 200 days). This time interval is limited by the duration of the rain seasons in Mexico and by the low resolution of the measurement technology of the meteorological stations (the minimum resolution is 1 day). However, our estimation of H is reasonably consistent with the H behavior reported by Peters et al. (2002) in the range from 10^3 to 10^5 minutes. In addition, our results are also consistent with the number of decades reported in the original work of Hurst [Sutcliffe et al. (2016); Hurst (1949)]. On the other hand, if we use the detrended fluctuation analysis (DFA) (Kantelhardt 2008) for the same data, we found that the DFA exponent α has the following values: $\alpha_1 = 0.57$, $\alpha_2 = 0.53$, $\alpha_3 = 0.55$, $\alpha_4 = 0.62$, $\alpha_5 = 0.62$ and $\alpha_6 = 0.61$, no so far from the relation $H \approx \alpha$, which is valid for α in the interval (0.5, 1) (Kantelhardt 2008). Interestingly, if we use the relation between the spectral exponent β and the Hurst exponent H mentioned in the "Introduction", that is, $H = \beta - 0.5$, we find that $\beta_1 = 1.07$, $\beta_2 = 1.1$, $\beta_3 = 1.1$, $\beta_4 = 1.15$, $\beta_5 = 1.14$ and $\beta_6 = 1.15$. All these values are very close to the so-called flicker noise or $1/f$ noise, which is a characteristic of self-organized critical systems (Bak et al. 1987, 1988).

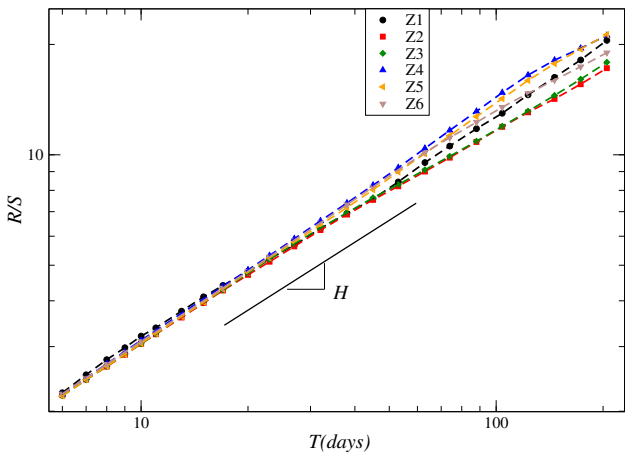

Fig. 4 Hurst exponents for the six zones

Conclusions

Peters and Christensen suggest that rain is an excellent example of a self-organized critical process (Peters and Christensen 2002). However, Andrade et al. (1998) had suggested since 1998 this same idea by analyzing rain data taken from several stations from several regions of the world. In the present paper, we have analyzed precipitation data from six zones of Mexico by means of two scaling approaches: the relative frequency N of rain events and the Hurst exponent.

Essentially, we found power laws with exponents in the same range reported by Peters and Christensen (2002), Andrade et al. (1998) and García-Marín et al. (2008), that is, our results support the hypothesis that the rain process has a SOC behavior. The precipitation data we used have inaccuracies for low-intensity values; nevertheless, seemingly the statistical behavior is robust enough to obtain scaling exponents within the intervals reported by other authors. In summary, the SOC hypothesis is very suitable to describe the different stages of the rain phenomenon as the relaxation output of the complex system, that is, the troposphere, which is the part of the atmosphere where the climatic phenomenon occurs. Finally, we suggest that it would be very interesting to investigate the cause of the finite-size effect in rain intensities proceeding perhaps by analogy with the possible cause of the finite-size effect observed in the Gutenberg–Richter law.

Acknowledgements This work is part of the doctoral research of FAF supported by a CONACyT fellowship. FAF thanks Professor Virginia García Acosta for fruitful discussions and the kind hospitality of CIESAS. IRR thanks CONACyT, COFAA-IPN and EDI-IPN from Mexico.

Compliance with ethical standards

Conflict of interest The authors declare no conflict of interest.

References

Andrade JS Jr, Wainer I, Mendes Filho J, Moreira JE (1995) Self-organized criticality in the El Nio Southern oscillation. Phys A 215:331

Andrade RFS, Schellnhuber HJ, Claussen M (1998) Analysis of rainfall records: possible relation to self-organized criticality. Phys A 254:557

Angulo-Brown F, Muñoz-Diosdado A (1999) Further seismic properties of a spring-block earthquake model. Geophys J Int 139:410–418

Bak P, Tang C, Weisenfeld K (1987) Self-organized criticality: an explanation of the 1/f noise. Phys Rev Lett 59:381
Bak P, Tang C, Weisenfeld K (1988) Self-organized criticality. Phys Rev A 38:364
Domino K, Blachowicz T, Ciupak M (2014) The use of copula functions for predictive analysis of correlations between extreme storm tides. Phys A 413:489
Fraedrich K, Lander C (1993) Scaling regimes of composite rainfall time series. Tellus 45A:289
García-Marín A, Jiménez-Ornero F, Ayuso JL (2008) La criticalidad autoorganizada y el análisis de datos históricos de lluvia en Córdoba (Andalucía). Ingeniería del Agua 15:13
Geller RJ, Jackson DD, Kagan Y, Mulargia F (1997) Earthquakes cannot be predicted. Science 275:1616
Grumbacher SK, McEwen KM, Halverson DA, Jacobs DT, Lindner J (1993) Self organized criticality: an experiment with sandpiles. Am J Phys 61:329
Gutenberg B, Richter CF (1944) Frequency of earthquakes in California Bull. Seism. Soc. Am. 34:185
Hurst HE (1949) The capacity needed in reservoirs for long-term storage. The Nile Basin, Supplement to, vol. VII. Government Press, Cairo
Hurst HE, Black RP, Simaika YM (1965) Long-term storage: an experimental study. Constable, London
Kanamori H, Anderson DL (1974) Theoretical basis of some empirical relations in seismology. Bull Seism Soc Am 54:1073–1095
Kantelhardt Jan W (2008) Fractal and Multifractal Time Series, arXiv:0804.0747v1 [physics.data-an]
Liebovicitch LS (1998) Fractals and chaos simplified for the life sciences. Oxford University Press, Oxford
López-Lambraño A, Carrillo-Yee E, Fuentes C, López- RA, López-Lambraño M (2017) Una revisión de los métodos para estimar el exponente de Hurst y la dimensión fractal en series de precipitación y temperatura Rev. Mex Fís 63:244
Lovejoy S, Schertzer D (eds) (1991) Nonlinear variability in geophysics: scaling and fractals. Kluwer, The Netherlands
Mandelbrot BB (1977) The fractal geometry of nature. WH freeman, New York
Mandelbrot BB (2002) Gaussian self-affinity and fractals. Springer, Berlin
Mandelbrot BB, Hudson R (2004) The (mis)behaviour of markets: a fractal view of risk, ruin and reward. Profile Books, London
Olami Z, Feder HJS, Christensen K (1992) Self-organized criticality in a continuous, nonconservative cellular automaton modeling earthquakes. Phys Rev Lett 68:1244–1248
Pacheco JF, Scholz CH, Sykes LR (1992) Changes in frequency-size relationship from small to large earthquakes. Nature 335:71–73
Peng C-K, Buldyrev SV, Havlin S, Simons M, Stanley HE, Goldberger AL (1994) Mosaic organization of DNA nucleotides. Phys Rev E 49:1685
Peters O, Christensen K (2002) Rain: relaxations in the sky. Phys Rev E 66:036120–1
Peters O, Hertlein C, Christensen K (2002) A complexity view of rainfall. Phys Rev Lett 88:018701–1
Rangarajan G, Sant DA (2004) Fractal dimension analysis of Indian climatic dynamics. Chaos Solit Fract 19:285–291
Rehman S, El-Gebeily M (2009) A study of Saudi climatic parameters using climatic predictability indices. Chaos Solit Fract 41:1055
Richter CF (1958) Elementary seismology. W. H. Freeman, New York
Schepers HE, van Beek JHGM, Bassingthwaighte JB (1992) Four methods to estimate fractal dimension from self-affine signals. IEEE Eng Med Biol 11:57
Scholz CH (1992) The mechanics of earthquakes and faulting. Cambridge University Press, Cambridge
Siu-Ngan Lam N, De Cola L (1993) Fractals in geography. Prentice Hall, Upper Saddle River
Sutcliffe J, Hurst S, Awadallah AG, Brown E, Hamed K (2016) Harold Edwin Hurst: the Nile and Egypt, past and future. Hydrol Sci J 61:1557–1570
Svensson C, Olsson J, Berndtsson R (1996) Multifractal properties of daily rainfall in twp different climate. Water Resour Res 32:2463
Utsu T, Seki A (1954) A relation between the area of aftershocks regions and the energy of main shock. J Seism Soc Jpn 7:233

Acta Geophysica (2018) 66:369–379
https://doi.org/10.1007/s11600-018-0146-x

RESEARCH ARTICLE - SPECIAL ISSUE

Assessment of satellite-based precipitation estimates over Paraguay

Fiorella Oreggioni Weiberlen[1] · Julián Báez Benítez[1]

Received: 15 November 2017 / Accepted: 11 April 2018 / Published online: 17 April 2018

Abstract
Satellite-based precipitation estimates represent a potential alternative source of input data in a plethora of meteorological and hydrological applications, especially in regions characterized by a low density of rain gauge stations. Paraguay provides a good example of a case where the use of satellite-based precipitation could be advantageous. This study aims to evaluate the version 7 of the Tropical Rainfall Measurement Mission Multi-Satellite Precipitation Analysis (TMPA V7; 3B42 V7) and the version 1.0 of the purely satellite-based product of the Climate Prediction Center Morphing Technique (CMORPH RAW) through their comparison with daily in situ precipitation measurements from 1998 to 2012 over Paraguay. The statistical assessment is conducted with several commonly used indexes. Specifically, to evaluate the accuracy of daily precipitation amounts, mean error (ME), root mean square error (RMSE), BIAS, and coefficient of determination (R^2) are used, and to analyze the capability to correctly detect different precipitation intensities, false alarm ratio (FAR), frequency bias index (FBI), and probability of detection (POD) are applied to various rainfall rates (0, 0.1, 0.5, 1, 2, 5, 10, 20, 40, 60, and 80 mm/day). Results indicate that TMPA V7 has a better performance than CMORPH RAW over Paraguay. TMPA V7 has higher accuracy in the estimation of daily rainfall volumes and greater precision in the detection of wet days (> 0 mm/day). However, both satellite products show a lower ability to appropriately detect high intensity precipitation events.

Keywords Precipitation · Satellites · TMPA V7 · CMORPH RAW · Paraguay

Introduction

In the atmospheric and water sciences it is important to recognize the spatial and temporal variability of precipitation to improve the understanding of the water and energy cycles. In addition, reliable long-term precipitation series are indispensable for the study of climate change and extreme events, and are crucial input data for a variety of climatological, hydrological, agricultural, and industrial applications (Ebert et al. 2007).

Precipitation data obtained through rain gauges are considered as the most reliable source of data since they are based on direct measurements on earth surface. Nevertheless, in developing countries and in remote areas of the world, these instruments are often scarce or non-existent, leading to poor spatial representation of precipitation patterns (Duan et al. 2016; Su et al. 2008). Additionally, precipitation time series collected at rain gauges frequently present gaps and inhomogeneities, which makes it difficult to use them as forcing data in applications that require continuous rainfall times series such as hydrological and climate models (Duan et al. 2016). Both limitations are true for Paraguay; therefore, it is important to find alternative sources of rainfall data to conduct in-depth research and develop decision support tools for different end users.

In this context, precipitation estimates obtained by remote sensors located on satellite platforms are a potential source of data due to their high spatial and temporal resolution, few quantity of missing data, online availability without restriction, and since they allow to obtain data in areas of difficult access for the human being (Su et al. 2008; Collischonn et al. 2001). These estimates use either the infrared (IR) information, the microwave (MW)

✉ Fiorella Oreggioni Weiberlen
fiorella.oreggioni@uc.edu.py

Julián Báez Benítez
julian_baez@uc.edu.py

[1] Department of Civil, Industrial and Environmental Engineering, Catholic University of Asuncion, Asunción, Paraguay

information, or a combination of IR and MW information (Duan et al. 2016). The IR information measured from Geosynchronous (GEO) orbit satellites, is used to estimate precipitation based on the established relationship between cloud-top temperature and precipitable water. A variety of retrieval algorithms were developed to convert IR information into precipitation estimates (e.g. Arkin and Meisner 1987). The MW information typically measured from passive microwave sensors (PMW) on low earth orbit (LEO) satellites, provides information about atmospheric constituents and cloud profiles, which are more physically related to precipitation rates (Zeng et al. 2018). Different retrieval algorithms can be applied to convert the MW information into precipitation estimates (e.g. Ferraro 1997 and Wilheit et al. 1994). Precipitation estimates from IR information (high temporal resolution and wide spatial coverage) and MW information (high accuracy; strong relation to rainfall) are often combined to complement each other to provide improved estimates (Ebert et al. 2007). Several satellite products were developed by blending IR and MW data such as the Tropical Rainfall Measurement Mission (TRMM) Multi Satellite Precipitation Analysis (TMPA) (Huffman et al. 2007) and the Climate Prediction Center Morphing Technique (CMORPH) (Joyce et al. 2004).

The performance of satellite precipitation products (SPPs) could differ by region (Zeng et al. 2018); therefore, numerous assessments have been carried out in several areas of the world at different temporal and spatial resolutions to analyze the quality of these estimates (Duan et al. 2016; Sun et al. 2016; Wu and Zhai 2012; Tian et al. 2007; Ebert et al. 2007). A number of studies were conducted over South America (Salio et al. 2015; Ruiz 2009; de Goncalves et al. 2006), La Plata basin (Su et al. 2008), Argentina (Sepulcri et al. 2009), Brazil (dos Reis et al. 2017; Quirino et al. 2017; Melo et al. 2016; De Almeida et al. 2015; Buarque et al. 2011), Bolivia (Blacutt et al. 2015), Chile (Zambrano-Bigiarini et al. 2017), Tropical, Subtropical and Central Andes (Hobouchian et al. 2017; Manz et al. 2016; Scheel et al. 2011), the Guiana Shield (Ringard et al. 2015), Colombia (Dinku et al. 2010), and Ecuador and Peru (Cabrera et al. 2016; Zubieta et al. 2015). However, there is no study conducted exclusively over Paraguay.

At a global scale, TMPA and CMORPH products are playing important roles mainly due to their long-term series datasets and adequate retrieval methods (Jiang et al. 2017). Moreover, studies reveal that these two SPPs provides the best precipitation estimates in the TRMM era (Jiang et al. 2016). Su et al. (2008) evaluated basinwide precipitation estimates from the TMPA V6 through comparison with available gauged data over La Plata basin at daily and monthly time scales. They concluded that TMPA V6 estimates agreed well (strong correlations and low bias) with the gridded gauge data (spatial resolution of 0.25°) at monthly times scales; however, this agreement was reduced at daily time scales, particularly for high rain rates. Moreover, they assessed the effectiveness of this satellite product for hydrologic prediction and they determined that TMPA V6 has a potential for hydrologic forecasting in data-sparse regions. Ruiz (2009) evaluated different methodologies for the calibration of the CMORPH version 0.x over Southeastern South America. As the first step in the calibration process he assessed the CMORPH version 0.x precipitation estimates through their comparison with gridded rain gauge data and he found that CMORPH version 0.x is capable to appropriately detect rainfall events but tends to overestimate precipitation amounts. It should be mentioned that Paraguay and other regions were not analyzed in this study due to the low quality of the rain gauge data available. Salio et al. (2015) evaluated six different satellite rainfall estimates, the TMPA V6, V7 and RT, the operational CMORPH version 0.x, the Hydroestimator (HYDRO) and the Combined Scheme algorithm (CoSch) over southern South America. The available rain gauge data from a dense Inter-Institutional station network were interpolated at 0.25° resolution to the comparison with the SPPs at daily scale. They concluded that satellite precipitation products that include microwave observations and surface observations in their adjustments show higher performances.

This study aims to establish a basis for understanding the characteristics of satellite precipitation products over Paraguay and to promote their use in research and in a variety of applications at national level. The widely used TMPA in its last version (version 7) and CMORPH satellite-only precipitation product in its last version (version 1.0) will be quantitatively validated relative to rain gauge observations from January 1998 to December 2012 over this country. The results are expected to reveal the capability of these satellite products to detect daily precipitation frequencies and amounts.

The remainder of this paper is organized as follows: "Materials and method" introduces the study area and provides a brief description of the two evaluated precipitation products and used rain gauge station data. The validation technique and statistical metrics are also presented in "Materials and method". Then "Results and discussion" presents the results and discussion, followed by the conclusions in the "Conclusions".

Materials and method

Study area

Paraguay is a country located in the center of South America bounded by three countries: Bolivia, Argentina and Brazil. It is comprised between 19°18′S and 27°36′S and between 54°19′W and 62°38′W, and despite of being a landlocked country, is bordered and crisscrossed by navigable rivers.

The Paraguay river divides the country into different eastern and western regions. Both the eastern region—officially called Eastern Paraguay—and the western region—officially called Western Paraguay—gently slope toward and are drained into the Paraguay river (Federal Research Division of the Library of Congress of the Unitated States Government 1990). The climate is tropical to subtropical and the amount of precipitation varied between 600 mm/year in the Norwest of the Western Paraguay to 1900 mm/year in the Eastern Paraguay.

Datasets

Tropical Rainfall Measurement Mission Multi-Satellite Precipitation Analysis (TMPA)

The first scientific mission devoted to studying tropical and subtropical precipitations by means of microwave and infrared sensors, was the so-called Tropical Rainfall Measuring Mission (TRMM). It was a joint mission between the National Aeronautics and Space Administration (NASA) and the Japan Aerospace Exploration Agency (JAXA) and its main objective was to increase the understanding of the water and energy cycles on earth through the improvement of knowledge of precipitation characteristics among the tropics (Braun 2011; National Space Development Agency of Japan 2001).

The mission comprised the TRMM satellite, which was launched in November 1997 from the Tanegashima Space Center (National Space Development Agency of Japan 2001). In July of 2014, the satellite began its descent because it ran out of fuel reserves. It was deactivated in April of 2015 and parts of it that resisted the descent entered the terrestrial atmosphere on June 17 of the same year (Huffman 2016).

It was a circular orbit satellite, not synchronized with the sun, with an inclination of 35° with respect to the equator. It orbited at a height of 403 km since August of the 2001 until its descent, before that, it orbited at a height of 350 km (National Aeronautics and Space Administration 2016). It had five instruments on board, a Precipitation Radar (PR), a Microwave Imager (TMI), a Visible Infrared Scanner (VIRS), a Clouds and Earth's Radiant Energy System (CERES) and a Lighting Imager Sensor (LIS) (National Space Development Agency of Japan 2001).

The PR, TMI, and VIRS were the TRMM rainfall measurement package. The PR was an electronically scanning radar that measures the three-dimensional rainfall distribution over both land and earth and define the layer depth of the precipitation. The TMI was a multichannel dual-polarized passive microwave radiometer that provided information on the integrated column precipitation content, cloud liquid water, cloud ice, rain intensity, and rainfall types. The VIRS was a five channel, cross-track scanning radiometer which provided high resolution observations on cloud coverage, cloud type, and cloud top temperatures. The LIS was an optical starting telescope and filter imaging system which detected the distribution and variability of both intracloud and cloud-to-ground lighting over the tropical region of the globe. The CERES was a cross-track scanner that failed after 8 months of flight. During that time, CERES measured the energy at the top of the atmosphere and estimated energy levels within the atmosphere and at the Earth's surface (Braun 2011; National Space Development Agency of Japan 2001).

The TRMM mission provides several products in real time and in post real time. In this study the latest version (version 7) of the post real time product called TRMM Multi-Satellite Precipitation Analysis (TMPA; TRMM 3B42) is used. TMPA estimates are basically produced in four stages according to Huffman et al. (2007) and Huffman (2013): (1) microwave data obtained through passive sensors located in low-orbit satellites are converted to precipitation estimates through different algorithms, then these estimates are calibrated and combined in grids of 0.25° × 0.25° every 3 h, (2) infrared data derived from an international constellation of geostationary orbit satellites are used to generate infrared precipitation satellite estimations using microwave-estimated precipitation, (3) microwave and infrared precipitation estimations are combined, and (4) estimates are calibrated with monthly data. TMPA V7 was implemented in May 2012, replacing all previews versions. Majors changes are summarized in Huffman and Bolvin (2017) and include the addition of microwave humidity soundings, a new IR brightness datasets, a uniformly reprocessed MW input data, a uniformly processed surface precipitation gauge analysis, and the use of a latitude-band calibration scheme for all satellites.

TMPA V7 have a spatial resolution of 0.25° × 0.25°, a temporal resolution of 3 h, and represent the rainfall intensity (mm/h) obtained from an average of the precipitation accumulated ± 90 min of the nominal hour. There are available on a global scale from 1998 and in binary format. Despite the descent of the TRMM satellite, TMPA

V7 is expected to continue to be generated until approximately mid-2018 (Huffman 2016).

Climate prediction center morphing technique (CMORPH)

CMORPH is a technique based on the Lagrangian approach to produce global precipitation estimates with a high spatial and temporal resolution (Joyce et al. 2004). It is being developed by the Climate Prediction Center (CPC) of the National Oceanic and Atmospheric Administration (NOAA).

The initial version, called version 0.x, uses cloud motion vectors derived from consecutive IR images from geostationary satellites to propagate the estimated precipitation amounts derived from microwave observations from passive microwave sensors (PMW) located at low earth orbit satellites. Therefore, CMORPH combines the high-quality precipitation estimates generated through microwave observations and the higher temporal and spatial resolution of the infrared data (Joyce et al. 2004). However, this version was reprocessed with a frozen algorithm and with input PMW retrievals from multiple low-orbit satellite sensors (SSM/I from DMSP 13, 14, and 15 satellites, AMSR-E from Aqua satellite, AMSU-B from NOAA-15, 16, and 17 satellites, and TMI from TRMM satellite), IR observations from each geostationary satellite operator (NOAA/CPC Merged 4-km Geostationary Satellite IR Tb Data), and with NESDIS daily snow maps throughout the data period (Xie et al. 2017). This reprocessed version (version 1.0) of the purely satellite-based CMORPH is called CMORPH RAW.

CMORPH RAW is available in three different spatial and temporal resolutions, 8°–30 min, 0.25°–3 h and 0.25°–1 day, covering the entire globe and is available for the entire TRMM/GPM era, i.e. from January 1998 until today. In this study, the CMORPH RAW with spatial and temporal resolution of 0.25°–3 h is used to facilitate the comparison with TMPA V7. Each gridded datum represents the accumulated precipitation + 180 min of the nominal hour (mm/3 h).

Rain gauge data

Daily precipitation data between 1998 and 2012 (15 years) from 22 conventional weather stations of the Directorate of Meteorology and Hydrology of the Paraguayan Directorate of Civil Aeronautics (DMH/DINAC) are used for being the most reliable data source at a national level (Fig. 1). These daily data represent a 24 h accumulation period at 12UTC.

Validation technique and method

Satellite estimations are gridded whereas rain gauge data are irregularly distributed. Hence, taking into account the low density of weather stations in the Paraguayan territory, interpolate rain gauge data into grid at the same spatial resolution of satellite estimations would lead to an introduction of false information and errors into the rain gauge data (Wu and Zhai 2012; Sepulcri et al. 2009). Therefore, this study was limited to a timely comparison between daily data of the satellite grids and daily data of rain gauge stations located within them (point-to-pixel analysis). This technique ensures consistency between observed data and satellite estimation, and provides a more accurate assessment of the ability of satellite products to detect precipitation (Wu and Zhai 2012). In this context, the first step to make the comparison between satellite estimates and rain gauge data is to place data sets into similar temporal resolutions. Thus, to obtain daily satellite precipitation estimates, data from the nominal hours 12UTC, 15UTC, 18UTC and 21UTC of 1 day to the nominal hours 00UTC, 3UTC, 6UTC and 9UTC of the following day were added in each satellite product. The software Grid Analysis and Display System (GrADS) was used to process the data.

The statistical assessment is conducted with several commonly used indexes. To quantitatively evaluate the accuracy of satellite estimates, the following statistics were used: (1) mean error (ME), which represents the average daily error of the estimation with respect to the observation indicating whether it is an overestimation or underestimation, (2) root mean square error (RMSE), which provides a measure of the mean error value of the estimation without indicating whether the estimate overestimates or underestimates the observed value, (3) BIAS, which quantitatively represents the relationship between precipitation amounts accumulated in the analyzed period by means of the estimated and observed data, expressed in relation to the total amount of observed rainfall, and (4) coefficient of determination (R^2), which is a measure of the goodness of the adjustment or reliability of the estimation against the observed data.

$$\mathrm{ME} = \frac{1}{N} \cdot \sum_{i=1}^{N} (F_i - O_i), \tag{1}$$

$$\mathrm{RSME} = \sqrt{\frac{1}{N} \cdot \sum_{i=1}^{N} (F_i - O_i)^2}, \tag{2}$$

$$\mathrm{BIAS} = \frac{\sum_{i=1}^{N} (F_i - O_i)}{\sum_{i=1}^{N} Q_i}, \tag{3}$$

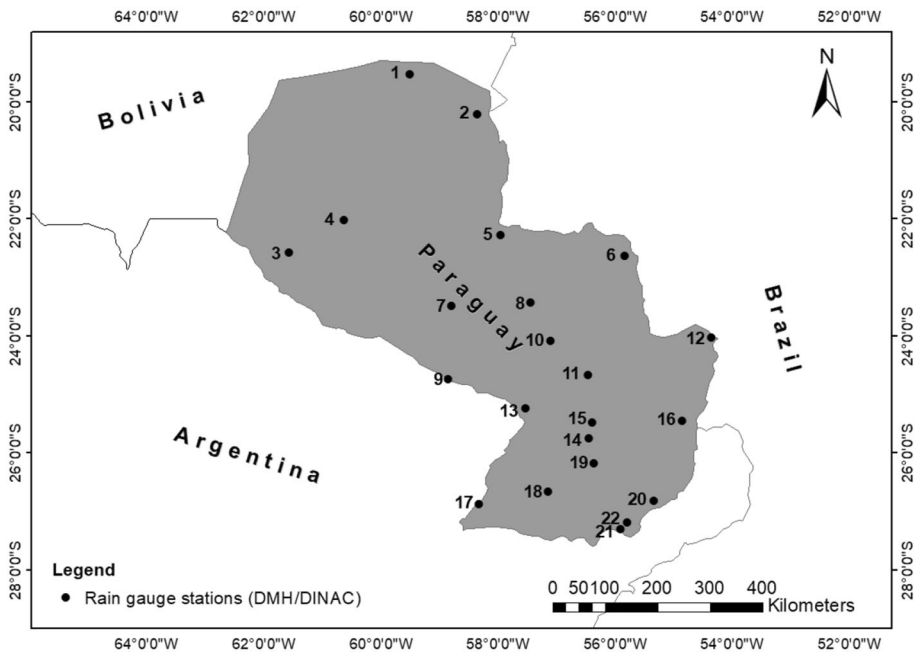

Fig. 1 Distribution of rain gauge stations used in this study

$$R^2 = \left[\frac{\sum_{i=1}^{N}(F_i - \bar{F}_i)(O_i - \bar{O}_i)}{\sum_{i=1}^{N}(F_i - \bar{F}_i)^2 \cdot \sum(O_i - \bar{O}_i)^2}\right]. \quad (4)$$

In Eqs. (1)–(4) the term F_i refers to values estimated by satellites (forecast), the term O_i refers to values observed in rain gauge stations (observed), and N is the number of pairs of data estimation-observation analyzed.

Furthermore, to quantitatively assess the ability of satellite products to detect precipitation events, the following indexes were used: (5) frequency bias index (FBI), which represents the proportion of the number of precipitation events detected by the satellite regarding the number of events detected by the gauges, thus indicating whether there is a tendency to overestimation (FBI > 1) or underestimation (0 ≤ FBI), and FBI = 1 if the frequency of precipitation events was perfectly estimated, (6) false alarm ratio (FAR), which measures the fraction of precipitation events that were detected by the satellite but not by the gauges, therefore, indicates false alarms present in satellite estimations; possible outcomes fluctuate between 0 and 1, where 0 indicates that the satellite data do not record false alarms, and (7) probability of detection (POD), which measures the fraction of occurrences of precipitation that were correctly detected by the satellite; possible results oscillate between 0 and 1, where 1 indicates a perfect detection.

$$\mathrm{FBI} = \frac{a+b}{a=c}, \quad (5)$$

$$\mathrm{FAR} = \frac{b}{a+b}, \quad (6)$$

$$\mathrm{POD} = \frac{a}{a+c}. \quad (7)$$

To calculate these indexes are necessary the resulting values of the 2 × 2 contingency table expressed in Wilks (2006), where; a is when the satellite and the rain gauge recorded precipitations, b is when the satellite recorded precipitation and the rain gauge did not, and c is when the rain gauge recorded precipitation and the satellite did not.

In addition, to assess the capability of satellite products to detect precipitation events of different intensities, the indexes FBI, FAR, and POD were calculated at different precipitation thresholds: 0.1, 0.5, 1, 2, 5, 10, 20, 40, 60 and 80 mm/day, using the 2 × 3 contingency table proposed by Wu and Zhai (2012), where; a is when satellites estimates and rain gauge observations are equal or higher than the threshold, b is when satellites estimates are greater than or equal to the threshold and rain gauge observations are lower than the threshold, and c is when satellite estimates are lower than the threshold and rain gauge observations are greater than or equal to the threshold.

Equations (1)–(7) can be found, for instance, in Prakash et al. (2018) Salio et al. (2015), Ringard et al. (2015), Wu and Zhai (2012) and Su et al. (2008).

Results and discussion

Accuracy assessment results

TMPA V7 shows slight underestimations and overestimations in daily rainfall amounts over different geographical areas of Paraguay; whereas, CMORPH RAW shows overestimations throughout the country (Fig. 2-ME). Specifically, TMPA V7 shows negative mean errors (underestimations) in six rain gauge stations, while in the others positive values were found (overestimations). In contrast, CMOPRH RAW shows positive ME values in all rain gauge stations analyzed. Furthermore, TMPA V7 shows lower mean errors than CMORPH RAW (Fig. 2-ME). The maximum ME value registered on the TMPA V7 is 0.49 mm/day at the rain gauge station #21, and the minimum value is -0.24 mm/day at the rain gauge station #18. However, the maximum ME value recorded in the CMORPH Raw is 1.89 mm/day at the rain gauge station #19, and the minimum value is 0.48 mm/day at the rain gauge station #4. With this regard, it can be observed that the maximum ME value of the TMPA V7 is close to the minimum ME value of the CMORPH RAW. Thus, CMORPH RAW estimates present a large daily overestimation of rainfall amounts. Wu and Zhai (2012) reported similar results between TMPA V6 and CMORPH v0.x over the Tibetan Plateau in China. Moreover, Ruiz et al. (2009) reported that CMORPH v0.x exhibit a tendency to overestimate precipitation amounts over South America.

Based on BIAS values, CMORPH RAW overestimates the total amount of precipitation in all rain gauge stations analyzed. On the contrary, TMPA V7 does not present a single pattern since underestimate the total precipitation amount in six rain gauge stations and in the others overestimate the total rainfall volume (Fig. 2-BIAS). Moreover, CMORPH RAW presents a greater overestimation of the total precipitation amounts than TMPA V7. Particularly, the highest overestimation recorded in CMORPH Raw has a value of 0.44 (44%) at the rain gauge station #19; nevertheless, the highest overestimation in the TMPA V7 product reaches a value of 0.1 (10%) at rain gauge stations #7 and #21. On the other hand, the lowest value recorded in the CMORPH Raw is 0.17 (17%) in rain gauge stations #5 and #6, and the lowest value registered in the TMPA V7 product is an underestimation of 5% (-0.05) at rain gauge stations #10 and #18. Similarly, Salio et al. (2015) reported that the operational CMORPH v0.x shows large overestimations of precipitation amounts (BIAS $>$ 50%) over the center and northeast Argentina (including Paraguay).

Moreover, CMORPH RAW records higher RMSE values than TMPA V7 in all rain gauge stations. Thus, it shows greater daily differences between estimates and observations (Fig. 2-RMSE). Additionally, both satellite products present higher RMSE values in the Eastern Paraguay than in the Western Paraguay. This finding could be explained by the difference in the daily rainfall amount between both regions (higher intensity in the Eastern Paraguay).

Finally, higher R^2 values were recorded in 14 of the 22 rain gauge stations for the product CMORPH RAW (Fig. 2-R^2). Nevertheless, the differences in R^2 values between CMORPH RAW and TMPA V7 are negligible. The greatest R^2 value registered in CMOPRH RAW is 0.614 in the rain gauge station #20 and the minimum value registered is 0.254 at the rain gauge station #4. Likewise, the maximum R^2 value recorded in the TMPA V7 is 0.582 in the rain gauge station #20 and the lowest value registered is 0.344 at the rain gauge station #2. Moreover, both satellite products show lower correlation with observed data in northern areas of Western Paraguay.

Precision assessment results

FBI values show that the CMORPH RAW product overestimate the number of precipitation events in all rain gauge stations analyzed. It reaches even a value of 2.87 in rain gauge station #21, which indicates that estimates of the number of precipitation events were almost three times the number of events registered in rain gauges (Fig. 3-FBI). On the contrary, FBI values show that the TMPA V7 does not have a unique pattern, since it overestimates the number of precipitation events in 17 rain gauge stations and underestimates it in 5. The highest FBI value registered in the TMPA V7 is 1.67 in rain gauge station #21 (overestimation of 67%). Conversely, the lowest FBI value recorded is 0.85 at rain gauge station #4 (underestimation of 15%). Nevertheless, in all rain gauge stations analyzed, FBI values from TMPA V7 are closer to the perfect estimation (FBI = 1); hence, it can be concluded that this satellite product has a greater precision in the estimation of the number of daily rainfall events.

Furthermore, in the entire number of rain gauge stations analyzed, higher FAR values are recorded in the CMORPH RAW (Fig. 3-FAR), which reveals that this satellite product has a higher percentage of false alarms. The maximum FAR value recorded in the CMOEPR RAW is equal to 0.67 (67%) in rain gauge station #21. Similarly, the maximum FAR value recorded in the TMPA V7 is 0.50 (50%) also in rain gauge station #21. Conversely, the lowest value recorded in the CMORPH Raw is 0.32 (32%) and in the TMPA V7 is 0.23 (23%), both registered in the rain gauge station #16.

CMORPH RAW seems to perform better than TMPA V7 estimates if only the POD index is analyzed, since higher POD values are recorded in all rain gauge stations

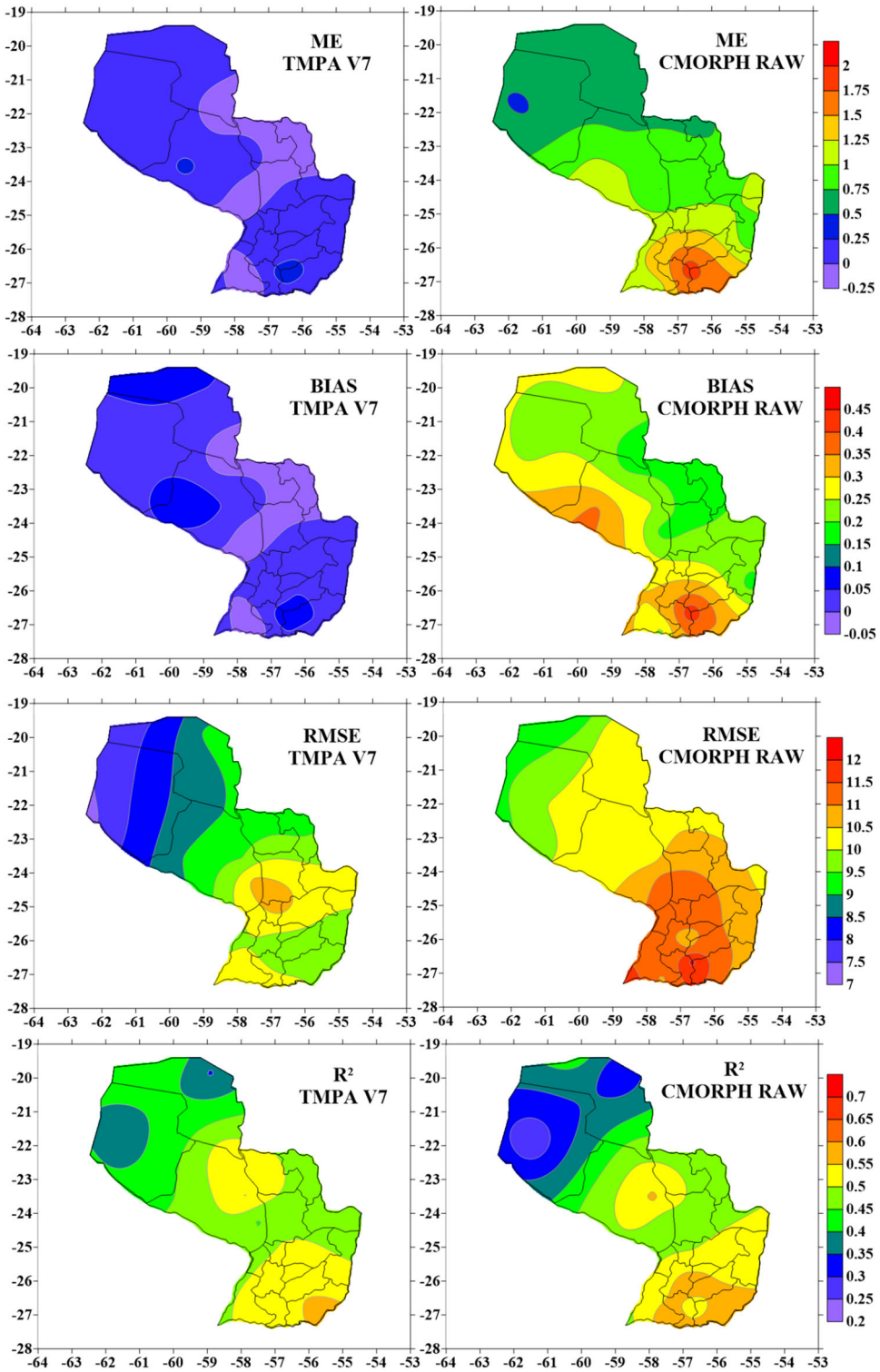

Fig. 2 Accuracy assessment results. Values were interpolated to provide an easier visualization of the results

(Fig. 3-POD). However, this improved capacity is probably due to the widespread overestimation of precipitation events presented in CMORPH RAW. Salio et al. (2015) found similar results over southern South America at low thresholds. POD values also show that satellite products have an improved ability in detect precipitation events in Eastern Paraguay rather than in Western Paraguay. This finding could also be associated with the daily amount of rainfall that characterizes each geographical zone.

The highest POD value recorded in the CMORPH RAW is 0.94 in rain gauge stations #20 and #21, which means that 94% of precipitation events are correctly detected. In

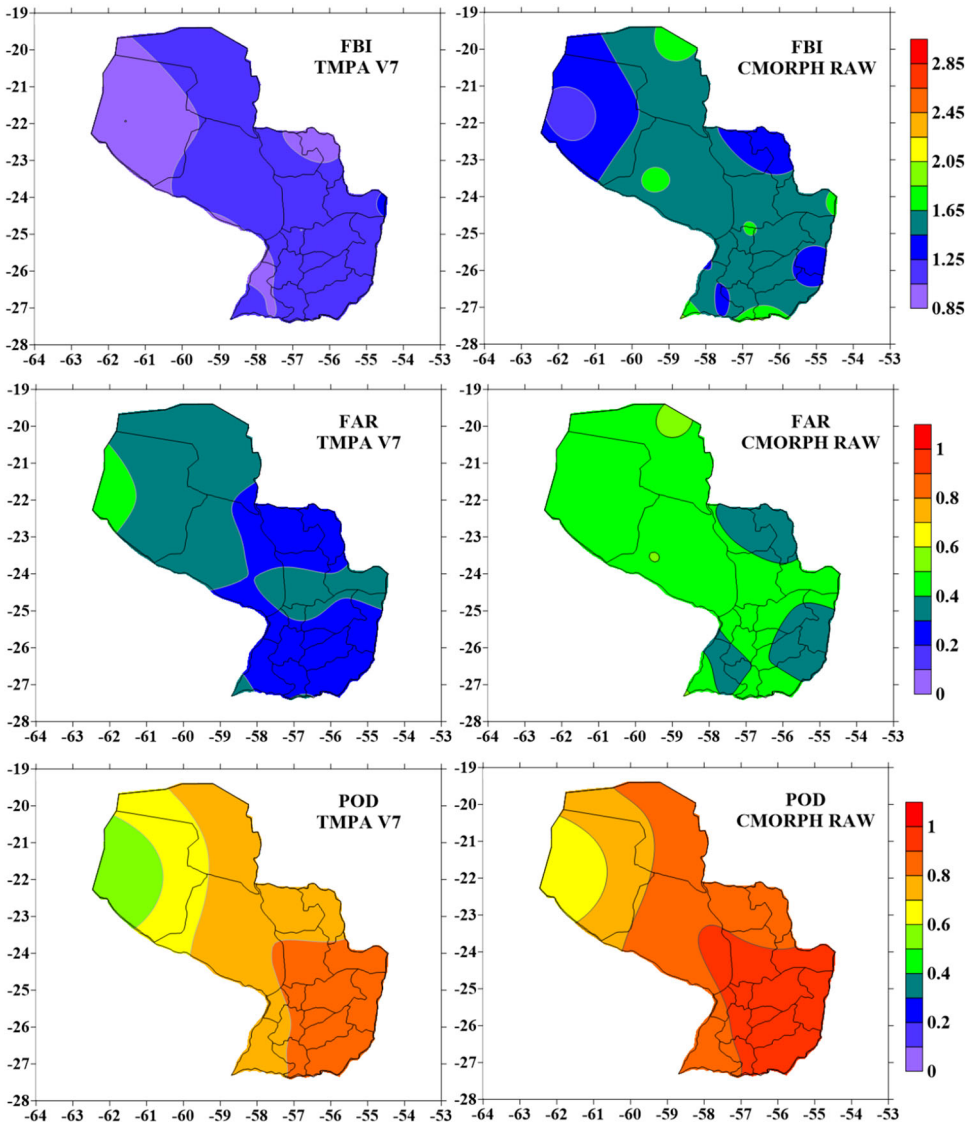

Fig. 3 Precision assessment results. Values were interpolated to provide an easier visualization of the results

contrast, the lowest value recorded is 0.61 in rain gauge station #4. On the other hand, regarding POD values in TMPA V7, the highest value recorded is 0.85 (85%) in the rain gauge station #20 and the lowest is 0.50 (50%) in the rain gauge station #4. These results denote that highest values are recorded in Eastern Paraguay and lowest values in the western region.

The indexes FBI, FAR, and POD were also evaluated at different precipitation thresholds to determine the capability of satellite products to detect precipitation events of different intensities. Similar results were obtained for both satellite products. Both satellite products present improvements in FBI values at low precipitation thresholds (2 mm/day $\leq$ threshold $\leq$ 10 mm/day), which show that satellites have a better precision in the detection of low intensity precipitation events (Fig. 4-FBI). Moreover, in most of the rain gauge stations analyzed, at higher precipitation intensities ($\geq$ 40 mm/day), FBI values increase as the intensity of the precipitation increases. Therefore, it can be noticed that satellite products tend to overestimate high intensity precipitation events.

FBI values are consistent with those from FAR and POD. FAR values increase as rainfall intensity increases, which indicate that satellite products tend to increase false alarms at higher precipitation intensities; hence, the ability of satellite products to correctly detect intense precipitation events is diminished (Fig. 4-FAR). Additionally, POD index values decrease as rainfall intensity increases. This exposes the low capability of satellite products to correctly detect high intensity precipitation events (Fig. 4-POD). Salio et al. (2015) reported similar results with the operational CMORPH v0.x and the TMPA V7 over southern South America.

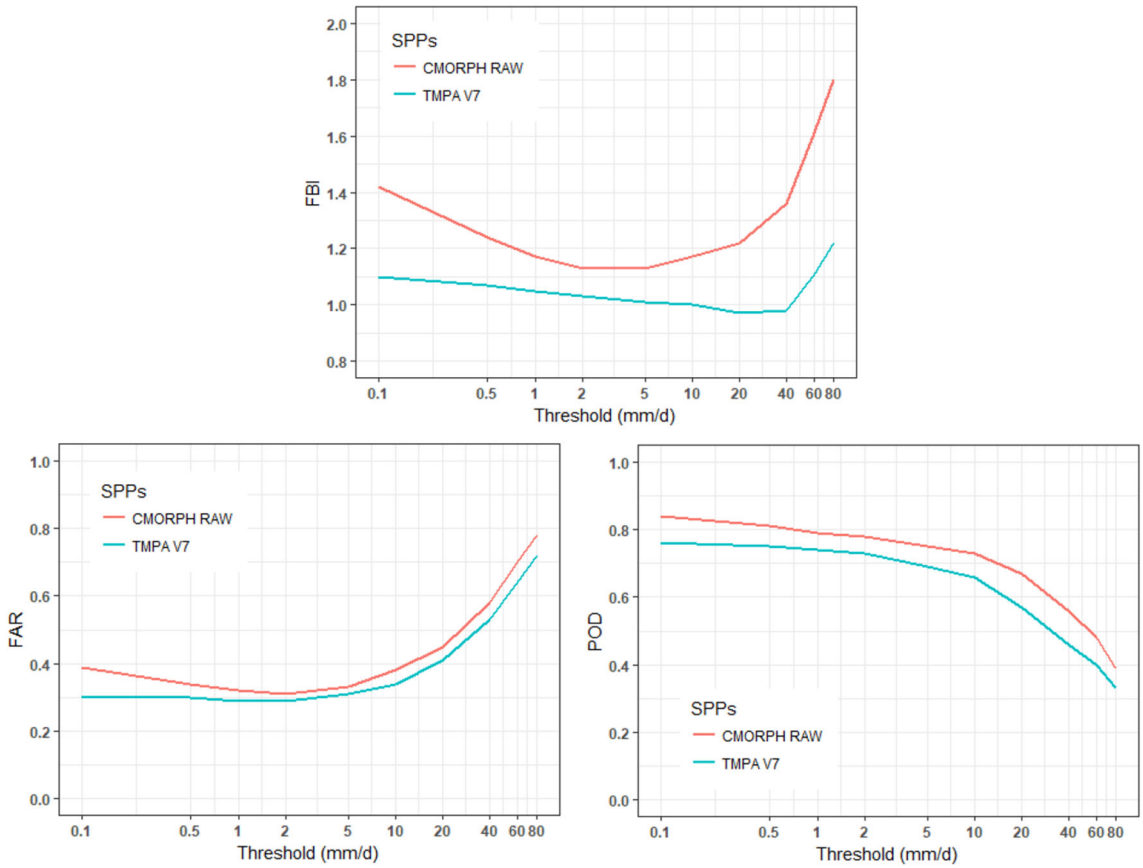

Fig. 4 Results of indexes FBI, FAR and POD in different precipitation thresholds. The *x* axis presents a logarithmic scale to improve the interpretation of the results in low intensity precipitation thresholds

Conclusions

Fifteen-year (1998–2012) precipitation estimates from the TMPAV7 and CMORPH RAW were evaluated with gauge-based precipitation over Paraguay. Our general conclusions are as follow:

- TMPA V7 shows fewer errors than CMORPH RAW; therefore, it presents a higher accuracy in the estimation of daily rainfall amounts over Paraguay.
- CMORPH RAW overestimates precipitation amounts throughout the country, while TMPA V7 does not present a single pattern.
- CMORPH RAW presents a general tendency to overestimate the number of precipitation events, while TMPA V7 tries to approach the observed precipitation events by showing slight overestimations and underestimations. Thus, TMPA V7 has a greater precision in the estimation of precipitation events.
- According to POD values, CMORPH Raw has a better ability to detect precipitation events. However, this improved capacity is probably due to the high overestimation of the number of those events.
- In both satellite products, R^2 and POD results present higher values in the Eastern Paraguay. Hence, satellite products have better adjustments with observed data and a better capability to correctly detect precipitation events in this region.
- Both satellite products present a greater ability to correctly estimate the occurrence of low intensity precipitation events (2–5 mm/day) and a tendency to overestimate high intensity precipitation events ($\geq$ 40 mm/day). Therefore, there is a lower ability of satellite products to correctly estimate the occurrence of high intensity precipitation events.

Acknowledgements This work was supported by the Inter-American Institute for Global Change Research (IAI) through the Collaborative Research Network (CRN-3035). The authors acknowledge the Paraguayan Directorate of Meteorology and Hydrology (DMH/DINAC) for the provision of rain gauge data, and NASA and NOAA for their ongoing efforts to develop high quality precipitation estimates.

References

Arkin PA, Meisner BN (1987) The relationship between large-scale convective rainfall and cold cloud over the western-hemisphere during 1982–84. Mon Weather Rev 115:51–74. https://doi.org/10.1175/1520-0493(1987)115<0051:TRBLSC>2.0.CO;2

Blacutt LA, Herdies DL, de Gonçalves LGG, Vila DA, Andrade M (2015) Precipitation comparison for the CFSR, MERRA, TRMM3B42 and combined scheme datasets in Bolivia. Atmos Res 163:117–131. https://doi.org/10.1016/j.atmosres.2015.02.002

Braun SA (2011) TRMM senior review proposal 2011. NASA Goddard Space Flight Center. pp 55. https://pmm.nasa.gov/resources/documents/trmm-senior-review-proposal-2011. Accessed 10 May 2017

Buarque DC, De Paiva RCD, Clarke RT, Mendes CAB (2011) A comparison of Amazon rainfall characteristics derived from TRMM, CMORPH and the Brazilian national rain gauge network. J Geophys Res Atmos 116(19):1–12. https://doi.org/10.1029/2011JD016060

Cabrera J, Yupanqui RT, Rau P (2016) Validation of TRMM daily precipitation data for extreme events analysis. The case of piura watershed in Peru. Proc Eng 154:154–157. https://doi.org/10.1016/j.proeng.2016.07.436

Collischonn B, Collischonn W, Tucci CEM (2001) Daily hydrological modeling in the Amazon basin using TRMM rainfall estimates. J Hydrol 360(1-4):207–216. https://doi.org/10.1016/j.jhydrol.2008.07.032

De Almeida CT, Delgado RC, De Oliveira JF, Gois G, Cavalcanti AS (2015) Avaliação das estimativas de precipitação do produto 3B43-TRMM do estado do Amazonas. Floresta e Ambiente 22(3):279–286. https://doi.org/10.1590/2179-8087.112114

de Goncalves LGG, Shuttleworth WJ, Nijssen B, Burke EJ, Marengo JA, Chou SC, Toll DL (2006) Evaluation of model-derived and remotely sensed precipitation products for continental South America. J Geophys Res 111:D16113. https://doi.org/10.1029/2005JD006276

Dinku T, Ruiz F, Connor SJ, Ceccato P (2010) Validation and intercomparison of satellite rainfall estimates over Colombia. J Appl Meteorol Climatol 49(5):1004–1014. https://doi.org/10.1175/2009JAMC2260.1

dos Reis J, Rennó C, Lopes E (2017) Validation of satellite rainfall products over a mountainous watershed in a humid subtropical climate region of Brazil. Remote Sens 9(12):1240. https://doi.org/10.3390/rs9121240

Duan Z, Liu J, Tuo Y, Chiogna G, Disse M (2016) Evaluation of eight high spatial resolution gridded precipitation products in Adige Basin (Italy) at multiple temporal and spatial scales. Sci Total Environ 573:1536–1553. https://doi.org/10.1016/j.scitotenv.2016.08.213

Ebert EE, Janowiak JE, Kidd C (2007) Comparison of near-real-time precipitation estimates from satellite observations and numerical models. Bull Am Meteorol Soc 88(1):47–64. https://doi.org/10.1175/BAMS-88-1-47

Federal Research Division of the Library of Congress of the United States Government (1990) Paraguay: a country study. In: Hanratty DM, Meditz SW (eds) Library of Congress, Washington. http://countrystudies.us/paraguay/2.htm. Accessed 10 July 2017

Ferraro RR (1997) Special sensor microwave imager derived global rainfall estimates for climatological applications. J Geophys Res 102:16715–16735. https://doi.org/10.1029/97JD01210

Hobouchian MP, Salio P, García Skabar Y, Vila D, Garreaud R (2017) Assessment of satellite precipitation estimates over the slopes of the subtropical Andes. Atmos Res 190:43–54. https://doi.org/10.1016/j.atmosres.2017.02.006

Huffman GJ (2013) Algorithm 3B42: TRMM merged HQ/infrared precipitation. https://trmm.gsfc.nasa.gov/3b42.html. Accessed 24 June 2017

Huffman GJ (2016) The transition in multi-satellite products from TRMM to GPM (TMPA to IMERG). https://pmm.nasa.gov/sites/default/files/document_files/TMPA-to-IMERG_transition_161025.pdf. Accessed 10 May 2017

Huffman GJ, Bolvin DT (2017) TRMM and other data precipitation data set documentation. ftp://meso-a.gsfc.nasa.gov/pub/trmmdocs/3B42_3B43_doc.pdf. Accessed 27 July 2017

Huffman GJ, Bolvin DT, Nelkin EJ, Wolff DB, Adler RF, Gu G, Stocker EF (2007) The TRMM Multisatellite Precipitation Analysis (TMPA): quasi-global, multiyear, combined-sensor precipitation estimates at fine scales. J Hydrometeorol 8(1):38–55. https://doi.org/10.1175/JHM560.1

Jiang S, Zhou M, Ren LL, Cheng XR, Cheng X, Zhang PJ (2016) Evaluation of latest TMPA and CMORPH satellite precipitation products over Yellow River Basin. Water Sci Eng 9(2):87–96. https://doi.org/10.1016/j.wse.2016.06.002

Jiang S, Liu S, Ren L, Yong B, Zhang L, Wang M, He Y (2017) Hydrologic evaluation of six high resolution satellite precipitation products in capturing extreme precipitation and streamflow over a medium-sized basin in China. Water (Switzerland) 10(1):1–17. https://doi.org/10.3390/w10010025

Joyce RJ, Janowiak JE, Arkin PA, Xie P (2004) CMORPH: a method that produces global precipitation estimates from passive microwave and infrared data at high spatial and temporal resolution. J Hydrometeorol 5(3):487–503. https://doi.org/10.1175/1525-7541(2004)005<0487:CAMTPG>2.0.CO;2

Manz B, Buytaert W, Zulkafli Z, Lavado W, Willems B, Robles LA, Rodríguez-Sánchez JP (2016) High-resolution satellite-gauge merged precipitation climatologies of the tropical andes. J Geophys Res 121(3):1190–1207. https://doi.org/10.1002/2015JD023788

Melo DDC, Xavier AC, Bianchi T, Oliveira PTS, Scanlon BR, Lucas MC, Wendland E (2016) Performance evaluation of rainfall estimates by TRMM Multi-satellite Precipitation Analysis 3B42V6 and V7 over Brazil. J Geophys Res Atmos 120:9426–9436. https://doi.org/10.1002/2015JD023797

National Aeronautics and Space Administration (2016) TRMM SATELLITE AND INSTRUMENTS—GES DISC—Goddard Earth Sciences Data and Information Services Center. https://pmm.nasa.gov/TRMM/trmm-instruments. Accessed 24 June 2017

National Space Development Agency of Japan (2001) TRMM data users handbook. http://www.eorc.jaxa.jp/TRMM/document/text/handbook_e.pdf. Accessed 10 Mar 2017

Prakash S, Mitra AK, AghaKouchak A, Liu Z, Norouzi H, Pai DS (2018) A preliminary assessment of GPM-based multi-satellite precipitation estimates over a monsoon dominated region. J Hydrol 556:865–876. https://doi.org/10.1016/j.jhydrol.2016.01.029

Quirino DT, Casaroli D, Jucá Oliveira RA, Mesquita M, Pego Evangelista AW, Alves Júnior J (2017) Evaluation of TRMM satellite rainfall estimates (algorithms 3B42 V7 & RT) over the Santo Antônio county (Goiás, Brazil). Revista Facultad Nacional de Agronomía 70(3):8251–8261. https://doi.org/10.15446/rfna.v70n3.61805

Ringard J, Becker M, Seyler F, Linguet L (2015) Temporal and spatial assessment of four satellite rainfall estimates over French Guiana and north Brazil. Remote Sens 7(12):16441–16459. https://doi.org/10.3390/rs71215831

Ruiz JJ (2009) Evaluación de Diferentes Metodologías para la Calibración de Precipitación CMORPH sobre Sudamérica.

Revista Brasileira de Meteorología 24(4):473–488. https://doi.org/10.1590/S0102-77862009000400009

Ruiz J, Saulo C, Kalnay E (2009) Comparison of methods used to generate probabilistic quantitative precipitation forecasts over South America. Weather Forecast 24(1):319–336. https://doi.org/10.1175/2008WAF2007098.1

Salio P, Hobouchian MP, García Skabar Y, Vila D (2015) Evaluation of high-resolution satellite precipitation estimates over southern South America using a dense rain gauge network. Atmos Res 163:146–161. https://doi.org/10.1016/J.ATMOSRES.2014.11.017

Scheel MLM, Rohrer M, Huggel C, Santos Villar D, Silvestre E, Huffman GJ (2011) Evaluation of TRMM Multi-satellite Precipitation Analysis (TMPA) performance in the Central Andes region and its dependency on spatial and temporal resolution. Hydrol Earth Syst Sci 15(8):2649–2663. https://doi.org/10.5194/hess-15-2649-2011

Sepulcri MG, Di Bella CM, Moschini RC (2009) Validación de la Ocurrencia de Lluvia Estimada a partir del Algoritmo 3B42 de TRMM con Datos Pluviométricos en la Región Pampeana. XIII Latin American and Iberian Congress of Meteorology and X Argentine Congress of Meteorology, 5–9 Oct 2009, Buenos Aires, Argentina

Su F, Hong Y, Lettenmaier DP (2008) Evaluation of TRMM Multisatellite Precipitation Analysis (TMPA) and its utility in hydrologic prediction in the La Plata Basin. J Hydrometeorol 9(4):622–640. https://doi.org/10.1175/2007JHM944.1

Sun R, Yuan H, Liu X, Jiang X (2016) Evaluation of the latest satellite-gauge precipitation products and their hydrologic applications over the Huaihe River basin. J Hydrol 536(March):302–319. https://doi.org/10.1016/j.jhydrol.2016.02.054

Wilheit T, Alder R, Avery S, Barrett E, Bauer P, Berg W et al (1994) Algorithms for the retrieval of rainfall from passive microwave measurements. Remote Sens Rev 11:163–194. https://doi.org/10.1080/02757259409532264

Wilks DS (2006) Statistical methods in the atmospheric sciences. Int Geophys Ser (Elsevier). https://doi.org/10.1002/met.16

Wu L, Zhai P (2012) Validation of daily precipitation from two high-resolution satellite precipitation datasets over the Tibetan Plateau and the regions to its east. Acta Meteorol Sin 26(6):735–745. https://doi.org/10.1007/s13351-012-0605-2

Xie P, Joyce R, Wu S, Yoo S-H, Yarosh Y, Sun F, Lin R (2017) Reprocessed, bias-corrected CMORPH global high-resolution precipitation estimates from 1998. J Hydrometeorol 18(6):1617–1641. https://doi.org/10.1175/JHM-D-16-0168.1

Zambrano-Bigiarini M, Nauditt A, Birkel C, Verbist K, Ribbe L (2017) Temporal and spatial evaluation of satellite-based rainfall estimates across the complex topographical and climatic gradients of Chile. Hydrol Earth Syst Sci 21(2):1295–1320. https://doi.org/10.5194/hess-21-1295-2017

Zeng Q, Wang Y, Chen L, Wang Z, Zhu H, Li B (2018) Intercomparison and evaluation of remote sensing precipitation products over China from 2005 to 2013. Remote Sens 10(3):168. https://doi.org/10.3390/rs10020168

Zubieta R, Getirana A, Espinoza JC, Lavado W (2015) Impacts of satellite-based precipitation datasets on rainfall-runoff modelling of the Western Amazon basin of Peru and Ecuador. J Hydrol 528:599–612. https://doi.org/10.1016/j.jhydrol.2015.06.064

Acta Geophysica (2018) 66:381–392
https://doi.org/10.1007/s11600-018-0138-x

RESEARCH ARTICLE - SPECIAL ISSUE

High-resolution spatio-temporal analyses of drought episodes in the western Mediterranean basin (Spanish mainland, Iberian Peninsula)

J. C. González-Hidalgo[1,2] · S. M. Vicente-Serrano[3] · D. Peña-Angulo[1,2] · C. Salinas[1,2] · M. Tomas-Burguera[4] · S. Beguería[4]

Received: 27 October 2017 / Accepted: 30 March 2018 / Published online: 6 April 2018

Abstract
The purpose of this research was to identify major drought events on the Spanish mainland between 1961 and 2014 by means of two drought indices, and analyze the spatial propagation of drought conditions. The indices applied were the standardized precipitation index (SPI) and the standardized evaporation precipitation index (SPEI). The first was calculated as standardized anomalies of precipitation at various temporal intervals, while the second examined the climatic balance normalized at monthly scale, incorporating the relationship between precipitation and the atmospheric water demand. The daily meteorological data from Spanish Meteorological Archives (AEMet) were used in performing the analyses. Within the framework of the DESEMON project, original data were converted into a high spatial resolution grid (1.1 km^2) following exhaustive quality control. Values of both indices were calculated on a weekly scale and different timescales (12, 24 and 36 months). The results show that during the first half of the study period, the SPI usually returned a higher identification of drought areas, while the reverse was true from the 1990s, suggesting that the effect from atmospheric evaporative demand could have increased. The temporal propagation from 12- to 24-month and 36-month timescales analyzed in the paper seems to be a far from straightforward phenomenon that does not follow a simple rule of time lag, because events at different temporal scales can overlap in time and space. Spatially, the propagation of drought events affecting more than 25% of the total land indicates the existence of various spatial gradients of drought propagation, mostly east–west or west–east, but also north–south have been found. No generalized episodes were found with a radial pattern, i.e., from inland to the coast.

Keywords Drought · SPI · SPEI · Spain · Spatial propagation

Introduction

Drought is one of the climate hazards that causes many negative impacts on natural and socioeconomic systems (Stahl et al. 2015, 2016; Van Loon et al. 2016). In addition, drought analysis is not an easy task, as it is quite difficult to accurately determine the spatial and temporal dimensions of drought events (Wilhite and Glantz 1985; Lloyd-Hughes 2014; Vicente-Serrano 2016). For this reason, synthetic tools—the drought indices–have been developed, mostly based on the climate information (e.g., Heim 2002; Keyantash and Dracup 2002). These indices have been widely used to analyze the spatial and temporal behaviors of droughts (e.g., Van der Schrier et al. 2006) to identify drought impacts over a variety of sectors (e.g., Williams et al. 2013; Vicente-Serrano et al. 2013), and also to develop the bases for drought-monitoring systems worldwide (Svoboda et al. 2002).

In addition to uncertainties concerning problems caused by imprecise identification of the phenomenon, drought

✉ J. C. González-Hidalgo
jcgh@unizar.es

[1] Department of Geography, University of Zaragoza, Saragossa, Spain

[2] IUCA, University of Zaragoza, Saragossa, Spain

[3] Instituto Pirenaico de Ecología (IPE-CSIC), Saragossa, Spain

[4] Estación Experimental Aula Dei (EEAD-CSIC), Saragossa, Spain

analyses face the problem of the scarcity of data available for detailed analysis (Seneviratne et al. 2012); therefore, because drought events are usually confined to a region (e.g., Soulé 1992; Lloyd-Hughes and Saunders 2002), studies using detailed spatial scales seem to be the best way to improve our knowledge on the behavior of the processes and associated impacts.

In the western Mediterranean basin and on the Spanish mainland, drought is a very frequent phenomenon, due to particular climate conditions. Different studies have identified ancient droughts by means of historical documents and different proxies (Domínguez-Castro et al. 2012; Tejedor et al. 2017), and during the instrumental period, several studies have also identified strong drought events during the last century (Vicente-Serrano 2006a). On the other hand, some studies have suggested that the Spanish mainland has witnessed an increased severity in droughts over the last few decades (Hoerling et al. 2012; Vicente-Serrano et al. 2014a), causing heavy environmental, agricultural and economic impacts (e.g., Camarero et al. 2015; Pascoa et al. 2017). This suggests that drought management plans should be put in place to cope with the risk more efficiently (Maia and Vicente-Serrano 2017).

These studies offer a promising starting point for research into the recent behavior of drought on the Spanish mainland; however, it is unsafe to generalize their conclusions at sub-regional scales, mostly because data with low-spatial density was used, and also because an important feature of drought events is their strong spatial variability (Vicente-Serrano 2006a). Thus, several poorly understood questions on drought behavior on the Spanish mainland remain, significant among which is how droughts propagate in space and time. This is a crucial issue that receives scant analysis in the scientific literature.

In this study, we present a descriptive analysis of the major drought events on the Spanish mainland in recent decades, based on a high-resolution climate dataset. The objectives of the study are (i) to identify the major drought episodes, (ii) to compare the differences in drought identification between two drought indices: the standardized precipitation index (SPI), and the standardized precipitation evapotranspiration index (SPEI), and (iii) to identify spatial propagation gradients of major drought episodes.

Data and methods

A recent gridded drought index database was used, covering the whole Spain for the period 1961–2014 at the temporal resolution of 1 week and spatial resolution of 1.1 km^2. The original dataset is based on the complete information digitalized from the archives of Spanish National Meteorological Agency (Agencia Estatal de Meteorología, AEMet), and includes precipitation, air temperature, relative humidity, hours of sunshine and wind speed needed to calculate the Potential Evapotranspiration or atmospheric evaporative demand (AED). The AED was calculated by means of the FAO-56 Penman–Monteith equation (Allen et al. 1998). Details of the data processing, gridding and drought index calculation are given in Vicente-Serrano et al. (2017). The dataset can be found at http://monitordesequia.csic.es.

The SPI and SPEI indices were calculated, which are two of the most widely used and recommended as drought indicators worldwide (WMO 2012); the standardized precipitation index (SPI) is based on precipitation data (McKee et al. 1993), and the standardized precipitation evapotranspiration index (SPEI) is based on the difference between precipitation and the AED (Vicente-Serrano et al. 2010), and includes a water balance. Therefore, by comparing both sets of results, the contribution of the AED on drought severity can be identified.

Major drought periods were defined using three criteria applied to the weekly time series of SPI and SPEI at a 12-month time lag: (i) a minimum duration of 3 weeks; (ii) the index threshold < -1.28 corresponding to return periods of 10 years, and represents an indication of drought severity; (iii) and drought conditions, as defined by index values, should affect more than 25% of the total Spanish mainland. Finally, to avoid over detection of periods, we included a new major episode when a minimum temporal lag of 3 weeks was found between well-identified drought episodes. In the present paper, our approach assumes stationary of the climatic conditions, which may not be the case, so the return periods should be taken with care. Although they are useful for spatial comparison as it is the purpose on this article, their validity as indicators of frequency of drought conditions does not hold under a climate change scenario.

Identification of the drought period focused on 12 months; we also analyzed 24 and 36 months timescales to determine time propagation, but only the 12-month results will be shown in detail. Droughts in Spain have very different dimensions, affecting agriculture, forests and the frequency of wild fires, but currently the most important impacts relate to the hydrological dimension, which may cause heavy losses in highly productive irrigated agriculture, reduce hydropower production, and cause problems for industry and the water supply (Jerez et al. 2013; Lorenzo-Lacruz et al. 2010, 2013). Due to dry summers and strong interannual variability of the climate in Spain, there is a very dense network of hydraulic infrastructures. Thus, after China, Spain has the second highest number of dams in the world, but the total surface area of the country is 5% that of China. The purpose of this dense network is to guarantee the water supply during the frequent drought

periods. For this reason, hydrological droughts in Spain are not affected by short term droughts, usually identified on short SPI/SPEI timescales. Thus, the dense reservoir network even allows a noticeable reduction in the impact of annual drought events (12-month) on hydrological drought conditions. For example, the one affecting Spain in 2015 was the most severe since records began, but it did not cause hydrological droughts due to the large amount of hydraulic infrastructures. On the contrary, climate drought conditions recorded during 2–3 years, limit the capacity of infrastructures to cope with drought events, and cause problems for irrigation and water supply, as widely observed between 1992 and 1995. For these reasons, this paper focuses on long-term drought indices (12, 24 and 36 months), since they are really useful to assess the severity of hydrological droughts and determine how annual drought conditions can persist over longer timescales. Lorenzo-Lacruz et al. (2010) clearly illustrated how the multiannual large reservoirs, which are frequent and the basis for water management in Spain, are responding to very long drought timescales > 24-month.

Results

Major drought events on the Spanish mainland

Table 1 shows the main drought periods identified for the Spanish mainland during the study on a 12-month timescale. Remember that identification of drought episodes combines duration, spatial effects and intensity, as described in Sect. "Data and methods". The table shows the start and end dates according to year, month and week, and includes the duration in weeks.

In the period analyzed, we identified a total of 15 major drought episodes in which at least 25% of land was under the drought conditions defined by an SPEI value of < -1.28. In general, both indices showed strong agreement in identifying the main drought periods between 1961 and 2014. Nevertheless, there are some differences regarding the start and end weeks of the drought episodes, and three episodes did not fulfill the requirements in SPI.

The duration of droughts also showed similar patterns, with the exception of the two main episodes identified at the end of the study period, when the SPEI detected drought conditions noticeably earlier and also provided an earlier end. Among the events identified with the SPEI, the most prolonged were recorded in 1989 (21 weeks), 1994–1995 (74 weeks), 1999 (27 weeks), 2005–2006 (56 weeks) and 2012 (38 weeks). The table also includes the main spatial propagation gradients (see below).

Comparison between SPI and SPEI is shown by the percentage of total land affected by droughts, including both thresholds (< -0.28, and < -0.84, with 10- and 5-year return period, respectively). Obviously, detection of the surface area differs as a function of the threshold, with the weakest ones being higher, but there were also some differences between SPI and SPEI for the three timescales

Table 1 Drought period identification (12-month scale) using SPEI and SPI threshold (< -1.84)

Event	Spatial gradient propagation	SPEI	Duration	SPI	Duration
1	W/E	1965-Jun-3/1965-Sep-4	14	1965-Jul-2/1965-Sep-3	10
2	E/W	1970-Dec-4/1971-Apr-2	15	1971-Jan-1/1971-Apr-1	13
3	W/E	1981-Feb-3/1981-March-4	6	1981-Feb-3/1981-Dec-3	8 + 8+6 + 10
4	W/E	1981-Nov-1/1981-Dec-3	7		
5	E/W	1983-Oct-3/1983-Dec-3	4 + 3	1983-Sep-4/1983-Dec-2	11
6	E/W	1986-May-3/1986-Sep-2	16	1986-Jan-3/1986-Sep-1	15
7	N/S	1989-Jun-3/1989-Nov-3	21	1989-Jun-2/1989-Nov-2	13 + 7
8	W/E	1992-Feb-1/1992-Jun-2	18	1992-Feb-1/1992-Jun-2	18
9	E/W	1994-Jan-3/1995-Dec-4	74	1994-Jan-1/1995-Dec-3	75
10	E/W	1999-Feb-1/1999-Feb-4	4	1999-Jan-4/1999-Oct-2	6 + 3+ 21
11	E/W	1999-Apr-2/1999-Oct-2	2 + 21		
12	E/W	2002-Feb-4/2002-May-3	6 + 5	2002-Feb-4/2002-May-4	13
13	W/E	2005-March-4/2006-Jun-1	53 + 3	2005-Apr-2/2006-May-2	45
14	W/E	2009-Oct-2/2009-Dec-3	10	/	
15	N/S/NW/SE	2012-Feb-3/2012-Dec-4	32 + 4 + 2	2012-March-2/2012-Sep-3	4 + 1 + 1 + 16

Duration in weeks. Dates indicate start/end in monthly week

Duration expressed as (+) indicates that between dates of event some weeks did not achieve the spatial threshold of 25% of total land. See text for explanation how to identify events

analyzed (Fig. 1). The 12-month scale identified many drought periods affecting more than 25% of territory. It means that extended areas of the Spanish mainland were very frequently affected by drought conditions and is clearly related to the high interannual variability of rainfall in areas with a Mediterranean climate. On the other hand, on the 24- and 36-month scales, fewer episodes were found; nevertheless, some of these affected over 50% of the Spanish mainland, particularly from 1980, when extended areas under drought conditions were identified on 24- and 36-month scales. However, the relationship between timescales is far from simple: some episodes on the 12-month scale were not identified on the 24- or 36-month scales (see Fig. 1).

Figure 2 gives the comparison of percentage of total land affected by drought according to the SPEI and SPI, where the lines represent the difference in the percentage of surface area affected. Positive values indicate a larger area of drought according to the SPEI and vice versa. The different behavior between the two drought indices shows that since 2000, SPEI has progressively expanded identification of longer and more severe drought episodes than the SPI, and suggests that the role played by the AED could be

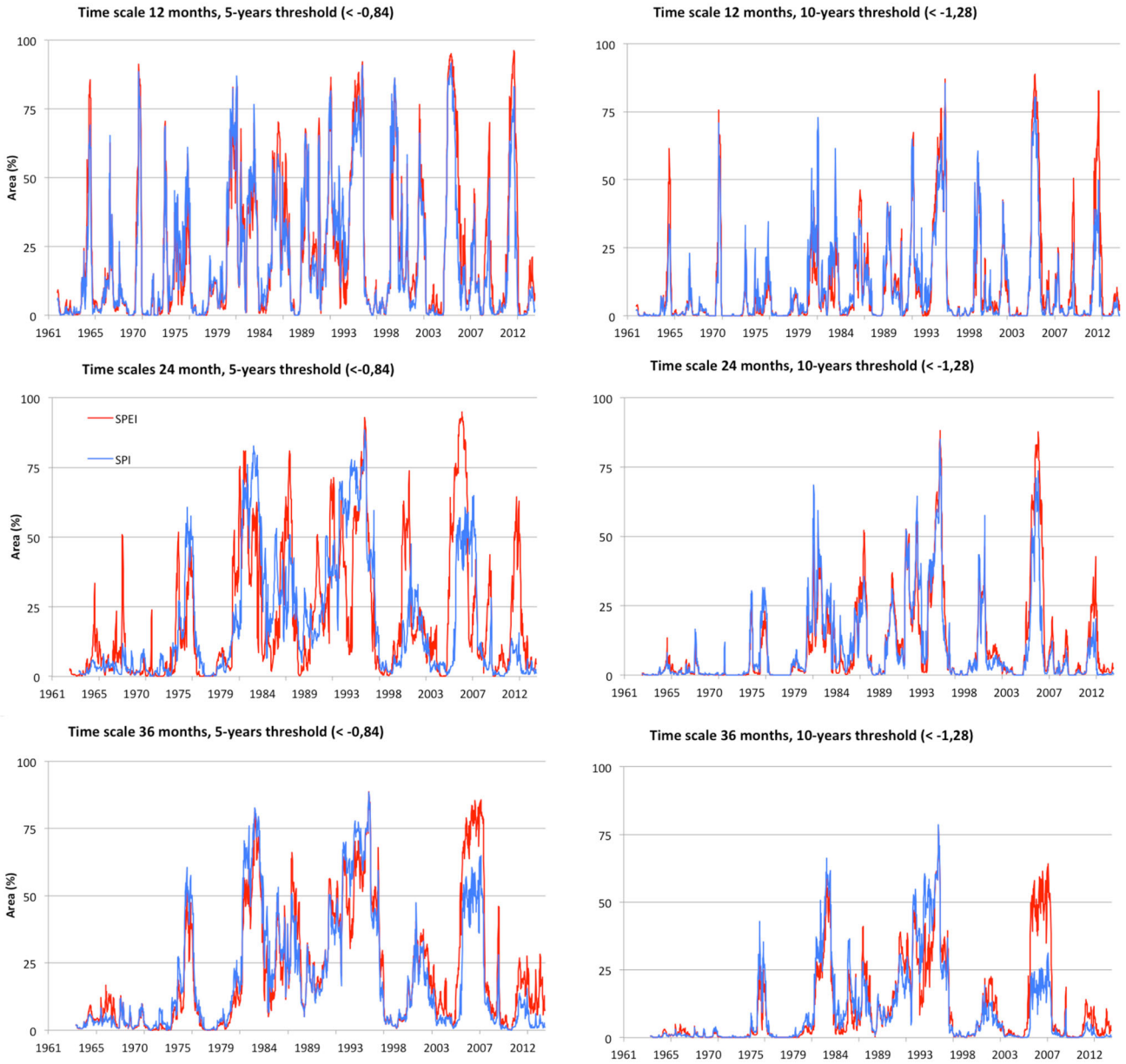

Fig. 1 Evolution of land affected (in %) accordingly SPEI (—) and SPI (—) at three temporal scales (12, 24 and 36 months) and two drought index thresholds (< -1.28 and < -0.84)

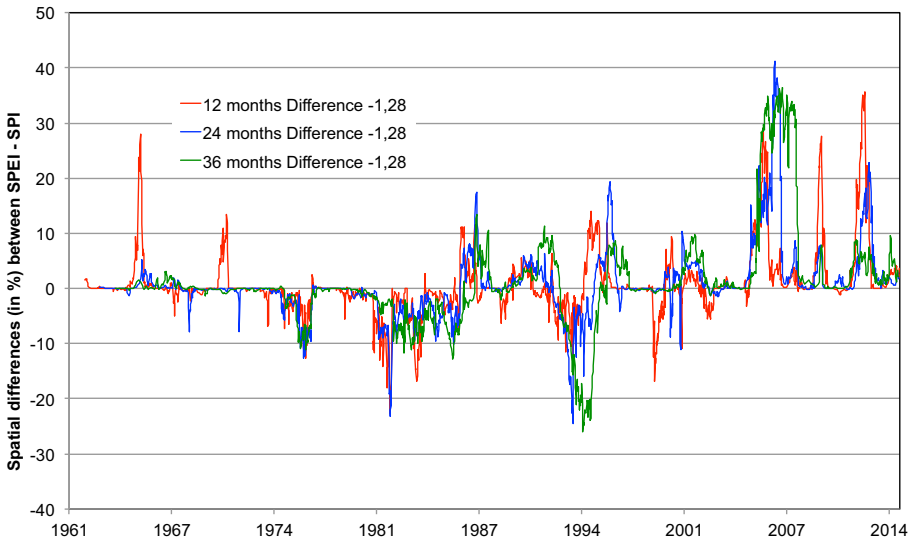

Fig. 2 Differences of land surface affected between SPEI and SPI at different times scales (12, 24 and 36 months). The values are accordingly (SPEI-SPI) percentage of land under < -1.28 threshold (10-year return period)

responsible for the increase in drought episodes on the Spanish mainland.

Filtering this information and isolating those events in which SPEI detected > 50% of Spanish mainland under the threshold of − 1.28 (Fig. 1), led to a logical reduction in the number and length of drought events (data not shown). This suggests that some of the drought events identified in Table 1 (e.g., 1981, 1983, 1986, 1989, 2002 and 2009) may have depended more on factors controlling precipitation (see discussion).

These results suggest that drought events on the Spanish mainland can affect extensive areas, and second, the relationship between temporal scales varies greatly among episodes and does not follow a straightforward pattern. In some cases, the events detected on 12-month scales did not propagate to longer timescales (episodes first and second from Table 1, see Fig. 1). In other cases, the relationships were much more complex, and the temporal propagation of drought events detected at shorter (i.e., 12-month) to longer scales (i.e., 24 and 36 months) was combined with new drought episodes recorded at a shorter timescale. This caused an overlap in detection of drought episodes (see below). Figure 3 shows the evolution of areas (as a percentage) affected by drought conditions according to different timescales during events occurring between 1989 and 1995. The figure provides information on the relationship between the three temporal scales analyzed and shows how temporal lags in some cases are well recognized (continuous lines), but in others, there is an effect from overlapping episodes, or perhaps from temporal scales not analyzed in this paper (dashed lines).

Spatial drought propagation

The spatial propagation of major drought episodes was analyzed by examining the sequential chart of weekly SPEI and SPI indices. Three general spatial propagation gradients were identified during the analyzed period for the major drought episodes, with the two longitudinal (W–E and E–W) being more frequent than the latitudinal (mostly N–S). These gradients are indicated in Table 1. The three spatial patterns were recognized in sequences of episodes between 1989 and 1995, during three successive events (numbers 7–9 on Table 1). The structure of this sequence, which may explain the total severity of the drought and also the complexity of drought analyses, was as follows:

North–South gradient. Episode 7, from 1989-June 3 to 1989-November-3

The areas affected by the defined threshold did not cover more than 50% of total land and the episode lasted for 21 weeks. This episode is the only one recorded in the dataset that shows a generalized north to south gradient, with clear asymmetry between the northern coastland and the Mediterranean region when the drought index returns positive values. The drought was particularly severe in November and the episode propagated to longer SPEI timescales in the expected temporal lag (Fig. 4).

West–East gradient. Episode 8. 1992-February-1–1992-June-2

The following episode was identified from 1992-February-1 and 1992-June-2 on the 12-month timescale, lasting for

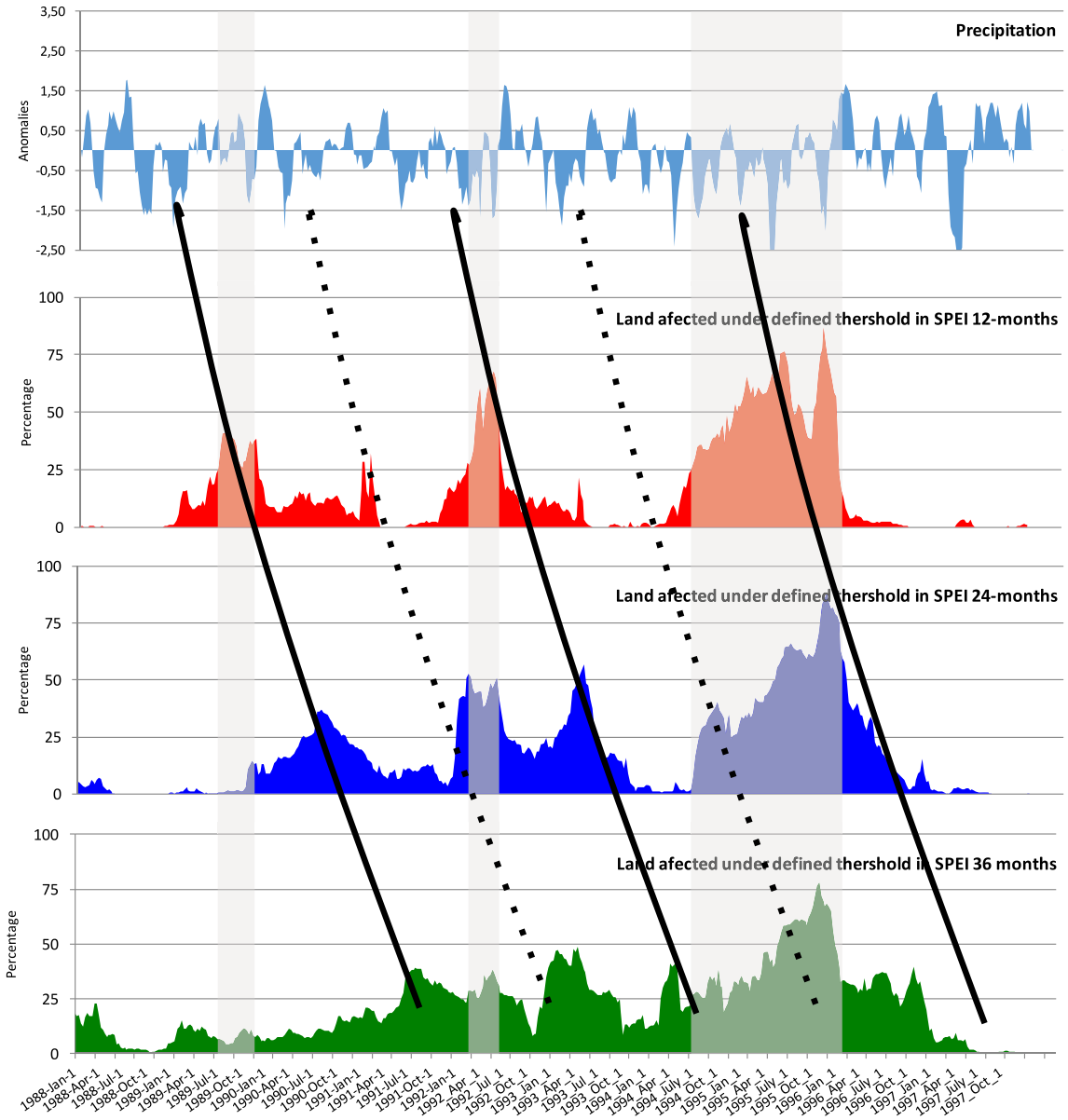

Fig. 3 The relationship between timescales in drought episodes. Figure shows from top to bottom (**a**) the precipitation, expressed as anomalies; (**b**) the percentage of land affected by defined threshold at 12 months; (**c**) at 24 months and (**d**) at 36 months, in the sequence of three episodes from 1989-June-3 to 1995-December-4 (from seventh to ninth episodes following Table 1). Slight shade (in vertical) indicates the duration of drought events. Continuous lines represent the relationships between monthly timescales, accordingly lags of 12–24–36 months for specific events identified at 12-month scale (see Table 1). Dashed lines indicate at 24 and 36 monthly scale episodes in which more than 25% of total land was under drought conditions not detected at 12-month scale

18 weeks. This episode overlapped the previous episode 7 of 1989, which did not recover at the 24- and 36-month timescales (see Fig. 3). For this reason, large areas affected by drought on the 12-month scale were also affected on the 24- and 36-month scales simultaneously, with more than 50% of total land under drought conditions. The spatial propagation of defined drought conditions on 12-month time-scales shows a clear gradient from west to east. Please note that there is no data from Portugal to avoid misinterpretation of the spatial gradient from the Atlantic coast of the Iberian Peninsula. In the eastern Mediterranean coastal areas, no general drought severity was detected (Fig. 5). Finally, the proper 12-month drought event (number 8) was propagated at 24- and 36 months according to the expected lags.

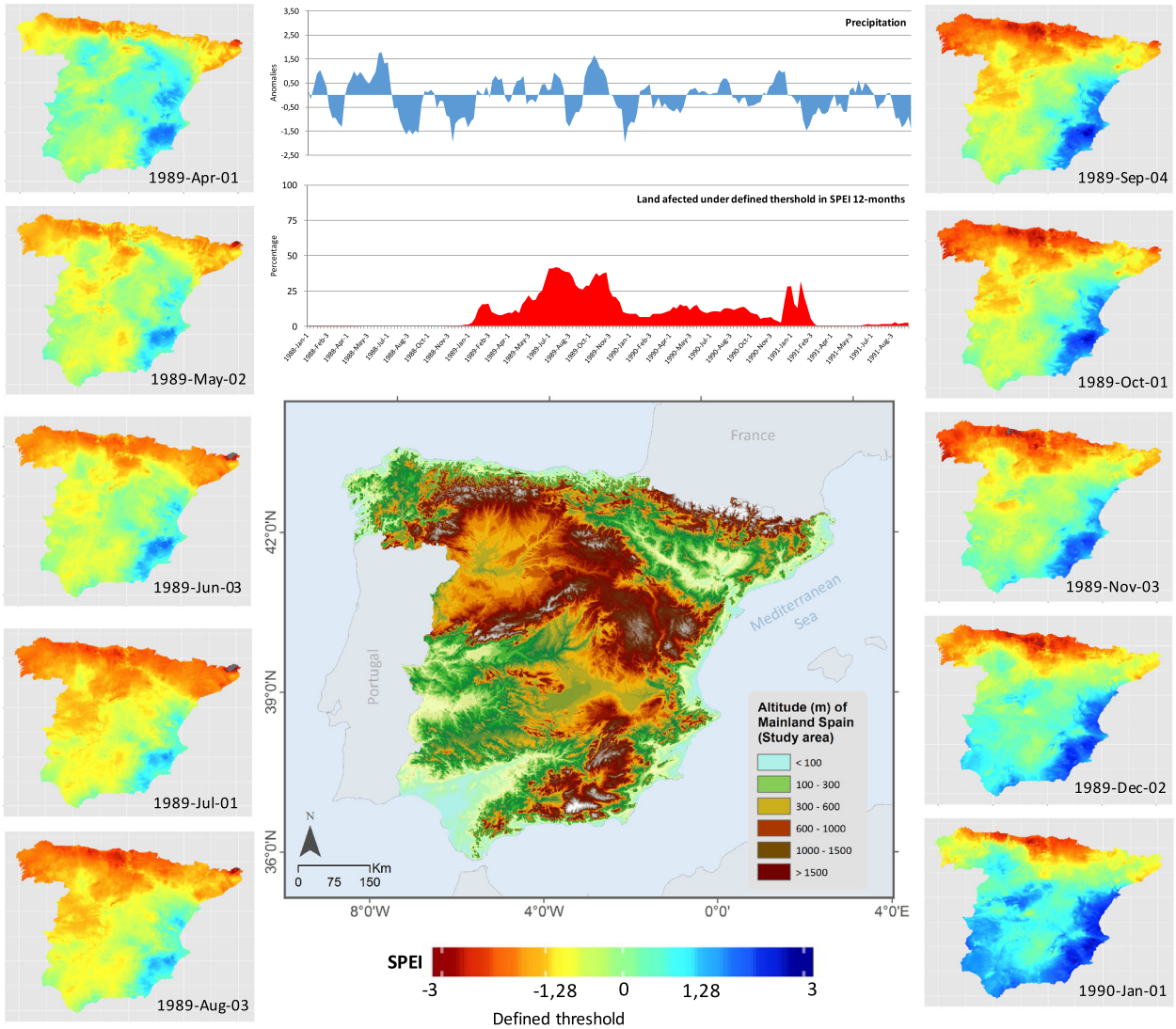

Fig. 4 Drought episodes from 1989-June-3 to 1989-November-3. The map collection shows the spatial evolution pattern (North–South) of SPEI values at selected weekly intervals

East–West gradient. Episode 9. 1994-January-3–1995-December-4

This sequence of drought periods finished with the longest episode recorded in the entire dataset. This ninth episode lasted for 74 weeks between June 1994 and December 1995. The new drought period identified on the 12-month timescale coincided with extended areas detected at 24 and 36 months relating to the previous episode, indicating a reactivation of the long-term drought conditions from the previous event. At the peak of highest severity, more than 85% of the Spanish mainland was under drought conditions on the 12- and 24-month timescales, and also more than 77% of the area was under drought conditions at 36-month SPEI in December 1995. This drought episode shows a clear gradient of propagation from east to west (Fig. 6).

Discussion

General comments

Droughts in Spain have very different dimensions, affecting agriculture, forests and the frequency of wild fires, but currently the most important impacts relate to the hydrological dimension, which may cause heavy losses in highly productive irrigated agriculture, reduce hydropower production, and cause problems for industry and the water supply (Jerez et al. 2013; Lorenzo-Lacruz et al. 2010, 2013). Due to dry summers and strong interannual variability of the climate in Spain, there is a very dense network of hydraulic infrastructures. Thus, after China, Spain has the second highest number of dams in the world,

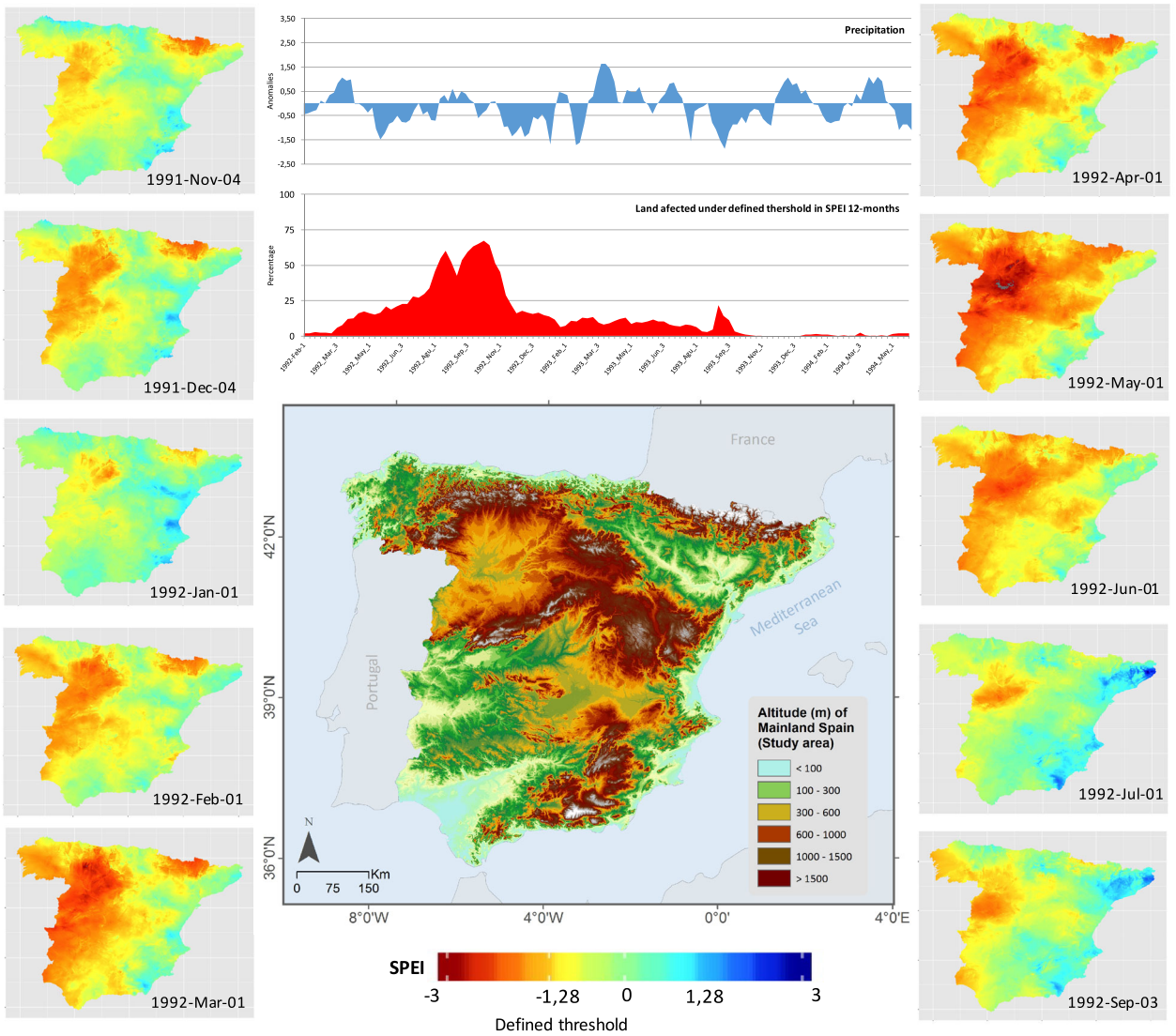

Fig. 5 Drought episode from 1992-February-1 to 1992-June-2. The map collection shows the spatial evolution pattern (West–East) of SPEI values at selected weekly intervals

but the total surface area of the country is 5% that of China. The purpose of this dense network is to guarantee the water supply during the frequent drought periods. For this reason, hydrological droughts in Spain are not affected by short term droughts, usually identified on short SPI/SPEI timescales. Thus, the dense reservoir network even allows a noticeable reduction in the impact of annual drought events (12-month) on hydrological drought conditions. For example, the one affecting Spain in 2015 was the most severe since records began, but it did not cause hydrological droughts due to the large amount of hydraulic infrastructures. On the contrary, climate drought conditions recorded during 2–3 years, limit the capacity of infrastructures to cope with drought events, and cause problems for irrigation and water supply, as widely observed between 1992 and 1995. For these reasons, this paper focuses on long-term drought indices (12, 24 and 36 months), since they are really useful to assess the severity of hydrological droughts and determine how annual drought conditions can persist over longer timescales. Lorenzo-Lacruz et al. (2010) clearly illustrated how the multiannual large reservoirs, which are frequent and the basis for water management in Spain, are responding to very long drought timescales > 24-month.

Defining a drought period involves deciding which thresholds to use, and we focused on episodes covering the largest surface areas under defined drought thresholds. This meant that some minor drought periods (regional to local) were not identified in this study, but there is evidence proving that they are frequent on the Spanish mainland (Vicente-Serrano et al. 2014; Peña-Gallardo et al. 2016). We hope in future to be able to analyze all drought periods

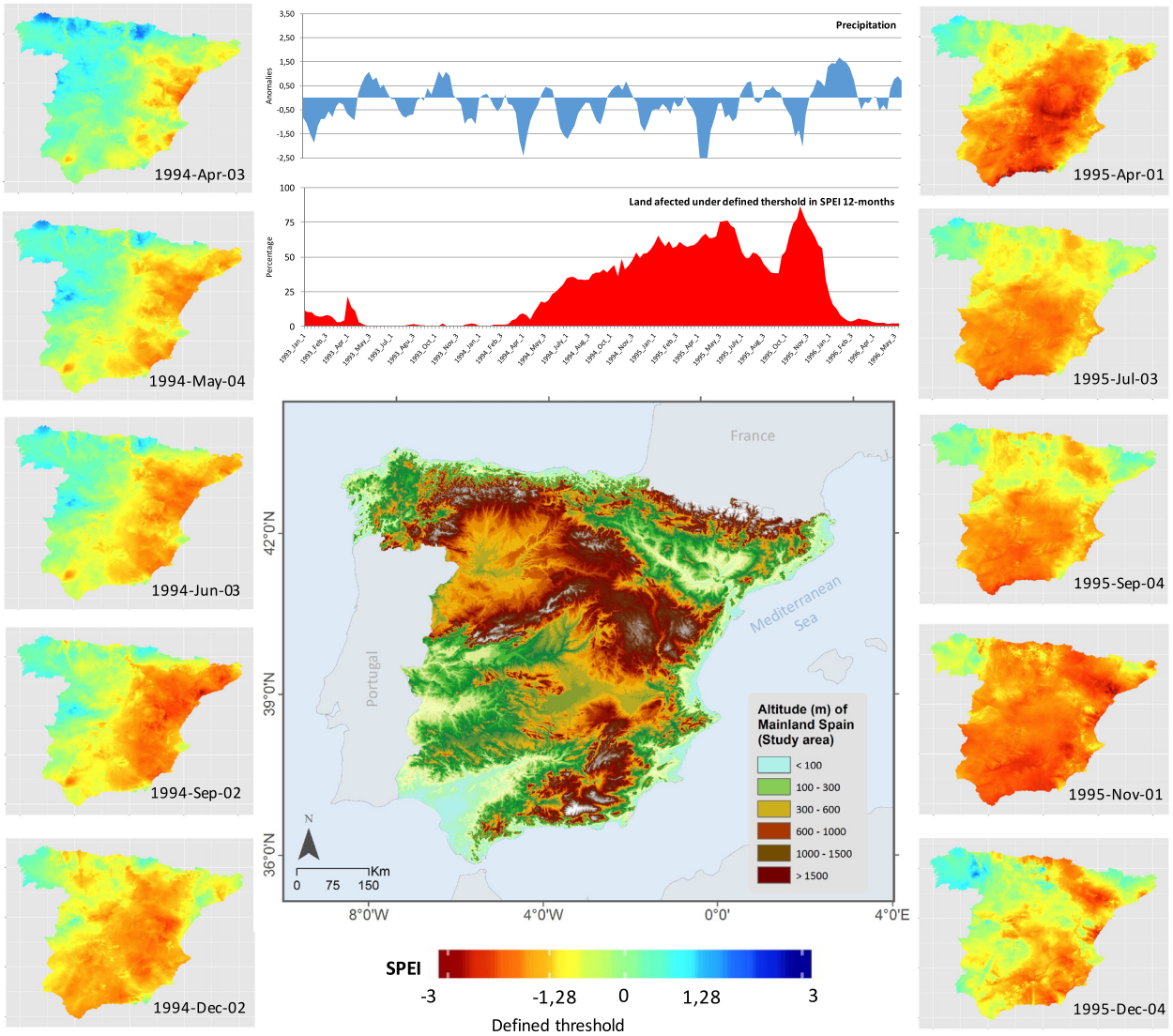

Fig. 6 Drought episode from 1994-June-3 to 1995-December-4. The map collection shows the spatial evolution pattern bottom (East–West) of SPEI values at selected weekly intervals

affecting the Spanish mainland to develop a drought catalog. In the meantime, this research shows that when identifying outstanding global drought events, the use of thresholds based on the drought index combined with the surface area affected by droughts are an interesting tool, even though they are insufficient to determine the real severity of these events at sub-regional scales. The use of different timescales is equally important for this purpose. Nevertheless, this is a difficult task, since a simple assumption of temporal propagation of the drought conditions across different timescales is not so simple, as illustrated in this paper, for events between 1989 and 1995. In summary, individual drought events must be put in a temporal context because in many circumstances they are promoted or exacerbated by past conditions.

In this study, we identified "simple" major drought episodes on a timescale of 12 months. These are the less complex droughts analyzed, and in general, they were found at the beginning of the study period. This became more complex when seeking to extend 12-month drought episodes to 24- and 36-month scales, when we detected overlapping effects at times. In these episodes, the eventual propagation from shorter to longer timescales is much more difficult to detect, since the drought conditions are not clearly identified at shorter timescales. This would be much more complex if shorter (< 12-month) and longer (> 36-month) scales were incorporated. In short, a drought episode must be understood according to its temporal context and never analyzed as an isolated feature.

Differences between drought indices

There is a progressively divergent evolution of the percentage of land affected by drought conditions defined by two different drought indices for the Spanish mainland. Given the diverse nature of the indices, it suggests that the triggering factors driving droughts on the Spanish mainland may have changed during the last few decades.

Various studies have suggested a possible role of global warming on drought severity on the global scale (e.g., Trenberth et al. 2014) following intensification of the hydrological cycle as a consequence of increased AED (Huntington 2006). Nevertheless, the uncertain availability of data is a serious drawback, and prevents a general conclusion being drawn on this issue on a global scale (Seneviratne et al. 2012). In this paper, we sought to avoid these constraints in our regional analyses of drought on the Spanish mainland using a high-resolution spatial dataset, and the main results suggest that the surface affected by droughts in the last two decades may be caused by different mechanisms from previous ones.

We found that the area detected under drought conditions prior to c. 1990 usually has a higher SPI than SPEI indicator. This result suggests that prior to 1990, droughts were mostly related to changes in precipitation, and after 1990 that, in addition to the role of precipitation variability, the atmospheric evaporative demand (AED) has acted as drought triggering factor. These results are coherent with temperature and precipitation evolution on the Spanish mainland, where the most recent studies have detected a general temperature increase from 1951 to 2010, particularly between 1970 and 1990, mostly affecting the spring and summer minimum records (Gonzalez-Hidalgo et al. 2015, 2017), while no significant trend in precipitation was found except for March and June (negative and significant) between 1946 and 2005, and particularly from 1970 (Gonzalez-Hidalgo et al. 2011); the results have been confirmed and updated to 2015 by Notivoli (2017). Furthermore, recent evaluation of AED on the Spanish mainland suggested a global increase of about 125 mm since 1960, which has been attributed to the increase in vapor pressure deficit (Vicente-Serrano et al. 2014b). These findings agree with the results of higher drought detection by SPEI than SPI in the last two decades, and suggest that the water supply to the atmosphere has not been sufficient to cope with the water demand, in line with the warming observed (Vicente-Serrano et al. 2014c). In brief, the global drought framework has recently been driven by new temperature conditions that control AED, irrespective of the evolution of precipitation.

Drought event propagation processes

Spatial variability of drought events is highly complex on a regional scale. This has been demonstrated in several regions of the world (e.g., Skaggs 1975; Song et al. 2014; Capra and Scicolone 2012), and also in previous analyses in the Iberian Peninsula (Vicente-Serrano 2006b) where it has been suggested that spatial drought patterns may differ as a function of the timescale of the drought index, and longer timescales may give rise to more diverse patterns, given the longer impact of the specific local precipitation events.

In the present study, we confirmed these previous findings at high-resolution level, but the results go further and show that there are different spatial gradients of drought propagation.

On mainland Spain, we found three spatial drought propagation gradients that could be linked to several factors controlling droughts. Various explanations have been suggested for precipitation and temperature evolution linked to global and local factors (e.g., Gonzalez-Hidalgo et al. 2011, 2017), in which different hemispheric circulation mechanisms, or more local ones, such as land use changes, have been suggested. Regardless of the exact reason, which is not the objective of this paper, we found that the onset of main drought episodes followed a coast-inland gradient, and no episodes were identified from inland to the coast. It is highly probable that this relates to the main sources of moisture from the Atlantic or Mediterranean water masses (Gimeno et al. 2010), and suggests that the low value of convective rainfalls on annual total precipitation, mostly produced in summer and highly irregular, thus with little effect on both drought indices.

The spatial propagation of droughts also shows the effect caused by the main relief features in the spatial distribution of affected areas, and resembles the well-known spatial areas affected by the most prominent teleconnection patterns. Thus, under west–east propagation episodes, the mountains act as a frontier separating the central-western Spanish conterminous land under drought conditions from the Mediterranean coastland that may be under moist conditions. These features closely resemble the spatial distribution of the North Atlantic Oscillation effects on precipitation and temperature, particularly during the Winter months. Under east–west propagation episodes, the same is true in the opposite direction, and resemble the areas affected by the Western Mediterranean Oscillation. This mountain border effect is more evident when the affected areas are less than 25% of total land (not analyzed in the present paper), but clearly recognized in the case of

1979–1980 episodes in the Mediterranean coastland (not presented).

The third most significant results concern the onset of drought. Apparently, drought episodes start at two different times: (i) the cold months from autumn (1971, 1981, 1994 and 1995), and (ii) the end of winter or beginning of spring (1965, 1992, 2005 and 2012). The differences in the onset of droughts would be able to explain the behavior of the event, and the differences found in the SPI and SPEI. In the first case, when drought starts at the end of autumn it seems to suggest that the previous summer avoided drought conditions by spring–summer precipitation delayed to the beginning of autumn, notwithstanding the positive significant trend of precipitation in October, this should be taken into account in future detailed research. In the second case, when drought starts at the end of winter, it seems to be related with scant winter precipitation. In brief, we can conclude that there are different types of drought, depending on their origin, sometimes promoted by scarce rainfall (the first case), or by means of a more complex mechanism combining low rainfall and the different factors controlling AED.

These findings could be the reason lying behind divergence in surface detection by SPI and SPEI, and also how drought spreads differently according to different temporal scales.

To conclude, the high-resolution analyses of drought on both scales, spatial and temporal, in the Spanish conterminous land indicates the extreme complexity of the phenomenon, the need for further research, and caution when extrapolating from general conclusions.

Acknowledgements This work is supported by the projects CGL2014-52135-C03-01, CGL2014-52135-C3-3-R and PCIN-2015-220, financed by the Spanish Government, Ministry of the Economy and Finance and FEDER, IMDROFLOOD financed by the Water Works 2014 co-funded call of the European Commission, INDECIS, financed by the ERA-NET Cofund for Climate Services of the European Research Area for Climate Services, and the Regional Government of Aragón DGA-FSE (Grupo de Investigación Consolidado 'Clima, Agua, Cambio Global y Sistemas Naturales'). Celia Salinas is a FPI-PhD student supported by the Ministry of the Economy and Finance. Miquel Tomas-Burguera was supported by the predoctoral FPU program 2013 (Ministry of Education, Culture and Sport). Original data from AEMet.

References

Allen RG, Pereira LS, Raes D, Smith M (1998) Crop evapotranspiration: guidelines for computing crop requirements, irrigation and drainage paper 56. FAO, Roma

Camarero JJ, Gazol A, Sangüesa-Barreda G, Oliva J, Vicente-Serrano SM (2015) To die or not to die: early warnings of tree dieback in response to a severe drought. J Ecol 103:44–57

Capra A, Scicolone B (2012) Spatiotemporal variability of drought on a short-medium timescale in the Calabria region (Southern Italy). Theor Appl Climatol 116:371–384

Domínguez-Castro F, Ribera P, García-Herrera R et al (2012) Assessing extreme droughts in Spain during 1750–1850 from rogation ceremonies. Clim Past 8:705–722

Gimeno L, Nieto R, Trigo RM, Vicente-Serrano SM, López-Moreno JI (2010) Where does the Iberian Peninsula moisture come from? An answer based on a Lagrangian approach. J Hydrometeorol 11:421–436

Gonzalez-Hidalgo JC, Brunetti M, de Luis M (2011) A new tool for monthly precipitation analysis in Spain: MOPREDAS database (Monthly precipitation trends December 1945–November 2005). Int J Climatol 31:715–731

Gonzalez-Hidalgo JC, Peña-Angulo D, Brunetti M, Cortesi C (2015) MOTEDAS: a new monthly temperature database for mainland Spain and the trend in temperature (1951–2010). Int J Climatol 35:4444–4463. https://doi.org/10.1002/joc.4298

Gonzalez-Hidalgo JC, Peña-Angulo D, Salinas-Solé C, Brunetti M (2017) A moving windows visual approach to analyze spatial variation of temperature trends in spanish mainland 1951–2010. Int J Climatol. https://doi.org/10.1002/joc.5288

Heim RR (2002) A review of twentieth-century drought indices used in the United States. BAMS 83:1149–1165

Hoerling M et al (2012) On the increased frequency of Mediterranean drought. J Clim 25:2146–2161

Huntington TG (2006) Evidence for intensification of the global water cycle: review and synthesis. J Hydrol 319:83–95

Jerez S, Trigo RM, Vicente-Serrano SM, Pozo-Vazquez D, Lorente-Plazas R, Lorenzo-Lacruz J, Santos-Alamillos F, Montavez JP (2013) The impact of the North Atlantic Oscillation on renewable energy resources in Southwestern Europe. J Appl Meteorol Climatol 52:2204–2225

Keyantash J, Dracup J (2002) The quantification of drought: an evaluation of drought indices. BAMS 83:1167–1180

Lloyd-Hughes B (2014) The impracticality of a universal drought definition. Theor Appl Climatol 117:607–611

Lloyd-Hughes B, Saunders MA (2002) A drought climatology for Europe. Int J Climatol 22:1571–1592

Lorenzo-Lacruz J, Vicente-Serrano SM, Lopez-Moreno JI, Begueria S, Garcia-Ruiz JM, Cuadrat JM (2010) The impact of droughts and water management on various hydrological systems in the headwaters of the Tagus River (central Spain). J Hydrol 386:13–26

Lorenzo-Lacruz J, Vicente S, González-Hidalgo JC, López-Moreno JI, Cortesi N (2013) Hydrological drought response to meteorological drought in the Iberian Peninsula. Clim Res 58:117–131

Maia R, Vicente-Serrano SM (2017) Drought planning and management in the Iberian Peninsula. In: Wilhite D, Pulwarty ES (eds) Drought and water crises: science, technology and management issues. CRC, Boca Raton

McKee TBN, Doesken J, Kleist J (1993) The relationship of drought frequency and duration to timescales. In: Proceedings of the Eighth Conference on Applied Climatology. American Meteorological Society, Boston, pp 179–184

Pascoa P, Gouveia CM, Russo A, Trigo RM (2017) The role of drought on wheat yield interannual variability in the Iberian Peninsula from 1929 to 2012. Int J Biometeorol 61:439–451. https://doi.org/10.1007/s00484-016-1224-x

Peña-Gallardo M, Gámiz-Fortís SR, Castro-Diez Y, Esteban-Parra MJ (2016) Comparative analysis of drought indices in Andalusia during the period 1901–2012. Cuadernos de Investigacion Geográfica 42:67–88

Seneviratne SI, Nicholls N, Easterling D, Goodess CM et al (2012). Changes in climate extremes and their impacts on the natural physical environment. In: Field CB, Barros V, Stocker TF, et al (eds) Managing the risks of extreme events and disasters to advance climate change adaptation . A Special Report of Working Groups I and II of the Intergovernmental Panel on Climate Change (IPCC). Cambridge University Press, Cambridge, UK, and New York, NY, USA, pp 109–230

Serrano-Notivoli Roberto (2017) Reconstrucción climática instrumental a escala diaria en España y análisis de extremos. PhD Thesis, University of Zaragoza, Spain

Skaggs RH (1975) Drought in the united states, 1931–40. Ann Assoc Am Geogr 65:391–402

Song X, Li L, Fu G et al (2014) Spatial-temporal variations of spring drought based on spring-composite index values for the Songnen Plain, Northeast China. Theor Appl Climatol 110:471–488

Soulé PT (1992) Spatial patterns of drought frequency and duration in the contiguous USA based on multiple drought event definitions. Int J Climatol 12:11–24

Stahl K, Kohn I, De Stefano L et al (2015) An impact perspective on pan-European drought sensitivity. Drought: Research and Science-Policy Interfacing. In: Proceedings of the International Conference on Drought: Research and Science-Policy Interfacing, pp 329–334

Stahl K, Kohn I, Blauhut V et al (2016) Impacts of European drought events: insights from an international database of text-based reports. Nat Hazards Earth Syst Sci 16:801–819

Svoboda M, LeComte D, Hayes M, Heim R, Gleason K, Angel J, Rippey B, Tinker R, Palecki M, Stooksbury D, Miskus D, Stephens S (2002) The drought monitor. BAMS 83:1181–1190

Tejedor E, Saz MA, Esper J et al (2017) Summer drought reconstruction in northeastern Spain inferred from a tree ring latewood network since 1734. Geophys Res Lett 44:8492–8500

Trenberth K et al (2014) Global warming and changes in drought: expectations, observations and uncertainties. Nat Clim Change 4:17–22

van der Schrier G, Briffa KR, Jones PD, Osborn TJ (2006) Summer moisture variability across Europe. J Clim 19:2818–2834

Van Loon AF, Gleeson T, Clark J et al (2016) Drought in the Anthropocene. Nat Geosci 9:89–91

Vicente-Serrano SM (2006a) Spatial and temporal analysis of droughts in the Iberian Peninsula (1910–2000). Hydrol Sci J 51:83–97

Vicente-Serrano SM (2006b) Differences in spatial patterns of drought on different timescales: an analysis of the Iberian Peninsula. Water Resour Manage 20:37–60

Vicente-Serrano SM (2016) Foreword: drought complexity and assessment under climate change conditions. Cuadernos de Investigación Geográfica 42:7–11

Vicente Serrano SM, González-Hidalgo JC, de Luis M, Raventós J (2004) Spatial and temporal patterns of droughts in the Mediterranean area: the Valencia region (East-Spain). Clim Res 26:5–15

Vicente-Serrano SM, Beguería S, López-Moreno JI (2010) A multiscalar drought index sensitive to global warming: the standardized precipitation evapotranspiration index. J Clim 23:1696–1718

Vicente-Serrano SM, Gouveia C, Camarero JJ et al (2013) The response of vegetation to drought time-scales across global land biomes. Proc Natl Acad Sci USA 110:52–57

Vicente-Serrano SM, Lopez-Moreno JI, Beguería S et al (2014a) Evidence of increasing drought severity caused by temperature rise in southern Europe. Environ Res Lett 9:044001. https://doi.org/10.1088/1748-9326/9/4/044001

Vicente-Serrano SM, Azorin-Molina C, Sanchez-Lorenzo A et al (2014b) Reference evapotranspiration variability and trends in Spain, 1961–2011. Glob Planet Change 121:26–40

Vicente-Serrano SM, Azorin-Molina C, Sanchez-Lorenzo A et al (2014c) Sensitivity of reference evapotranspiration to changes in meteorological parameters in Spain (1961–2011). Water Resour Res 50:8458–8480

Vicente-Serrano SM, Tomas-Burguera M, Beguería S et al (2017) A high resolution dataset of drought indices for Spain. Data 2:22. https://doi.org/10.3390/data2030022

Wilhite DA, Glantz MH (1985) Understanding the drought phenomenon: the role of definitions. Water Int 10:111–120

Williams AP, Allen CD, Macalady AK et al (2013) Temperature as a potent driver of regional forest drought stress and tree mortality. Nat Clim Change 3:292–297

World Meteorological Organization (2012) Standardized Precipitation Index User Guide (M. Svoboda, M. Hayes and D. Wood). (WMO-No. 1090), Geneva

Acta Geophysica (2018) 66:393–403
https://doi.org/10.1007/s11600-018-0127-0

RESEARCH ARTICLE - SPECIAL ISSUE

Investigating dynamical features in the long-term daily maximum temperature time series recorded at Adrián Jara, Paraguay

Luciano Telesca[1] · Julián Báez Benitez[2]

Received: 13 October 2017 / Accepted: 13 March 2018 / Published online: 28 March 2018

Abstract
In this study, we analyse the daily series of maximum temperature measured at Adrián Jara, Paraguay, to disclose features possibly linked with climatological indices that are thought to regulate, in general, the climatic variability of South America. This station is well suited to perform this investigation because it is located in a rural not urbanized area. Our findings reveal that the analyzed series is modulated by several cycles: the annual and half-annual cycle; the 8-year cycle that could be driven by 8-year cycle of the baroclinic waves at the Southern Hemisphere; the 2–3-year periodicity, which seems linked with the Pacific Decadal Oscillation; the 15–16 years periodicity that seems to be induced by the low-frequency fluctuations of SST in the North Atlantic. It is also found an apparent shift in the maximum temperature in the late 1989 that seems to be in agreement with similar findings by other studies that documented such potential jump in the climate system.

Keywords Temperature · Paraguay · Statistical analysis

Introduction

Our environment and society could be seriously impacted by the occurrence of extreme temperature events, given by long-lasting hot or cold spells. Several studies performed on the analysis of recorded temperature in many areas worldwide showed some relevant variations in the occurrence of extremes. During the twentieth century, the mean surface temperature of the globe increased by about 0.6 °C and many regions have been characterized by relevant warming in the last 50 years (Folland et al. 2001). Such warming could not be uniformly distributed in space nor in time, but weather projections indicate that it will continue and probably joined with more extreme climate events. Due to the higher and higher vulnerability of our society and infrastructure to severe climatic events, it is crucial to carefully monitor extreme events and to keep on searching for clear changes in climate extremes.

South America has been the subject of several studies focused on the time variability of extremes in temperatures. Rusticucci and Barrucand (2004), for instance, analyzed trends in averages, variances, and extreme events in summer (December–February) and winter (June–August) for temperature time series spanning from 1959 to 1998 in Argentina; they found that the number of cold nights and warm days decrease, but that of warm nights and cold days increase in various sites, especially in summer.

Investigating the warming phenomenon in several areas of Brazil, it was interpreted that land-use changes, including also the growth of metropolis likes São Paulo and Rio de Janeiro, would have been contributed to the increase of temperature (Marengo 2001, 2003; Sansigolo et al. 1992). Quintana-Gomez (1999), studied the time series of night time temperature in Colombia, and found a steady increase during the last 30–40 years. For the Amazon, it was revealed a warming trend of 0.56 °C/100 years until 1997 (Victoria et al. 1998), which was updated by Marengo (2003) with a value of 0.85 °C/100 years until 2002. Since the 1960s a significant warming trend was identified in the increase of the minimum temperature for southern Brazil,

✉ Luciano Telesca
luciano.telesca@imaa.cnr.it

[1] Consiglio Nazionale delle Ricerche, Istituto di Metodologie per l'Analisi Ambientale, C.da S.Loja, 85050 Tito, PZ, Italy

[2] Facultad de Ciencias y Tecnología, Centro de Tecnología Apropiada, Universidad Católica Nuestra Señora de la Asunción, Tte. Cantaluppi y G. Molinas, Asunción, Paraguay

in comparison with the maximum temperature during winter, leading to a decrease of the day-time temperature variability (Vincent et al. 2005).

Coronel and Baez (2009) analyzed several indices of climate change detection including maximum temperature at six sites in Paraguay; although no strong evidence of positive trend was found in the maximum temperature, a positive trend was detected in minimum temperature.

In this paper, we perform a multi-parametric statistical analysis of the daily maximum temperature measured at station Adrián Jara, Paraguay, whose location in a not-urbanized rural area makes it suited to possibly identify in the time variation of the maximum temperature signatures of climatological indices that are generally considered as drivers of the climate of South America.

Data

The station analyzed correspond to Adrián Jara, Department of Alto Paraguay, located at the north of the country (Fig. 1). The station is in a rural area, so the measured temperature could not be affected by urbanization. The daily maximum temperature series analyzed in the present study spans from May 1973 till February 2013 (Fig. 2a). Some sparse daily gaps exist, and the whole 1988 is missing. The station is located at (19°32′28.32″S, 59°29′38.94″W) at altitude of 139 m a.s.l. The site is characterized by a tropical wet-and-dry climate bordering on semi-arid. Rainfall is light (Fig. 2b shows the daily variation of rainfall at Adrián Jara), varying from 500 to 1000 mm per year mostly concentrated in the summer months.

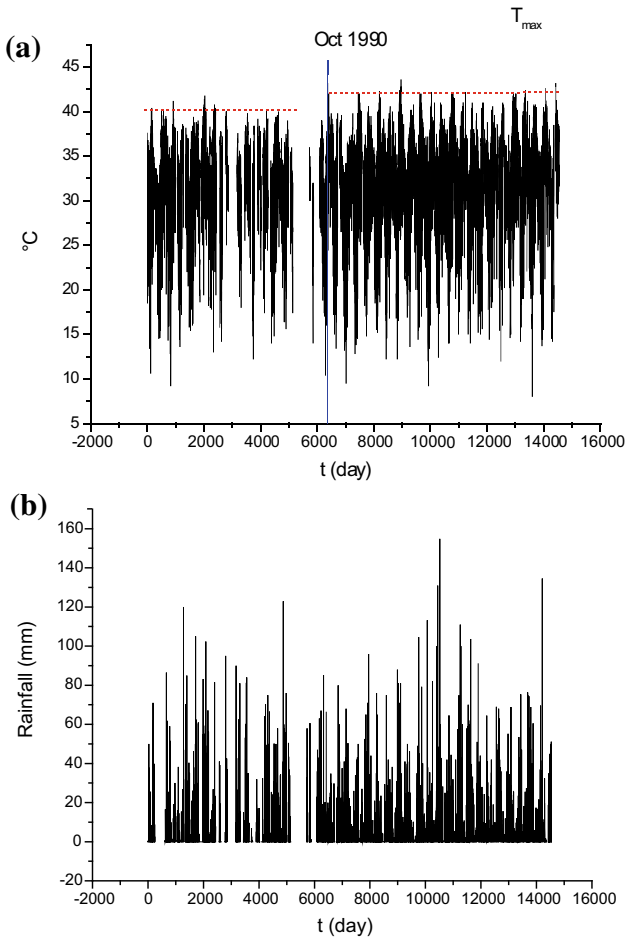

Fig. 2 **a** Daily variation of maximum temperature; **b** daily variation of rainfall at Adrián Jara

Fig. 1 Location of Adrian Jara meterological station

Methods

Robust periodogram method

A natural phenomenon is characterized by several complex features, among which periodicities represent those components that it is crucial to detect and investigate to have information about cyclic forcing that can govern its time dynamics.

Among several tools used to calculate the frequency content of a signal, Wichert et al. (2004) developed a formally assessed statistic test methodology for the cycle identification, on the basis of the Fisher's g-statistic, whose distribution for hypothesis zero can be exactly obtained assuming the Gaussian noise. Let's consider the simple model of cyclic process as follows:

$$y_n = \beta \cos(wt + \phi) + \varepsilon_n, \tag{1}$$

where $\beta > 0$, $0 < \omega < \pi$, ϕ is a uniform distribution in $(-\pi, \pi]$, and $\{\varepsilon_n\}$ is an uncorrelated random process with mean 0 and variance σ^2, independent of ϕ.

Using the following equation

$$I(\omega) = \frac{1}{N}\left|\sum_{n=1}^{N} y_n e^{-i\omega n}\right|^2, \quad 0 \le \omega \le \pi \tag{2}$$

the periodogram can be calculated at normalized frequencies:

$$\omega_l = \frac{2\pi l}{N}, \quad l = 0, 1, \ldots, a \tag{3}$$

where N is the number of samples of the series, $a = [(N-1)/2]$ and $[x]$ indicates the integer part of x. In case the series is significantly modulated by a periodicity with frequency ω_0, the periodogram will be very likely peaked at that frequency. In case the series is a random process ($\beta = 0$ in Eq. 1) the periodogram appears approximately flat at any frequency (Priestley 1981).

Ahdesmäki et al. (2005) proposed to robustly detect periodicities in signals using the autocorrelation function. Due to the equivalence between the periodogram $I(\omega)$ and the correlogram spectral estimator, we have that

$$S(\omega) = \sum_{k=-N+1}^{N-1} \hat{r}(k) e^{-i\omega k}, \tag{4}$$

where

$$\hat{r}(m) = \frac{1}{N}\sum_{k=1}^{N-m} y_k y_{k+m} \tag{5}$$

is the biased estimator of the autocorrelation function. It is well known that the sample correlation function between two sequences with length N is:

$$\rho(m) = \frac{\frac{1}{N}\sum_{i=1}^{N}(x_i - \bar{x})(y_i - \bar{y})}{\sigma_x \sigma_y}, \tag{6}$$

where the bar over the symbol indicates the average; Ahdesmäki et al. (2005) derived the following robust spectral estimator by means of the relationship between the estimator of the autocorrelation function $\hat{r}(m)$ and the estimator of correlation function $\tilde{\rho}(m)$ between the sequences $\{y_k\}$ and $\{y_{k+m}\}$:

$$\tilde{S}(\omega) = 2\Re\left(\sum_{k=0}^{L} \tilde{\rho}(k) e^{-i\omega k}\right) - \tilde{\rho}(0), \tag{7}$$

where $\Re(x)$ means the real part of x, L is the maximal lag at which the correlation coefficient $\tilde{\rho}(k)$ is calculated.

Singular spectrum analysis

The singular spectrum analysis (SSA) (Vautard and Ghil 1989) decomposes seemingly noisy signals into a set of independent components that can be interpreted as trend, cycles or quasi-cycles or simply noise (Hassani 2007).

The Toeplitz lagged correlation matrix is computed, whose entries are function only of lag M that represents the maximum number of components of the analyzed series. The selection of M is a crucial step in the SSA method, because large M guarantees large quantity of information and small M guarantees high value of statistical confidence (Ghil et al. 2002). Vautard et al. (1992) recommended that the M has to be lower than $N/5$. As a rule of thumb, SSA would identify about $M/10$ significant components before oscillations begin to be lumped together. Therefore, M has be larger than the longer periodicity under investigation, but also smaller than $N/5$ and larger than about $M/10$ times the number of significant components that might be present. Khan and Poskitt (2010) proposed that the maximum M is $M = (log\ \ N)^c$, $1.5 \le c \le 2.5$. We calculate the eigenvalues λ_k and the eigenvector E_{kj} for the lagged Toeplitz correlation matrix. Then the reconstructed components r_{ik} of the series y_i are then obtained by the following equation:

$$r_{ik} = \frac{1}{M}\sum_{j=1}^{M} a_{i-j,k} E_{jk}, \quad M \le i \le N - M + 1, \tag{8}$$

where a_{ik} is the k-th principal component given by

$$a_{ik} = \sum_{j=1}^{M} y_{i+j} E_{jk}, \quad 0 \le i \le N - M. \tag{9}$$

λ_k represents the fraction of the variance of the original series displayed by the k-th r_{ik}. Sorting λ_k in decreasing order with k from 1 to M, and maintaining the same order for the reconstructed components, the information about

the original series contained in the reconstructed components will be decreasing for k from 1 to M (Schoellhamer 2001). Generally, the first reconstructed components contain most of the variance, while the remaining ones contain merely noise. Two reconstructed components with close value of λ_k represent a cycle with period less than M (Vautard and Ghil 1989).

The coefficients of variation

The time-clustering behavior of a point process can be investigated using the coefficient of variation C_v. It is defined as

$$C_v = \frac{\sigma}{\mu}, \tag{10}$$

where σ and μ are the standard deviation and the mean of the interoccurrence intervals, respectively. Depending on the numerical value of C_v, the point process is regular (or cyclic) (< 1), Poissonian ($= 1$) or time-clusterized (> 1) (Kagan and Jackson 1991). A recent measure for quantifying the local time-clustering behavior of a point process is the local coefficient of variation L_v developed by Shinomoto et al. (2005), and in a recent study employed by Telesca et al. (2016) to get information on the local time-clustering characteristics of the seismicity occurred at El Hierro volcano, Canary Islands (Spain). This is defined as follows:

$$L_v = \frac{1}{N-1}\sum_{i=1}^{N-1} 3\frac{(T_i - T_{i+1})^2}{(T_i + T_{i+1})^2}, \tag{11}$$

where T is the interoccurrence time. Like the C_v, also the L_v assumes values smaller, equal or larger than 1 for periodic, Poissonian or clustered point processes, respectively. However, C_v measures the time-clustering of a point process at a global scale and could be affected by event rate fluctuations, while L_v measures local stepwise variability of interevent times and it does not depend much on slow varying average rate. To better visualize the difference between the two time-clustering measures, consider one point process obtained joining two periodic processes (Fig. 3); for this process $C_v \gg 1$ because globally the process is given by two distinct clusters, but $L_v \sim 0$, because locally the process is periodic.

The Allan factor

The Allan factor (AF) is a well-known measure, which permits the identification of the timescale range over which the point process is clusterized. Fixing a specific box size of duration τ, that is the timescale, the time axis is divided in a certain number of nonoverlapping boxes of that duration; then a series of counts $\{N_k(\tau)\}$ is obtained, where $N_k(\tau)$ is the number of events contained within the k-th box (Thurner et al. 1997). The Allan factor is defined as the following function:

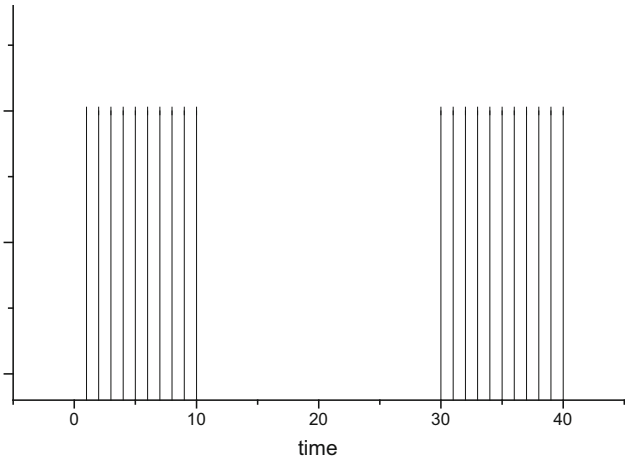

Fig. 3 Two superimposed periodic point processes

$$\mathrm{AF}(\tau) = \frac{<(N_{k+1}(\tau) - N_k(\tau))^2>}{2<N_k(\tau)>}, \tag{12}$$

and it relates with the fluctuations of successive counts (Thurner et al. 1997); the symbol $<\ldots>$ indicates the average. The AF has been largely used to investigate the time dynamics of point processes of different types (Telesca et al. 2001, 2005).

For Poisson point process (that is formed by independent events), the AF is rather flat at all timescales and assumes value around 1 (except for very large timescales due to finite-size effects (Telesca et al. 2012); but if the process is time-clustered, AF changes with τ. In particular, if the point process is fractal (self-similar) in time, the AF behaves as a power-law (scaling behavior):

$$\mathrm{AF}(\tau) = 1 + \left(\frac{\tau}{\tau_1}\right)^{\alpha}, \tag{13}$$

where the exponent α quantifies how much clusterized the process is; τ_1 is the so-called fractal onset time and indicates the lowest timescale above which the scaling behavior of AF is significant (Thurner et al. 1997). Therefore, if $\alpha \sim 0$ for Poisson process, while if $\alpha > 0$ it is clusterized.

Data analysis

Figure 2 shows the daily variation of maximum temperature recorded at Adrian Jara. It is visible a highly oscillating behavior ranging between 8 and 43.6 °C. It appears that around the end of 1990 (vertical blue line) the

maximum temperature is characterized by a slight increase (horizontal dot red lines).

First of all, we investigated the presence of dominant frequencies in the time variability of the maximum temperature. We applied the robust periodogram method and Fig. 4 shows the results. Two main periodicities are clearly visible at 1 year and 6 months.

To better explore the time dynamics of the maximum temperature recorded at Adrian Jara, we applied the SSA to identify the inner components of the time series and distinguish between oscillatory, long-term trend and noisy components. To identify at least the annual periodicity, we used $M = 365$ and decomposed, therefore, the time series into 365 independent components. The eigenvalue spectrum (Fig. 5) shows that the first seven eigenvalues are well distinguished by the rest; these seven eigenvalues are also associated with the most significant components of the series, which we will focus on.

Figure 6 shows the first seven components and Fig. 7 shows their robust periodogram. The first two components (R_1 and R_2) represent the annual cycle (Fig. 6). The components R_4 and R_5 represent the semi-annual cycle, as it can be argued from the corresponding robust periodogram. The components R_6 and R_7 show the dominance of a cycle of about 4 months and a sub-monthly cycle of 17 days.

The component R_3 appears quite interesting for its richness in time structure. First of all, this component seems to be characterized by an increasing behavior [that confirms what was evidenced by visual inspection in the original time series (Fig. 3)]. Furthermore, the robust periodogram shows a variability of periodicities from semi-annual to the multi-annual, peaked on the 8-year periodicity.

We analyzed the time clustering properties of the set of values of the maximum temperature T_{max} recorded at

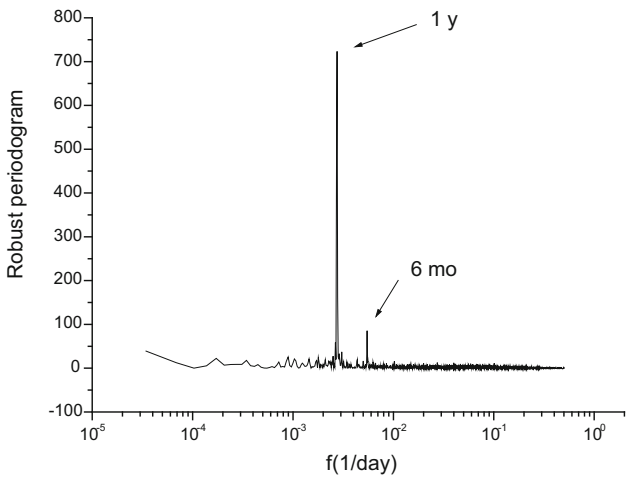

Fig. 4 Frequency spectrum of Adrian Jara data calculated using the robust periodogram method

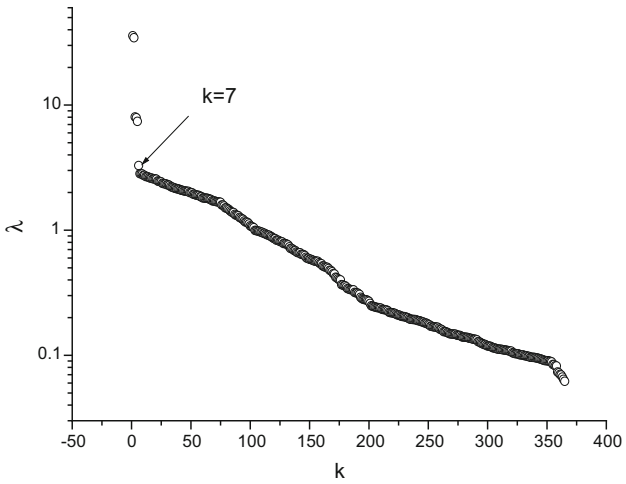

Fig. 5 Eigenvalues of Adrian Jara

Adrian Jara above a certain threshold. Fixing the threshold of 95% of the distribution of T_{max} (Fig. 8a) (corresponding to the T_{max}= 39.22) we constructed the point process ($^{95\%}T_{max}$) (Fig. 8b).

It is visible a certain temporal change of density of $^{95\%}T_{max}$ events since October 1990 (as we saw in the other results shown above): before this date the number of $^{95\%}T_{max}$ events is clearly lower than after. This is also an evidence of the change in the variability of maximum temperature occurring at the end of 1990.

Figure 9 shows the sequence of the interevent times calculated as the intervals of two successive $^{95\%}T_{max}$ events. The shape of the sequence of the interevent times confirms the increase of density of $^{95\%}T_{max}$ events since the beginning of the recording period. We computed the coefficients of variation and we obtained $C_v \sim 4.08$ and $L_v \sim 1.10$. The significance of coefficients of variation was calculated on the base of 1000 Poissonian random sequences having same size and mean interevent time as the original sequence. The 95% confidence band (delimited by the 2.5th and 97.5th percentiles of distribution of C_v and L_v of the Poissonian random sequences) is [0.92, 1.08] for C_v and [0.91, 1.09] for L_v. The obtained values of the coefficients of variation indicate that globally the distribution of $^{95\%}T_{max}$ events is clusterized while locally is quasi-Poissonian at 95% confidence.

Figure 10 shows the AF for the sequence of $^{95\%}T_{max}$ events plotted in Fig. 8. It is clearly visible that the AF curve shows a linear behavior in log–log scales from about 2 weeks to about 5 months, with scaling exponent of about 1, indicating that the sequence is characterized by a fractal behavior within this time scale range. The drop at about 1 year suggests the presence of annual periodicity that would modulate the time distribution of the sequence of $^{95\%}T_{max}$ events. To check whether this behavior depends on

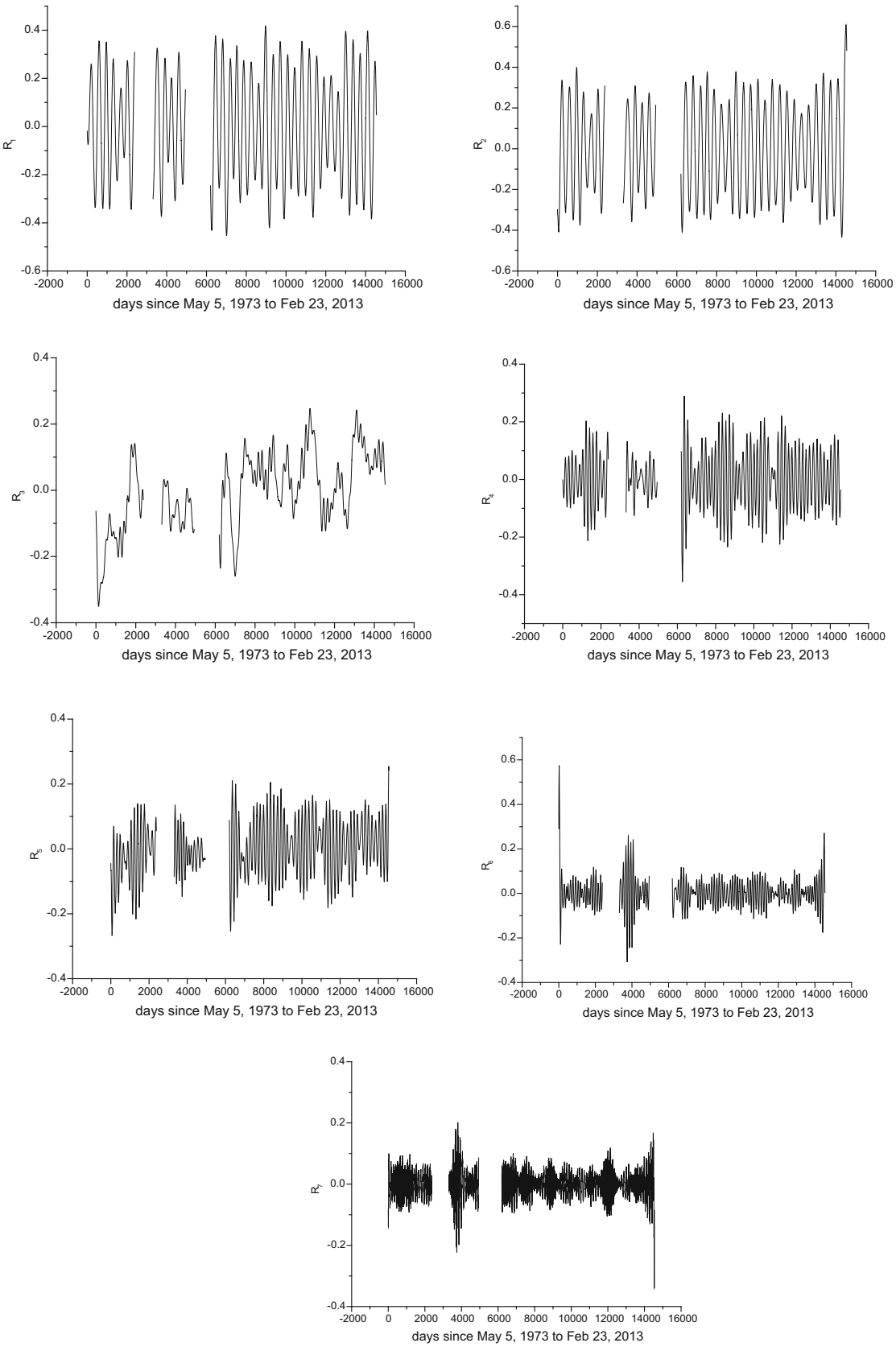

Fig. 6 The seven reconstructed components

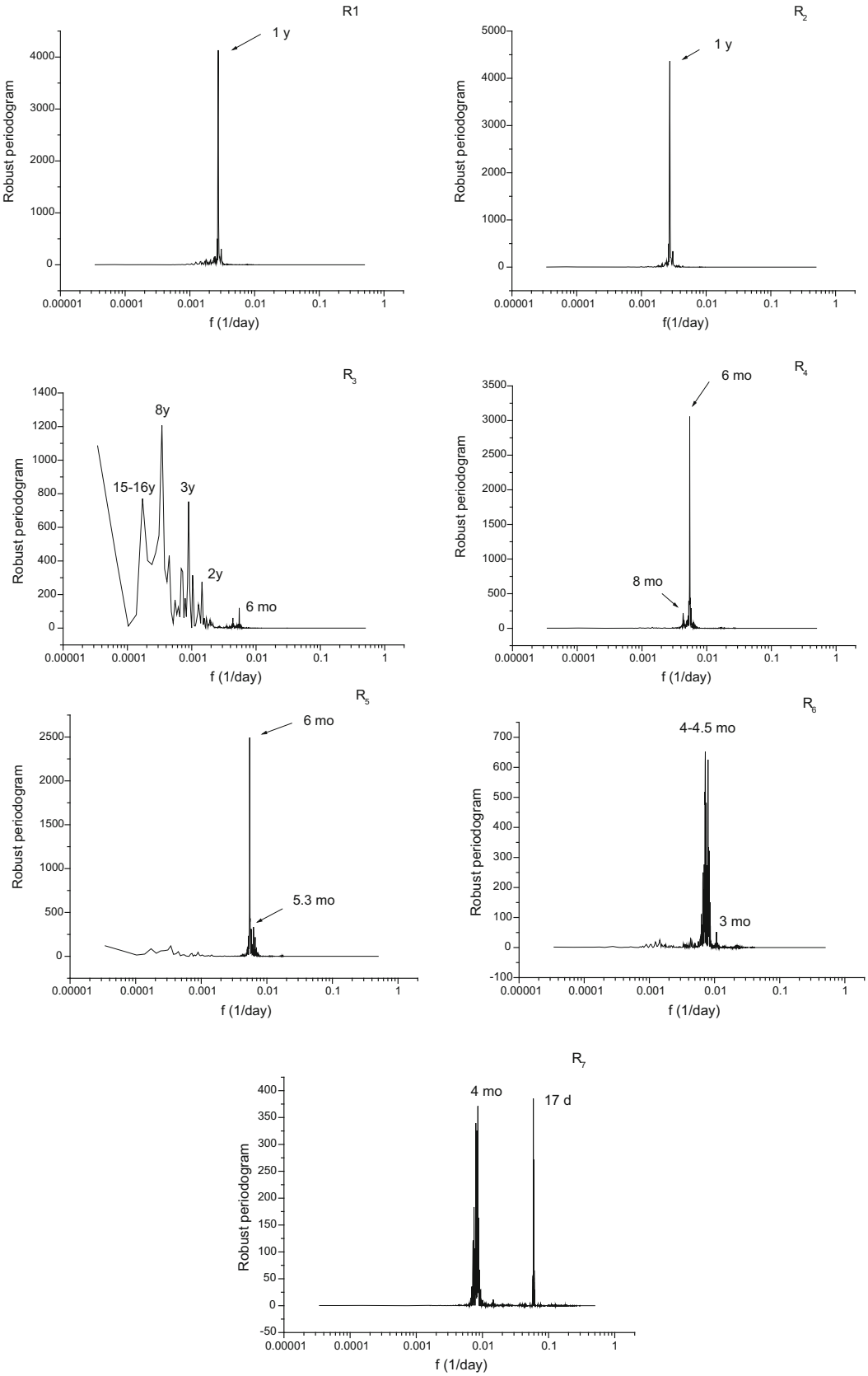

Fig. 7 Robust periodogram of the reconstructed components shown in Fig. 6

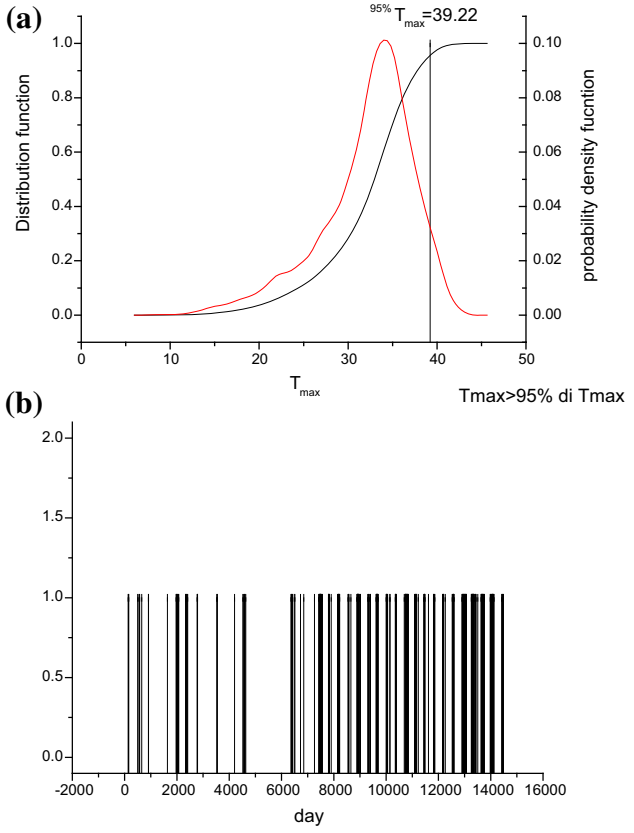

Fig. 8 **a** Distribution of $T_{\max}$ and **b** the point process of ${}^{95\%}T_{\max}$ constructed with a threshold of 95% of $T_{\max}$ distribution

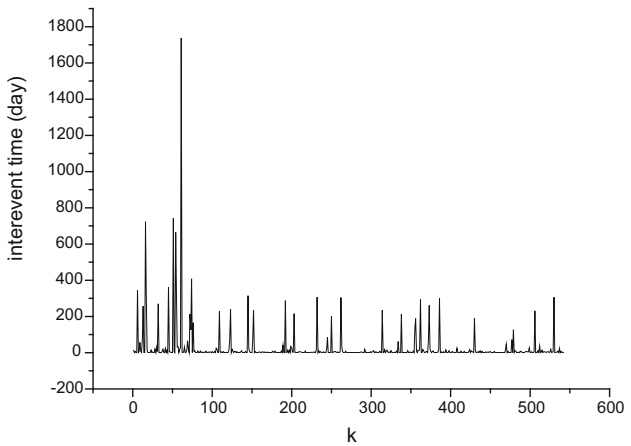

Fig. 9 The sequence of the interevent times

the threshold, we calculated the AF for 98, 99 and 99.9% threshold (Fig. 11). The AF curves for 98 and 99% threshold are almost overlapped on that at 95% indicating that the temporal behavior of the largest events of the maximum temperature does not depend on the threshold. Even the drop at about 1 year is present for the sequence of ${}^{98\%}T_{\max}$ and ${}^{99\%}T_{\max}$ events.

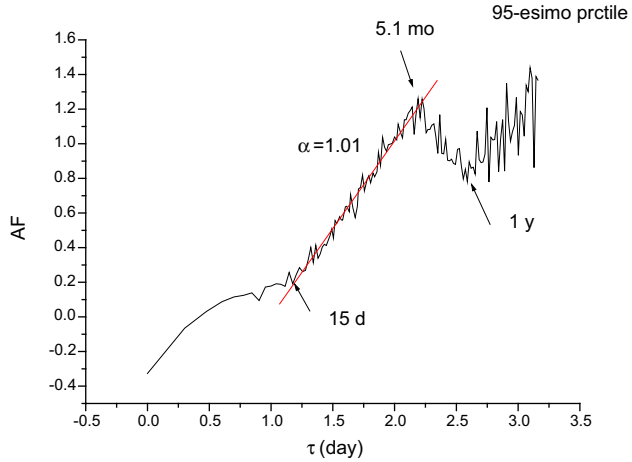

Fig. 10 AF for sequence of ${}^{95\%}T_{\max}$ events of Adrian Jara

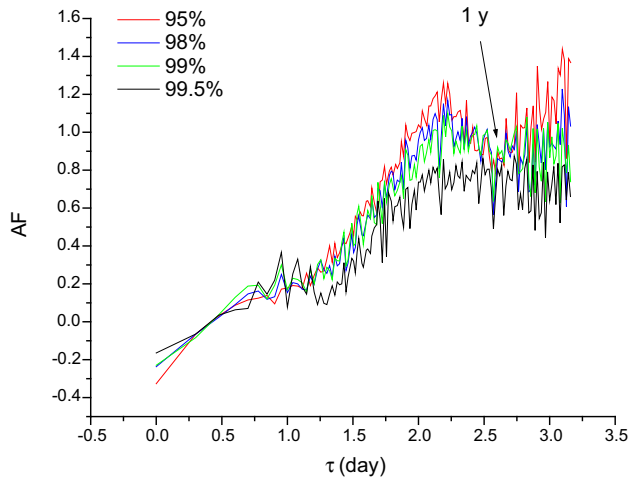

Fig. 11 AF for different thresholds

The sequence of ${}^{99.9\%}T_{\max}$ events, although the fractal behavior within the time scale range from about 2 weeks to about 5 months is still present, does not show evidence of the drop at about 1 year.

Discussion

The analysis performed on the time series analysis of maximum temperature for Adrian Jara, Paraguay by integrated several statistical techniques has allowed to get insight the complex behavior of this time series.

The main findings of our study are the following:

1. The time series of the maximum temperature is clearly characterized by an annual cycle, visible in the robust periodogram of the whole time series (Fig. 4) and in that of the reconstructed components R_1 and R_2 (Fig. 7); such periodicity is clearly linked with the

annual meteorological cycle that influences the climatic conditions of the site. The annual oscillation was also evident in the point process of the maximal temperature above 95th, 98th and 99th percentile (Fig. 11).

2. The reconstructed component R_3 shows a very rich spectral content, being characterized by several interannual cycles, at 15–16 years, 8 years, and 2–3 years. The highest peak is represented by the 8-year cycle. Barrucand et al. (2008) investigated for South America several indices of extreme temperature, and among these they found that the series of warm days are principally featured by two signals, one in the band of 2–4 years and the other at around 8 years, although in their study the 8-year signal was found more intense in the frequency of cold nights rather than warm nights (although this last is referred to the minimum temperature), however, the findings of almost the same periodical signals strengthen our results. The 8-year modulation of climatic signals was also detected in several different climatic indices that are thought to regulate the climatic variability of South America. Barrucand et al. (2008) applying the wavelet transform to the Southern Anular Mode (SAM) SAM [defined by Marshall (2003)] considering a zonal average of sea level pressure at 40° and 65° based on six stations close to each of the latitudes) identified a clear 8-year dominant frequency. Rao et al. (2003) investigated the connections between the interannual variations of storm tracks in the Southern Hemisphere and the Antarctic Oscillation and found a dominant cycle at 8.33 years. On the base of these evidences, the 8-year signal identified in the daily time series of the maximum temperature of Adria Jara in Paraguay would suggest that even the climate variability of the area around our meteorological station could be driven by 8-year cycle of the baroclinic waves at the Southern Hemisphere, as it was revealed by Barrucand et al. (2008) in their analysis of the temperature extremes in the south of South America.
3. The 2–3-year periodicity band seems much more linked with the Pacific Decadal Oscillation (PDO) that is defined by the leading empirical orthogonal function of the monthly anomalies of sea surface temperature in the Pacific poleward of 20°N (Mantua et al. 1997; Mantua and Hare 2002; Deng et al. 2013). Such teleconnection pattern was considered in several studies to explain the Southern Hemisphere cyclones and anti-cyclones (Schneider 2005; Pezza et al. 2007). Although the source of the PDO and its relationship with ENSO are not well known yet (Newman et al. 2003; Schneider and Cornuelle 2005), the PDO is generally depicted as an ENSO-like phenomenon, due to the very close similarity of its cold and warm phases with El Niño and La Niña events (Garreaud et al. 2008). Rusticucci and Renom (2008) applied the multitaper method (MTM) to four temperature indices linked with the frequency of warm days (TX90), cold days (TX10), warm nights (TN90) and cold nights (TN10) in Uruguay from 1961 to 1990, and found that for some stations the TN90 index was characterized by significant periods of 3.4 and 2.4 years, probably correlated with ENSO; while all the indices showed a significant oscillation of 2–2.5 year period. Yu et al. (2010), investigating the subtropics-related interannual SST variability in the central equatorial Pacific, identified two components of interannual SST variability, Type-1 related to eastern Pacific SST and Type-2 not related to them, with leading periodicity in the band 2–4 years and linked with ENSO. The found periodicity range between 2 and 3 years for the daily time series of maximum temperature of our meteorological station in Paraguay confirm the results obtained by these previous studies and reinforce the documented climatic anomalies in southeastern South America, that are related to a different response of ENSO and PDO (Andreoli and Kayano 2005).
4. The robust periodogram of the reconstructed component R_3 also evidence a longer cycle at around 15–16 years. Previous studies showed the presence of similar periodicity band in different types of data. Chu (1984) found a periodicity of 12.7–14.9 years in the rainfall of the Nordeste–Brazil put in relationship with a cold SST in the North Atlantic. Decadal climate variation appeared in the $\delta^{18}O$ record from Quelccaya ice core (Thompson and Mosley-Thompson, 1984), which showed a periodicity of 12–14 years correlated with the low-frequency fluctuations of SST in the North Atlantic. The SST can, then, be supposed as the forcing influencing the decadal variability of the reconstructed component R_3 of the maximum temperature at Adrian Jara, inducing a modulation at periods of 15–16 years.
5. The cycle of 6 months is possibly due the climatic region where the station is located: the station, in fact, is in a tropical region (19°32′25.03″S; 59°29′36.52″O) that is characterized only by the transition between summer to a short winter occurring almost every six months.
6. An interesting feature is represented by the apparent shift in the maximum temperature of Adrian Jara in the late 1990 (Fig. 3), also visible in the reconstructed component R_3 (Fig. 6) and in the density of ${}^{95\%}T_{\max}$ events (Fig. 8), indicating a quasi abrupt change in the climatic conditions of the investigated site. Such change seems to be in agreement with similar findings

by other studies. Barrucand et al. (2008) performing the cross-wavelet transform between some reference cold nights series and the standardized series SST30 (SST of a box in the Atlantic centered at approximately 30°S–48°W) in spring, they found that generally the series are in antiphase, indicating an increase in the temperature in the oceanic areas associated with a decreasing temperature of cold events in spring. However, such relation disappears in the late 1980s, possibly indicates that the climate system could have changed at the beginning of the 1990s. Zhang et al. (1997) mentioned such potential jump in the climate system. Huth and Canziani (2003) found a change in behavior of the hemispheric potential vorticity (PV) fields at the 650 K isentropic level during the years around 1990 that appeared to be important for climate evolution, in concomitance with change in the ozone fields at middle latitudes that should have had a crucial impact on their climatology.

Conclusions

Several independent approaches have been applied to the time series of the daily maximum temperature measured at Adrián Jara (Paraguay), which is located in a rural area; this makes the analysis of such series very interesting, because the identification of specific features and changes in it would not be an effect of urbanization, but, rather, could be induced by meteo-climatic changes. Our results point out to the following findings: (1) the time series of the maximum temperature is visibly modulated by the annual cycle, linked with the annual meteorological cycle; (2) several interannual cycles can be identified, at 15–16 years (probably in relationship with the SST in the north Atlantic), 8 years (also detected in several different climatic indices that are thought to regulate the climatic variability of South America) and 2–3 years (probably linked with the Pacific decadal oscillation); (3) an apparent change in the maximum temperature of Adrian Jara in the late 1990 that seems in agreement with similar findings by other studies. Our statistical investigation, which was performed using several methods (Robust Periodogram, SSA, global and local coefficient of variation and AF), highlights that the daily variability of maximum temperature at Adrián Jara could be driven by several climatological indices that are thought to regulate, in general, the climatic variability of South America.

Acknowledgements The authors acknowledge the financial support of CNR (Italy) and CONACYT (Paraguay).

References

Ahdesmäki M, Lähdesmäki H, Pearson R, Huttunen H, Yli-Harja O (2005) Robust detection of periodic time series measured from biological systems. BMC Bioinform 6:117

Andreoli RV, Kayano MT (2005) ENSO-related rainfall anomalies in South America and associated circulation features during warm and cold Pacific decadal oscillation regimes. Int J Clim 25:2017–2030

Barrucand M, Rusticucci M, Vargas W (2008) Temperature extremes in the south of South America in relation to Atlantic Ocean surface temperature and Southern Hemisphere circulation. J Geophys Res 113:D20111

Chu PS (1984) Time and space variability of rainfall and surface circulation in the northeast Brazil-tropical Atlantic sector. J Meteor Soc Japan 62:363–370

Coronel G, Baez J (2009) Indices de cambio climático en Paraguay, Sociedad Científica del Paraguay (SCP). Sociedad Científica del Paraguay (SCP) 14:213–218

Deng W, Wei G, Xie L, Ke T, Wang Z, Zeng T, Liu Y (2013) Variations in the Pacific Decadal Oscillation since 1853 in a coral record from the northern South China Sea. J Geophys Res Oceans 118:2358–2366

Folland CK, Rayner NA, Brown SJ, Smith TM, Shen SS, Parker DE, Macadam I, Jones PD, Jones RN, Nicholls N, Sexton DMH (2001) Global temperature change and its uncertainties since 1861. Geophys Res Lett 106:2621–2624

Garreaud R, Barichivich J, Christie D, Maldonado A (2008) Interannual variability of the coastal fog at Fray Jorge relicts forests in semiarid Chile. J Geophys Res 113:G04011

Ghil M, Allen MR, Dettinger MD, Ide K, Kondrashov D, Mann ME, Robertson AW, Saunders A, Tian Y, Varadi F, Yiou P (2002) Advanced spectral methods for climatic time series. Rev Geophys 40:1003

Hassani H (2007) Singular spectrum analysis: methodology and comparison. J Data Sci 5:239–257

Huth R, Canziani P (2003) Classification of hemispheric monthly mean stratospheric potential vorticity fields. Ann Geophys 21:805–817

Kagan YY, Jackson DD (1991) Long-term earthquake clustering. Geophys J Int 104:117–134

Khan MAR, Poskitt DS (2010) Description length based signal detection in singular spectrum analysis. Monash Econometrics and Business Statistics Working Papers 13/10, Monash University, Department of Econometrics and Business Statistics

Mantua NJ, Hare SR (2002) The pacific decadal oscillation. J Oceanogr 58:35–44

Mantua NJ, Hare SR, Zhang Y, Wallace JM, Francis RC (1997) A Pacific interdecadal climate oscillation with impacts on salmon production. Bull Am Meteorol Soc 78:1069–1079

Marengo J (2001) Mudanças climáticas globais e regionais: avaliação do clima atual do Brasil e projeções de cenários climáticos do futuro. Rev Bras Meteor 16:1–18

Marengo J (2003) Condições climáticas e recursos hídricos no Norte Brasileiro. In: Tucci CE, Braga B (eds) Clima e Recursos Hídricos no Brasil. Associação Brasileira de Recursos Hídricos FBMC/ANA, Porto Alegre, pp 117–161

Marshall G (2003) Trends in the Southern annular mode from observations and reanalysis. J Clim 16:4134–4143

Newman M, Compo GP, Alexander MA (2003) ENSO-forced variability of the pacific decadal oscillation. J Clim 16:3853–3857

Pezza A, Simmonds I, Renwick J (2007) Southern Hemisphere cyclones and anticyclones: recent trends and links with decadal variability in the Pacific Ocean. Int J Climatol 27:1403–1419

Priestley MB (1981) Spectral analysis and time series. Academic Press, London

Quintana-Gomez RA (1999) Trends in maximum and minimum temperatures in northern South America. J Clim 12:2104–2112

Rao VB, Do Carmo A, Franchito S (2003) Interannual variations of storm tracks in the Southern Hemisphere and their connections with the Antarctic oscillation. Int J Climatol 23:1537–1545

Rusticucci M, Barrucand M (2004) Observed trends and changes in temperature extremes over Argentina. J Clim 17:4099–4107

Rusticucci M, Renom M (2008) Variability and trends in indices of quality-controlled daily temperature extremes in Uruguay. Int J Climatol 28(8):1083–1095

Sansigolo C, Rodriguez R, Etchichury P (1992) Tendencias nas temperaturas médias do Brasil, vol 1. Congresso Brasileiro de Meteorologia, Brasileiro de Meteorologia, Sao Paulo, pp 367–371

Schneider N (2005) The forcing of the Pacific decadal oscillation. J Clim 18:4355–4373

Schneider N, Cornuelle BD (2005) The forcing of the Pacific decadal oscillation. J Clim 18:4355–4373

Schoellhamer D (2001) Singular spectrum analysis for time series with missing data. Geophys Res Lett 28:3187–3190

Shinomoto S, Miura K, Koyama S (2005) A measure of local variation of inter-spike intervals. BioSystems 79:67–72

Telesca L, Cuomo V, Lapenna V, Macchiato M (2001) Identifying space–time clustering properties of the 1983–1997 Irpinia–Basilicata (Southern Italy) seismicity. Tectonophysics 330:93–102

Telesca L, Bernardi M, Rovelli C (2005) Intra-cluster and inter-cluster time correlations in lightning sequences. Phys A 356:655–661

Telesca L, Mohamed AE-EA, ElGabry M, El-hady S, Abou Elenean KM (2012) Time dynamics in the point process modelling of seismicity of Aswan area (Egypt). Chaos Solitons Fractals 45:47–55

Telesca L, Lovallo M, Lopez C, Martì Molist J (2016) Multiparametric statistical investigation of seismicity occurred at El Hierro (Canary Islands) from 2011 to 2014. Tectonophysics 672–673:121–128

Thompson LG, Mosley-Thompson E (1984) El Nino Southern oscillation events recorded in the stratigraphy of the tropical Quelccaya Ice Cap, Peru. Science 226:50–53

Thurner S, Lowen SB, Feurstein MC, Heneghan C, Feichtinger HG, Teich MC (1997) Analysis, synthesis, and estimation of fractal-rate stochastic point processes. Fractals 5:565–595

Vautard R, Ghil M (1989) Singular spectrum analysis in nonlinear dynamics, with applications to paleoclimatic time series. Physica D 35:395–424

Vautard R, Yiou P, Ghil M (1992) Singular spectrum analysis: a toolkit for short noisy chaotic signals. Physica D 58:95–126

Victoria R, Matinelli L, Moraes J, Ballester M, Krusche A, Pellegrino G, Almeida R, Richey J (1998) Surface air temperature variations in the Amazon region and its border during this century. J Clim 11:1105–1110

Vincent LA, Peterson TC, Barros VR et al (2005) Observed trends in indices of daily temperature extremes in South America 1960–2000. J Clim 18:5011–5023

Wichert S, Fokianos K, Strimmer K (2004) Identifying periodically expressed transcripts in microarray time series data. Bioinformatics 20:5–20

Yu J-Y, Kao H-Y, Lee T (2010) Subtropics-related interannual sea surface temperature variability in the central equatorial Pacific. J Clim 23:2869–2884

Zhang Y, Wallace JM, Battisti DS (1997) ENSO-like interdecadal variability: 1900–93. J Clim 10(5):1004–1020

Acta Geophysica (2018) 66:405–414
https://doi.org/10.1007/s11600-018-0126-1

RESEARCH ARTICLE - SPECIAL ISSUE

Analysis of synoptic patterns in relationship with severe rainfall events in the Ebre Observatory (Catalonia)

Núria Pérez-Zanón[1] · M. Carmen Casas-Castillo[2] · Juan Carlos Peña[3] · Montserrat Aran[3] · Raúl Rodríguez-Solà[4] · Angel Redaño[5] · German Solé[6]

Received: 30 November 2017 / Accepted: 9 March 2018 / Published online: 23 March 2018

Abstract

The study has obtained a classification of the synoptic patterns associated with a selection of extreme rain episodes registered in the Ebre Observatory between 1905 and 2003, showing a return period of not less than 10 years for any duration from 5 min to 24 h. These episodes had been previously classified in four rainfall intensity groups attending to their meteorological time scale. The synoptic patterns related to every group have been obtained applying a multivariable analysis to three atmospheric levels: sea-level pressure, temperature, and geopotential at 500 hPa. Usually, the synoptic patterns associated with intense rain in southern Catalonia are featured by low-pressure systems advecting warm and wet air from the Mediterranean Sea at the low levels of the troposphere. The configuration in the middle levels of the troposphere is dominated by negative anomalies of geopotential, indicating the presence of a low or a cold front, and temperature anomalies, promoting the destabilization of the atmosphere. These configurations promote the occurrence of severe convective events due to the difference of temperature between the low and medium levels of troposphere and the contribution of humidity in the lowest levels of the atmosphere.

Keywords Synoptic patterns · Severe rainfall · Southern Catalonia · Meteorological temporal scales · Intensity weighted index · Multivariate analysis

Introduction

Overview

In mid-latitude Mediterranean areas, intense rain is usually produced by intense convective systems, often embedded in larger low-pressure structures, with a particular organization highly affected by seasonal and local factors. In the specific case of Catalonia, located in the northeast of the Iberian Peninsula, with an intricate topography delimited in the north by the Pyrenees range and in the east by the Mediterranean Sea and the Prelitoral Range, the proximity of the sea is one of the most relevant factors (Fig. 1).

To investigate the trigger factors of a meteorological extreme rain situation, both the spatial and time rain organization must be analyzed by studying the association between the maximum amounts recorded in different temporal intervals for the same rain episode (Lorente and Redaño 1990; Casas et al. 2004). Thus, an objective classification of the intense rainfall episodes can be carried out

✉ Núria Pérez-Zanón
nuria.perez@urv.cat

[1] Centre for Climate Change (C3), Department of Geography, University Rovira i Virgili, Joanot Martorell 15, 43480 Vila-seca, Spain

[2] Departament de Física, ESEIAAT, Universitat Politècnica de Catalunya · BarcelonaTech (UPC), Colom 1, 08222 Terrassa, Spain

[3] Servei Meteorològic de Catalunya, Berlín 38-46, 08029 Barcelona, Spain

[4] Departament de Física, ETSEIB, Universitat Politècnica de Catalunya · BarcelonaTech (UPC), Diagonal 647, 08028 Barcelona, Spain

[5] Departament de Física Aplicada, Facultat de Física, Universitat de Barcelona (UB), Martí i Franqués 1, 08028 Barcelona, Spain

[6] Observatori de l'Ebre, Terra Alta 38, 43520 Roquetes, Spain

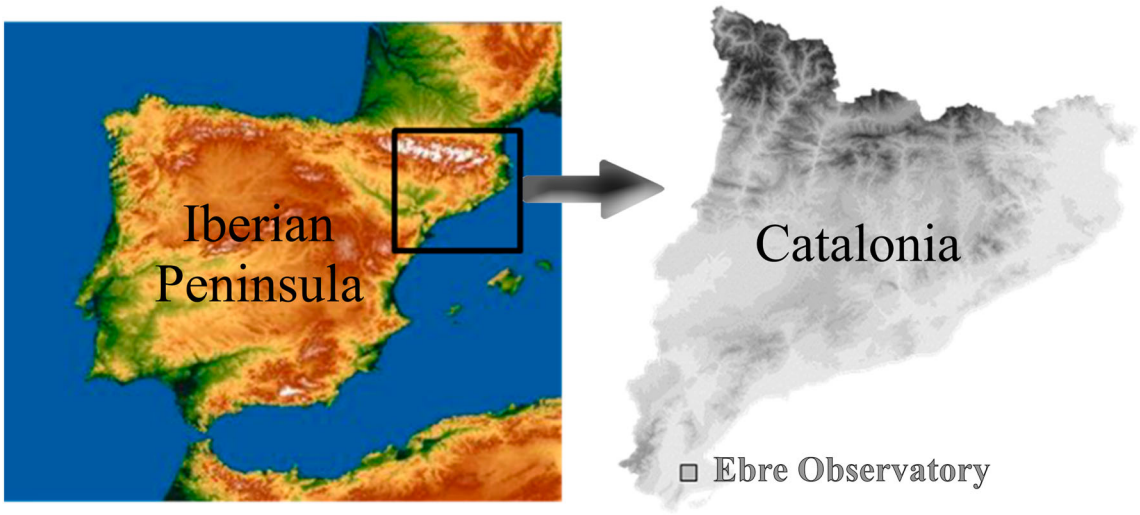

Fig. 1 Geographical location of the Ebre Observatory

in base of their different temporal organizations. Some studies obtained classifications of extreme rain events registered at several locations of the Eastern seaside area of Catalonia, as Casas et al. (2004, 2010) who analyzed a selection of intense storms registered in the Fabra Observatory of Barcelona between 1927 and 1992 by a Jardí gauge, and by the urban rain gauge network of this city between 1994 and 2001, and Pérez-Zanón et al. (2015) who obtained the classification of severe storms from an almost centennial rainfall register (1905–2003) of the Ebre Observatory near Tortosa (Tarragona). In both cases, the selected storms resulted classified by cluster analysis in four groups, attending on their temporal characteristics: microscale, mesoscale, synoptic scale, and a fourth group of complex events. This last group showed high rainfall rates for a large temporal range associated with phenomena of different scales acting together, for instance, mesoscale organizations embedded into synoptic systems, situation that usually produce extremely intense rainfall and occasionally flooding.

The degree of severity or exceptionality of an extreme rainfall event is usually quantified in terms of the total amount of water collected in a given period of time. Thus, this period of time is commonly chosen depending on the geomorphological characteristics of the catchment area to determine, for instance, the time of concentration and response to exceptional rainfall in this particular area. Casas et al. (2004) suggested an intensity weighted index (IP) to establish an objective method of classification based on the rain amounts exceptionality for four representative durations of the characteristic scales of atmospheric motion: 5 min, 1, 2, and 24 h, representing microscale weather phenomena, meso-γ, meso-β, and synoptic scale, respectively (Thunis and Bornstein 1996). This index IP is useful to provide a single measure of the rainfall severity from a meteorological point of view, regardless of the consequences in a particular type of watershed. The index IP was applied by Pérez-Zanón et al. (2015) to quantify the degree of exceptionality of the high intense episodes recorded in the Ebre Observatory.

Multivariate analysis techniques are extensively used to find relationships between atmospheric circulation patterns and exceptional meteorological events, such as very intense rain (Vicente-Serrano et al. 2009; Martínez et al. 2008; Martín-Vide et al. 2008; Houssos et al. 2008). A methodology based on cluster analysis (CA) and principal component analysis (PCA) was employed by Peña et al. (2011) to get a catalogue of synoptic patterns to explain the strong wind episodes in Catalonia, and by Aran et al. (2011) to characterize the typical meteorological conditions producing hailstorms on the inland Catalonian area of the Lleida plain. In the present work, this methodology has been applied to the selection of exceptional storms registered in the Ebre Observatory between 1905 and 2003, to identify the synoptic patterns contributing to the generation of such extreme rainfall events in this area.

Previous work

Rainfall data used in this study were obtained from the digitalized records of two siphon gauges situated in the Ebre Observatory (Fig. 2) between 1905 and 2003, with an interruption from April 4, 1938, to May 1, 1939 due to the Spanish civil war.

After a frequency analysis performed on the maximum rain amounts for 16 different durations (5, 10, 15, 20, 25, 30, 35, 40, 45, 50, 55, and 60 min, and 2, 6, 12, and 24 h), Pérez-Zanón et al. (2015) calculated the intensity–

Fig. 2 Location of recording rain gauges at the Ebre Observatory

duration–frequency (IDF) curves for the Ebre Observatory. According to those IDF curves, Pérez-Zanón et al. (2015) analyzed and classified a selection of 28 rainfall events with amounts exceeding the ID curve corresponding to 10 years of return period for any of the considered time intervals.

These 28 selected events were studied by Pérez-Zanón et al. (2015) to analyze the prevailing meteorological time scales involved and were classified using a cluster analysis in four Rainfall Intensity Groups (RIG): a first group (I) of microscale or highly local episodes, with a clear diurnal cycle and seasonal influence, a second group (II) of the events showing intense rainfall for mesoscale durations, a third group (III) of synoptic rainfall events, and a fourth group (IV) of complex episodes showing high intensities for a large time range, indicating that different scale meteorological processes have contributed together to produce precipitation. The values of the IP index measuring the degree of complexity of these events were also calculated.

Objective of the present work

The aim of the present study is to obtain a classification of the synoptic patterns related to extreme rain events registered in the Ebre Observatory (1905–2003) taking their meteorological time scales into consideration to better understand high intense rainfall intensity events in the south of Catalonia and their possible forecasting in the future. By applying multivariate analysis, it is desired to obtain the synoptic patterns associated with these extreme events and study their link to the four RIG groups (I, II, III, and IV) to characterize the prevailing meteorological conditions favouring the different kind of heavy rainfall episodes in the area.

Compared to similar studies, the present work is providing two novelties: the first is related to the identification of the precipitation episode according to its meteorological time scale, while the second is the methodology followed to obtain the synoptic patterns; a multivariate analysis taking into account the main dynamic and thermodynamic atmospheric processes giving rise to rainfall.

Data

For the 28 extreme episodes with a return period not less than 10 years for any duration from 5 min to 24 h registered in the Ebre Observatory between 1905 and 2003 (Pérez-Zanón et al. 2015), the synoptic patterns were determined from the daily grids of the mean sea-level pressure (SLP), temperature at 500 hPa (T_{500}) and geopotential at 500 hPa (Z_{500}), obtained from the twentieth century V2 Reanalysis Project (20CRP, Compo et al. 2011), extending the time coverage of the NCEP/NCAR Reanalysis Project (Kalnay et al. 1996). The 20CRP produces reanalyzes of weather maps with a horizontal spatial resolution of 2° from 1871 onwards.

Methods

The synoptic patterns have been obtained by a multivariable analysis based on three steps: PCA, CA, and discriminant analysis (DA), applied to three atmospheric levels (SLP, T_{500}, and Z_{500}) to detect the principal dynamic and thermodynamic atmospheric processes (Fig. 3). The variables employed are the daily anomalies of SLP, Z_{500}, and T_{500} (aSLP, aZ_{500}, and aT_{500}), corrected each grid point by the squared root of the latitude.

Principal component analysis

The use of PCA for classifying synoptic patterns is twofold (Huth et al. 2008). In our analysis, PCA has been employed for the reduction of the variables dimension. This procedure has been performed on every third data set by the use

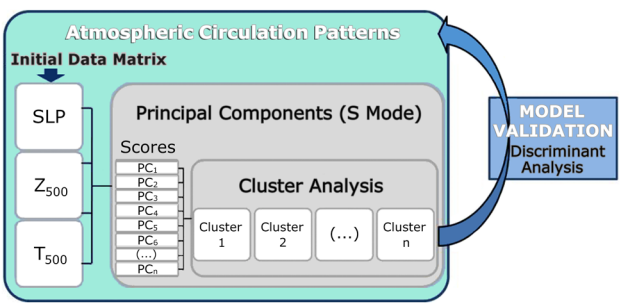

Fig. 3 Scheme of the different multivariable analysis methodologies applied

of an S-mode data matrix, with grid points as variables and observations as days. Both the correlation matrix and the Scree test have been employed to identify the principal components (Huth 1996; Cattell 1966). The Orthogonal Varimax procedure has been applied to rotate the components for minimizing the number of variables which have high factorial loadings (Richman 1986).

Cluster analysis

The main synoptic patterns in relationship with heavy rainfall were detected using the non-hierarchical K-means technique performed on the matrix built by the individual factor scores matrix resulting from the PCA. For using this algorithm, the number of groups to obtain has to be defined beforehand. Despite different techniques were developed for other authors (Tibshirani et al. 2001; Jain 2010; Debatty et al. 2014), the election of the number clusters is still quite subjective. For this study, the "elbow method" was applied, which is based in choosing a number clusters, so that adding another cluster, the data would not be significantly better explained. Different parameters could be used to decide the number of initial clusters: the variance explained by clusters against the number of clusters (Thorndike 1953) or, the selected parameter for the present study, sum of squares (SSD) within clusters (Aran et al. 2011; Zhang et al. 2016).

To determine the proper number of clusters to classify the extreme rain events spatial configuration, the next steps have been followed. First, the SSD for different number of clusters (from 1 to 28 in this case) considered are obtained by applying Ward method. The Ward method is similar to K-means (minimize SSD); however, it does not need a initial number of clusters. The graphical representation of SSD in front of the number of cluster considered allows to apply the elbow method to select the number of clusters: it corresponds to the position in which the highest change in the slope is found. This number of clusters will be initially used on the K-means to define the groups (Aran et al. 2011).

Discriminant analysis

DA has been applied as a validation of the model and for re-classifying the bordering events (Fernandez 2002; Michailidou et al. 2009). Since predefined classes are needed to perform a categorization by DA (Sioutas and Flocas 2003), the previous classification obtained from CA has been taken into account. Thus, the CA step has been used as a predictor for DA, that is, a CA specific group has been assigned to each day of the factor scores matrix of DA. Then, the discriminant functions, useful to re-classify new data, have been obtained by applying the Wilks' lambda criterion (Diab et al. 1991).

Synoptic patterns related to RIG composites

To characterize the spatial configuration of the state of the atmosphere for each RIG, composites have been obtained. Thus, the mean value of each grid point has been computed for the days belonging to each RIG for SLP, $T_{500,}$ and Z_{500}. The spatial configuration of the synoptic patterns and the composites has been compared by the Pearson Product Moment correlation coefficient applied to SLP fields.

Results

The synoptic patterns characterizing the atmosphere during the 28 extreme rainfall events have been obtained. The PCA applied to individual variables gives a reduction of seven components to explain SLP, nine in the case of $T_{500,}$ and six for Z_{500}. From the CA, seven clusters have been determined as the number of clusters necessaries to characterize the state of the atmosphere during these events. However, when applying DA, the number of clusters decreases to 5 due to the redistribution of the events in the group: at the beginning (after DA), the number of clusters were 6 (8) in the synoptic type 1, 1 (0) in the synoptic type 2, 2 (2) in type 3, 11 (12) in type 4, 5 (4) in type 5, 2 (2) in type 6, and 1 (0) in synoptic type 7. Thus, synoptic type 2 and 7, which originally had 1 event, disappeared.

After determining RIG composites, the correlation analysis was computed between them and the synoptic patterns (see Table 1 and Figs. 4, 5, 6, 7, 8). The highest correlation for RIG I is 0.89 with synoptic type 4. As it was described by Pérez-Zanón et al. (2015), this group is indicative of highly local or microscale rain episodes, characteristics of the late summer and fall with a clear diurnal surface heating effect involved in their convective development, since all them occurred after midday. The IP is low–medium index for this group, with values less than

Table 1 Correlation coefficients of Pearson between the composites of the Rainfall Intensity Group (RIG) and the synoptic patterns computed from the multivariable analysis

RIG	IP range	Synoptic pattern	Correlation
I	0.55–0.80	4	0.89
IIA	0.64–0.86	5	0.91
IIB	0.74–1.02	6	0.77
III	0.48–0.75	3	0.33
IV	1.26–1.62	1	0.79

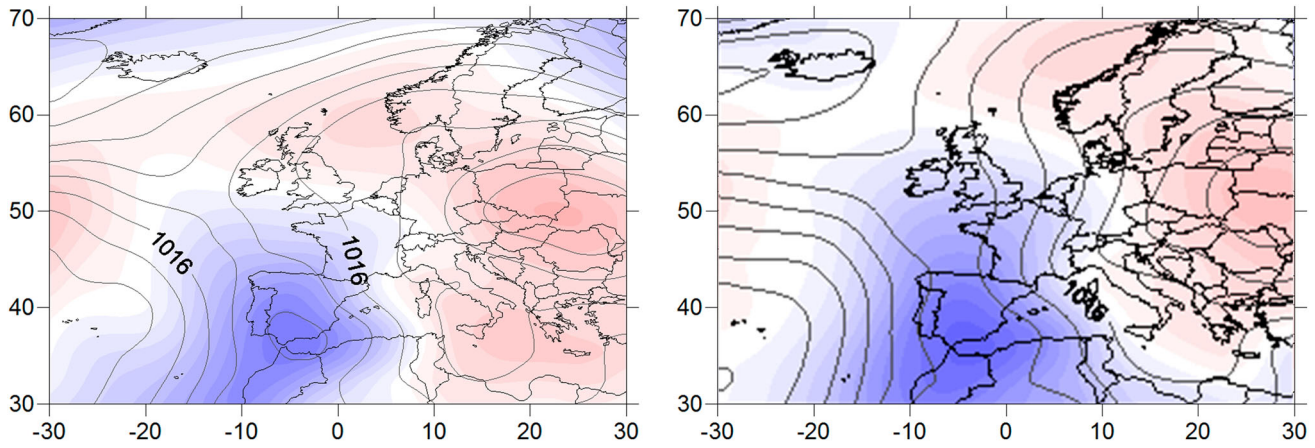

Fig. 4 Composites of RIG I (left) and the maximum correlated synoptic type 4 (right). Lines represent SLP (hPa), while colored areas are aSLP with blue (red) colors represent negative (positive) anomalies. The synoptic configuration promotes precipitation in south Catalonia due to the SE flux linked to pressure and geopotential negative anomalies over the west of the Iberian Peninsula

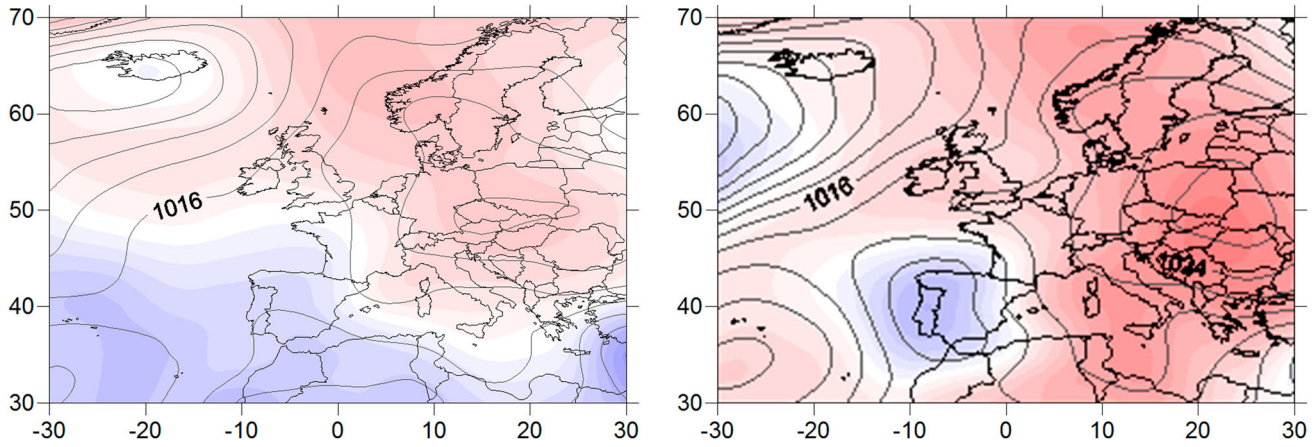

Fig. 5 Composites of RIG IIA (left) and the maximum correlated synoptic type 5 (right). Lines represent SLP (hPa), while colored areas are aSLP with blue (red) colors represent negative (positive) anomalies. The synoptic configuration is related to the cut-off low-pressure system with cold air in the middle levels of the troposphere promoting instability and the occurrence of severe thunderstorms

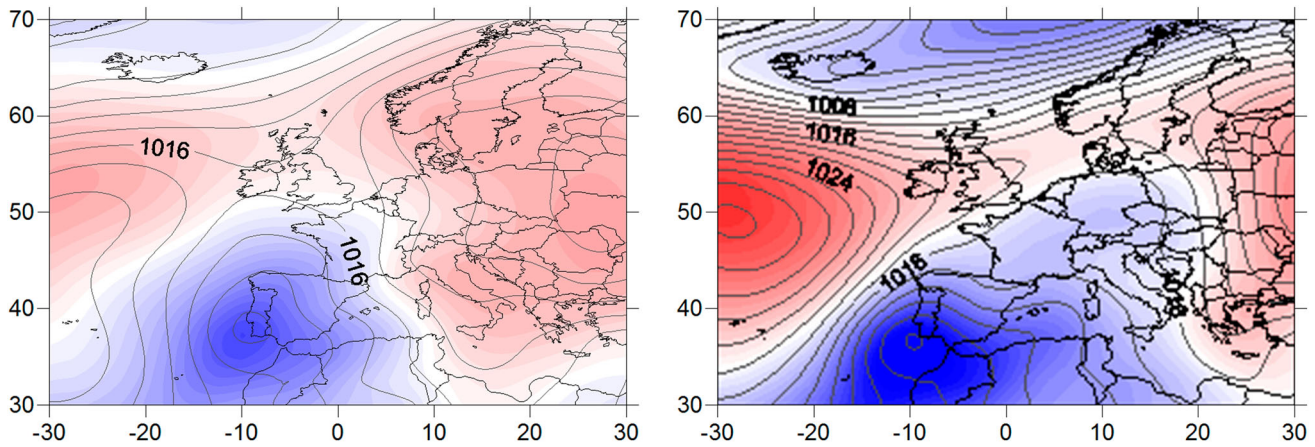

Fig. 6 Composites of RIG IIB (left) and the maximum correlated synoptic type 6 (right). Lines represent SLP (hPa), while colored areas are aSLP with blue (red) colors represent negative (positive) anomalies. The synoptic configuration promotes precipitation in south Catalonia due to the east flux linked to pressure and geopotential negative anomalies over the Mediterranean area

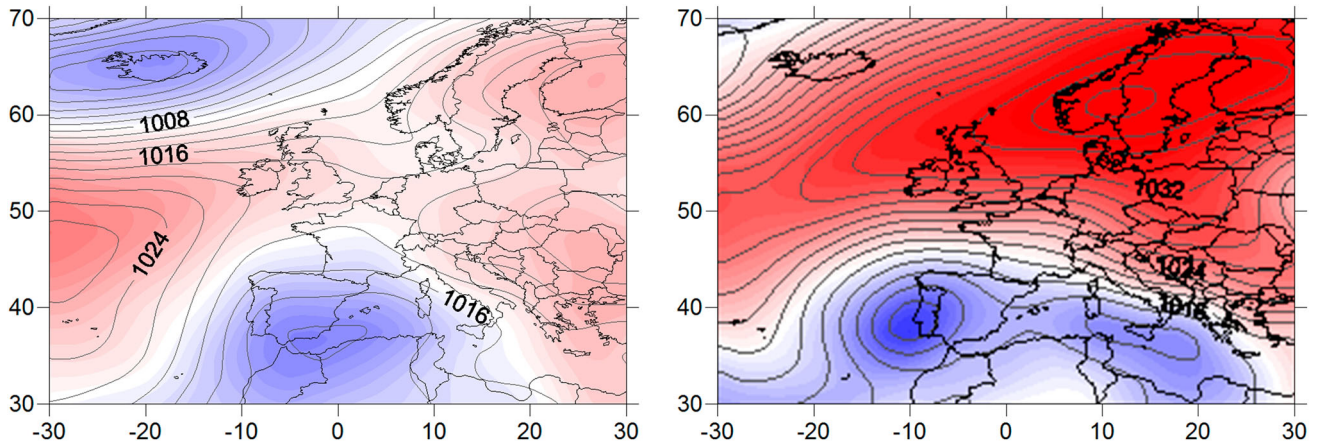

Fig. 7 Composites of RIG III (left) and the maximum correlated synoptic type 3 (right). Lines represent SLP (hPa), while colored areas are aSLP with blue (red) colors represent negative (positive) anomalies. The synoptic configuration promotes precipitation in south Catalonia due to the east flux linked to pressure and geopotential negative anomalies over the Mediterranean area

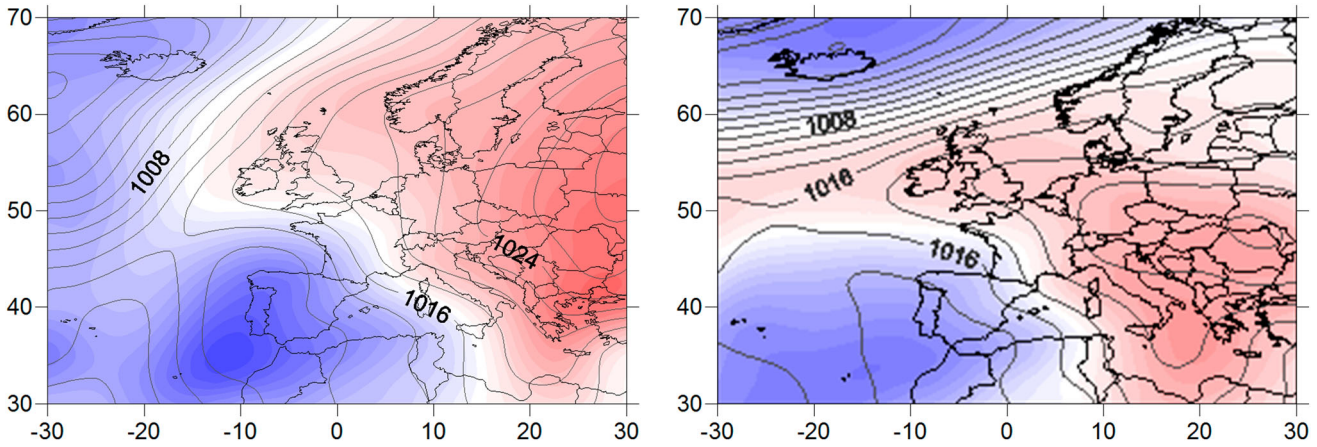

Fig. 8 Composites of RIG IV (left) and the maximum correlated synoptic type 1 (right). Lines represent SLP (hPa), while colored areas are aSLP with blue (red) colors represent negative (positive) anomalies. The synoptic configuration promotes precipitation in south Catalonia due to the SE flux linked to pressure and geopotential negative anomalies over the Iberian Peninsula

1. The synoptic configuration promotes the precipitation in Catalonia due to the south-east flux linked with pressure and geopotential negative anomalies over the west of the Iberian Peninsula. The conjunction of wet and warm low flow from the Mediterranean Sea with cold air in the middle levels of the troposphere promotes atmospheric instability and the occurrence of thunderstorms.

The maximum correlation of RIG IIA has been 0.91 with synoptic type 5. The four events grouped as IIA showed high intensities until 35–60 min and were identified by Pérez-Zanón et al. (2015) as meso-γ-scale convective systems, at the edge of microscale. The IP is medium index, with values between 0.64 and 0.86. The synoptic configuration promotes the precipitation in Catalonia due to the south flow linked with pressure and geopotential negative anomalies over the Iberian Peninsula. The cut-off low-pressure system with cold air in middle levels promotes instability and the occurrence of severe thunderstorms.

The second division of group II, as it also characterizes mesoscale phenomena, RIG IIB has maximum correlation (0.77) with synoptic type 6. It presents high intensities for 12–24 h what is linked to meso-α and meso-β scales, typically in relationship with very dynamic Atlantic fronts moving slowly with strong mesoscale rain systems embedded (Pérez-Zanón et al. 2015). The IP shows a medium–high index, with values between 0.74 and 1.02. The synoptic configuration promotes the precipitation in Catalonia due to the east flow linked with pressure and geopotential negative anomalies over the Mediterranean area. The intense flow of east or south-eastern linked to this configuration with the anomalies of geopotential and temperature in middle levels stimulates intense thunderstorms,

and a stagnation of this situation can cause long-lasting rainfall episodes.

RIG III, which shows a maximum correlation of 0.33 with synoptic type 3, corresponds to synoptic rain events, whose intensity is higher than the 10-year return period level for durations longer than 9 h. In this case, the IP is a low index, with values between 0.48 and 0.75. The synoptic configuration promotes the precipitation in Catalonia due to the east flow linked with pressure and geopotential negative anomalies over the Mediterranean area. The flow of east linked to this configuration with the anomalies of geopotential and temperature in the middle levels of the troposphere provoke rainfall in Catalonia: advective and long-largest rainfall with low intensities.

Finally, the RIG IV has a correlation of 0.79 with synoptic type 1. This RIG is associated with the most intricate storms, showing the combined action of processes corresponding to several meteorological scales. This kind of complex events is usually constituted by synoptic situations causing large-scale rain simultaneously to mesoscale convective systems producing extremely intense rainfall, with even embedded smaller convective cells. These episodes are the main cause of flooding in the area. The IP shows a high index, with values between 1.26 and 1.62. The synoptic configuration promotes the precipitation in Catalonia due to the south-east flow linked with pressure and geopotential negative anomalies over the Iberian Peninsula. The flow of south-east (warm and wet) provokes long-lasting rainfall in Catalonia. This rainfall may be both convective due to the high degree of the tropospheric instability and advective due to the anticyclonic blocking, which prevents the progress of the low-pressure center to the east.

Discussion

Regarding similar studies, the analysis made provides two novelties: the first is related to the identification of the extreme precipitation episodes, while the second is the methodology to obtain the synoptic patterns associated with.

A precipitation event is usually defined as extreme when it exceeds a certain threshold of cumulative precipitation. However, different criteria are used to define this threshold (for more information, see Merino et al. 2017). In the present study, a return period of 10 years was used as threshold in the selection of the extreme rainfall episodes registered in the Ebre Observatory between 1905 and 2003 (Pérez-Zanón et al. 2015), classified in RIGs after taken into consideration their meteorological time scales. Then, the multivariate analysis in three steps (PCA, CA, and DA) has been carried out to obtain the specific synoptic patterns associated with the RIGs. This analysis has been performed on three atmospheric levels (SLP, $T_{500,}$ and Z_{500}) to detect the principal dynamic and thermodynamic atmospheric processes related to intense rainfall generation. Furthermore, this technique can be used to re-classify new data (Aran et al. 2011; Peña et al. 2011).

The results show that the methodology used has been useful to obtain the synoptic patterns related to the four RIG groups (I, II, III, and IV), to better understand high intense rain intensity episodes in the south of Catalonia and their forecasting in the future. The prevailing synoptic conditions that favour heavy rainfall in this area have shown a good correspondence with the RIG classification.

The synoptic patterns are characterized by low-pressure systems that interact with the Mediterranean warm-air mass promoting the destabilization the atmosphere. The atmospheric configuration in Z_{500} (Fig. 9) is dominated by negative anomalies of geopotential and temperature, showing the presence of a low-pressure center or an Atlantic cold front (Casas et al. 2004, 2010; Pérez-Zanón et al. 2015). These types of configurations enhance the occurrence of convective events due to the difference of temperature between T_{500} and T_{850} (warm air from the Mediterranean Sea and negative anomalies of temperature in middle levels) and the humidity input in the lowest levels of the atmosphere. Furthermore, the presence of a high-pressure system over Europe can provoke a stagnation of the synoptic situation causing long-lasting rain over the studied area.

Two different types of heavy rain can affect the lower part of the Ebre basin (Merino et al. 2017): (1) advective precipitations during winter and spring with low or medium convectivity linked to a zonal disposition of the synoptic configuration, producing heavy accumulated precipitation over several days and (2) the extremely convective summer and autumn storms are linked to the cyclones that become more intense over the Mediterranean Sea, producing long-lasting and intense rain due to the Mediterranean warm-air mass, the orographic uplift of the air mass, and the instability produced by negative anomalies of geopotential height at the middle levels of the troposphere (Peña et al. 2015).

Flood represents a high natural hazard for mid-latitude Mediterranean regions (Llasat et al. 2013); therefore, the precipitation rate behaviour must be contemplated for designing hydraulic works, and evaluate natural risk due to eventual extreme rain events (Casas et al. 2004, 2010; Beguería et al. 2011; Pérez-Zanón et al. 2015; Merino et al. 2017; Rodríguez-Solà et al. 2017). Particularly, in the south of Catalonia, heavy precipitation is normally connected with peak discharges measured in Tortosa (MAGRAMA 2015), located in the lower part of the Ebre basin, near of Ebre Observatory (Ruiz-Bellet et al. 2015). Two types of

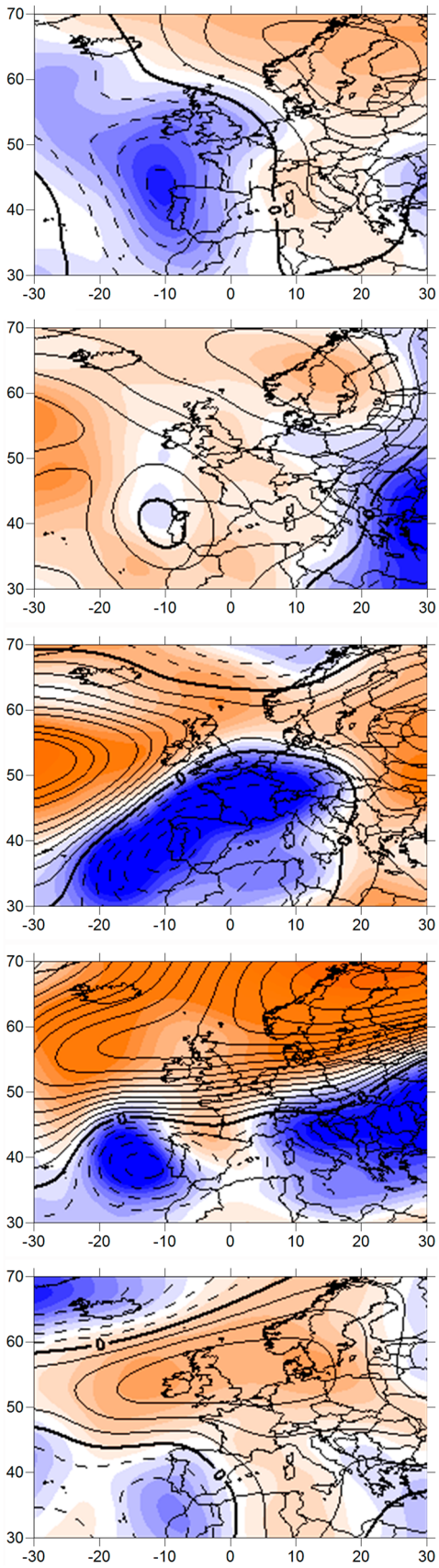

◀**Fig. 9** Composites of the synoptic patterns 4, 5, 6, 3, and 1 (up to down) for 500 hPa. Lines represents aZ_{500} (m) and colored areas are aT_{500} (0 °C) with blue (red) colors represent negative (positive) anomalies

behaviour within the flood series are detected in several analyses (Mazon et al. 2014; Ruiz-Bellet et al. 2015; Pino et al. 2016). The differences are linked to the two types of rainstorms. A more frequent behaviour related to flat-peak discharges might be caused by winter and spring advective rainfall of low or medium convectivity, while a less frequent one associated with high-peak discharges might be caused by highly convective summer and autumn storms. Therefore, extreme hydrological events in the Ebre basin seem to be controlled by the atmospheric dynamics acting both in the Mediterranean area (high-convectivity rainfall) and in the North Atlantic (long-lasting and advective rainfall). The most important flood events are a combination of the two atmospheric process and is related to the RIG group number IV (IP > 1.25). The main characteristics of the synoptic patterns corresponding to this complex rain episodes (14% of the investigated cases) are the existence of an Atlantic depression at the south-west of the Iberian Peninsula and a strong blocking anticyclone over Europe (Casas et al. 2004, 2010; Pérez-Zanón et al. 2015). In these situations, there is usually a moist and warm advective flow from the Mediterranean Sea, since the predominant wind over Catalonia is from the south-east both at 850 hPa and on the surface. These atmospheric configurations cause long-lasting advective rain while simultaneously convective phenomena associated with the south-east warm flow in low levels produce extremely intense precipitation (Peña et al. 2015; Pérez-Zanón et al. 2015).

It is important to remark that trends of extreme rainfall records over the twenty-first century are nowadays one of the most interesting topics in climate change studies (Beguería et al. 2011). The spatial and time analysis of precipitation data is a relevant research for a better understanding and prevention of the possible effects of climate change in rainfall extremes.

Conclusions

The multivariate analyses have been a success to identify the main features to detect of the main dynamic and thermodynamic atmospheric processes. The synoptic patterns, which characterize the origin of the extreme rainfall in the Observatori de l'Ebre, have been found by a multivariate analysis applied independently to three atmospheric variables over the European sector. Therefore, the synoptic

patterns, in addition to being able to characterize the spatial configuration of the atmosphere, capture differences in the intensity and temporal distribution at local scale of the rain.

The synoptic patterns associated with severe rain in southern Catalonia are featured by low-pressure systems advecting wet and warm air from the Mediterranean Sea in the low levels of the atmosphere. The most predominant flow is from south-east, followed by the east. The configuration in the middle levels of the troposphere is dominated by negative anomalies of geopotential, indicating the presence of a low or a cold front, and temperature anomalies, promoting the destabilization of the atmosphere. These types of configurations promote the occurrence of severe convective events due to the difference of temperature between the two levels analyzed (warm air from the Mediterranean Sea and negative anomalies of temperature at middle levels) and the humidity contribution in the lowest levels. Furthermore, the presence of a blocking high-pressure system over Europe can cause the stagnation of the synoptic configuration and produce long-lasting precipitation.

Acknowledgements We are grateful to the Meteorological Service of Catalonia, the Ebre Observatory, the DOE INCITE project, BER and NOAA.

Compliance with ethical standards

Conflict of interest On behalf of all authors, the corresponding author states that there is no conflict of interest.

References

Aran M, Peña JC, Torà M (2011) Atmospheric circulation patterns associated with hail events in Lleida (Catalonia). Atmos Res 100(4):428–438. https://doi.org/10.1016/j.atmosres.2010.10.029

Beguería S, Angulo-Martínez M, Vicente-Serrano SM, López-Moreno JL, El-Kenawy A (2011) Assessing trends in extreme precipitation events intensity and magnitude using non-stationary peaks-over-threshold analysis: a case study in northeast Spain from 1930 to 2006. Int J Climatol 31:2102–2114. https://doi.org/10.1002/joc.2218

Casas MC, Codina B, Redaño A, Lorente J (2004) A methodology to classify extreme rainfall events in the western Mediterranean area. Theor Appl Climatol 77:139–150. https://doi.org/10.1007/s00704-003-0003-x

Casas MC, Rodríguez R, Redaño A (2010) Analysis of extreme rainfall in Barcelona using a microscale rain gauge network. Meteorol Appl 17:117–123. https://doi.org/10.1002/met.166

Cattell RB (1966) The scree test for the number of the factors. Multivar Behav Res 1:245–276

Compo GP, Whitaker JS, Sardeshmukh PD, Matsui N, Allan RJ, Yin X, Gleason BE, Vose RS, Rutledge G, Bessemoulin P, Brönnimann S, Brunet M, Crouthamel RI, Grant AN, Groisman PY, Jones PD, Kruk MC, Kruger AC, Marshall GJ, Maugeri M, Mok HY, Nordli Ø, Ross TF, Trigo RM, Wang XL, Woodruff SD, Worley SJ (2011) The twentieth century reanalysis project. Q J R Meteorol Soc 137:1–28. https://doi.org/10.1002/qj.776

Debatty T, Michiardi P, Mees W, Thonnard O (2014) Determining the k in k-means with MapReduce. EDBT/ICDT Workshops, pp 19–28

Diab RD, Preston-Whyte RA, Washington R (1991) Distribution of rainfall by synoptic type over Natal, South Africa. Int J Climatol 11(8):877–888

Fernandez GC (2002) Discriminant analysis, a powerful classification technique in data mining. In: Proceedings of the SAS users international conference, pp 247–256

Houssos EE, Lolis CJ, Bartzokas A (2008) Atmospheric circulation patterns associated with extreme precipitation amounts in Greece. Adv Geosci 6:5–11. https://doi.org/10.5194/adgeo-17-5-2008

Huth R (1996) Properties of the circulation classification scheme based on the rotated principal component analysis. Meteorol Atmos Phys 59:217–233

Huth R, Beck C, Philipp A, Demuzere M, Ustrnul Z, Cahynová M, Kyselý J, Tveito OE (2008) Classifications of atmospheric circulation patterns. Recent advances and applications. trends and directions in climate research. Ann N Y Acad Sci 1146:105–152. https://doi.org/10.1196/annals.1446.019

Jain AK (2010) Data clustering: 50 years beyond K-means. Pattern Recognit Lett 31(8):651–666. https://doi.org/10.1016/j.patrec.2009.09.011

Kalnay E, Kanamitsu M, Kistler R, Collins W, Deaven D, Gandin L, Iredell M, Saha S, White G, Woollen J, Zhu Y, Leetmaa A, Reynolds B, Chelliah M, Ebisuzaki W, Higgins W, Janowiak J, Mo KC, Ropelewski C, Wang J, Jenne R, Joseph D (1996) The NCEP/NCAR 40-year reanalysis project. Bull Am Meteorol Soc 77(3):437–472. https://doi.org/10.1175/1520-0477(1996)077<0437:tnyrp>2.0.co;2

Llasat MC, Llasat-Botija M, Petrucci O, Pasqua AA, Rossello J, Vinet F, Boissier L (2013) Towards a database on societal impact of Mediterranean floods within the framework of the HYMEX project. Nat Hazards Earth Syst Sci 13(5):1337–1350. https://doi.org/10.5194/nhess-13-1337-013

Lorente J, Redaño A (1990) Rainfall rate distribution in a local scale: the case of Barcelona City. Theor Appl Climatol 41:23–32. https://doi.org/10.1007/BF00866199

MAGRAMA (2015) Ministerio de Agricultura, Alimentación y Medio Ambiente: Anuario de aforos. http://sig.magrama.es/aforos/visor.html. Accessed: 18 Nov 2015

Martín-Vide J, Sánchez-Lorenzo A, López-Bustins JA, Cordobilla MJ, García-Manuel A, Raso JM (2008) Torrential rainfall in northeast of the Iberian Peninsula: synoptic patterns and WeMO influence. Adv Sci Res 2:99–105

Martínez C, Campins J, Jansà A, Genovès A (2008) Heavy rain events in the Western Mediterranean: an atmospheric pattern classification. Adv Sci Res 2:61–64. https://doi.org/10.5194/asr-2-61-2008

Mazon J, Balasch JC, Barriendos M, Ruiz-Bellet JL, Pino D, Tuset J (2014) Meteorological reconstruction of major floods in early instrumental period in Catalonia (NE Iberian Peninsula). In: EMS annual meeting abstracts, 11, EMS2014–141

Merino A, Fernández-González S, García-Ortega E, Sánchez JL, López L, Gascón E (2017) Temporal continuity of extreme precipitation events using sub-daily precipitation: application to floods in the Ebro basin, northeastern Spain. Int J Climatol. https://doi.org/10.1002/joc.5302

Michailidou C, Maheras P, Arseni-Papadimititriou A, Kolyva-Machera F, Anagnostopoulou C (2009) A study of weather types at Athens and Thessaloniki and their relationship to circulation types for the cold-wet period, part II: discriminant analysis. Theor Appl Climatol 97(1–2):179–194

Peña JC, Aran M, Cunillera J, Amaro J (2011) Atmospheric circulation patterns associated with strong wind events in

Catalonia. Nat Hazards Earth Syst Sci 11:145–155. https://doi.org/10.5194/nhess-11-145-2011

Peña JC, Schulte L, Badoux A, Barriendos M, Barrera-Escoda A (2015) Influence of solar forcing, climate variability and atmospheric circulation patterns on summer floods in Switzerland. Hydrol Earth Syst Sci Discuss 11:13843–13890. https://doi.org/10.5194/hessd-11-13843-2014

Pérez-Zanón N, Casas-Castillo MC, Rodríguez-Solà R, Peña JC, Rius A, Solé JG, Redaño A (2015) Analysis of extreme rainfall in the Ebre Observatory (Spain). Theor Appl Climatol 124(3–4):935–944. https://doi.org/10.1007/s00704-015-1476-0

Pino D, Ruiz-Bellet JL, Balasch JC, Romero-León L, Tuset J, Barriendos M, Mazon J, Castelltort X (2016) Meteorological and hydrological analysis of major floods in NE Iberian Peninsula. J Hydrol 541:63–89. https://doi.org/10.1016/j.jhydrol.2016.02.008

Richman MB (1986) Rotation of principal components. J Climatol 6:293–335

Rodríguez-Solà R, Casas-Castillo MC, Navarro X, Redaño A (2017) A study of the scaling properties of rainfall in Spain and its appropriateness to generate intensity-duration-frequency curves from daily records. Int J Climatol 37(2):770–780. https://doi.org/10.1002/joc.4738. http://hdl.handle.net/2117/87312

Ruiz-Bellet JL, Balasch JC, Tuset J, Monserrate A, Sánchez A (2015) Improvement of flood frequency analysis with historical information in different types of catchments and data series within the Ebro River basin (NE Iberian Peninsula). Z Geomorphol Suppl Issues 59(3):127–157. https://doi.org/10.1127/zfg_suppl/2015/S-59219

Sioutas MV, Flocas HA (2003) Hailstorms in Northern Greece: synoptic patterns and thermodynamic environment. Theor Appl Climatol 75:189–202

Thorndike RL (1953) Who belongs in the family? Psychometrika 18(4):267–276

Thunis P, Bornstein R (1996) Hierarchy of mesoscale flow assumptions and equations. J Atmos Sci 53(3):380–397. https://doi.org/10.1175/1520-0469(1996)053

Tibshirani R, Walther G, Hastie T (2001) Estimating the number of clusters in a data set via the gap statistic. J R Stat Soc Ser B (Stat Methodol) 63(2):411–423

Vicente-Serrano SM, Beguería S, López-Moreno JI, El Kenawy AM, Angulo M (2009) Daily atmospheric circulation events and extreme precipitation risk in the Northeast Spain: the role of the North Atlantic Oscillation, Western Mediterranean Oscillation, and Mediterranean Oscillation. J Geophys Res 114:DO8166. https://doi.org/10.1029/2008JD011492

Zhang Y, Moges S, Block P (2016) Optimal cluster analysis for objective regionalization of seasonal precipitation in regions of high spatial–temporal variability: application to Western Ethiopia. J Clim 29:3697–3717. https://doi.org/10.1175/JCLI-D-15-0582.1

Acta Geophysica (2018) 66:415–424
https://doi.org/10.1007/s11600-018-0122-5

RESEARCH ARTICLE - SPECIAL ISSUE

A single scaling parameter as a first approximation to describe the rainfall pattern of a place: application on Catalonia

M. Carmen Casas-Castillo[1] · Alba Llabrés-Brustenga[2] · Anna Rius[2] · Raúl Rodríguez-Solà[3] · Xavier Navarro[4]

Received: 8 November 2017 / Accepted: 13 February 2018 / Published online: 17 February 2018

Abstract

As well as in other natural processes, it has been frequently observed that the phenomenon arising from the rainfall generation process presents fractal self-similarity of statistical type, and thus, rainfall series generally show scaling properties. Based on this fact, there is a methodology, simple scaling, which is used quite broadly to find or reproduce the intensity–duration–frequency curves of a place. In the present work, the relationship of the simple scaling parameter with the characteristic rainfall pattern of the area of study has been investigated. The calculation of this scaling parameter has been performed from 147 daily rainfall selected series covering the temporal period between 1883 and 2016 over the Catalonian territory (Spain) and its nearby surroundings, and a discussion about the relationship between the scaling parameter spatial distribution and rainfall pattern, as well as about trends of this scaling parameter over the past decades possibly due to climate change, has been presented.

Keywords Simple scaling · Fractal analysis · Rainfall intensity · Intensity–duration–frequency curves · Climate change · Catalonia

Introduction

The intensity–duration–frequency curves (IDF curves), which have been a matter of considerable interest to engineers and hydrologists for over a century, remain nowadays as an important tool to analyze the risk of natural hazards for hydrological purposes. The mathematical relationships more often used to describe the IDF curves are empirical, sometimes in the form of a generalized equation for the rainfall intensity $I(t,T)$, valid for all durations t, and return periods T considered. This equation usually has the generalized form $\frac{a(T)}{b(t)}$, where $a(T)$ and $b(t)$ are functions independent of each other. The function $a(T)$ can be found empirically (Casas et al. 2004), although there are authors (Koutsoyiannis et al. 1998) who proposed the use of a function of statistical probability of the maximum rainfall intensity to determine it. Other authors (Burlando and Rosso 1996; Menabde et al. 1999) considered the fractal property of scale invariance of the rainfall series to find an analytical relationship for the IDF curves taking into account the scaling behavior. Burlando and Rosso (1996) were pioneers in applying scaling relationships to

✉ M. Carmen Casas-Castillo
m.carmen.casas@upc.edu

Raúl Rodríguez-Solà
raul.rodriguez@upc.edu

Xavier Navarro
javier.navarro@upc.edu

[1] Department of Physics, ESEIAAT, Universitat Politècnica de Catalunya · BarcelonaTech (UPC), Colom 1, 08222 Terrassa, Spain

[2] Servei Meteorològic de Catalunya, Berlin, 38-46, 08029 Barcelona, Spain

[3] Department of Physics, ETSEIB, Universitat Politècnica de Catalunya · BarcelonaTech (UPC), Diagonal 647, 08028 Barcelona, Spain

[4] Department of Physics, EPSEVG, Universitat Politècnica de Catalunya · BarcelonaTech (UPC), Víctor Balaguer s/n, 08800, Vilanova i la Geltrú, Barcelona, Spain

the statistical moments of the annual maximum rainfall series. There is also a methodology based on the property of scale invariance (Menabde et al. 1999; Yu et al. 2004; Desramaut 2008; Bara et al. 2010) to obtain IDF curves in those places where daily rainfall data are the only available. For instance, Aronica and Freni (2005) analyzed extreme rainfall data from a rain gauge network within the metropolitan area of Palermo (Italy) with the aim of combining and taking advantage of high-resolution rain gauges with a short working period along with low-resolution rain gauges with longer data records to obtain plausible depth-duration-frequency (DDF) curves. Applying this scaling approach, Aronica and Freni (2005) found better results than those coming from the classical sub-hourly rainfall regression formulas (Bell 1969; Ferreri and Ferro 1990). Likewise, studying the scaling properties of selected rainfall quantiles and applying this methodology, Bara et al. (2009) derived the IDF curves for durations shorter than a day, calculated from a historical data set covering the whole territory of Slovakia. In a recent paper, Rodríguez-Solà et al. (2017) used this methodology also to reproduce the well-known empirical IDF curves of three Spanish locations: Barcelona (Casas et al. 2004; Rodríguez et al. 2014), the Ebre Observatory (Pérez-Zanón et al. 2015), and Madrid (Casas-Castillo et al. 2018), taking into consideration the scaling behavior of rainfall. In addition, Rodríguez-Solà et al. (2017) obtained the IDF curves for a hundred of Spanish locations for which only daily rainfall data were available, and found a spatial distribution of the observed scaling behavior over Spain in concordance with the characteristic rainfall pattern in diverse areas. In this work, the influence of geographical location and the different mechanisms of rainfall generation in the scaling behavior has been investigated and discussed.

The simple scaling approach

Many atmospheric processes, rainfall generation among them, act in a wide temporal range giving rise to phenomena which accomplish self-similarity, i.e., that look the same regardless of the temporal scale at which they are observed. This kind of processes can be considered of fractal type, with properties manifesting power laws of the scale parameter λ, which is the ratio t/t_0 between any two durations t and t_0 within a scaling regime. In general, the fractal self-similarity of natural processes has a statistical nature; thus, the scaling properties of rainfall can be expressed by statistical relationships (Schertzer and Lovejoy 1987; Gupta and Waymire 1990; Schertzer and Lovejoy 2011). For instance, it has been widely observed (Koutsoyiannis and Foufoula-Georgiou 1993; Burlando and Rosso 1996; Menabde et al. 1999) that the probability distribution of the annual maximum rainfall intensity satisfies scale relationships, meaning that the probability distribution of the annual maximum intensity for a duration t, I_t, and the distribution at other time scale $t_0 = \lambda t$, $I_{\lambda t}$, can be related by a factor that is a power function of the scale parameter λ. This property, usually referred as "simple scaling in the strict sense" (Gupta and Waymire 1990; Yu et al. 2004), can be expressed by Eq. (1):

$$I_t \overset{\text{dist}}{=} \lambda^{\beta} I_{\lambda t} \tag{1}$$

where the symbol $\overset{dist}{=}$ indicates equality of probability distributions, and β is a scaling parameter. This equation implies that the statistical moments of these two distributions fulfill the equality, as well as their quantiles and the rest of statistical features. In terms of the statistical moments of order q of the rainfall intensity for a duration t, $\langle I_t^q \rangle$ [Eq. (2)], the scaling relationship can be expressed as Eq. (3):

$$\langle I_t^q \rangle = \frac{\sum_{i=1}^{n} I_{t_i}^q}{n} \tag{2}$$

$$\langle I_t^q \rangle = \lambda^{\beta q} \langle I_{\lambda t}^q \rangle. \tag{3}$$

The exponent βq can be considered as the linear case of a general scaling function $K(q)$, a function resulting non-linear in the multifractal case. The simplest procedure to determine the scaling parameter β from daily data is to calculate the statistical moments using Eq. (2) of maximum annual series calculated by aggregation from daily series (with rainfall amounts for 2, 3, 4… days) for different values of the order q, and perform a linear regression between the logarithmic values of these moments and the logarithm of the duration t for every value of q. The straight lines obtained, each one of them with a slope of value βq, evidence scale invariance.

The equality of the quantiles of the probability distributions of Eq. (1) implies that these quantiles may also be related by the same scaling relationship. In particular, the scaling relationship which corresponds to an extreme rainfall intensity $I(t, T)$, with a return period T, and a duration t, i.e., IDF curves, can be expressed by Eq. (4), where daily duration appears as a reference duration $t_0 = 24$ h:

$$I(t, T) = \left(\frac{t}{24}\right)^{\beta} I(24, T). \tag{4}$$

Once known the scaling parameter β, Eq. (4) can be used to downscale daily values $I(24, T)$ to IDF values for sub-daily durations t, under the assumption that the simple scaling relationship is fulfilled by sub-daily durations, which can only be considered as an approximation. Rodríguez-Solà et al. (2017) applied this technique to reproduce the well-known IDF curves of three Spanish locations, which were very satisfactorily reproduced by

downscaling daily records for durations above 1 h, with mean relative differences lower than 7%. Discrepancies between the downscaled values and the known values $I(t,T)$ for durations shorter than 1 h resulted slightly higher (around 20% in the worst cases) and seemed to depend on the kind of measuring instrument.

Because of its definition, the values of the simple scaling parameter are expected to be higher than − 1. The limit value of $\beta = -1$ would correspond to rainfall samples with isolated annual maximum values; in the case of daily rainfall, a maximum value for a specific day P_1 surrounded by dry days. Thus, the process aggregation leads to series where the precipitation for n days, P_n, is the same. Then, in terms of intensity, $I_n = I_1/n$, which corresponds to a scaling exponent of $\beta = -1$ compared to the scaling relationship for $q = 1$ (mean), $I_1/n = n^{\beta} I_1$. The opposite (and hypothetical) case would be a totally regular sample where all days (within the n-aggregation) present the same rainfall amount, which implies the same intensity for all durations, and consequently, $\beta = 0$. In real rainfall cases, the scaling parameter ranges between $\beta = -1$ and a value close to $\beta = -0.5$. It seems reasonable then to expect some relationship between the scaling parameter values and rainfall series regularity, with the lowest values close to − 1 corresponding to areas where rainfall is usually very irregular, with sudden isolated maximum values, and higher values for rainy areas with a more regular rainfall pattern. For instance, Menabde et al. (1999) compared two sets of rainfall data representing two examples of quite different climate types, and found a scaling exponent of −0.65 for Melbourne (Australia), a city with a mid-latitude temperate climate and rainfall throughout the year, and a value of − 0.76 for Warmbaths (South Africa), having a semiarid climate with summer convective rainfall, and concluded that the scaling exponent appears to be dependent on the rainfall/climate characteristics. In addition, Bara et al. (2009) found scaling exponents around − 0.75 for three locations representing the western (Kuchyňa–Nový Dvor), central (Liptovský Hrádok), and eastern (Humenné) areas of Slovakia, and Yu et al. (2004) found three types of rainfall scaling behavior over northern Taiwan, related to the change in topography and the influence of the northeast monsoon. Rodríguez-Solà et al. (2017) found a general concordance between the spatial distribution of β over the Iberian Peninsula and the mean annual precipitation distribution, with high values between − 0.55 and − 0.66 in rainy areas and low between − 0.84 and − 0.92 for the dry ones, with some discrepancies related to the kind of precipitation contributing to high rainfall amounts and the proportion of convective rainfall in total. In particular for Catalonia, Rodríguez-Solà et al. (2017) assigned a range of the scaling parameter between − 0.77 and − 0.83, based on the analysis of series from few stations located in this area. To investigate, in more detail for this area, the influence of geographical location and the different mechanisms of rainfall generation in the scaling behavior, a new calculation of the simple scaling parameter has been performed in this work from 147 daily rainfall series registered in the Catalonian territory (Spain) and surroundings, and a spatial distribution of its values has been presented and analyzed.

Rainfall series scaling analysis

The scaling analysis presented has been performed from the available rainfall database of the Servei Meteorològic de Catalunya (SMC) after a rigorous quality control based on a relative comparison between daily values measured at candidate stations and selected reference stations according to their distance, difference in elevation and daily correlation. Previously to the daily comparison, each series had been classified according to its absolute quality by an index which was designed to take into consideration the most common problems that daily rainfall series could present (errors from the digitization process, encoding errors, etc.). In this way, the daily comparison is performed selecting series of initially very probable high quality, when available. Figure 1 shows the temporal evolution of the number of series available from the SMC database (2142 in total). In this figure, blue line indicates a first selection of high-quality series (1817) which accomplished a completeness of 100% and less than 5% of data errors detected. Among the latter, the most restrictive black line corresponds to those series with length longer than 30 years of high-quality data, which are the 147 series used in the present work. These 147 daily selected series cover the whole Catalonian territory and its nearby surroundings during the temporal period between 1883 and 2016, with a higher density of measuring sites (over 50 series used per year) in the period 1942–2006. The whole set has a mean of 45.8 years of data per series.

By aggregation from the selected daily data, series of annual maximum of accumulated rainfall on 1–15 days have been obtained and analyzed. The q order statistical moments of rainfall intensities have been calculated [Eq. (2)] for values of q of 0.5, 1, 1.5, 2, 2.5 and 3, and a linear regression between their logarithmic values and the logarithm of the duration t has been performed for every value of q with the aim to evidence scale invariance and to find the value of the scaling parameter β in every case. The empirical β values found in this study range between − 0.87 and − 0.65 for Catalonia and they have been spatially analyzed to obtain its dependence to geographical and climatic features.

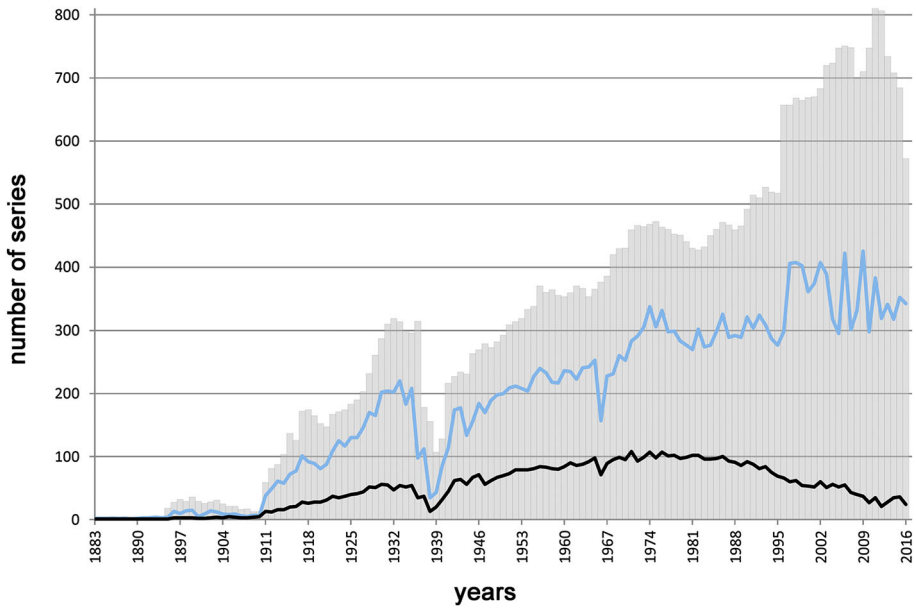

Fig. 1 Number of rainfall series over the temporal period 1883–2016. Grey bars indicate the total available series from the SMC database (2142), blue line those with high annual quality (1817), and the more restrictive black line corresponds to series used in the present work (147)

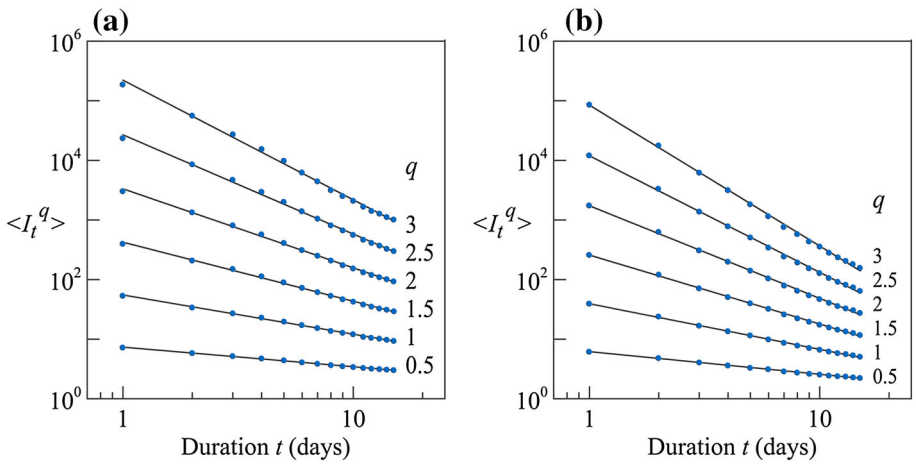

Fig. 2 Statistical moments for different values of q of the annual maximum intensity calculated for the aggregated series from: **a** Vielha and **b** Lleida. Straight lines indicate scale invariance over a temporal range from 1 to 15 days, with slopes determining the scaling function K(q)

As an example, Fig. 2 shows the log–log plots of the statistical moments against duration corresponding to two stations: Vielha (VA010) and Lleida (SE020). These two stations have been selected, because they correspond to two different climates in Catalonia and they present quite different values of empirical β (Vielha with -0.71 and Lleida -0.83). Vielha is located in the Val d'Aran County, a part of Catalonia where the Atlantic influence dominates over the Mediterranean and its climate is characterized by a regular precipitation through the year with high accumulated total amounts. On the other hand, Lleida's climate, in Segrià County, is classified as Dry Continental Mediterranean and rainfall characteristics imply low annual amounts in an irregular pattern with seasonal maxima in spring and autumn. In Fig. 2, straight lines fitted by linear regression, each of them with a slope of value $K(q)$, indicate scaling invariance. The values of these slopes have been displayed in Fig. 3, where the linear behavior of the scaling function $K(q)$ ($-0.71\ q$ for Vielha station and $-0.83\ q$ for Lleida) shows the monofractal or simple scaling behavior of these two specific series, which is a general result for all the analyzed stations.

The empirical results found for β show a wide variability within a short distance with a standard deviation value of 0.04 for the whole territory. The observed variability might be caused by the fact that different series have a different number of years available, being the series with just 30 years more influenced by particular episodes. However, the performed spatial analysis yields a certain pattern, namely higher values mainly concentrated in the northwest. While the 90% of the empirical values range between -0.84 and -0.70 and have a mean of -0.79, there are two distinct zones which have been detected: (1) a northern area with a mean value of -0.75, matching a mountainous area with some Atlantic influence at its most northwestern end, and (2) a western area with a mean value

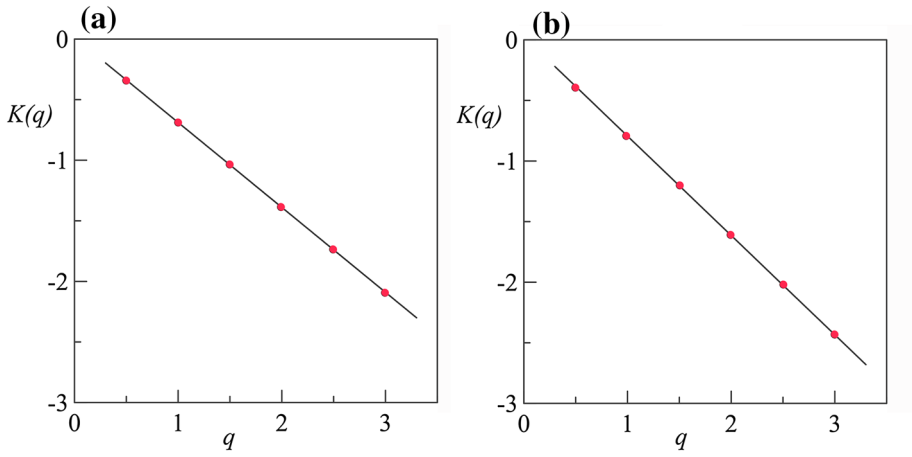

Fig. 3 Linear scaling functions K(q) for **a** Vielha (− 0.71 q) and **b** Lleida (− 0.83 q)

of β of − 0.81, in great concordance with the driest areas in Catalonia. Indeed, a statistical analysis of the values obtained in these zones, i.e., Kolmogorov–Smirnov test for two samples, shows that the northern zone (Zone N in Fig. 4) and the western zone (Zone W) come from different distributions, and hence, the samples are distinct. The different results of β values in these two distinct zones can be seen in Fig. 4 where empirical values are shown grouped in boxplots according to the detected zones.

The northern zone has higher β values at its most northwestern corner where some features of Atlantic climate are observed. In the northwestern area of Catalonia, the climate is less influenced by the Mediterranean because of its distance to the coastline and the blockage of the high mountains of the Pyrenees. Moreover, the northwestern corner is often influenced by Atlantic fronts and its climate is characterized by high amounts of rain collected regularly through the year.

On the other hand, Zone W has a climate characterized by scarce rainfall, recorded mainly during Autumn and Spring. This western dry area presents some of the lowest β values obtained over Catalonia supporting its climatic observations of irregular rainfall patterns. Not so differently from the Zone N, the Zone W is not extremely influenced by the Mediterranean, being far from the coastline, it has a more continental climate than other areas in Catalonia; the main difference with the Zone N is the dryness regarding total annual amounts and the irregularity of the rainfall pattern with two seasons where the most part of the rain is collected.

Nevertheless, the pattern of β values empirically obtained shows other areas characterized by high or low values, such as low values in the eastern coastline where the rainfall pattern is known to be irregular, but these areas are more difficult to spot because of the high variability of the empirical results. To better analyze the spatial pattern of scaling parameter and its relationship to climatic characteristics, the empirical values have been interpolated. The interpolation has been performed using a simple kriging technique through a wave exponential model to fit the variogram (see Fig. 5 for fitting details).

The spatial distribution of β after interpolation is shown in Fig. 6. The distinct zones previously discussed (namely, Zone N of high β values and Zone W of low β values) are clearly captured by the interpolation, being the distinction between the northwestern area and the western zone the most clear feature. Moreover, a third zone in the east, near the north part of Catalonia's Mediterranean coast, presents

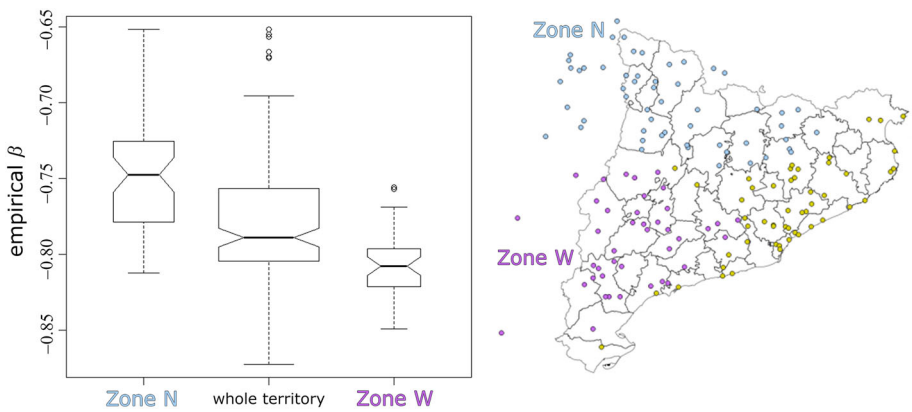

Fig. 4 Empirical values of the β parameter grouped in boxplots according to the North (Zone N) and West (Zone W) of Catalonia

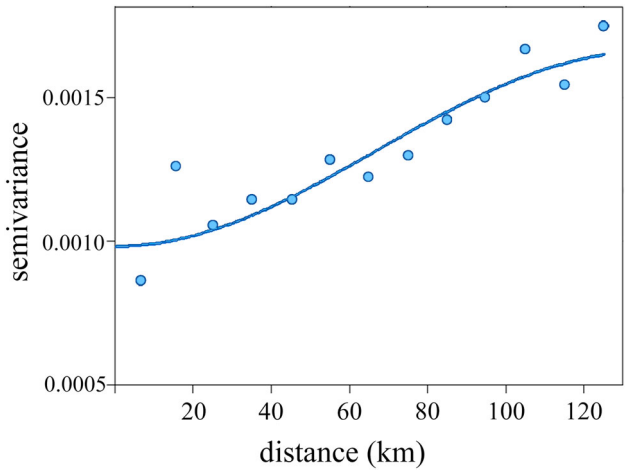

Fig. 5 Kriging variogram

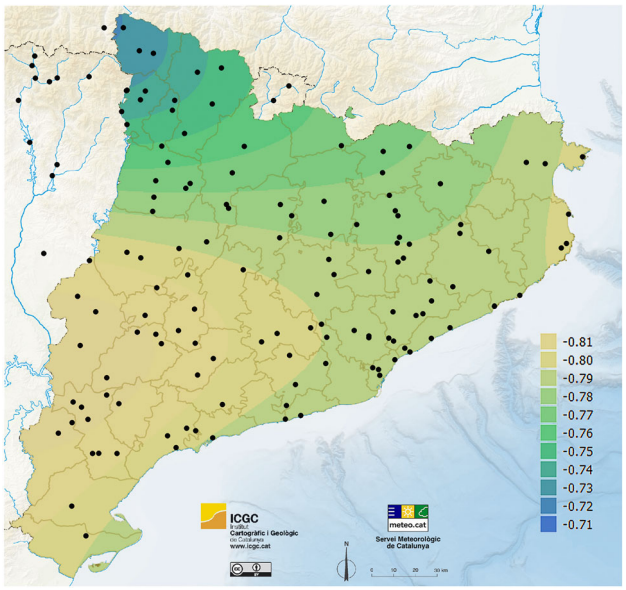

Fig. 6 Spatial distribution of the scaling parameter β over Catalonia

low values of interpolated β. The eastern coastline is clearly influenced by the Mediterranean and heavy rain episodes occur often associated with Mediterranean low-pressure systems that bring wet eastern winds to this area. The rainfall pattern of this eastern area is characterized by low total annual amounts collected mainly in Autumn. Therefore, the climatic characteristics of this area support the rainfall irregularity suggested by the empirical β values.

Overall, a negative gradient of β values is observed to increase towards the coastline where the rainfall pattern becomes more influenced by the Mediterranean Sea, with the exceptions of the central and southern coastline in its most proximity to the Sea. This exception is actually caused by an area of lower β values in the west associated with an irregularity of the rainfall pattern not caused, in this case, by the Mediterranean influence but by the droughtiness of the region. The regularity of the rainfall pattern associated with high β values is clearly supported by the climatic rainfall characteristics of the northwestern area.

As it can be seen in Fig. 7a, a significant correlation between the scaling parameter and mean annual rainfall can be observed, β increasing with mean annual rainfall. This correlation has been especially noticed in the two distinct zones highlighted before (high β values and annual rainfall amounts in the NW in contrast to western low β values and dry areas). Figure 7b shows that β increases with the percentage of annual precipitation amount that occurs during the maximum rainfall day. This contribution of the maximum rainfall day to the total amount is related with rainfall irregularity. Figure 8a, b shows that no dependence has been observed between β and longitude, whereas there is some correlation with latitude, β increasing towards north. There is also some correlation with altitude (Fig. 9a), β being higher to greater height, and with the distance to coastline (Fig. 9b).

Climate trends of the scaling parameter β

It is commonly assumed that one of the consequences of global warming will be an intensification of the hydrological cycle (Huntington 2006) which may lead to an increase of precipitation, among other hydrological variables. In fact, an increase in total rainfall in the last decades has been reported in middle and high latitudes (IPCC 2007). Despite of this, several studies have evidenced a decreasing trend of total precipitation over the Mediterranean area: one of the conclusions of the Regional Climate Change Report of the CLIVAR-Spain network (Pérez and Boscolo 2010) was that in the last decades, the annual precipitation in the Iberian Peninsula has significantly decreased compared to the 1960s and 1970s, especially at the end of winter, whereas an increase of extreme rainfall was observed. Some regional climate model projections pointed a potential increase in intensity and frequency of heavy and torrential rainfall in many areas of Europe for the 21st century (Christensen and Christensen 2003), despite a general decreasing trend in average summer precipitation. Buonomo et al. (2007) found also an increase of extreme rainfall over Europe, greater as both the return period of the rainfall becomes longer and the duration considered becomes shorter, and Rodríguez et al. (2014) obtained a slightly higher increase of the expected hourly rainfall in Barcelona (Catalonia, Spain) compared to daily rainfall increase. Due to its apparent connection to rainfall pattern characteristics, some changes in the rainfall scaling behavior are expected to be detected along with this

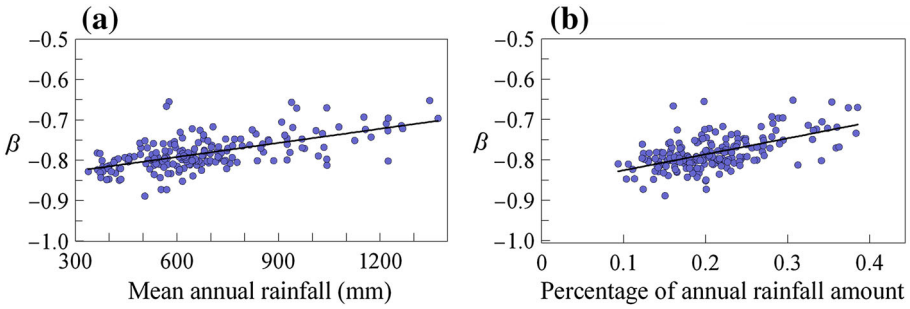

Fig. 7 Dependence of the scaling parameter β on **a** mean annual rainfall and **b** ratio between the maximum daily and mean annual rainfall

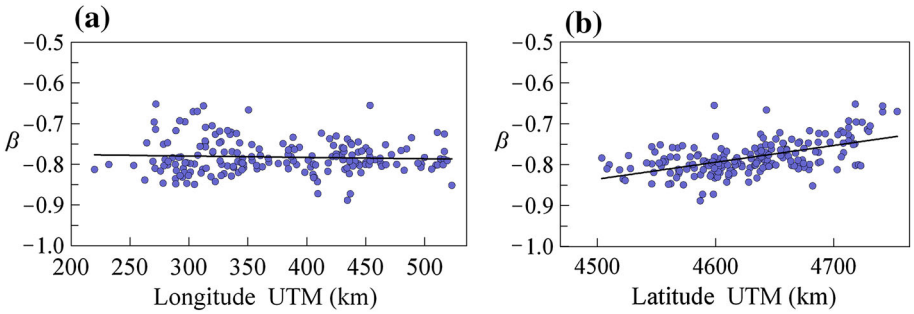

Fig. 8 Dependence of the scaling parameter β on **a** longitude and **b** latitude

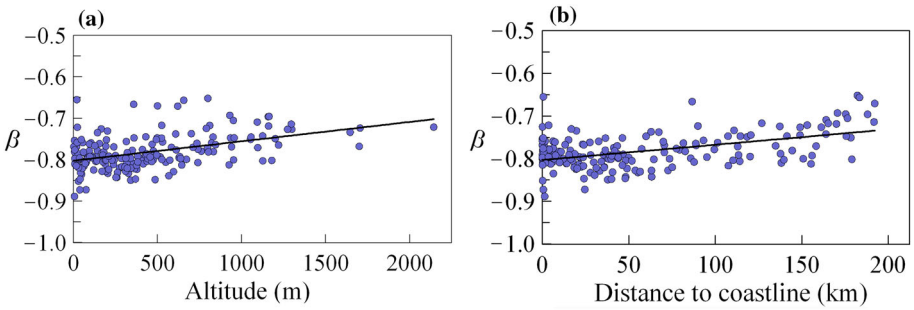

Fig. 9 Dependence of the scaling parameter β on **a** altitude above sea level and **b** distance to coastline

assumed trend of decrease in annual precipitation and relative increase in extreme rainfall.

To analyze the temporal evolution of the scale parameter β during the twentieth century and the beginning of the current century, the values of this parameter have been calculated by taking sliding intervals of 30 years varying the temporal range in 1 year. The mean value of the β parameter of the set of stations in Catalonia has been slightly decreasing as the 20th century progressed (Fig. 10), although only in the Western Pyrenees area, the downward trend has statistical significance for a 95% confidence level ($p < 0.05$) according to the non-parametric method of Mann–Kendall (Mann 1945; Kendall 1975) (Fig. 11). In the sequence corresponding to the Western Pyrenees, there is a greater decrease of the β parameter from the second half of the 20th century. This result seems compatible with the reduction of the amount of annual rainfall detected since 1950 in some studies carried out in Catalonia and nearby areas (SMC 2016; Esteban et al. 2013). The Annual Bulletin of Climate

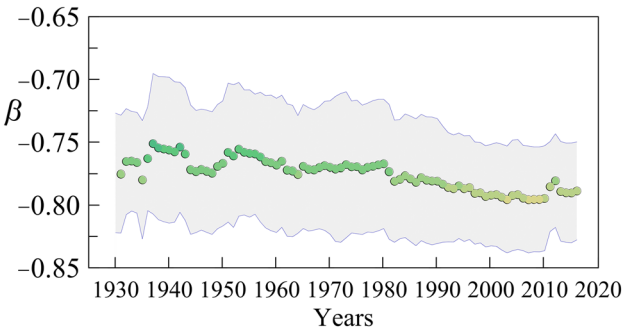

Fig. 10 Temporal evolution of the scaling parameter β in Catalonia. Points show the mean of all values; shaded areas represent data dispersion ($\pm$ σ)

Indicators (SMC 2016) shows that almost all the territory of Catalonia has registered a slight decreasing trend of precipitation since 1950, but the rainfall decline only exceeds the threshold of statistical significance in some areas of the Pyrenees, the Pre-Pyrenees, and the center of the territory. The SMC (2016) study shows also that the

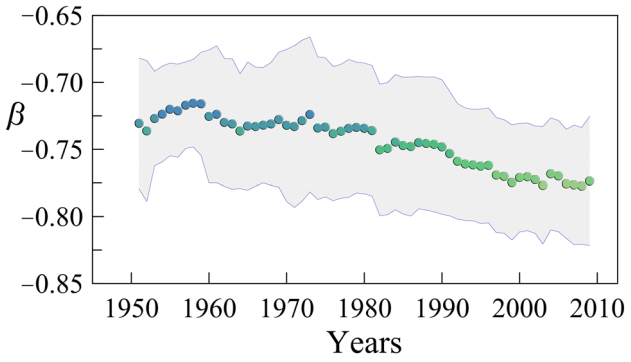

Fig. 11 Temporal evolution of the scaling parameter β in Western Pyrenees. Points show the mean of all values; shaded areas represent data dispersion ($\pm\ \sigma$)

SDII climate index (annual total precipitation divided by the number of days with precipitation higher than 1 mm) in the area of the Pyrenees presents a statistically significant positive trend which indicates that annual precipitation is divided by fewer days of precipitation. In the same area, the CWD index (maximum number of consecutive days in a year with precipitation equal to or greater than 1 mm) shows a trend with statistical significance towards the decrease. Esteban et al. (2013) also recorded a significant fall in annual rainfall in Andorra (Pyrenees) for the second half of the 20th century and the beginning of the current century.

It is remarkable that the β sequence obtained from the centennial daily rainfall series registered at the Ebre Observatory (1905–1916) clearly shows a decreasing trend with statistical significance (Fig. 12). The Ebre Observatory is located in the south of Catalonia, in a region with values of β lower than $-$ 0.80. The temporal evolution of the climate index SDII in the Ebre Observatory shows a gradual increase of +0.14 mm/day per decade, at the limit of the statistical significance ($p = 0.05$) (SMC 2016).

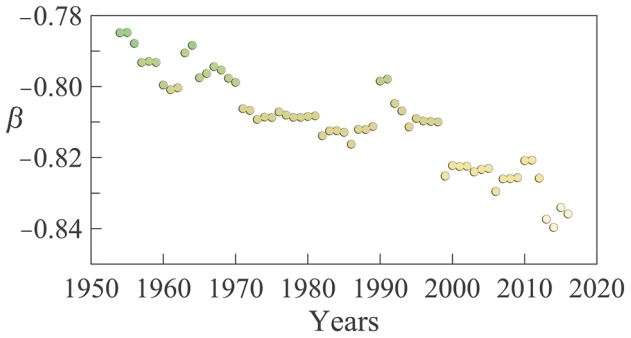

Fig. 12 Temporal evolution of the scaling parameter β in the Ebre Observatory

Conclusions

In most part of the Catalonian territory, the empirical values of the scaling parameter β range between $-$ 0.84 and $-$ 0.70, with a mean of $-$ 0.79. Despite of the high variability of this parameter, which seems to depend on the longitude of the sample and the presence of particular high intense episodes in it, a spatial analysis yields a certain configuration which can be related to some specific climatic rainfall characteristics. Analyzing the spatial distribution of this parameter, two distinct zones have been detected: (1) a northern area with a mean value of $-$ 0.75, matching a mountainous area with some Atlantic influence at its most northwestern end, and (2) a western area with a mean value of $-$ 0.81, in great concordance with the driest areas in Catalonia. Apart from these distinct zones, at the East, low β values are distributed over areas of clear Mediterranean influence where convective rainfall occurs often. On the other hand, the highest values of β are found mainly in the NW where large rainfall accumulations are most often caused by episodes of continuous rain. This results are in agreement with those obtained by Rodríguez-Solà et al. (2017), who found a general concordance between the spatial distribution of β over the Iberian Peninsula and the mean annual precipitation distribution, with high values in rainy areas and low for the dry ones, with some discrepancies related to the kind of precipitation contributing to high rainfall events and the proportion of convective rainfall in total. Thus, a good correlation between the scaling parameter and mean annual rainfall has been observed, β increasing with mean annual rainfall. This correlation has been especially noticed in the two distinct zones highlighted before (high β values and annual rainfall amounts in the NW in contrast to western low β values and dry areas). However, an increase of the value of β with the percentage of annual precipitation amount that occurs during the maximum rainfall day has been observed also; an expected result, since the contribution of the maximum rainfall day to the total amount is related with rainfall irregularity. No dependence has been observed between β and longitude, whereas there is some correlation with latitude, β increasing northward. As expected, there is also some correlation, with altitude, β being higher at greater elevation, and with the distance to coastline attributed to the influence of the Mediterranean Sea. A general negative gradient of β values is observed to increase towards the coastline, with the exceptions of central and southern coast due to the low β values observed in the arid western area of Catalonia. The regularity of the rainfall pattern associated with high β values is clearly supported by the climatic rainfall characteristics of the northwestern area.

The analysis of the temporal evolution of the scaling parameter β during the 20th century has allowed us to detect some remarkable changes in the rainfall scaling behavior in Catalonia. The mean value of the scaling parameter β for all stations shows a slight decreasing trend over the past century and the beginning of the current one. This trend is statistically significant in the Western Pyrenees, where the greater decrease of β has been found from the second half of the 20th century, in concordance with the decreasing trend of the annual precipitation detected in this area since 1950. In addition, in the southern area of the Catalonian territory where values of β are mostly lower than -0.80, the sequencing of β obtained from the centennial daily rainfall series registered at the Ebre Observatory (1905–1916) clearly shows a decreasing trend with statistical significance during the second half of the 20th century. These results are compatible with the expected trend of decrease in annual precipitation and relative increase in extreme rainfall in many areas of Europe projected by several regional climate models for the 21st century (Pérez and Boscolo 2010; Christensen and Christensen 2003).

Acknowledgements We gratefully acknowledge to Servei Meteorològic de Catalunya (Generalitat de Catalunya) and Observatori de l'Ebre for providing the data analyzed in this work. We are also grateful to the anonymous referees for their useful suggestions.

Compliance with ethical standards

Conflicts of interest On behalf of all authors, the corresponding author states that there is no conflict of interest.

References

Aronica GT, Freni G (2005) Estimation of sub-hourly DDF curves using scaling properties of hourly and sub-hourly data at partially gauged site. Atmos Res 77(1–4):114–123. https://doi.org/10.1016/j.atmosres.2004.10.025

Bara M, Kohnová S, Gaál L, Szolgay J, Hlavčová K (2009) Estimation of IDF curves of extreme rainfall by simple scaling in Slovakia. Contrib Geophys Geod 39(3):187–206

Bara M, Gaál L, Kohnová S, Szolgay J, Hlavčová K (2010) On the use of the simple scaling of heavy rainfall in a regional estimation of IDF curves in Slovakia. J Hydrol Hydromech 58(1):49–63. https://doi.org/10.2478/v10098-010-0006-0

Bell FC (1969) Generalised rainfall–duration–frequency relationships. J Hydraul Division ASCE 95(1):311–327

Buonomo E, Jones E, Huntingford C, Hammaford J (2007) On the robustness of changes in extreme precipitation over Europe from two high resolution climate change simulations. Quart J R Meteorol Soc 133:65–81. https://doi.org/10.1002/qj.13

Burlando P, Rosso R (1996) Scaling and multiscaling models of depth-duration-frequency curves for storm precipitation. J Hydrol 187:45–64. https://doi.org/10.1016/S0022-1694(96)03086-7

Casas MC, Codina B, Redaño A, Lorente J (2004) A methodology to classify extreme rainfall events in the western Mediterranean area. Theoret Appl Climatol 77:139–150. https://doi.org/10.1007/s00704-003-0003-x

Casas-Castillo MC, Rodríguez-Solà R, Navarro X, Russo B, Lastra A, González P, Redaño A (2018) On the consideration of scaling properties of extreme rainfall in Madrid (Spain) for developing a generalized intensity-duration-frequency equation and assessing probable maximum precipitation estimates. Theor Appl Climatol 131(1):573–580. https://doi.org/10.1007/s00704-016-1998-0

Christensen JH, Christensen OB (2003) Severe summertime flooding in Europe. Nature 421:805–806. https://doi.org/10.1038/421805a

Desramaut N (2008) Estimation of intensity Duration Frequency Curves for Current and Future Climates [Thesis of Master], Department of Civil Engineering and Applied Mechanics, McGill University, Montreal, Quebec (Canada). http://digitool.library.mcgill.ca/R/-?func=dbin-jump-full&object_id=40816&current_base=GEN01

Esteban P, Prohom M, Aguilar E (2013) Tendencias recientes e índices de cambio climático de la temperatura y la precipitación en Andorra, Pirineos (1935-2008). Pirineos. Revista de ecología de montaña 167:89–108. https://doi.org/10.3989/Pirineos.2012.167005

Ferreri G, Ferro V (1990) Short-duration rainfalls in Sicily. J Hydraulic Eng ASCE 116(3):430–435. https://doi.org/10.1061/(ASCE)0733-9429(1990)116:3(430)

Gupta VK, Waymire E (1990) Multiscaling properties of spatial rainfall and river flow distributions. J Geophys Res 95(D3):1999–2009. https://doi.org/10.1029/JD095iD03p01999

Huntington TG (2006) Evidence for intensification of the global water cycle: review and synthesis. J Hydrol 319(1–4):83–95. https://doi.org/10.1016/j.jhydrol.2005.07.003

Kendall MG (1975) Rank correlation methods. Charles Griffin, London, p 6

Koutsoyiannis D, Foufoula-Georgiou E (1993) A scaling model of storm hyetograph. Water Resour Res 29(7):2345–2361. https://doi.org/10.1029/93WR00395

Koutsoyiannis D, Kozonis D, Manetas A (1998) A mathematical framework for studying rainfall intensity-duration-frequency relationships. J Hydrol 206(1–2):118–135. https://doi.org/10.1016/S0022-1694(98)00097-3

Mann HB (1945) Nonparametric tests against trend. Econometrika 13:245–259

Menabde M, Seed A, Pegram G (1999) A simple scaling model for extreme rainfall. Water Resour Res 35(1):335–339. https://doi.org/10.1029/1998WR900012

Pérez FF, Boscolo R (2010) Clima en España: Pasado, presente y futuro. Informe de Evaluación del Cambio climático Regional. Red Temática CLIVAR-España. http://clivar.iim.csic.es/files/informe_clivar_final.pdf

Pérez-Zanón N, Casas-Castillo MC, Rodríguez-Solà R, Peña JC, Rius A, Solé JG, Redaño A (2015) Analysis of extreme rainfall in the Ebre Observatory (Spain). Theor Appl Climatol 124(3–4):935–944. https://doi.org/10.1007/s00704-015-1476-0

Rodríguez R, Navarro X, Casas MC, Ribalaygua J, Russo B, Pouget L, Redaño A (2014) Influence of climate change on IDF curves for the metropolitan area of Barcelona (Spain). Int J Climatol 34:643–654. https://doi.org/10.1002/joc.3712

Rodríguez-Solà R, Casas-Castillo MC, Navarro X, Redaño A (2017) A study of the scaling properties of rainfall in Spain and its appropriateness to generate intensity-duration-frequency curves from daily records. Int J Climatol 37(2):770–780. https://doi.org/10.1002/joc.4738

Schertzer D, Lovejoy S (1987) Physical modelling and analysis of rain and clouds by anisotropic scaling multiplicative processes. J Geophys Res 92(D8):9693–9714. https://doi.org/10.1029/JD092iD08p09693

Schertzer D, Lovejoy S (2011) Multifractals, generalized scale invariance and complexity in geophysics. Int J Bifurc Chaos 21(12):3417–3456. https://doi.org/10.1142/S0218127411030647

Servei Meteorològic de Catalunya (2017) Butlletí Anual d'Indicadors Climàtics 2016. Departament de Territori i Sostenibilitat. Generalitat de Catalunya. http://static-m.meteo.cat/wordpressweb/wp-content/uploads/2017/05/29072030/00_BAIC-2016_TOT.pdf

Yu PS, Yang TC, Lin CS (2004) Regional rainfall intensity formulas based on scaling property of rainfall. J Hydrol 295(1–4):108–123. https://doi.org/10.1016/j.jhydrol.2004.03.003